Dissertation

zur

Erlangung der Doktorwürde (Dr. rer. nat.)

der

Naturwissenschaftlich-Mathematischen Gesamtfakultät

der

Ruprecht-Karls-Universität Heidelberg

Thema

Engineering of Aerosol-Jet Printed Carbon Nanotube Network Transistors

Vorgelegt von

Marcel Rother

geboren in Meißen

Gutachter

Prof. Dr. Jana Zaumseil

Prof. Dr. Uli Lemmer

Tag der mündlichen Prüfung: 08. März 2019

Dissertation

to obtain the degree of

Doctor of the Natural Sciences (Dr. rer. nat.)

submitted to the

Combined Faculty of Natural Sciences and Mathematics

at

Heidelberg University, Germany

Topic

Engineering of Aerosol-Jet Printed Carbon Nanotube Network Transistors

Presented by

Marcel Rother (M. Sc.)

born in Meißen

Reviewer

Prof. Dr. Jana Zaumseil

Prof. Dr. Uli Lemmer

Oral examination: March 08th, 2019

If you thought science was certain – well, that is just an error on your part.

Richard P. Feynman

ACKNOWLEDGEMENTS

This thesis and the experimental work behind it would not have been possible without the help, support, guidance, and cooperation of a vast number of friends, colleagues, partners, and family.

First of all, I want to thank **Jana Zaumseil** not only for enabling to work on the scientific projects included in this work and the associated academic advice, constructive criticism, and guidance, but also for the possibility to accompany several non-academic projects and develop the workflows in this group, the thereby trusted confidence in my work, and the expressed appreciation.

During the years in the Nanomaterials for Optoelectronics (NMOE) group I had the pleasure to share offices (in 2 cities and 3 buildings) with **Florentina Gannott**, **Stefan Schießl**, **Manuel Schweiger**, **Stefan Grimm**, **Maximilian Brohmann**, **Maik Matthiesen**, **Kevin Synnatschke**, and **Felix Berger**, who made late work and long days more bearable and beyond that became good friends that helped in various situations and ensured enjoyable after-work activities.

A lot more full-time group members supported me, became friends, and/or were involved in activities in and out of the lab, namely **Martin Held**, **Severin Schneider**, **Florian Jakubka**, **Julia Binder**, **Yuriy Zakharko**, **Katrin Ludwig**, **Arko Graf**, **Claudia Backes**, **Farnia Rashvand**, **Chloe Francis**, **Fabian Paulus**, **Katelyn Goetz**, **Thomas Higgins**, **Vaishnavi Rao**, **Jan Lüttgens**, **Sebastian Grieger**, **Maximilian Krings**, **Steffen Ott**, and **Merve Balci**.

There have been several students under my supervision that evaluated new materials, tested parameters, optimized processes and thereby contributed to this work whether visibly or invisibly: **Andreas Malhofer**, **Shuyi Yang**, **Steffen Ott**, **Caroline Krzyszkowski**, **Adelaide Kruse**, and **Marian Rosenthal**.

At the chair for Applied Physical Chemistry, quite a few people organized or assisted with administrative issues: **Karin Jordan**, **Svetlana Duchnay**, **Benjamin Scherke**, **Rainer Dahint**, **Michael Zharnikov**, and **Matthias Jankowski**.

A lot of experiments or setups for fabrication and evaluation would not have been possible without the technical stuff of the mechanics workshop, **Klaus Schmitt**, **Marco Billmaier**, **Mert Kaya**, **Andreas Kreiter**, **Jonas Windelband**, or IT and technical support from **Peter Jeschka**, **Günter Meinusch**, and **Reinhold Jehle**.

Right at the beginning of my work for this thesis, I had the opportunity to stay at the University of Minnesota and get first-hand experience on the aerosol-jet printer that would accompany me for more than 3 years thereafter. Thanks to **Daniel Frisbie** and **Scott White** for hosting and supporting me, as well as **Dayne Plemmons**, **Boo Schliep** and all the others I met during the time who made it very enjoyable and informative.

In Heidelberg also a lot more supporters need to be mentioned as they helped with advice, support, and information of all kinds: **Silke Koser** from the Institute for Organic Chemistry, **Stefan Kauschke**, **Olaf Skibbe**, and **Martina Anselmann** from the Center of Advanced Materials, **Thomas Peissig**, **Karsten Bensch**, **Kai Sudau**, **Martin Gutfleisch**, **Gerardo Hernández-Sosa**, **Sebastian Stolz**, **Tobias Rödlmeier**, **Hildegard Merkle**, and **Anne-Katherine Mang** from the InnovationLab GmbH, **Alexey Tarasov**, **Marcin Filipiak**, and **Natalie Haustein** from BioMedX GmbH.

A special thanks to all the proofreaders that helped to free this thesis of typos and other errors.

Many of those I spent time with working and learning in the last decade became and stayed very good friends. I especially want to thank those that made it possible to stay in contact even after scattering all about Germany and its neighboring countries. Every time we manage to meet despite the distances and full calendars, it feels like we met the last time just a week before. Thanks to all my friends for mental, emotional, and practical support, for the fun times we had and will have in the future. Thanks to the ones I became friends with through school or handball while still living in **Kleinwallstadt**. Thanks to my friends from **Würzburg**, **Toronto**, and **Erlangen**. We spent a lot of time together during the studies and had a great time together. Thanks to everyone I met in **Heidelberg** and I am still happy to meet anytime soon again, although some of you already moved and now I followed this trend and left Heidelberg after some time. Unfortunately, I cannot name all of you in person or this document would get even much longer.

Ein besonderer Dank geht an meine **Familie**, vor allem an meine **Eltern** für die Unterstützung vor, während und nach dem Studium, für viele liebgemeinte und ernste Ratschläge, für die Zeit die Ihr für mich aufgewendet habt, und dafür, dass ihr immer für mich da seid, sowie meine **Großeltern** für die jahrelange Unterstützung.

Last but not least I want to thank **Fiona** for being with me, being there for me, supporting me, enduring my flaws, and pushing me to finishing up this work.

ABSTRACT

Thanks to their extremely high mobilities, semiconducting carbon nanotubes (CNTs) are a promising material for high speed electronics. Beyond that, CNT networks are inherently flexible and stretchable and can be processed from dispersions resulting in devices with still remarkable electronic properties. They can fulfill many of the various requirements for novel applications including fast switching speeds and high currents at low drive voltages. Depending on the intended use, one or another device property might be more important. CNT networks, processes, and architectures can be tailored to yield devices that can serve the respective purpose. Highly purified semiconducting CNTs are, however, still rather expensive and direct-write techniques are thus preferred to enable variable designs and reduce manufacturing costs.

In this work, aerosol-jet printing is investigated as a deposition technique for CNTs that works with small ink volumes but can also be upscaled by parallelization and integrated into high-throughput roll-to-roll printing processes. After the development of printable inks, it is shown that the printing process itself has no influence on the quality of the CNTs although sonication is used to transfer the ink into an aerosol. The electronic properties of CNT networks incorporated in an established transistor structure exhibit reproducibility comparable to other deposition techniques. Moreover, additive manufacturing enables the deposition of several layers on top of each other to increase the overall film thickness up to optically dense films visible to the naked eye. Field-effect mobilities and on-conductances increase and the hysteresis decreases for thicker films compared to dense but thin networks.

Based on these findings, CNT films are printed with a thickness of 50–600 nm and vertical charge transport is demonstrated. These films are subsequently sandwiched between electrodes and electrolyte-gating results in doping of CNT films throughout electrode overlap areas of several hundred μm^2. The vertical device architecture decouples the printing accuracy from the critical device dimensions while supporting high currents for a small footprint. A comparison of different printed electrode materials reveals the superior properties of printed metals over mixed (metallic and semiconducting) CNTs. Electrodes based on inkjet-printed gold nanoparticles are additionally used on flexible substrates and stable device performance even after several hundred bending cycles is demonstrated for vertical and lateral CNT network transistors. These all-printed devices are promising for further development of electronic circuits that do not require high operating frequencies but rather flexibility, high-currents, and small footprints.

KURZFASSUNG

Dank ihrer extrem hohen Ladungsträgermobilität sind halbleitende Kohlenstoff-Nanoröhrchen (*engl.* carbon nanotubes, CNTs) ein vielversprechendes Material für Anwendungen in der Hochgeschwindigkeitselektronik. Darüber hinaus sind Netzwerke aus CNTs flexibel, dehnbar und können aus Dispersionen abgeschieden werden. Transistoren basierend auf CNT-Netzwerken weisen noch immer bemerkenswerte elektronische Eigenschaften auf. Sie sind daher für diverse neue Anwendungen geeignet, welche nicht nur hohe Schaltgeschwindigkeiten und Ströme – bei gleichzeitig niedrigen Spannungen – benötigen. Je nach gewünschter Anwendung ist hierbei die eine oder andere Eigenschaft maßgebend. CNT-Netzwerke, Prozesse und Bauteil-Architekturen können entsprechend angepasst werden, um Transistoren zu fertigen, welche die jeweiligen Anforderungen optimal erfüllen. Da das aufgereinigte Material jedoch noch immer relativ teuer ist, wird die Abscheidung mittels direkt strukturierender Prozesse bevorzugt, um variable Designs zu ermöglichen und die Herstellungskosten zu senken.

In dieser Arbeit wird das Aerosol-Jet-Drucken als eine Möglichkeit zur Abscheidung betrachtet, welche auch mit kleinen Tintenvolumina arbeiten und gleichzeitig durch Parallelisierung hochskaliert und in Rolle-zu-Rolle-Prozesse mit hohem Durchsatz integriert werden kann. Zunächst werden druckbare Tinten entwickelt, bevor gezeigt wird, dass der Druckprozess selbst keinen Einfluss auf die Qualität der CNTs hat, obwohl Ultraschall zur Aerosol-Bildung eingesetzt wird. Die Reproduzierbarkeit der Transistoreigenschaften, welche in einem ähnlichen Bereich wie jene anderer Abscheidungstechniken liegt, wird mittels einer etablierten Transistor-Architektur, in welche die gedruckten CNT-Netzwerke eingebaut werden, untersucht. Durch das Drucken von mehreren Schichten übereinander ist es weiterhin möglich, dicke Filme zu erhalten, welche mit bloßem Auge sichtbar sind. Verglichen mit dichten aber dünnen Netzwerken, weisen Transistoren mit dickeren Filmen höhere Feld-Effekt-Mobilitäten und Ströme bei gleichzeitig niedrigerer Hysterese auf.

Anhand von Schichten mit einer Dicke von 50–600 nm wird anschließend der Ladungstransport in vertikaler Richtung durch den CNT-Film demonstriert. Der Ladungstransport durch Filme, welche zwischen Goldelektroden eingebettet sind, kann mittels einer an einer dritten Elektrode angelegten Spannung und eines Elektrolyten als Dielektrikum, selbst bei einem Überlapp der Elektroden von mehreren hundert Quadratmikrometern, ein- und ausgeschaltet werden. Diese vertikale Transistor-Architektur entkoppelt die kritischen Transistor-Dimensionen von der

Genauigkeit des Druckprozesses, während hohe Ströme bei einer kleinen Grundfläche realisierbar sind. Ein Vergleich verschiedener gedruckter Elektrodenmaterialien zeigt sich die Überlegenheit von metallischen Materialien gegenüber gemischten (metallischen und halbleitenden) CNT-Netzwerken. Mittels Inkjet-gedruckten Elektroden aus Gold-Nanopartikeln kann ein stabiles Transistor-Verhalten auch nach mehreren hundert Biegezyklen auf flexiblen Substraten gezeigt werden. Diese vollständig gedruckten Transistoren sind vielversprechend für die weitere Entwicklung von elektronischen Schaltkreisen, welche mechanische Flexibilität und hohe Ströme bei niedrigem Flächenbedarf anstelle hoher Schaltfrequenzen benötigen.

CONTENTS

CHAPTER 1

INTRODUCTION

For more than 70 years transistors have been the fundamental components of virtually all modern electronic products and ensure the operation of a wide range of electronic devices from simple circuits, sensors, and controllers, to telecommunication and data processing in combination with computers and mobile phones. Over the last decades, the improvement of transistors and their applications has been mostly driven by cost reduction and miniaturization.

More recently, the restrictions of traditional rigid silicon and other inorganic semiconductors were sought to be overcome to achieve freedom of design and shape as well as overall flexibility of the final products. Existing prototypes, design drafts, and already available products include rollable or foldable displays, light-sources, and solar cells, stretchable sensors, intelligent clothing, and more. The realization of unlimited flexibility and stretchability, requires new materials and/or device architectures that are compatible with mechanical deformation.

Moving towards flexible devices simultaneously introduces the necessity to develop new fabrication methods. Batch production – often requiring vacuum and/or high temperature processing – is traditionally used in silicon electronics with areal material deposition that requires subsequent high-resolution patterning (top-down). Flexible substrates on the other hand enable roll-to-roll processing technologies known from newspaper printing with direct and additive patterning of the deposited material (bottom-up). Printing technologies could reduce the manufacturing costs of electronic devices, due to high throughput, fast and simple variation of the printing patterns and low processing temperatures. However, the achievable resolution and registration are limited.

Networks of single-walled carbon nanotubes (CNTs) are one of the promising material candidates for printed electronics on flexible or stretchable substrates. While a mixture of ⅓ metallic and ⅔ semiconducting nanotubes is produced during synthesis, recent advances in sorting techniques enable the dispersion of almost purely semiconducting species.[1] Printed nanotube networks can thus not only be used as electrodes but also as the semiconductor in light-emitting diodes, photovoltaics, and transistors. Although nanotube networks cannot reach the charge carrier mobilities of individual CNTs (up to several thousand $\mathrm{cm^2\ V^{-1}\ s^{-1}}$) due to limitations by nanotube–nanotube junctions, current CNT network field-effect transistors were able to achieve charge carrier mobilities of more than 100 $\mathrm{cm^2\ V^{-1}\ s^{-1}}$.[2] Utilized as conductors, sheet resistances of less than 100 $\Omega\ \square^{-1}$ were reported even for semi-transparent CNT layers.[3, 4]

Besides their favorable mechanical and electronic properties, CNTs can be readily dispersed in organic solvents or water, which makes them ideal candidates for printing processes at low temperatures.[1] Although various printed electronic devices have been demonstrated, it remains to be evaluated, which deposition method is most suitable for the different layers of a transistor. Depending on the application, transistors based on printed CNTs have to fulfill a number of requirements, *e.g.* reproducibility, high on/off-ratios, fast switching speeds, long-term stability, high current densities, small footprint, flexibility, and stretchability. Moreover, compared to photolithographic structuring methods, the achievable resolution and layer-to-layer registration is lower by several orders of magnitude. Hence, the printing parameters have to be carefully optimized and device architectures have to be adapted or specifically developed.

Especially for transistors with variable designs, prototypes, or proof-of-concept studies, direct-write technologies that do not waste a large amount of material and can work with small ink volumes are desired, as purified nanotube material containing almost only semiconducting CNTs is still rather precious. The inks should also be free of additives as far as possible to avoid any negative impact on the charge transport through the deposited networks. These requirements are fulfilled by aerosol-jet printing,[5] a relatively new printing method that is used in this work for the deposition of networks of semiconducting (6,5) CNTs. After analyzing the reproducibility of device performance in a conventional transistor architecture, this technique was also used to deposit rather thick films for vertical charge transport in all-printed devices that overcome resolution limitations. Finally, lateral and vertical devices were fabricated on flexible polymer substrates and evaluated with respect to bending.

Chapter 2 gives an overview about carbon nanotubes including their band structure, electronic properties, and synthesis methods. Furthermore, methods to separate metallic and semiconducting CNTs and to determine the chirality of a CNT are introduced. The theoretical framework to understand unipolar and ambipolar transistors is provided and device architectures and patterning processes are explained. After an overview of materials and techniques used for printed electronics and the previously demonstrated devices, aerosol-jet printing as the main method used and evaluated in this work is presented.

Chapter 3 details the experimental procedures employed for device fabrication and characterization followed by the exact descriptions of materials and devices in **chapter 4.**

The results of the experimental work are presented in the subsequent sections. **Chapter 5** starts with the formulation of carbon nanotube inks suitable for aerosol-jet printing of the semiconducting layer in transistors. After evaluating the stability of these inks, the reproducibility of transistors printed from this material is examined with an established device structure. The initially rather high hysteresis is decreased by different techniques and applications of the printed CNT films, *e.g.* in electrochromic devices and transistors for different studies, based on the findings made before, are presented. This section ends with the description of limitations encountered during the preparation of CNT films via aerosol-jet printing.

While the focus of chapter 5 was mainly on the semiconducting nanotube network and thus photolithographically structured electrodes were used, **chapter 6** utilizes a recently developed vertical device architecture to avoid device dimensions that are incompatible with printing resolution and alignment accuracy. The necessary demonstration of three-dimensional charge transport and efficient electrolyte-gating of the whole nanotube network is followed by the resulting device characteristics and the comparison with lateral transistors fabricated from the same materials. Different electrode materials are subsequently evaluated with regard to the final device performance.

In **Chapter 7** the established procedures for lateral and vertical transistors based on aerosol-jet printed semiconducting CNTs are utilized to fabricate bendable devices on plastic substrates.

Chapter 8 summarizes the insights gained in this thesis and gives suggestions for future experiments and potential applications.

CHAPTER 2

BACKGROUND

This chapter provides the theoretical background on carbon nanotubes and transistors followed by an overview about methods and materials for printed electronics including aerosol-jet printing.

2.1. Carbon Nanotubes

2.1.1. Overview

For a long time, only amorphous carbon and two ordered carbon modifications have been known – diamond and graphite. Both modifications are well-studied and exhibit unique properties: Diamond is the hardest naturally occurring material and graphite shows – due to its planar crystal structure – strong anisotropy in its physical properties.[6] The discovery of new nano-scale carbon modifications started in 1985 with zero-dimensional fullerenes,[7] followed by one-dimensional carbon nanotubes (CNTs) which were first synthesized in 1991.[8] The two-dimensional graphene, essentially a single layer of graphite, was eventually found in 2004 and completed the range of low-dimensional carbon allotropes.[9] Further modifications of these structures were synthesized later, *e.g.* graphene nanoribbons (laterally confined graphene),[10, 11] carbon nano-onions (multi-walled fullerenes),[12, 13] or carbon nano-horns.[14] While multi-walled carbon nanotubes were synthesized and investigated as well, single-walled CNTs are particularly interesting because of their unique electronic properties. In this work, only single-walled CNTs were used and thus the term *carbon nanotube* refers to them only in this context.

Defect-free graphene consists of sp^2-hybridized carbon atoms arranged in hexagons within a two-dimensional plane. CNTs can be described as rolled-up graphene sheets forming one-dimensional hollow tubes. Depending on the direction and circumference of this rolled-up graphene sheet, different nanotubes are possible. The (n,m) notation commonly used to distinguish different CNT chiralities describes the vector along the nanotube circumference which is derived from the linear combination of the unit vectors $\mathbf{a}_1$ and $\mathbf{a}_2$ of the graphene unit cell, where $a = 0.246$ nm is the lattice constant (compare **Figure 2.1**):[1]

$$\boldsymbol{c} = n \cdot \boldsymbol{a_1} + m \cdot \boldsymbol{a_2} = n \cdot \frac{a}{2} \cdot \left(\sqrt{3}, 1\right) + m \cdot \frac{a}{2} \cdot \left(\sqrt{3}, -1\right) \qquad (2.1)$$

The alternative description of a CNT with the nanotube diameter d and the chiral angle Θ can be directly derived from this vector $\boldsymbol{c}$. Note that the chiral angle is defined as the angle between the chiral vector and the chiral vector of a zigzag nanotube, *i.e.* a nanotube with $m = 0$.

$$d = \frac{|c|}{\pi} = \frac{a}{\pi} \cdot \sqrt{n^2 + 2 \cdot n \cdot m + m^2} \qquad (2.2)$$

$$\Theta = \arctan\left(\frac{\sqrt{3} \cdot m}{2 \cdot n + m}\right) \qquad (2.3)$$

Nanotubes with a chiral angle of 30°, *i.e.* $n = m$, are called armchair nanotubes relating to the C–C bond structure following the hexagon outlines along the circumference of the CNT. Both zig-zag and armchair nanotubes are achiral. All other nanotubes with $0° < \Theta < 30°$ are chiral nanotubes. Larger chiral angles do not define new nanotubes but rather duplicates of the already mentioned possibilities. While nanotubes enantiomers, *i.e.* (n,m) and (m,n), were examined and even separated,[15-17] they are usually not distinguished especially for applications in electronics and for the chiral indices (n,m) with $n \geq m$ is used.

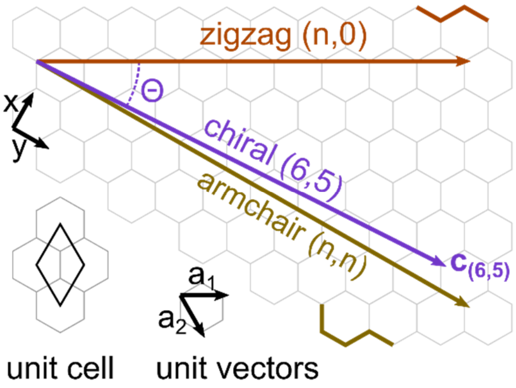

Figure 2.1: *Depiction of CNT chiralities with chiral angle Θ and chiral vector* **c**. *as well as the unit cell, and the unit vectors* $\mathbf{a}_1$ *and* $\mathbf{a}_2$ *leading to the (n,m) notation. Additionally, zigzag and armchair CNTs are illustrated with the direction of their chiral vectors and the structure of the C-C bonds along the circumference.*

2.1.2. Band structure

This section provides a very brief overview on the band structure of graphene and how to derive the band structure of carbon nanotubes therefrom. Detailed calculations and explanations can be found in literature.[18-26] Due to the sp^2-hybridization in defect free graphene and CNTs, the σ-bonds lie along the C–C axis and the delocalized π-electrons are found above and below the plane of carbon hexagons. As mentioned above, CNTs can be described as rolled-up graphene and the electronic structure of nanotubes can thus be derived from graphene. Using the tight-binding approximation as described in literature, the electronic structure of graphene is given by:[18]

$$E_{g2D}^{\pm}(\boldsymbol{k}) = \frac{\epsilon_{2p} \mp \gamma_0 \cdot w(\boldsymbol{k})}{1 \mp s \cdot w(\boldsymbol{k})} \qquad (2.4)$$

where

$$w(\boldsymbol{k}) = \sqrt{1 + 4 \cdot \cos\left(\frac{\sqrt{3} \cdot k_x \cdot a}{2}\right) \cdot \cos\left(\frac{k_y \cdot a}{2}\right) + 4 \cdot \cos^2\left(\frac{k_y \cdot a}{2}\right)} \qquad (2.5)$$

with the wave vector $\boldsymbol{k}$, the energy of the $2p$ atomic orbital ϵ_{2p}, the carbon–carbon interaction energy of nearest neighbors γ_0, and the tight-binding overlap integral s. **Figure 2.2** shows the band structure of graphene and the contour plot of the *Brillouin zone* for $\gamma_0 = -3.033$ eV and $s = 0.129$ including the high symmetry points Γ, K, and K'.[19] The π and π^* bands cross at the Fermi level and form a Dirac cone at the K-point, which is crucial for the electronic properties of graphene.[20]

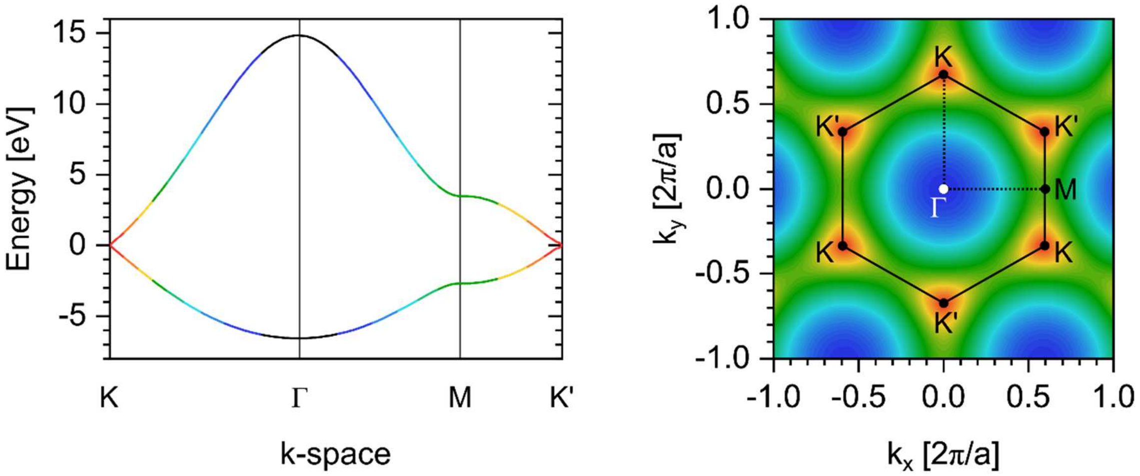

***Figure 2.2**: Band structure of graphene along K–Γ–M–K' (left) and contour plot of the valence band energy in the Brillouin zone with the high symmetry points Γ, K, K', and M (right).*

For one of the two atoms in the graphene unit cell, three different phases of the K-point wave function are possible: 0, $^2/_3\pi$, and $^4/_3\pi$ corresponding to 0°, 120°, and 240°. When rolling-up the graphene sheet into a CNT, carbon atoms with either a matching or mismatching phase are rolled on top of each other. In case of a phase match, the wave function can remain unchanged, *i.e.* the nanotube does not exhibit a bandgap and is thus metallic. If a phase mismatch occurs, the resulting wave function cannot go through the K point as it needs an additional enveloping wave function that compensates the phase by modulating it along the circumference of the CNT. This opens a band gap E_g which is inversely proportional to the diameter d and the resulting nanotube is semiconducting:[21]

$$E_g \approx \frac{0.7\ \text{nm}}{d}\ \text{eV} \tag{2.6}$$

With three different possible phases, one third of the nanotubes are thus metallic. The chiral indices of metallic nanotubes have a difference of zero or a multiple of 3, *i.e.* $(n\!-\!m) \bmod 3 = 0$, hence all armchair nanotubes are metallic. While the metallic CNTs theoretically show no band gap, mechanical deformation such as stress, torsion, or the inherent bending along the CNT circumference, can induce a small band gap, especially in small diameter tubes.[22, 23] Band gap changes of up to 100 meV at 1 % strain were found, thus exceeding the thermal energy at room temperature and presumably hindering charge transport through metallic CNTs.[23]

The one-dimensional band structure and hence the density of states (DOS) of CNTs can be derived using so-called parallel cutting lines in the reciprocal space.[24] In real space, the nanotube unit cell is defined by the chiral vector $\boldsymbol{c}$ along the circumference and a translation vector $\boldsymbol{T}$ along the CNT axis with

$$\boldsymbol{T} = \sqrt{3} \cdot \hat{\boldsymbol{z}} \times \boldsymbol{c} = (2m + n) \cdot \boldsymbol{a_1} - (2n + m) \cdot \boldsymbol{a_2} \tag{2.7}$$

where $\hat{z}$ is the orthogonal base vector in z-direction and $\boldsymbol{T}$ is thus orthogonal to $\boldsymbol{c}$ in the graphene plane. For cases of a common divisor of $(2m{+}2)$ and $(2n{+}m)$ the translational vector can be reduced:

$$\boldsymbol{T} = t_1 \cdot \boldsymbol{a_1} + t_2 \cdot \boldsymbol{a_2} \tag{2.8}$$

Transforming $\boldsymbol{T}$ and $\boldsymbol{c}$ into the reciprocal space leads to two orthogonal vectors $\boldsymbol{K_c}$ and $\boldsymbol{K_T}$:

$$\boldsymbol{K_c} = (t_1 \cdot \boldsymbol{b_2} - t_2 \cdot \boldsymbol{b_1}) \cdot N^{-1} \tag{2.9}$$

$$\boldsymbol{K_T} = (m \cdot \boldsymbol{b_1} - n \cdot \boldsymbol{b_2}) \cdot N^{-1} \tag{2.10}$$

where N is the number of hexagons in the CNT unit cell, and $\boldsymbol{b_1}$ and $\boldsymbol{b_2}$ are the unit vectors of graphene in the reciprocal space. The cutting lines have the length and direction of the axial vector $\boldsymbol{K_T}$ and propagate along with the circumferential vector $\boldsymbol{K_c}$ with a distance of $\pm|\boldsymbol{K_c}|$ (see **Figure 2.3**). The middle of the central cutting line is always at the Γ point and $N/2$ lines are possible along ±$\boldsymbol{K_c}$. If one cutting line (or its elongation) is passing through the K point, the respective nanotube is metallic, otherwise it is semiconducting.[24]

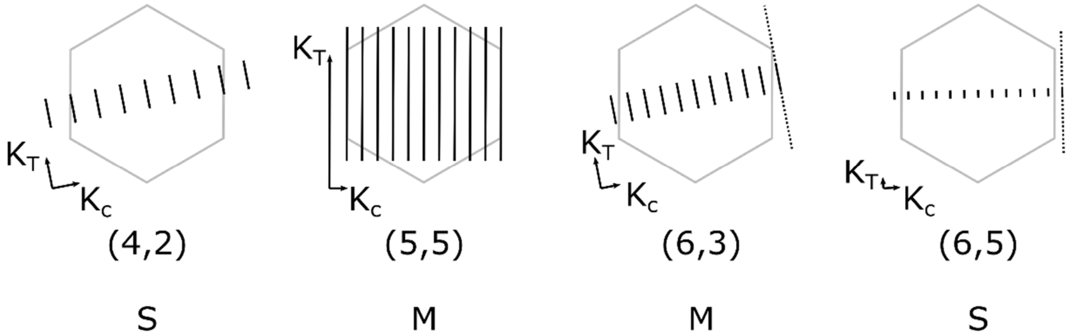

***Figure 2.3**: Cutting lines for four different CNT chiralities: semiconducting (4,2) and (6,5) as well as metallic (5,5) and (6,3). The reciprocal vectors* $\boldsymbol{K_c}$ *and* $\boldsymbol{K_T}$ *are given next to each depiction. The edges of the grey hexagon are the K and K' points, while the Γ point is in the center of the hexagon. The dashed lines elongate the cutting lines for (6,3) and (6,5) CNTs for better visibility of the cutting through the K point.*

With the zone-folding model, the band structure along the one-dimensional *Brillouin zone* (from the edge X via Γ to the second edge $X' = -X$) of the carbon nanotube can be derived.[24, 25] By using this model, the energy bands are extracted from the graphene band landscape at the cutting lines. The energy bands are then superimposed ("folded") into the CNT *Brillouin zone* yielding the band structure. It should be noted, that this model uses the band structure of flat graphene to derive the CNT band structure. This is however only true for large diameter nanotubes, as curvature effects distort the perfect hexagons and thus influence the actual situation. As a consequence, this concept can only represent an approximation of the band structure for small diameter CNTs. The density of states of carbon nanotubes exhibits sharp van Hove singularities (see **Figure 2.4**) where the cutting lines are tangential to the contours of the energy in the reciprocal space, *i.e.* at the local extrema of the one-dimensional energy bands.[24] This can also be seen in the calculation of the DOS where $dE_\mu(k)/dk \approx 0$ at the local extrema:[26]

$$DOS(E) = \frac{2}{N}\sum_{\mu=1}^{N}\int\left|\frac{dE_\mu(k)}{dk}\right|^{-1}\delta\big(E_\mu(k) - E\big)dE \qquad (2.11)$$

The possible optical transitions can be directly deduced from the DOS diagram (see **Figure 2.4**).

Only transitions with an energy E_{jj} between corresponding occupied (below the band gap) and unoccupied (above the band gap) state are possible, all other transitions are dipole-forbidden.

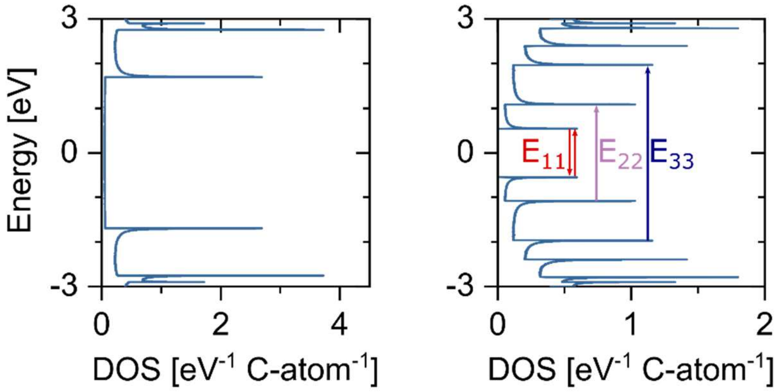

***Figure 2.4**: Density of states for a metallic (5,5) CNT (left) and a semiconducting (6,5) CNT (right). Note that DOS ≠ 0 between the first van Hove singularities for the (5,5) CNT but equals 0 for the (6,5) CNT. The optical transitions of emission (E_{11}) and absorption (E_{11}, E_{22}, E_{33}) are depicted for the (6,5) CNT (right). A dataset supplied by Maruyama was used for plotting the DOS.*[27]

2.1.3. CNT Chirality determination

The van Hove singularities in the DOS lead to defined absorption and emission spectra of carbon nanotubes with sharp peaks. This can be utilized for assigning chiralities present in liquid dispersions or solid films with different methods, *e.g.* absorption, Raman, or excitation–emission spectroscopy. The calculated possible transition energies of metallic and semiconducting CNTs and their relation to the nanotube diameter were summarized in the so-called *Kataura plot*.[28] Additional studies revealed differences between empirically derived values and calculated data that hint towards additional influences, *e.g.* of the solvent and dispersing agents,[29, 30] and the data were extrapolated to create an *empirical Kataura plot*.[31] The detailed plot allows chirality assignment as implied for (6,5) CNTs in **Figure 2.5**.

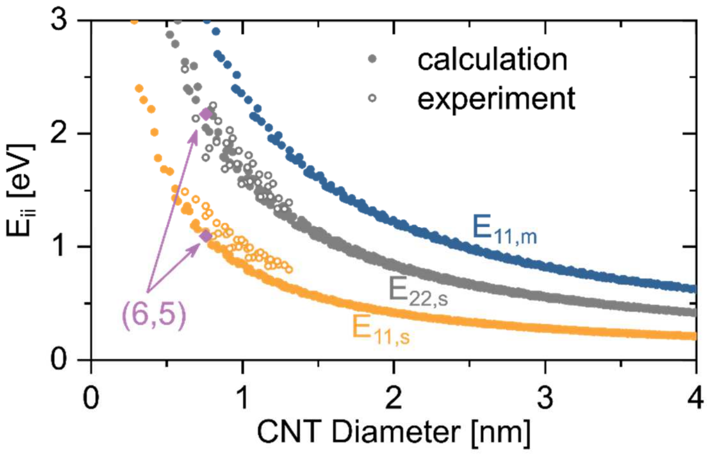

***Figure 2.5**: Kataura plot for calculated (solid symbols) and experimentally determined (open symbols) optical transitions for semiconducting (E_{11} and E_{22}) and metallic (E_{11} only) CNTs. The position of the E_{11} and E_{22} transitions of (6,5) CNTs is highlighted as an example. A dataset supplied by Maruyama was used for plotting the calculated transitions.*[32]

Absorbance spectroscopy is the easiest experimental method to gain a rough idea about the present CNT chiralities and can be used in dispersion as well as on solid films with a sufficient thickness to reach a reasonable signal-to-noise ratio. The absorbance of CNTs is strongest at the E_{11} transition. For small diameter ($d < 2$ nm) nanotubes this absorption falls in the near- to mid-infrared spectrum ($\lambda_{11} = 800$–3000 nm, $E_{11} = 1.6$–0.4 eV) while the weaker E_{22} transitions are often in the visible regime ($\lambda_{22} = 400$–750 nm, $E_{22} = 3.1$–1.6 eV). Further transitions, *e.g.* E_{33}, can be found at even higher energies (lower wavelengths) but show even further decreased intensities. As shown in **Figure 2.6**, sharp peaks with a linewidth of less than 25 meV are observed. Direct chirality assignment based on absorbance spectroscopy alone is not possible and spectra of two dispersions might exhibit peaks at the same position which originate from different chiralities, *i.e.* the E_{11} transition of (8,7) and (10,5) CNTs are barely distinguishable. The assignment is further hindered by the red-shift of the spectrum due to the influence of the polymer used to select only few CNT chiralities (compare section 2.1.6). The combination with emission-excitation or Raman spectra albeit enables the assignment of individual absorption peaks to certain chiralities.

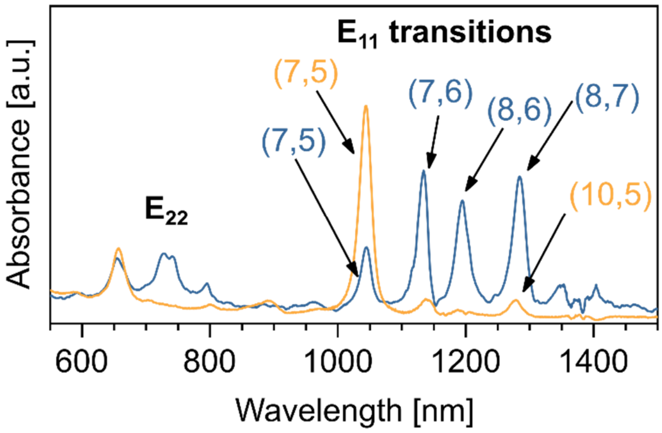

***Figure 2.6**: Absorbance spectra of two different CNT dispersions containing different CNT chiralities measured in toluene dispersion. Chiralities are labelled in the E_{11} transition area (1000–1500 nm). The E_{22} transitions are in the visible range (600–800 nm).*

Excitation–emission spectroscopy uses photoluminescence (PL) and the combination of E_{11} (emission) and E_{22} (excitation) for unambiguous chirality assignment.[29] Emission spectra of a dispersion or film are measured depending on the excitation wavelength and yield a map with peaks at the respective combinations of E_{11} and E_{22} (see **Figure 2.7**). For the case of individual nanotubes, the peaks visible in the photoluminescence maps are unique for a distinct CNT chirality, as no different chiralities with identical E_{11} and E_{22} exist. The line-shapes visible in the maps result from non-specific excitation of the wrapping-polymer and energy transfer to the nanotubes with smaller bandgaps. This feature can also occur if bundles are present or the nanotubes form a dense network in a deposited film.[33]

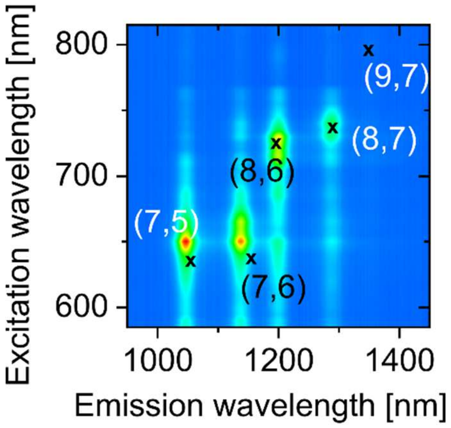

Figure 2.7*: Excitation–emission map of a dispersion of polymer-wrapped CNTs in toluene. Reproduced with permission from ACS Appl. Mater. Interfaces 2016, 8, 5571–5579.*[33]

Raman spectroscopy can be used to determine the diameter of a CNT by analyzing the so-called radial breathing modes (RBM) which are found in the Raman spectrum at wavenumbers of 100–350 cm^{-1}. The RBM describes the stretching and compression (the "breathing") of a nanotube around its circumference, *i.e.* the dynamic change of the nanotube diameter. The Raman shift associated with this breathing is inversely proportional to the nanotube diameter

$$\omega_{RBM} = \frac{C_1}{d} + C_2 \qquad (2.12)$$

where $C_1 = 220\text{–}260\ \mathrm{cm}^{-1}$ and $C_2 = 0\text{–}20\ \mathrm{cm}^{-1}$ are constants depending on substrate, environment, and degree of nanotube individualization.[34] The intensity of the RBM is significantly larger when the excitation is performed in resonance with the optical transitions of the CNT, *i.e.* when the laser wavelength is close to the absorption wavelength. The CNT type (metallic/semiconducting) and even the chirality can thus be determined by combining the calculated diameter based on the RBM frequency with the energy of the laser in reference to the *Kataura plot*.

CNT Raman spectra exhibit further modes for $\omega > 350\ \mathrm{cm}^{-1}$. The G-modes (~ 1590 cm^{-1}) display in-plane vibrations of sp^2-hybridized carbon, where the G^+-mode reflects displacement along the nanotube axis and the G^--mode those along the CNT circumference. The D-mode (~ 1350 cm^{-1}) is related to defects in the carbon lattice and amorphous carbon and thus a measure of the quality of the analyzed CNTs.[35, 36] All Raman modes can be attenuated by chemical, electrochemical, or electrostatic doping.[37, 38] The environmental conditions and temperature as well as mechanical stress can also shift the peak position and alter the peak width.[39, 40]

2.1.4. Electronic properties

The outstanding capability of charge transport within a carbon nanotube is illustrated by the extremely high mobility values measured in field-effect transistors with one individual CNT. At room temperature, mobilities of up to 10^4 cm^2 V^{-1} s^{-1} were reported.[41] In general, the mobility is largely dependent on the nanotube diameter and temperature. The transport within short ($\leq$ 1 µm) CNTs is largely unaffected by scattering and can thus be seen as ballistic.[42] The intra-tube resistance of one individual nanotube was theoretically predicted and measured at very long (4 mm) semiconducting CNTs with around 6–8 kΩ µm^{-1} at room temperature.[42, 43] For practical applications in combination with printed electronics, transistors based on a single CNT are however not feasible due to the short channel lengths, printing resolution, and alignment accuracy that would be necessary. Instead, nanotube networks can be utilized even in larger channels and do not require the alignment of contacts on an individual CNT.

Although the intra-tube resistance is not negligible within nanotube networks,[44] the inter-tube resistance at the junctions of the CNTs probably has the highest influence on the device properties. Experimentally determined values for the junction resistance vary by several orders of magnitude (10^2–10^5 kΩ).[45-47] Temperature-dependent measurements of CNT networks show thermally activated transport, *i.e.* a decreasing resistance with increasing temperature. This suggests a hopping transport mechanism at the nanotube–nanotube junctions whose details are yet to be revealed.[48, 49] The overall network resistance depends on the diameter and range of carbon nanotube chiralities, *i.e.* the distribution of energy levels, the channel and nanotube length as well as the orientation, *i.e.* the number of junctions that have to be overcome to cross the channel, and the density of deposited CNTs, *i.e.* the number of available percolation paths through the network.[50] The charge transport through the network might be further hindered by traces of small bandgap nanotubes that constitute a shallow trap for charge transport in mixed networks.[33] As a result of the resistances within the network, the achievable charge carrier mobilities are reduced to several 10 cm^2 V^{-1} s^{-1} for random CNT networks and a few 100 cm^2 V^{-1} s^{-1} for aligned arrays.[1, 51-53] Large bandgap nanotubes exhibit lower mobilities, as the phonon backscattering is increasing with the diameter.[41] On the other hand, they might be advantageous to achieve a high ratio between on- and off-currents in eventual devices (on/off-ratio), as the off-currents are mainly determined by the bandgap.[54] When using nanotube networks it is thus always important to find the optimum balance between the different aspects influencing the final device properties.

2.1.5. Synthesis

Carbon nanotubes can be synthesized by different methods that vary widely in terms of quantitative and qualitative output. Established methods are arc-discharge and laser ablation processes that basically rely on the same principle: Transition metal particles are added to graphite and the resulting composite target is evaporated either with a laser or via the arc-discharge. The evaporated carbon particles are able to form carbon nanotubes supported by the likewise evaporated metal nanoparticles serving as a catalyst.[8, 55] The variations in catalyst particle size and local evaporation conditions produce a rather large diameter range and mixture of various nanotube chiralities.[56] In contrast to the two batch processes, the plasma torch method produces a continuous output. Usually, an argon plasma is used to atomize a gas mixture of catalyst and carbon source that is inserted with continuous flow.[57] Over the last few years a new manufacturer specialized on the continuous production of CNTs with a diameter of around 2 nm entered the market. The product is sold under the trademark TUBALL and is produced at low cost with a yearly output of more than 60 tons. The production process involves an iron and/or other transition metal catalyst evaporated *in-situ* by plasma-assisted arc-discharge and a hydrocarbon source, *e.g.* alkanes or alkenes with less than 10 carbon atoms, in a continuously operating reactor with permanent CNT extraction.[58, 59] Besides their low prize and long length, the latter nanotubes are relatively large and have their main applications in conductive and antistatic coatings, battery electrodes, and composites with increased mechanical stability.

Chemical vapor deposition (CVD) methods for the synthesis of CNTs are able to use precisely controlled metal nanoparticles as catalysts. The carbon precursor is delivered via the gas phase and the catalyst particles are either deposited on a substrate (heterogeneous CVD, “grow-in-place”) or added to the gas phase together with the carbon source (homogenous CVD, “grow-then-place”).[60] While the grow-in-place process can be advantageous as direct control of deposition area can be realized, it has special substrate requirements due to the high synthesis temperatures that are not compatible with all substrate materials. The direct growth of CNTs on a substrate can also be combined with alignment techniques to achieve oriented networks, *e.g.* with an electric field controlling the dipole orientation of the nanotubes,[61-63] or directed growth along steps or trenches of the substrate and a resulting high nanotube–substrate interaction along those features.[64-66] Homogeneous CVD methods on the other hand can be used with a continuous flow, are more easily scalable, and already reached a high level of product quality and productivity.

The two commercial manufacturing techniques yielding small diameter (~1 nm) CNTs widely used for research on carbon nanotube electronics both utilize carbon monoxide as a precursor. The HiPCO-process (**hi**gh **p**ressure **c**arbon mon**o**xide) works at high pressures (30–50 bar) and temperatures (900–1100 °C) with iron pentacarbonyl as the precursor for the iron catalyst particles.[67, 68] The output consists of up to 97 % single-walled CNTs with a narrow diameter distribution of around 0.8–1.2 nm. The CoMoCAT-process (**co**balt **mo**lybdenum **cat**alyst) uses lower pressures (1–10 bar) and temperatures (700–950 °C) in a fluidized bed reactor with CoMo catalyst particles on a support. It allows to narrow down the diameter range to 0.7–0.9 nm with a favored production of (7,5) and (6,5) CNTs.[69]

2.1.6. Chirality separation

Despite continuous progress on tailoring synthesis methods and parameters in order to yield single chiralities, these methods are either not yet commercially available or still produce a mixture of different metallic and semiconducting nanotubes.[70-73] Applications in electronic devices ideally would be based on single to few chiralities.[33, 44, 74] However, transistors require purely semiconducting CNTs to enable switching from the on- to off-state with a difference in current of several orders of magnitude. In addition to different chiralities, the nanotube raw material also contains amorphous carbon and catalyst residuals. Purification of the nanotubes and separation of different chiralities can be achieved by various techniques based on selective interaction of CNTs with surfactants and solvents. As the nanotubes are present in dense bundles after synthesis, sonication or application of high shear forces is necessary to individualize the CNTs and enable access of the surfactant.

Deoxyribonucleic acid (DNA) was shown to effectively disperse and stabilize carbon nanotubes in water.[75] It is furthermore even possible to separate individual chiralities with tailored DNA sequences in combination with subsequent ion exchange chromatography.[76, 77] Another separating technique uses DNA or sodium cholate (SC) as dispersing agent and separates the different chiralities by density gradient ultracentrifugation.[78, 79] During centrifugation the nanotubes are here separated by their buoyant density (including the surfactant) which depends on the tube diameter and type. SC-dispersed CNTs can be also sorted by aqueous two-phase extraction. For that two water-soluble polymers poly(ethylene glycol) (PEG) and dextran are mixed with the nanotube dispersion and sodium dodecyl sulfate (SDS). After mixing, two phases are formed, one rich in PEG and s-CNTs and one rich in dextran and m-CNTs.[80] The extraction of individual CNT chiralities can be achieved in a multi-step process with carefully adjusted SDS concentrations and was shown for small and large diameter CNTs.[81, 82]

SDS itself is also a dispersion agent for CNTs in water but does not offer any initial type or size selection. The SDS-dispersions can however be separated by type using gel chromatography (GC) columns with agarose gel. The degree of interaction of a nanotube with the gel is determined by its electronic nature and diameter. Eluting a GC column – saturated with CNT dispersion – with pure aqueous SDS, first yields a fraction rich in metallic CNTs as their interaction is weakest. The succeeding fractions contain s-CNTs sorted by diameter. This method can thus be used to individualize single nanotube chiralities.[83-88] The chirality purification of this method is to date the best achievable and even enantiomer separation was demonstrated for several CNT chiralities.[89, 90]

All of the above mentioned methods rely on non-selective dispersion of nanotubes and subsequent separation while a centrifugation step to remove undispersed material is implemented in-between. Nish *et al.* introduced an alternative concept, *i.e.* directly dispersing only certain chiralities in organic solvents.[91] They used different conjugated polyfluorenes and aromatic solvents and found the highest selectivity for CNTs from various CNT sources (*e.g.* HiPCO and CoMoCAT) with poly(9,9-dioctylfluorenyl-2,7-diyl) (PFO) and poly[(9,9-dioctylfluorenyl-2,7-diyl)-*alt-co*-(1,4-benzo-2,1′,3-thiadiazole)] (PFO-BT) in toluene. A largely reduced selectivity was observed in other organic solvents such as tetrahydrofuran (THF) and chloroform. From this starting point a vast amount of conjugated polymers was tested for dispersion selectivity including polyfluorenes with different side chains,[92] and polyfluorene copolymers,[93-99] but also polythiophenes,[100, 101] polycarbazoles, [96, 102] and others.[103-105] While a large number of conjugated polymers is able to disperse CNTs, the selectivity and yield vary widely. In various studies, the influence of solvents,[91, 98, 99, 106, 107] molecular weight,[52, 106, 108] and sidechains was studied and guidelines for polymer and solvent selection were provided.[92, 100] An experimentally simple one-pot method yielding nearly monochiral (6,5) dispersions was established with a polyfluorene-bipyridine copolymer (PFO-BPy) in toluene from CoMoCAT raw material.[109] Similar to other dispersion methods, sonication was used to debundle the raw material and support efficient wrapping of the polymer around the nanotubes. The non-dispersed material, *i.e.* other unwrapped CNTs, amorphous carbon, catalyst, and remaining bundles were removed by subsequent centrifugation. Recently, a method to scale up this process was introduced that relies on shear-force mixing instead of sonication to individualize the CNTs during the wrapping step.[110]

Conjugated polymers exhibit much lower carrier mobilities than CNTs and usually have a much larger bandgap. Thus they do not contribute to the transport in a polymer-CNT composite but rather impede fast hopping of charges between nanotubes. It is therefore necessary to minimize the amount of polymer by ultracentrifugation at high centrifugal forces (> 200 000 g) in combination with washing steps and redispersion in pure solvent of the sediment containing the chirality selected CNTs. Alternatively, vacuum filtration can be used to reduce the amount of free polymer.[111, 112] Further removal even of the polymer directly wrapped around the CNTs can be realized by employing designed copolymers that decompose under certain conditions (temperature, acid treatment) or by complexation and stripping with a Rhenium salt.[113-115] However, even if the polymer wrapped around the CNTs is not completely removed, the coverage should be less than 20 % and thus leave sufficient space for direct nanotube–nanotube junctions.[44]

2.2. Carbon Nanotube Transistors

2.2.1. Overview

Transistors are three-terminal devices that control the charge transport between the source and drain electrodes with a voltage applied at the gate electrode V_g. They require several components deposited and structured on a suitable substrate: A semiconductor, source and drain electrodes for charge injection and extraction into and out of the semiconductor, a gate electrode to control the current flow through the semiconductor and a dielectric insulating the gate from the semiconductor to prevent current flow between source/drain electrode and gate electrode.

The general performance of a field-effect transistor also depends on the device dimensions illustrated in **Figure 2.8**. The distance between source and drain electrodes defines the channel length L and the length of the electrodes defines the channel width W. The schematic figure also shows the applied voltages V_g, V_d, and V_s. The currents at the respective electrodes are I_g, I_d, and I_s. Usually, the source electrode is grounded, *i.e.* $V_s = 0$ V, and in this work the terms source–drain voltage V_{ds} and source–drain current I_{ds} will be used. As the gate current I_g originates from charge carriers leaking through the gate dielectric, it is often also called gate leakage. The thickness of the dielectric determines the dielectric capacitance C as well as the electric field across the insulator. In unipolar FETs only one charge carrier type, *i.e.* holes or electrons, can be transported through the channel, while ambipolar semiconductors such as carbon nanotubes are able to conduct both charge carriers.

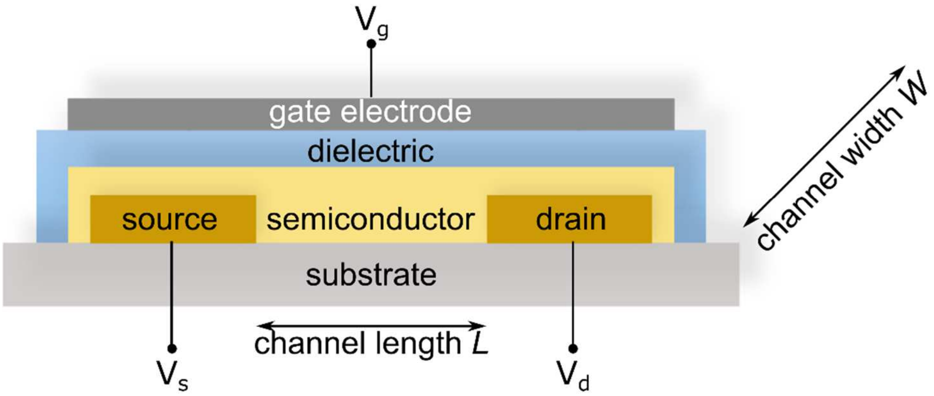

***Figure 2.8**: Important notations illustrated in a staggered top-gate transistor.*

2.2.2. Device architectures

Different device architectures to realize the required order of layers are possible and each exhibit certain advantages and disadvantages (see **Figure 2.9**). The two different possible stacks are named staggered (gate–dielectric–semiconductor–source/drain) and coplanar (gate–dielectric–source/drain–semiconductor). Depending on the position of the substrate (in contact with the gate or not), they are further divided into bottom-gate and top-gate. In all cases, the applied gate voltage causes a charge carrier accumulation in the semiconductor at the interface to the dielectric. While in coplanar structures charges can only be injected into the semiconductor at the edge of the source and drain electrodes, the staggered configuration enables charge injection also at the surface of these electrodes thus leading to current crowding and a reduced injection barrier. During fabrication, often rather harsh processing conditions are used: elevated temperatures during deposition and annealing, as well as solvents and corrosive solutions for structuring, *e.g.* when using photolithography. These techniques may affect the final device, especially the properties of the semiconducting layer. The decision for top-gate or bottom-gate structures thus mainly depends on the processing conditions best fitting the used materials, *i.e.* the thermal and chemical stability, the possibility to use orthogonal solvents, and the sensitivity of individual layers. For very sensitive semiconductors the coplanar bottom-gate structure is most suitable as all structuring and deposition steps are completed before the final deposition of the active material. On the other hand, the staggered top-gate architecture improves the charge carrier injection and permits a precise patterning of all layers including the gate and thus enables high performance transistors when resistant dielectrics and semiconductors are used.

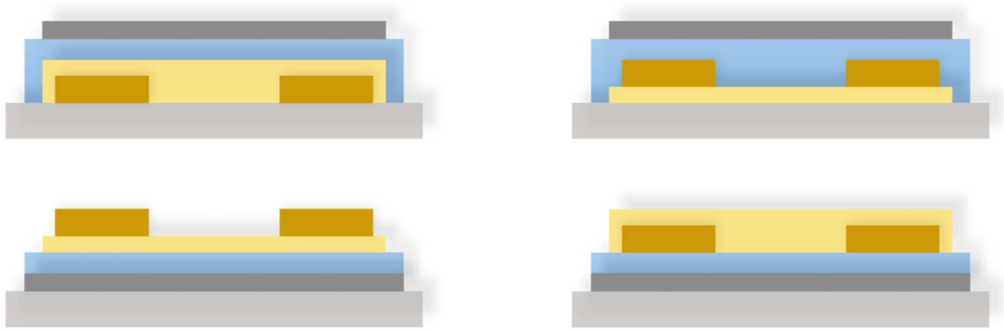

Figure 2.9: *Device architectures for thin-film transistors: Staggered (left) and coplanar (right) stacks with top and bottom gate.*

2.2.3. Layer Deposition and Structuring

While the dielectric is usually non-structured and deposited over the whole sample, other layers need to be structured during or after their deposition. Especially the source and drain electrodes usually require very precise patterning as they define the final device dimensions (see **Figure 2.8**). Depending on the application or planned measurements, a structured semiconductor is useful to define the channel area more exactly, *i.e.* limit edge effects and reduce leakage currents through the gate dielectric as well as cross-talk between neighboring devices. Conventional device fabrication mainly relies on top–down processes, *i.e.* large-area deposition of materials and subsequent structuring.

The deposition of **conductive materials** for electrodes is usually performed by evaporation or sputtering. The material is transferred to the gas phase in both techniques and hence processing in vacuum is required. Thermal evaporation is also used for the deposition of **semiconductors**, although casting from solution ideally at ambient conditions is preferred. A wide range of techniques is used here, *e.g.* spin-coating, dip-coating, immersion, and drop-casting, depending on the amount of material available, the required homogeneity and film thickness, and the ease of processing. Concerning the unpatterned **dielectric,** a completely closed layer is essential to avoid shorts to the gate electrode in the final devices. Often used deposition methods are spin- and dip-coating, physical or chemical vapor deposition (PVD and CVD), or atomic layer deposition (ALD).

Structuring of individual layers can be done by shadow masks, photolithography and subsequent etching and/or lift-off. While shadow masks are simply placed between the sample and deposition source, *e.g.* evaporation crucible, sputter target, or airbrush gun, and thus have no impact on the layers beneath, their resolution and alignment accuracy are usually limited. In contrast to that, very precise alignment and high resolutions (< 1 µm) can be achieved via photolithography. A photoresist is spin- or dip-coated on the sample surface and exposed to ultraviolet light through a chrome-on-glass mask. The exposed areas either become soluble to the subsequently used developer due to degradation (positive resist) or they cross-link and thus become insoluble (negative resist). The prepared structure is then used as a mask for material deposition. With the subsequent resist removal (lift-off) the material deposited on the resist is stripped off and the desired structures, *e.g.* the source and drain electrodes, are created. The resist can also be used for patterned etching where it is protecting the covered areas. This can be used to pattern a previously deposited (*e.g.* via spin- or dip-coating) semiconductor with oxygen plasma or use corrosive materials for wet-etching of metals.

The most important disadvantages of top–down processes is the large amount of material wasted during structuring or deposition and the necessity of structuring processes potentially harmful to the afore deposited material. In contrast to that, printing processes inherently produce patterned layers and hence additionally reduce the number of required processing steps (see section 2.3).

2.2.4. Unipolar Thin-Film Field-Effect Transistors – Basic Principles

In this section, an n-type transistor, *i.e.* electrons as charge carriers, will be described, while the same principles apply to hole transport with the corresponding positive charge carriers.[116-118] For calculations of the current flow in FETs, edge effects are generally ignored and the gradual channel approximation is used as a simplification, *i.e.* the electric field between source and drain (distance of several micrometers) is assumed to be significantly smaller than the electric field across the dielectric (thickness of usually less than 1 µm). An applied gate voltage leads to an accumulation of mobile charges at the interface of dielectric and semiconductor. The gate voltage has to be larger than the so-called threshold voltage V_{th}. This threshold voltage depends on charge traps, impurities, dipoles, and the charge carrier density achieved for the applied gate voltages which can be increased by increasing the areal dielectric capacitance C.[116] The number of mobile charge carriers per unit area Q_{mob} without any applied source–drain voltage is

$$Q_{mob} = C \cdot (V_g - V_{th}) \tag{2.13}$$

For $V_{ds} \neq 0$ V the local potential along the channel (along x) has to be taken into account, *i.e.*

$$Q_{mob} = C \cdot (V_g - V_{th} - V(x)) \tag{2.14}$$

The resulting current I_{ds} depending on the charge carrier mobility μ, the channel width W, the local electric field $F(x)$ and the number of mobile charge carriers is

$$I_{ds} = W \cdot \mu \cdot Q_{mob} \cdot F(x) \tag{2.15}$$

The local electric field is defined as

$$F(x) = \frac{dV}{dx} \tag{2.16}$$

Integrating over the whole channel length from $x = 0$ to $x = L$ with $V(x)$ from 0 to V_{ds} results in

$$I_{ds} = \frac{W \cdot C}{L} \cdot \mu \cdot \left((V_g - V_{th}) \cdot V_{ds} - \frac{V_{ds}^2}{2} \right) \tag{2.17}$$

For $V_{ds} \ll V_g - V_{th}$ the quadratic term of equation (*2.17*) can be neglected and a simplified linear correlation results

$$I_{ds} = \frac{W \cdot C}{L} \cdot \mu \cdot (V_g - V_{th}) \cdot V_{ds} \tag{2.18}$$

For $V_{ds} \geq V_g - V_{th}$ the channel is pinched off as the local potential is smaller than the threshold voltage and a depletion zone is formed next to the drain electrode. A current flow through the depletion zone is still possible, the current is however space-charge-limited and a further increase of V_{ds} does not increase the saturation current I_{ds}. In the saturation regime, V_{ds} can thus be substituted by $V_g - V_{th}$ and equation (*2.17*) can be transformed to

$$I_{ds} = \frac{W \cdot C}{2L} \cdot \mu \cdot \left(V_g - V_{th}\right)^2 \qquad (2.19)$$

The resulting overall dependence of the source-drain current on the drain voltage for a constant gate voltage give the so-called output characteristics and is plotted in **Figure 2.10**.

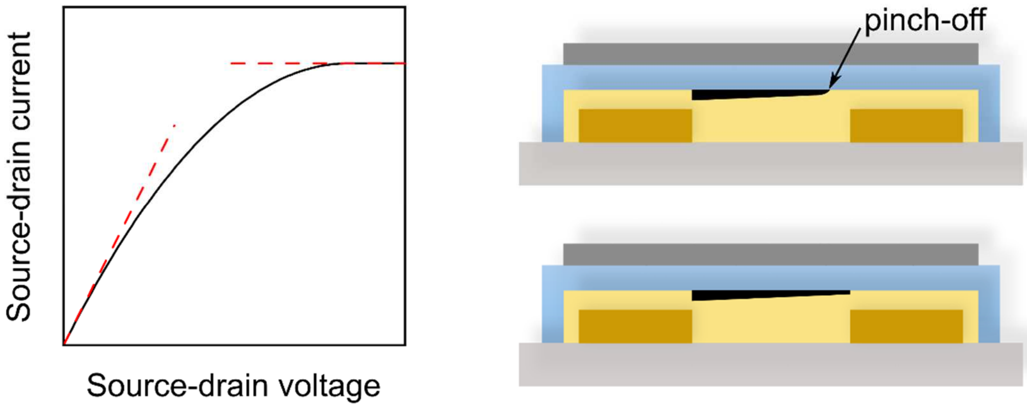

Figure 2.10*: Output characteristics for a constant gate voltage with linear and saturation regime (left). Schematic illustrations of charge carrier accumulation in the linear regime (right, bottom) and pinch-off point in the saturation regime (right, top).*

Below the threshold voltage an exponential dependence of the current on V_g is observed until the current reaches a minimum for V_g smaller than the turn-on voltage V_{on} (see **Figure 2.11**). The occurrence of this subthreshold-region is a consequence of interfacial traps and in an ideal transistor V_{on} and V_{th} would be identical. The threshold voltage can be determined from the *x*-intercept of a linear fit of $\sqrt{I_{ds}}$ as evident from equation (*2.19*).

The turn-on voltage is extracted at the point where I_{ds} gets larger than I_g as depicted in the semi-logarithmic plot of the transfer characteristics (I_{ds} *vs* V_g) in **Figure 2.11**.

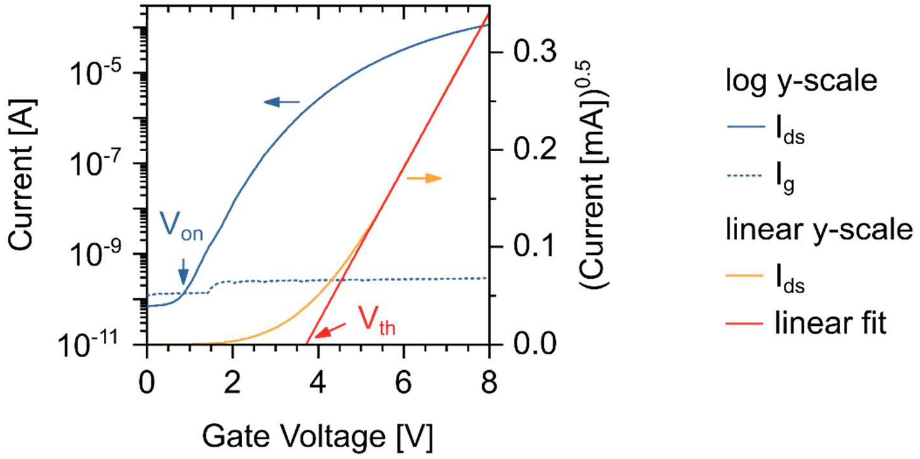

***Figure 2.11**: Determination of turn-on and threshold voltage from the transfer characteristics in semi-logarithmic (left axis, blue curves) and linear (right axis, yellow and red curves) current scales.*

2.2.5. Extraction of Device Parameters

From the measured device characteristics the main figures of merit for thin-film transistors can be extracted from equations (*2.18*) and (*2.19*). The **charge carrier mobilities** μ_{lin} and μ_{sat} for the linear and saturation regime, respectively, can be calculated as follows:

$$\mu_{lin}\,[\mathrm{cm^2\,V^{-1}\,s^{-1}}] = \frac{dI_{ds}}{dV_g}\cdot\frac{L}{W\cdot C\cdot V_{ds}} \tag{2.20}$$

$$\mu_{sat}\,[\mathrm{cm^2\,V^{-1}\,s^{-1}}] = \frac{d^2I_{ds}}{dV_g^2}\cdot\frac{L}{W\cdot C} \tag{2.21}$$

As the mobility is an often used metric to compare different semiconductors and devices, special care should be taken with the extraction of this value.[118, 119] The apparent value of the mobility of a semiconductor may depend on contact resistances at the electrode–semiconductor interface as well as the exact and correct determination of the dielectric capacitance and channel length. Contact resistance usually leads to an underestimation of the mobility value due to the decreased effective V_{ds}, but high contact resistances that are reduced with increasing V_g can also result in an overestimation if the wrong part of the non-ideal device characteristics is chosen for mobility extraction.[120] Ideally the contact resistance of a device should be accounted for by 4-point-probe measurements to extract the intrinsic semiconductor mobility.

The **dielectric capacitance** can be measured in a quasi-metal-insulator-semiconductor structure between the gate electrode and the combined source, semiconductor, and drain electrode. Care has to be taken that the device is turned on completely, *i.e.* that the semiconductor contributes to the capacitor electrode, and a measuring frequency as low as possible is applied to obtain the static capacitance value. While increased noise and scattering limits the low boundary of the frequencies, the capacitance is lower at high frequencies and too high mobility values would thus be calculated. Typical measurement frequencies are around 1 kHz, while slightly lower frequencies would be preferable.[118] The measured dielectric capacitance has to be divided by the respective area A, as the areal capacitance is necessary for the current equations and mobility calculations introduced above. The capacitance can also be calculated from the plate–plate capacitor model with the relative permittivity of the used dielectric material ϵ_r, the vacuum permittivity ϵ_0, and the layer thickness d:

$$C\left[\mathrm{F\ cm^{-2}}\right] = \frac{\epsilon_r \epsilon_0}{d \cdot A} = \frac{C_{meas}}{A} \qquad (2.22)$$

However, the electrostatic coupling and quantum capacitance of the CNT network has to be considered for the correct determination of the areal capacitance. Using the plate–plate capacitor model hence leads to larger deviations from the actual capacitance and the direct measurement at the device in the on-state is preferable.[121]

Regarding **contact resistances**, a reliable extraction of the intrinsic mobility of the semiconductor is only possible with knowledge of the exact potential applied at the channel. This can be extracted via 4-point-probe measurements where the potential is measured additionally within the channel.[44] Alternatively, the transmission-line-method allows the extraction of contact resistances through measurements of the same homogeneous semiconductor in devices with different channel lengths.[52, 122] In case of crystalline materials or carbon nanotubes, the effective channel width can be significantly lower than the geometric dimension W. For CNT networks, additionally nanotube–nanotube resistances further reduce the mobility and the extracted values are thus not comparable to the intrinsic mobility of single CNTs.

Considering all points mentioned above, in case of carbon nanotubes, it is more appropriate to talk about an **apparent device mobility** that is not an intrinsic parameter of the semiconductor but also includes the device architecture, dimensions and semiconductor structure, *i.e.* the network composition and orientation (aligned or random) as well as the CNT density. Mobilities reported in this work are thus always apparent device mobilities and were extracted with capacitances measured at the channel and without taking into account contact resistances.

Besides the mobility as an important property of a transistor, the achievable channel conductance and current densities should be considered for the evaluation of the device performance. The **on-current** depends on the applied source–drain voltage and can be easily extracted from the device characteristics. The channel-width corrected **on-conductance** G_{on}/W reported in S mm^{-1} can be compared more easily for devices with different geometries:

$$\frac{G_{on}}{W}\ [\mathrm{S\ mm^{-1}}] = \frac{I_{on}}{V_{ds} \cdot W} \qquad (2.23)$$

The **current density** is defined as the current flowing through a cross-section of the semiconductor with a certain area. For the usually present lateral transport between source and drain electrode, a realistic assumption of the channel thickness (in z-direction) is therefore necessary. For vertical charge transport (see chapter 6), the current density is defined by the overlap area of the electrodes between which the current is flowing in z-direction.

The **subthreshold swing** SS is a measure for the concentration of shallow charge carrier traps which are limiting fast switching speeds. A small subthreshold swing is thus essential for high frequency applications. The subthreshold swing is the inverse of the slope of the transfer characteristic for $V_g < V_{th}$, *i.e.* a fast turn-on with quickly increasing currents results in a small subthreshold swing. The subthreshold swing is given in V dec^{-1}, *i.e.* the change in gate voltage necessary to increase the current by a factor of 10.[119]

$$SS\ [\mathrm{V\ dec^{-1}}] = \left(\frac{d(\log(I_{ds}))}{dV_g}\right)^{-1} \cdot \frac{\log(\mathrm{A})}{\mathrm{dec}} \qquad (2.24)$$

A large **on/off-ratio**, *i.e.* a high difference of on-current I_{on} and off-current I_{off} is crucial. The value is extracted from the maximum I_{on} for holes or electrons and the current in the off-state. I_{off} is often limited by residual metallic nanotubes or the gate leakage I_g. Typical on/off-ratios for CNT transistors range from 10^2 to more than 10^8, depending on the quality, *i.e.* semiconducting purity, device architecture, especially regarding I_g and CNT alignment, and the bandgap of the utilized CNTs which determines the minimum I_{off} in this ambipolar semiconductor.[54]

2.2.6. Ambipolar Field-Effect Transistors

Carbon nanotubes are one representative of ambipolar semiconductors, but also a number of polymers,[123, 124] single crystals,[125, 126] fullerenes,[127-129] and other materials are able to transport both charge carriers, *i.e.* electrons and holes.[116, 130, 131] Furthermore mixed or stacked layers of n- and p-type semiconductors can be used to achieve ambipolar charge transport through the transistor channel.[132, 133] Ambipolar transport is only possible, if the electrode material exhibits a suitable work function W_F to inject both charge carrier types, which is true for carbon nanotubes due to their narrow bandgap.

In an ambipolar transistor, the electron and the hole current, both contribute to the total current through the device.[134] The device characteristics can thus be seen as a superposition of a unipolar n-type and a unipolar p-type transistor. In the following, the threshold voltages / mobilities for holes and electrons are named $V_{th,h}$ / μ_h and $V_{th,e}$ / μ_e, respectively. The given conditions for V_{ds} and V_g assume that $V_s = 0$ V, $V_{ds} > 0$ V, and $V_{th,h} < V_{th,e}$. Depending on the applied voltages, the transistor characteristics can be divided into three different regimes.

(1) Unipolar electron transport: $V_g > V_{th,e}$

Only electron transport occurs in the semiconductor and contributes to the current, *i.e.* the equations for unipolar behaviour (see chapter 2.2.4) remain valid:

$$I_{ds} = \frac{W \cdot C}{L} \cdot \mu_e \cdot \left(\left(V_g - V_{th,e}\right) \cdot V_{ds} - \frac{V_{ds}^2}{2} \right) \qquad (2.17)$$

(1a) For $V_{ds} < V_g - V_{th,e}$ electron transport occurs in the linear regime.

(1b) For $V_{ds} \geq V_g - V_{th,e}$ electron transport occurs in the saturation regime.

(2) Unipolar hole transport: $V_g - V_{ds} < V_{th,h}$

Here, only hole transport contributes to the current through the channel

$$I_{ds} = -\frac{W \cdot C}{L} \cdot \mu_h \cdot \left(\left(V_g - V_{th,h}\right) \cdot V_{ds} - \frac{V_{ds}^2}{2} \right) \qquad (2.25)$$

(2a) For $V_{ds} < V_g - V_{th,h}$ hole transport occurs in the linear regime

(2b) For $V_{ds} \geq V_g - V_{th,h}$ hole transport occurs in the saturation regime, hence (*2.25*) has to be altered with $V_{ds} \rightarrow V_g - V_{th,h} - V_{ds}$ and results in

$$I_{ds} = \frac{W \cdot C}{2 \cdot L} \cdot \mu_h \cdot \left(V_{ds} - V_g + V_{th,h}\right)^2 \tag{2.26}$$

(3) Ambipolar transport: $V_g > V_{th,e}$ and $V_g - V_{ds} < V_{th,h}$

In the ambipolar regime both charge carriers contribute to the overall current. With holes and electrons injected at the drain and source, respectively. This results in a series of a hole and an electron channel and both saturation currents have to be summed up to obtain I_{ds}:

$$I_{ds} = \frac{W \cdot C}{2 \cdot L} \cdot \left(\mu_e \cdot \left(V_g - V_{th,e}\right)^2 + \mu_h \cdot \left(V_{ds} - V_g + V_{th,h}\right)^2\right) \tag{2.27}$$

The different operation regimes of an ambipolar transistor are illustrated in the output and transfer characteristics in **Figure 2.12**. The device parameters are usually derived from the unipolar operating regimes.

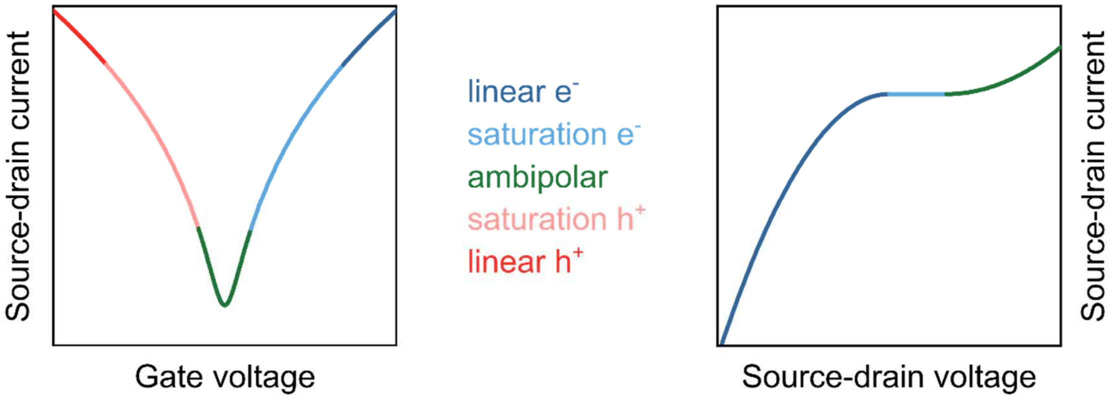

***Figure 2.12**: Transfer characteristics (left) and output characteristics for positive voltages (right) of ambipolar transistors.*

2.2.7. Networks and Arrays of CNTs as Thin-Film Semiconductors

Originating from the one-dimensional structure, the charge transport properties in carbon nanotubes exhibit a strong anisotropy. Additionally, barriers at the junctions of different CNT chiralities but also hopping between nanotubes of the same kind further hinder the charge transport. It is therefore important for the overall transistor performance, how many nanotube–nanotube junctions of which barrier height have to be overcome to cross the channel, *i.e.* the nanotube orientation, length, and mixture of species in the network are important. In general, four different patterns of nanotubes constituting the semiconductor can be distinguished: individual nanotubes, arrays of parallel CNTs, aligned networks, and random networks (see **Figure 2.13**).

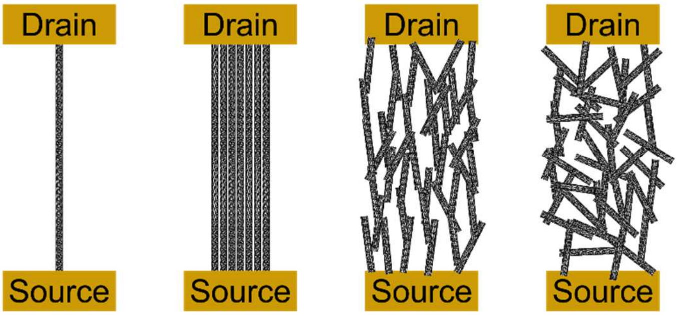

***Figure 2.13**: Schematic of different CNT film structures: individual tubes, parallel arrays, aligned networks, and random networks (left to right).*

Incorporating individual CNTs into transistors requires high precision, alignment, and structuring and is therefore limited due to the high fabrication costs involved. However, individual CNT properties can be studied, and sub-10 nm channel lengths with very high switching speeds and mobilities were realized.[135-137]

Directly growing aligned CNT arrays simplifies device fabrication while maintaining the advantage of direct connections between the source and drain electrode without any junctions. Furthermore, the arrays exhibit overall larger currents and templated growth from deposited catalyst along surface features or external electric fields result in predictable CNT patterns that enable fast alignment of subsequent layers to complete the devices.[61, 64, 65, 138] However, as monochiral growth was still not achieved for a wide range of CNT species, metallic CNTs are usually present in these devices and perturb the device performance. Additionally, high temperatures are usually necessary and thus only a limited choice of substrates is suitable and all other transistor layers have to be deposited afterwards.

Solution processing of CNT dispersions is the most favorable method to deposit nanotubes for electronics, as it opens the perspective for rather low cost fabrication methods and the possible integration into roll-to-roll processes. However, deposition from solution results into nanotube networks that exhibit a number of junctions along the charge transport path through the transistor channel and do usually not show any alignment. The variety of used deposition methods ranges from simple immersion,[50, 100, 139-141] dip-coating,[142] spin-coating,[44, 121, 143, 144] and drop casting,[145, 146] to printed films that exhibit the advantage of direct patterning.[99, 147-153]

Certain methods can produce aligned networks of carbon nanotubes from solution. The alignment between pre-patterned electrodes with an applied electric field during drop-casting or immersion is called dielectrophoresis and simultaneously achieves a structured deposition at the electrode area.[33, 154-159] Pulling a substrate out of a water reservoir with a thin layer of nanotubes deposited on top of the liquid surface, so-called floating evaporative self-assembly (FESA) results in ribbons of aligned CNT films.[51, 160, 161] Utilizing the coffee stain effect, nanotubes can also be aligned by completely evaporating the solvent around a vertically oriented substrate that was initially immersed in the CNT dispersion.[162]

Carbon nanotube transistors fabricated or annealed in inert atmosphere show balanced hole and electron transport with comparable on-currents and mobilities within the same order of magnitude. These properties can be preserved by encapsulation, *e.g.* by oxide dielectrics,[33, 163] epoxy resin,[157] or glued class covers,[157, 159]. Without encapsulation, the CNT transistors show hole doping due to water and oxygen adsorption when exposed to air.[164, 165]

Depending on the structure of the CNT layer, the deposition and fabrication methods, the degree of alignment, the channel length, and the semiconducting purity of the CNT network, the range of reported mobility values and on/off-ratios varied by several orders of magnitude. **Figure 2.14** gives an overview about some of the published values and illustrates that the sole comparison of achieved numbers is not expedient. It is instead rather important to compare the devices in the context of their fabrication method, device architecture, and desired application. The application is also decisive for the choice of crucial parameters: While fast switching speeds are important for integrated circuits, display backplanes need a high stability, and large on/off-ratios are favorable for detectors to achieve high signal-to-noise ratios. Especially printed devices often cannot achieve outstanding numbers for all device parameters simultaneously and individual layers as well as the complete architecture have to be optimized in the context of possible or wanted applications.

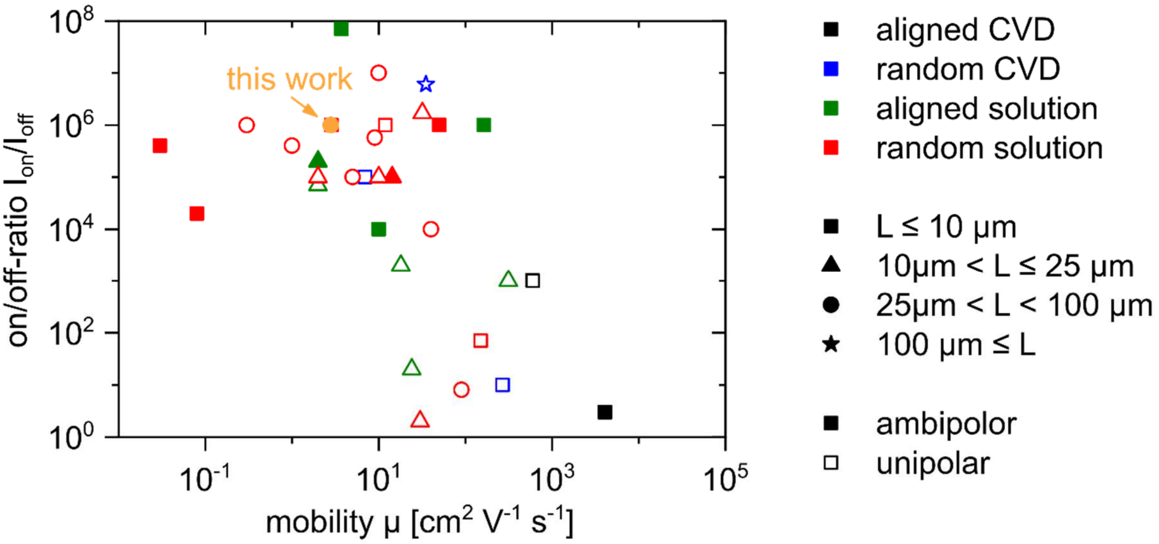

***Figure 2.14**: Mobility vs on/off-ratio for various published CNT transistors depending on alignment, channel length and deposition method.* [2, 50, 52, 100, 140, 144-147, 150, 162, 166-176] *"This work" indicates the performance of aerosol-jet printed (6,5) CNTs in a staggered top-gate transistor.*

2.2.8. Electrolyte-Gated Transistors

In field-effect transistors with a conventional dielectric between semiconductor and gate electrode, charge transport can only occur within a few nanometers of the semiconductor–dielectric interface.[177] Furthermore, the dielectric capacitance and the gate leakage scale inversely with the thickness of the dielectric, but the breakdown strength, *i.e.* the applicable potential difference, are directly proportional to the thickness. In case of non-flat semiconductor surfaces, such as carbon nanotube films, the subsequently deposited dielectric is subject to locally concentrated electric fields and thus increased gate leakage and possible breakdown of the device at potential differences remaining well below the breakdown of an ideal, flat layer. The achievable charge carrier density is hence limited to usually less than 10^{13} e cm^{-1}. While very thin (few nm) dielectrics can be used for low voltage transistors, printable dielectrics require a minimum thickness and thus higher voltages to enable sufficiently high drain currents.

Instead of conventional dielectrics, electrolytes can be used for gating.[178] The electrolyte covers the semiconductor surface and the mobile ions are even able to penetrate into porous semiconductors such as carbon nanotube films.[112] When a positive (negative) bias is applied to the gate electrode, the anions (cations) and cations (anions) move within the electric field and accumulate at the gate and the semiconductor, respectively. An electric double-layer (Helmholtz layer) is formed and compensating opposite charge carriers are injected and accumulated within the semiconductor. Due to the nm-thickness of the electric double-layer, an effective capacitance of several µF cm^{-2}, *i.e.* orders of magnitude higher than those of conventional dielectrics, can be achieved (see device schematics in **Figure 2.15**).[179]

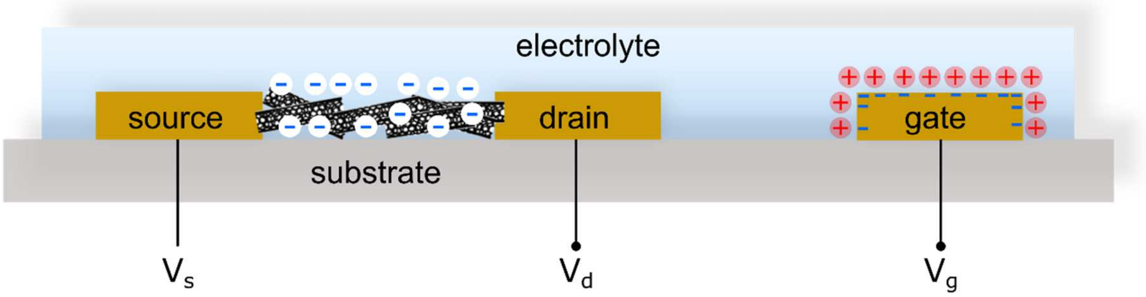

***Figure 2.15**: Cross-sectional view of an electrolyte-gated transistor with semiconducting CNTs and a side-gate. The accumulation of cations and anions (red and blue, respectively) is depicted for negative gate voltages. The electric double-layer is depicted at the gate electrode only. Holes are accumulated in the CNT film.*

A model for electrolyte-gating was described in detail by Bernards *et al.*,[180, 181] assuming an electronic and an ionic circuit as shown in **Figure 2.16**. The electronic circuit includes current transport through a tunable resistor R_{ch} between the source and drain electrodes. The ionic circuit involves capacitors at the semiconductor–electrolyte (channel capacitor C_{ch}) and the electrolyte–gate (gate capacitor C_g) interfaces that are connected via the electrolyte as a resistor R_{EL}. The resistor in the electronic circuit is tuned by charging the channel capacitor as a result of the applied gate voltage. This channel capacitor exhibits a high capacity for impermeable semiconductors and can be described similar to FETs.[182] For porous or permeable semiconductors, the capacitance can no longer be described by a parallel plate model but rather a volumetric capacitance has to be used. The nm-thickness of the double-layer and even more the three-dimensional gating results in a significantly larger charge carrier density in the semiconductor at low voltages. The source–drain currents are hence significantly higher at comparably gate voltages of usually less than 3 V, which was demonstrated for various semiconductors.[148, 183-186] It should be noted that nomenclature is not consistent in literature and this type of devices is found with different names, *e.g.* organic electrolyte-gated transistor (OEGT), organic electrochemical transistor (OECT), electric double-layer transistor (EDLT), and ion-sensitive field-effect transistor (ISFET).[182] Often, devices with permeable or impermeable semiconductors are referred to as OECT and OEGT, respectively.[181] The electrolyte-gated transistors described in this thesis consist of porous CNT networks and hence enable three-dimensional gating but the ions are not expected to penetrate inside the individual nanotubes. The electric double-layer is thus formed around the nanotubes and the devices will be referred to as EGTs. They operate in accumulation mode, *i.e.* the channel is in the off-state when no voltage is applied and charges are accumulated for transport upon application of a gate voltage. On the other hand, devices working in the depletion mode, *i.e.* ion penetration into the semiconductor leads to the compensation of fixed dopant ions and thus reduces the channel conductivity, are also possible, *e.g.* with PEDOT:PSS as the semiconductor.[181]

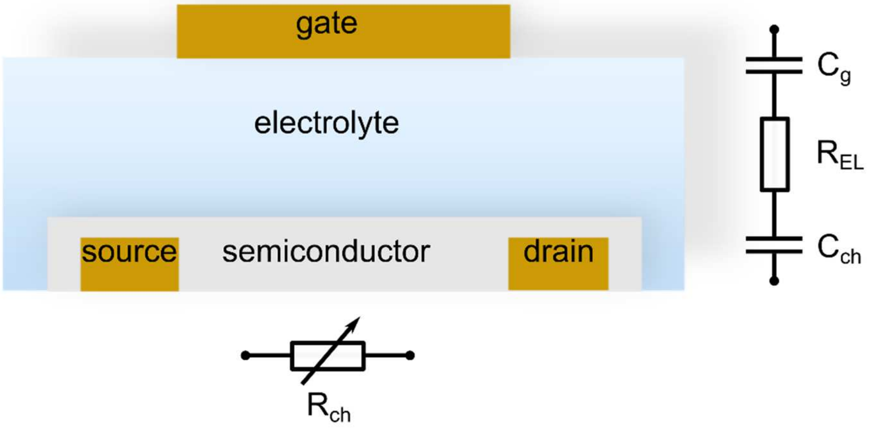

***Figure 2.16**: Illustration of electronic (bottom) and ionic (right) circuits in an electrolyte gated transistor as adopted from literature.[181]*

The high currents that can be reached in EGTs at low voltages come with the disadvantage of rather slow response times, especially for volumetric gating. The polarization time of an electrolyte is described by $R{\cdot}C$, *i.e.* the ionic resistance of the electrolyte R and the double-layer capacitance C. A smaller value for $R{\cdot}C$ corresponds to a faster formation of the double-layer and hence higher switching speeds. For an electrolyte, $R{\cdot}C$ is given by

$$R \cdot C = \frac{t_{EL} \cdot C'}{\sigma} = \frac{t_{EL} \cdot \epsilon_r \cdot \epsilon_o}{t_{EDL} \cdot \sigma} \qquad (2.28)$$

where t_{EL} is the thickness of the electrolyte, C' the specific capacitance of the double-layer, σ the ionic conductivity, and t_{EDL} the thickness of the electric double-layer.[182] In most cases, the limiting factor for the switching speed of the device is the ionic conductivity σ, which is on the order of 10^{-5} to 10^{-2} S cm^{-1}. While theoretically operation frequencies in the kHz (OECTs) to MHz (non-porous OEGTs) regime are possible, the device geometry, semiconductor thickness, and charge carrier mobility influence the switching speed as well and often lead to longer response times.[182] However, devices with response times fast enough for various applications, *e.g.* OLED drivers and biosensors, have been reported frequently.[182, 187-192]

Electrolyte-gating has a long history going back to the first transistors by Bardeen and Brattein.[193] The recent renaissance of practical electrolyte-gated transistors, especially in organic electronics, started with transistors containing solid polymer electrolytes, *e.g.* $LiClO_4$-doped poly(ethylene oxide), and polyelectrolytes that exhibited rather low switching speeds due to the strongly limited mobility of the ions within the polymer.[178, 181, 182] A replacement with ionic liquids, *i.e.* salts that are liquid around room temperature, improved the switching speeds but required a frame for containment which prevents practical applications beyond sensors.[179] Mixing the ionic liquid with certain polymers results in ion gels that may exhibit slightly reduced ionic mobility (with respect to the pure ionic liquids) but can be spin-coated or even printed onto devices and form a quasi-solid layer.[194-196] The ionic liquids and gels are stable within an electrochemical window of about ±2.5 V, depending on the utilized ions and exclusion of oxygen and water.[179, 182] In case of mechanically stable ion-gels, the gate electrode can be placed on top of the channels, however the ion mobility also allows to use a side-gate laterally removed from the channel that can be structured with the source and drain electrodes which reduces the number of processing steps.[112, 157, 197] For liquid electrolytes, a gate electrode, *e.g.* a platinum wire, can also be directly inserted into the liquid.

In addition to low-voltage operation and large currents, electrolyte-gating provides further advantages: Ion-gels can be processed from solution, the gel is inherently flexibility, and the coverage of non-flat semiconductors and surfaces such as paper is possible without negatively influencing the device performance.[179, 198] The thickness of the ion gel is not limiting the current and can be large. Ion-gels are hence compatible with printing techniques and printable inks were already demonstrated (see section 2.3). Electrolyte-gating is furthermore especially interesting for sensing applications. Even pure water is a good electrolyte for EGTs due to its self-ionization. Analyte molecules present in aqueous solutions can change the device characteristics, *i.e.* they can alter the double-layer capacitance, the threshold voltage, the on/off-ratio, or the charge carrier mobility.[189] The sensing mechanism can be based on different effects. While a response of the unmodified semiconductor to the analyte is possible, it is usually non-selective, which is especially adverse for sensing in biological samples. Modifying the semiconductor or the gate electrode with a receptor, *e.g.* an antibody for proteins or complexes for ion detection, results in high selectivity and extremely low detection limits with a dynamic range, *i.e.* detectable concentration of the analyte, of more than 5 orders of magnitude.[158, 190] Further applications of EGTs that exceed the scope of this work include sensing of neural activity, mimicry of biological neural networks (neuromorphic devices), and memories.[181]

2.3. Printed Electronics

2.3.1. Overview

The term *printed electronics* includes a wide range of materials, additive deposition techniques, and possible applications on brittle, flexible, and eventually even stretchable substrates. The resulting devices vary in terms of complexity, feature sizes, integration density, and requirements concerning long-term stability, conformity, tolerances, and environmental compatibility. In contrast to the established and market-dominating circuits based on silicon technology, flexible and stretchable substrates require low-temperatures but could eventually enable fast and low-cost fabrication with roll-to-roll processes, ideally in ambient environment. For transistor-based applications, the cost-reduction of silicon devices has so far been achieved via increasing the packing density of integrated circuits. Printed electronics on the other hand aim to combine materials that are generally processable from solution or dispersion with rather low-cost substrates and high-throughput fabrication methods that are not compatible with silicon technologies. Moreover, varying designs can be realized efficiently even for small batch sizes as no fabrication of masks is necessary.

The possible and partly already demonstrated applications cover antennas, light-emitting diodes (LEDs), photovoltaics, individual transistors as well as integrated circuits, chemical, optical, mechanical, and biological sensors, extending to complete RFID tags,[199] displays,[200-205] and neuromorphic networks.[206] The following sections will give an overview about different printing techniques and materials. In the context of this work, the main focus will be on transistors, nevertheless including further applications.

2.3.2. Materials for Printed Transistors

All materials used for printed transistors and circuits have to meet one common requirement, *i.e.* the processability from a solution, dispersion, or paste, depending on the printing method (see section 2.3.3). In case of flexible or stretchable substrates, the allowed (post-)processing temperatures are additionally limited.

Conductors represent the fundamental material class of all printed electronics. The contacts of devices, interconnects, and leads have to be free of disruptions as those would result in fatal device damage. Depending on the application, high conductivities and suitable work functions are necessary for charge transport and injection.[198] The utilized materials were typically either metals, polymers, or based on carbon allotropes. The highest conductivities were exhibited by structures printed from metallic inks which were usually based on nanoparticles, nanowires, or metal-organic precursors.[207] An annealing step was necessary here to either remove surfactants and dispersing agents from colloidal inks or ensure the decomposition of precursor-based inks. Additionally, it was often necessary to sinter the deposited metal to further reduce the resistance. Annealing and sintering were most often performed via simple heating, but other techniques based on lasers,[208, 209] microwave or UV radiation,[210-212] and electric currents to selectively heat only the metallic material were developed.[213] The choice of metal depends on the electrical suitability and processing conformity, but also on the price and availability of printable inks. Currently, most commercially available ink formulations are based on silver nanoparticles, but also gold nanoparticles are available.[198] Transistors based on printed silver nanoparticle electrodes were hence found most frequently,[112, 147, 151, 153, 214-228] but also examples for silver nanowires or gold nanoparticles were demonstrated.[153, 217, 229-232] Although graphene and carbon nanotubes were both used as electrode materials and dispersions could be prepared easily, there are only few reports on printed transistor electrodes from these materials, probably due to the rather high sheet resistances when compared to printed metals.[153, 233-236] Concerning polymer conductors, the blend of poly(3,4-ethylenedioxythiophene) and poly(styrene sulfonic acid) (PEDOT:PSS) was used most often,[149, 219, 237-240] but demonstrations of conducting polyaniline were published as well.[198, 241] Composite materials with PEDOT:PSS and reduced graphene oxide or silver nanowires also showed reasonable stretchability.[242, 243] Although the majority of reports used metallic electrodes, other materials are of special interest for flexible and stretchable applications. Polymers, nanowires, and carbon nanotubes might be used where brittle metals hit their limits and several reports about the fabrication of stretchable electrodes – although not all of them were printed – were published. [244-252]

Semiconductors used in printing processes cover a wide range of especially synthesized but also commercially available polymers, small molecules,[222, 240] metal oxides,[253, 254] and carbon nanotubes. As most polymers can be processed from solution, they are ideal candidates for deposition via printing and were thus widely used. Printed semiconducting layers for transistors were shown for poly(3-hexylthiophene) (P3HT) and several other thiophenes,[223, 232, 233, 238, 239, 255-258] but also polyarylamines and other commercial polymers were utilized.[224, 225, 237, 259] In contrast to oxides that are usually brittle, polymers also exhibit flexibility and stretchability at least to a certain degree and were used in stretchable transistors.[250, 260-262] The high number of publications about printable polymers possibly originates from easier preparation of inks as most polymers can be dissolved in suitable solvents without the necessity of additional surfactants. Carbon nanotubes on the other hand need dispersing agents that might be detrimental to printing. However, dispersions containing mainly semiconducting species could already be deposited by gravure,[263, 264] aerosol-jet,[151] [149, 265] and inkjet printing.[152, 221, 266-268] The main advantage of a semiconductor constituted of a nanotube network is the high carrier mobility while maintaining the inherent flexibility and stretchability.[1, 269] Stretchable devices utilizing carbon nanotubes were also presented with CNT layers created by film transfer, spin coating, drop-casting, or immersion.[147, 227, 236, 270-276]

Dielectrics should exhibit a high permittivity as well as breakdown strength to ensure high capacities and low leakage currents. However, the oxides widely used to fulfill these requirements are usually not printable and hence other materials have to be utilized here. As already mentioned with respect to semiconducting materials, polymers are most often printable and thus polyvinylphenol (PVP), [217, 222, 223, 225] polyimide, [226] and other commercial polymers were used in printed dielectric layers for transistors.[224, 256] Furthermore, the usually spin-coated fluoropolymer Cytop™ was deposited via inkjet and flexo printing.[240, 259] In stretchable applications, ionic liquids and ion-gels were used widely and printing of these materials was previously demonstrated.[148, 149, 151, 152, 233, 234, 239, 255, 277] Composites of barium titanate nanoparticles with different polymers such as poly(methyl methacrylate) (PMMA) and poly(dimethylsiloxane) (PDMS) were used in flexible and stretchable transistors. These materials result in high dielectric constants of up to 17 and are commercially available.[147, 221, 227, 236, 237] The wide range of solution-processable materials that were usually applied via spin-coating but have the potential to be printed was subject of a current review that lists a large number of ion-gels, polymers, polymer blends, organic/inorganic blends and bi-layers, including cross-linkable species to prevent dissolution in subsequent fabrication steps.[278]

State-of-the-art devices with carefully chosen materials and deposition processes already enabled completely printed, stretchable devices. Transistors based on CNTs as electrode and semiconductor material combined with a $BaTiO_3$/PDMS composite dielectric were able to withstand more than 50 % strain.[236] Although post-deposition patterning was required due to drop casting involved in the process, the necessary masks were also printed. However, the majority of stretchable devices still relied on additional non-printing steps. Photolithographic patterning and metal evaporation for electrodes,[270, 273] or top-down patterning of the semiconductor are often necessary.[236, 268, 272, 273, 275, 277] Additionally, devices or individual layers are often fabricated on rigid substrates and later transferred to elastomers to ensure stretchability.[268, 273, 279] An often utilized technique for increasing the stretchability is the so-called buckling that can be achieved when pre-stretching the substrates.[270, 274, 280, 281] Layers transferred on pre-stretched substrates buckle upon stress-release and the tolerable range of deformation could be increased. All-printed flexible transistors were demonstrated based on printed silver electrodes, semiconducting carbon nanotubes or small molecules, and a barium titanate / polymer composite dielectric. For these devices, bending radii of a few millimeters down to 140 µm when fabricated on ultra-thin substrates were reported.[147, 227, 282] However, the majority of reports still relied on non-printing techniques for some of the deposited layers.[173, 271, 283-285] Additionally, flexible substrates were used for some completely printed devices but without quantification of the performance stability with respect to bending.[148, 263-265, 267, 286, 287]

Although a wide range of materials that can be printed and/or stretched was demonstrated, the majority of reports did not combine these favorable properties for all layers of the devices and publications about all-printed, stretchable or flexible transistors are still rare. However, the availability of materials and demonstrations of devices withstanding intensive stress, strain, bending, or other environmental impact is promising for future applications.

2.3.3. Printing methods

One possibility to categorize printing techniques is to distinguish between contact and non-contact methods, but also other categories such as direct-write *vs* using a physical mask, or batch *vs* roll-to-roll processing are possible. Gravure, offset, and flexographic printing all require structured or pretreated cylinders that come in contact with the substrate and thereby transfer the ink. Further examples of contact printing techniques are screen printing and microcontact printing. Systems that use masks for patterned deposition, *e.g.* airbrush spraying, can also be added to this category.

The main non-contact printing methods are inkjet and aerosol-jet printing that are both capable of directly writing the desired patterns without any masks or contact to the substrate.[198, 288-291]

High-throughput roll-to-roll printing techniques require pre-structured printing cylinders increasing the initial costs of manufacturing. A graphical overview about some methods is given in **Figure 2.17**. **Flexography** is a relief printing technique that uses a soft, structured roll with elevated features to transfer the ink to the substrate. Conducting features were successfully printed with flexography for organic photovoltaics with failure-free deposition over several 100 m.[292, 293] The main disadvantages are non-uniform heights of printed structures, swelling and elasticity changes of the printing cylinder due to organic solvents used in the process and wear of the rather soft material. While features are elevated in flexography, **gravure printing** uses pre-patterned grooves in a hard cylinder for ink transfer. The printing results in a pixelated image on the substrate and the individual pixels have to connect by ink flow after deposition.[294] As the solid engraved cylinders are not deformable, a uniform contact with the substrate requires a flat surface and this technique is hence most suitable for patterning the first layer of a device. Material deposited before a gravure printing step can be damaged due to high mechanical pressure or lower spots might be not in contact with the printing roll and thus hinder material transfer. **Offset printing** cylinders are not three-dimensionally patterned but exhibit a difference in surface energy of individual areas on one of the printing cylinders.[198, 290] While this technique is used frequently in classical printing, especially the required viscoelastic properties of the ink, *i.e.* a very high viscosity and a pronounced shear thinning, which can only be reached with additives, prevent a widespread use in printed electronics. A modification of this printing process is called **reverse offset printing**. The completely coated flat cylinder is here rolled over an engraved glass plate to partially transfer the ink to elevated glass areas. The ink remaining on the cylinder is then transferred to the substrate and enables sub-micron resolution.

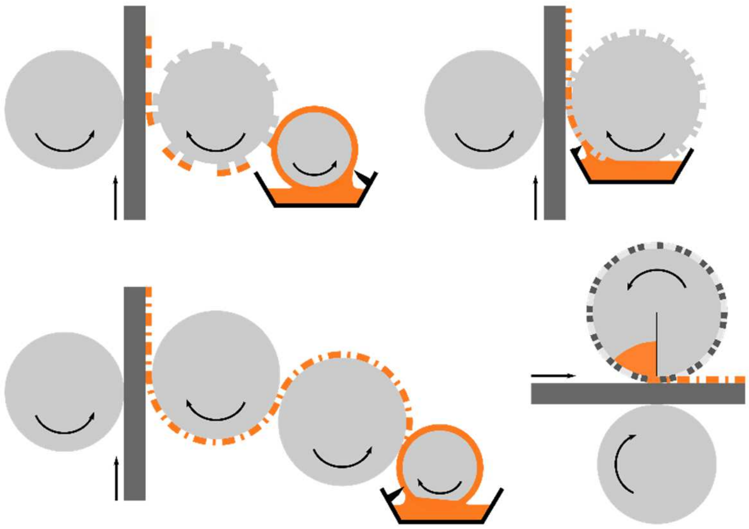

Figure 2.17*: Schematic illustration of different printing methods: flexography (top left), gravure printing (top right), offset printing (bottom left), and rotary screen printing (bottom right).*

In contrast to the above mentioned methods that rely on ink transfer, other techniques use masked deposition. **Spray deposition** through shadow masks can be used for various materials but results in a high material loss due to the large areas coated during the process. Nevertheless, it was used for various materials on the lab scale for electrodes and semiconductors in field-effect transistors, sensors, photovoltaics and other devices.[111, 179, 295-301] The material is deposited from a dispersion with a commercial airbrush gun and the resolution mainly depends on the used shadow masks. In case of heated substrate stages, metal-organic precursors can form an oxide due to pyrolysis occurring at the substrate. In the **screen printing** process, the ink is squeezed through a mesh that is partially closed to form a mask. This enables the realization of unconnected patterns that are not possible with shadow masks.[198, 290] While flatbed screen printing is a batch process, rotary screen printing, *i.e.* using a patterned mesh on a cylinder, can be incorporated in roll-to-roll processes. The current state regarding throughput, and resolution as well as examples of printed layers for transistors are summarized in Table 2.1.

Table 2.1: Overview of different printing techniques

Printing technique	Max. speed [m min^{-1}]	Resolution [µm]	Examples		
			Conductors	**Semi-conductors**	**Dielectrics**
Flexography	500 [198]	30 [198]	[219, 226, 292, 293]	[253, 254, 257]	[219, 226]
Gravure	1000 [290]	2 [302]	[147, 224, 240, 303, 304]	[219, 224, 257, 259, 303, 304]	[147, 219, 224, 257, 303, 304]
Offset	1000 [198]	20 [198]	[219, 237]		
Reverse offset	3 [305]	< 1 [258]	[258, 305, 306]		
Screen	35 [307]	50 [198]	[227, 233, 259, 308]	[259, 308]	[227, 259, 308]
Rotary Screen	100 [307]	100 [309]	[309]		
Spray	N/A	10-100	[111, 297]	[179, 298-301, 310]	
Inkjet	100 [198]	10 [294]	[222, 238, 266, 311-319]	[222, 238, 256, 257, 266, 312, 320-324]	[227, 259, 308, 325]
Aerosol-jet	N/A	10 [326]	[152, 239, 265, 327-330]	[148, 149, 153, 187, 192, 233, 239, 255, 265, 327-334]	[149, 187, 192, 239, 255, 329, 330]

Inkjet printing is a technique that works in the non-contact mode and does not require physical masters for pattern creation.[335] Additionally, the required ink volumes are rather small. While the throughput is rather low, it can be easily upscaled by parallelization, *i.e.* the simultaneous use of several print nozzles, and reach printing speeds of up to 100 m min^{-1}. The ink viscosities are comparably low with 1–40 mPa·s and depend on the nozzle diameter.[198] The low viscosities enable the use of highly purified materials even in low concentration without the need of additional binders in the ink. In a typical inkjet printer, the printer head and nozzle consist of an ink reservoir with a piezoelectric constrictor and a fine opening towards the printing substrate. The constrictor is deflected by an applied voltage and thus generates a pressure wave that pushes ink through the nozzle opening. The constrictor then straightens again which causes another pressure change in the ink and a droplet is formed of the material previously pushed through the nozzle.[294] The ejected material is hence deposited in small droplets that define the printing resolution of down to less than 10 µm. For the creation of closed layers, the droplet spacing has to be small enough to result in continuous paths. Smaller droplets thus enable a higher resolution but also decrease the throughput as the number of droplets that have to be deposited to generate a continuous line increases. The optimum drop spacing has to be determined for each ink and nozzle size to avoid discontinuities as well as bulges that result from too low spacing und thus too much ink.

Conductive paths of metals,[222, 311-313] polymers,[238, 266, 314, 315] and carbon nanotubes were prepared with inkjet printing that can serve as electrodes in transistors and photovoltaics.[316-319] Carbon nanotubes,[266, 312, 320-324] pentacene precursor,[222, 324] oxides,[321, 323] and polymers were printed as semiconductors for transistor applications.[238, 256] Moreover, inkjet printing of electrodes was used in combination with dewetting structures to enable submicron channel lengths or completely inkjet printed devices.[222, 315]

Fully inkjet-printed transistors with silver electrodes, a commercial p-type polymer semiconductor, and PVP dielectric were demonstrated and thoroughly analyzed for device failure causes originating from the printing process. Besides particles or material impurities, the main failure reasons were discontinuities in electrodes or dielectrics due to nozzle clogging, and source-drain shorts due to droplets deposited aside of the printing pattern.[225] These issues can also easily occur in transistors utilizing printed CNTs. Carbon nanotube transistors were presented using CNTs as electrode and semiconductor material. Specifically functionalized nanotubes were used with a PEG dielectric in a process that does not rely on previous sorting of CNTs.[336] By tuning the CNT coverage of unsorted CNTs, the conductivity and eventually the switching behaviour could be tailored in an electrolyte-gated transistor with a channel length of several millimeters with a mobility of 1–4 $\mathrm{cm^2\ V^{-1}\ s^{-1}}$ and an on/off-ratio of up to 10^5, although at very low overall currents.[337]

In combination with other patterning or deposition techniques, inkjet printed CNTs were also successfully used in transistors and even complimentary logic circuits. The individual transistors exhibited mobilities of around 10 $\mathrm{cm^2\ V^{-1}\ s^{-1}}$ and on/off-ratios of up to 10^7.[221, 266]

Aerosol-jet printing is a further non-contact method successfully used for printing of various materials, including conductors and carbon nanotubes. As this method was mainly used within this work, it will be explained in more detail in the next section.

In the last years, various methods, materials, and devices were also the subject of several review articles.[182, 198, 289-291, 294, 307, 326, 335, 338-343]

2.4. Aerosol-Jet Printing

2.4.1. Working principle

Aerosol-jet printing relies on the aerosolization of a liquid ink, *i.e.* transferring the ink into a nebular phase of small droplets with a size of 1–5 µm. This process can be either realized with a pneumatic atomizer or – as utilized in this work – with an ultrasonic atomizer. The printing process is illustrated in **Figure 2.18**. For ultrasonic atomization, the ink is placed into a glass vial with a thinned bottom. The vial is closed while a gas inlet and an aerosol outlet remain open. In a temperature controlled water bath a transducer generates ultrasonic waves with a frequency of around 13 MHz. Through the water bath and the thin vial bottom, the ultrasonic power can be transferred to the ink. An aerosol can be formed in the vial, if the ink has a suitable viscosity of 1–10 mPa·s. A suitable viscosity is not only important for the aerosolization process but also influences the flow of deposited material on the substrate. Most solvents of active materials, such as toluene for carbon nanotubes, exhibit rather low viscosities and need a highly viscous co-solvent to reach the desired viscosity range. The aerosol is then transported with a carrier gas through a tube attached at the aerosol outlet. The aerosol enters the printer head centrally and a focusing gas (also called sheath gas) is added. For both, the carrier and the sheath gas, usually dry nitrogen is used. Due to the printer head geometry, the focusing gas completely surrounds the aerosol, so that with ideal printing conditions, no contact of the material to be deposited to the printer nozzle occurs. Within the printer head and the nozzle, the stream is further focused to the inner nozzle diameter which is 100–300 µm at the outlet.

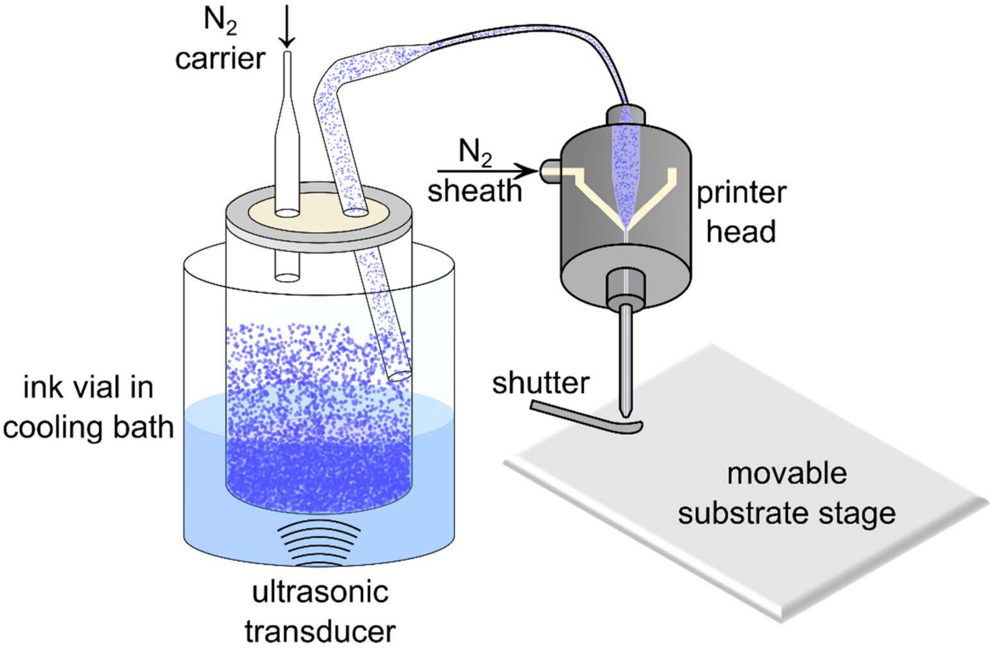

Figure 2.18*: Illustration of aerosol-jet printing setup with an ultrasonic atomizer. Adopted with permission from Adv. Electron. Mater. 2017, 3, 1700080.*[150]

The aerosol stream exiting the nozzle remains focused over a distance of several millimeters and thus enables printing on flat as well as uneven substrates without a loss of spatial resolution in contrast to inkjet printing.[344] Because the output is continuous and not just on demand, a spoon shaped shutter below the printer nozzle is used to control the deposition of material. In the benchtop version of the printer used in this work, the substrate is placed on a heated stage that can be moved automatically in the *x*- and *y*-direction. Other machines of the so-far only supplier Optomec Inc. are equipped with a 5-axial stage or can be incorporated into roll-to-roll printing systems.

The output volume as well as the line width, thickness, and shape are mainly controlled by the gas flows, the nozzle size, and the stage speed. Additionally, also the stage temperature and the ink composition influence the final printing pattern as they control the evaporation of solvents and interaction with the substrate, and thereby the flow of deposited material on the substrate. While too little interaction between substrate and ink can result in discontinuities of printed lines, excessive wetting leads to a significant loss of spatial resolution. The influences of nozzle size, stage speed, and flow rates were previously examined in detail for a silver nanoparticle ink.[345] The line width decreased – and thereby the line thickness increased – with decreasing nozzle size and increasing ratio of sheath and carrier gas. This ratio was named focusing ratio and shown to have significant importance on the printing process. An increased carrier gas flow rate at constant focusing ratio did not lead to increased line width but only increased thickness. Additionally, the stage speed only influenced the line width when below a certain velocity. At higher stage velocity, when ink spreading was less important, the line width was independent of the stage speed but only depended on the focusing ratio. The thickness of the deposited material line was however again dependent on the stage speed. Four different line shapes were explained by this observations: discontinuous lines (at too low carrier gas flow or too high stage speed), ill-defined edges, *i.e.* flow of material out of the line shape (at too high carrier gas flow or too low stage speed), unfocused lines (at too low focusing ratios), and optimized lines with the focusing ratio, stage speed, and carrier gas flow adapted to each other. The printing parameters for each possible ink must hence be optimized.

2.4.2. (Partially) Aerosol-Jet Printed Devices

One main focus of aerosol-jet printing was the creation of conducting pathways, especially utilizing silver nanoparticle based inks. Besides simple conductive paths and electrodes,[5, 152, 265, 327, 328, 346-349] grid-shaped and thus semi-transparent electrodes as indium tin oxide substitutes in photovoltaics and LEDs were reported.[350-352] With fast-drying inks, even the creation of three-dimensional structures and interconnects is possible. Additional conductive structures as electrodes were fabricated using PEDOT:PSS.[187, 239, 327, 329, 330, 353] With regard to semiconducting materials, devices with carbon nanotubes,[148, 149, 153, 265, 328, 331-334] P3HT,[187, 192, 233, 239, 255, 327, 330] and oxides were demonstrated. [327, 329] Aerosol-jet printed ion-gels were presented as dielectrics that also support flexibility and stretchability of the resulting devices.[149, 187, 192, 239, 255, 329, 330]

The so far demonstrated completely aerosol-jet printed transistors relied on established materials, *i.e.* silver, PEDOT:PSS, CNTs, and ion-gels.[151, 334, 354] Usually aqueous CNT inks were used that were not previously enriched in semiconducting species. In contrast to that, Zhao *et al.* dispersed the nanotubes with 2,2-azobisisobutyronitrile in dimethylformamide.[334] Due to the presence of predominantly semiconducting species, they were able to achieve on/off-ratios of up to more than 10^3 for a majority of their devices. Further publications on aerosol-jet printed transistors used photolithographically patterned source and drain electrodes and were hence not all-printed but resulted in improved device characteristics with on/off-ratios of up to 10^5 and mobilities of around 10 $cm^2\ V^{-1}\ s^{-1}$.[148, 149] In a study comparing different aerosol-jet printed electrodes (gold, silver, and carbon nanotubes) with aerosol-jet printed semiconducting CNTs, an oxide-covered silicon substrate was used as a common bottom-gate.[153] Although the number of reports is still low, it was already demonstrated that aerosol-jet printing can be a suitable fabrication techniques for all layers of a transistor.

Besides transistors, aerosol-jet printing was also used as the sole manufacturing technique for photodiodes,[355] photodetectors,[356] sensors,[357] as well as band-pass and polarization filters.[358] Additionally, active layers in solar cells were printed.[359] The range of printable materials exceeds electronic components and reaches up to photoresist and biomolecules.[360-362]

In conclusion, aerosol-jet printing was proven to be a versatile tool for the deposition of numerous materials on a wide range of substrates that do not necessarily have to be completely flat. With respect to carbon nanotubes, printing was successfully used for the fabrication of semiconducting layers in transistors. As a wide range of materials was already printed, (area selective) doping and the addition of analyte materials can probably be realized via aerosol-jet printing. The flexible pattern design of the additive manufacturing process further allows a fast evaluation of new architectures and the combination of materials that is not possible with conventional fabrication techniques.

CHAPTER 3

EXPERIMENTAL

This chapter details the experimental procedures performed to obtain the results presented in this work.

3.1. Alterations to the Optomec Aerosol-Jet System

In this work, aerosol-jet printing was widely used to deposit CNTs as well as metallic electrodes. Aerosol-jet printing systems are manufactured by Optomec Inc., Albuquerque, NM, United States. Within this work, their benchtop Aerosol Jet 200 system equipped with an ultrasonic atomizer was used. The delivered version of this system came with a sophisticated atomizer unit that was developed by Optomec. As shown in **Figure 3.1**, the ink vial is placed in a small water bath with continuous water flow and cooling via a heat exchanger. The position of the vial is fixed within the water bath enabling reproducible sonication strength for a defined flow, water level, and current through the ultrasonic transducer.

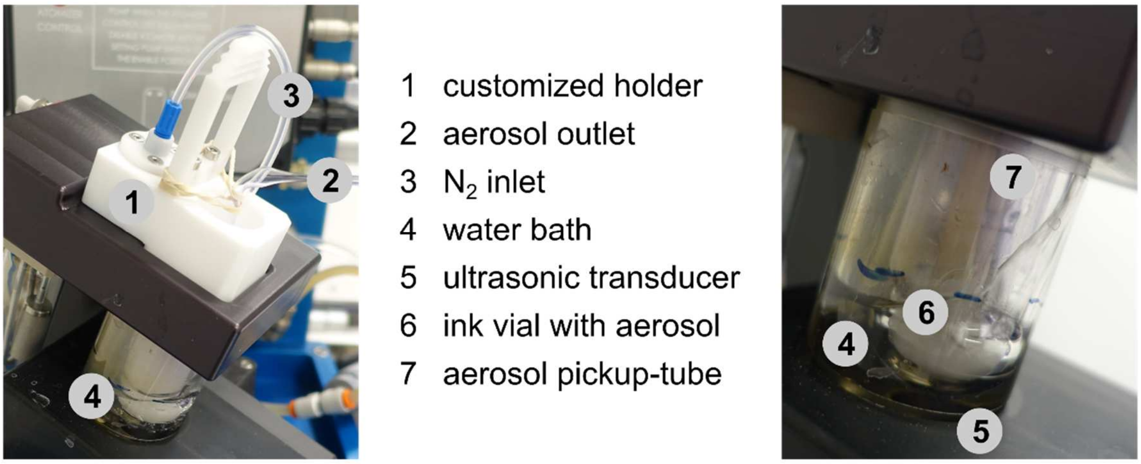

***Figure 3.1**: Aerosol Jet 200 atomizer unit.*

In the original system, the ink vial is screwed into a holder consisting of several parts that also contain the carrier gas inlet, a stainless steel pickup-tube for the aerosol outlet, and sealing rings (see **Figure 3.2**). The disadvantage of this system is the labor intensive cleaning that is necessary when switching between different inks, especially when changing from conductive to semiconducting materials where contamination has to be avoided. The holder system was hence customized to reduce the number of fixed parts that are used with every ink. The adapted holder could be equipped with single-use components, *i.e.* modified glass pipettes for the gas inlet and outlet that were punched through the sealing membrane of the ink vial cap. These alterations were based on earlier systems manufactured by Optomec. With this configuration, only the printer head and nozzles are contaminated with ink and have to be cleaned after each printing process. This modification also enabled a quick change of materials and consecutive printing of different inks for electrodes and semiconductors with reduced down-time for cleaning.

***Figure 3.2**: Photographs of the original (top) and customized (bottom)* via*l holders depicting all individual parts (left) and the completely assembled holders (right). The customized holder enables the use of disposable parts directly in contact with the ink.*

During the process, the created aerosol is transported from the atomizer unit to the printer head that is mounted with the process camera and the alignment camera on a joint unit that can be moved in z-direction. Both cameras can be focussed individually and enable the observation of the printing process as well as alignment of the printer head to previously created patterns on the substrate. For the realization of versatile patterns, the system was equipped with a heated stage (maximum temperature 100 °C) that could be moved in x- and y-direction with a precision in the micrometer range and a shutter below the printing nozzle (see **Figure 3.3**).

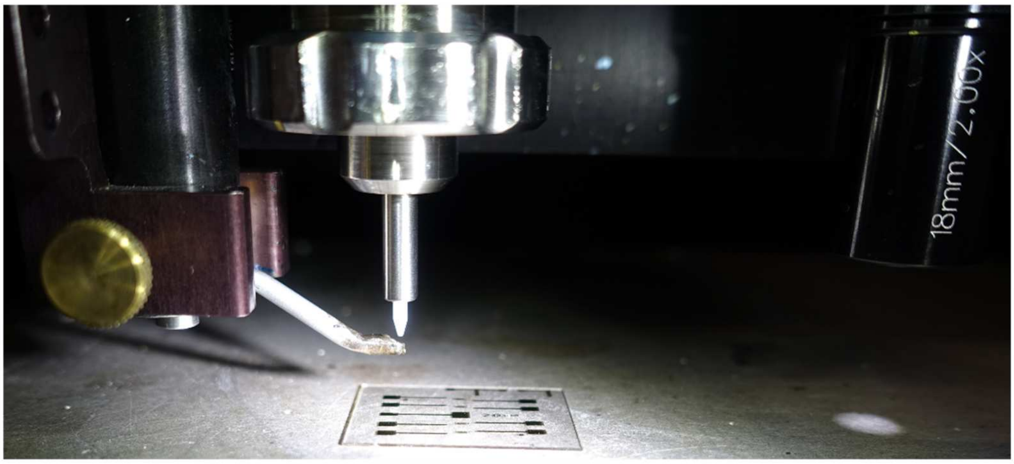

***Figure 3.3**: Close-up photograph of the stage area of the aerosol-jet printer. A substrate is placed on the movable stage; the distance to the printer nozzle is several millimeters. The shutter can be seen below the printer head and nozzle. The alignment camera is visible in the right part of the image.*

3.2. Device Fabrication

3.2.1. Carbon Nanotube Dispersions

Dispersions of semiconducting (6,5) carbon nanotubes were prepared with the polymer-wrapping method.[94] First, 0.5 g L^{-1} of poly[(9,9-dioctylfluorenyl-2,7-diyl)-*alt-co*-(6,6′-(2,2′-bipyridine))] (PFO-BPy) were dissolved in anhydrous toluene. The CoMoCAT carbon nanotube raw material (diameter range 0.6–1.1 nm) was added at a concentration of 0.38 g L^{-1}. Instead of the more widely used sonication to debundle the nanotubes to facilitate efficient polymer-wrapping of individual CNTs, a shear force mixer was used for 72 hours at 10 230 rpm.[110] Undispersed material, *i.e.* amorphous carbon, left-over catalyst and other CNT chiralities, was removed by centrifugation at 60 000 g for 45 min. The collected supernatant contained wrapped nanotubes as well as excess polymer. This polymer was removed either by pelletizing the CNTs via centrifugation at 268 400 g for 20 hours or vacuum filtration through a poly(tetrafluoroethylene) (PTFE) filter (pore size 0.1 µm) and subsequent washing with tetrahydrofuran (THF). The filter cake or centrifugation pellet were redispersed in fresh toluene by 30–60 min bath sonication immediately prior to further use.

During a repair-related down-time of the shear force mixer, the dispersion process had to be altered. The polymer was dissolved in toluene at 80 °C at a concentration of 2 mg mL^{-1}. After cooling down, 1.5 mg mL^{-1} of nanotube raw material were added and the dispersion was bath sonicated for 90 min. The dispersion was then centrifuged at 60 000 g for 45 min to remove undispersed material and CNT bundles. The supernatant was collected and again centrifuged with the same parameters. Removal of excess material was realized by pelletizing the polymer-wrapped nanotubes at 284 600 g for 20 hours. The pellet was then washed and redispersed in fresh toluene as described for the filter cakes above. Note that sonicated nanotubes are generally shorter than shear-force mixed CNTs.[110]

Dispersions of mixed semiconducting and metallic carbon nanotubes as electrode material were produced in a different way. The raw material used was TUBALL CNTs with a diameter range of 1.2–2.0 nm. They are produced on a large scale and at low cost. Non-selective dispersion of CNTs can be achieved by sodium cholate in water. 1 g L^{-1} TUBALL CNTs were added to an aqueous solution of sodium cholate (6 g L^{-1}). The debundling and dispersion of the CNTs was induced by bath (1 h), tip (15 min, taper tip, 20 % power, 1 s on/off cycles) and further bath (1 h) sonication. The removal of undispersed material was realized by centrifugation at 2970 g for 90 min. The resulting dispersion was diluted 1:224 with 2 g L^{-1} sodium cholate in DI water, filtered (PTFE, 5 µm pore size) and further diluted (1:1 in DI water). This dispersion was directly used for spray-coating as is.

3.2.2. Electrode Patterning

Four different types of electrodes were used for this work: evaporated metal, aerosol-jet-printed silver nanoparticles, airbrush-sprayed TUBALL nanotubes, and inkjet-printed gold nanoparticles. While the printed electrodes were already patterned, evaporated or sprayed electrodes required additional structuring by photolithography or shadow masks.

The easiest patterning method is the use of stainless steel **shadow masks**. However, these masks are usually limited to feature sizes of several tens of micrometers. They were used for airbrush-spraying of TUBALL electrodes as well as thermal evaporation of silver gate electrodes and gold source, drain and side-gate electrodes.

Photolithography was used as a precise and reliable patterning technique with high resolution (≤ 1 µm) and accuracy especially for interdigitated source and drain electrodes. Each layer of the double layer resist (LOR5B and S1813) was spin-coated at 3000 rpm for 30 s and annealed at 185 °C for 4 min or 115 °C for 1 min, respectively. Chromium-coated soda lime masks were used for patterned UV exposure with a mask aligner at a dose of 182 mJ cm^{-2}. The samples were then developed in MF319 Developer for 20–25 s, rinsed with deionized water and blown dry. During exposure, the positive photoresist S1813 became soluble at the exposed areas and could be removed in the developing step. LOR5B is not photoactive and was removed when exposed to the developer, *i.e.* after selective S1813 removal, LOR5B was removed in the same areas and additionally an undercut was realized. The undercut was beneficial to improve the lift-off of the subsequently evaporated metals at the structure edges. The process was completed by dissolving the unexposed photoresist (and lift-off of the metal layer on top of it) in *N*-Methyl-2-pyrrolidone (NMP) leaving metal only in the areas defined by the UV exposure.

Metal evaporation was performed in an electron-beam or thermal evaporator at pressures lower than $1\cdot10^{-6}$ mbar and deposition rates of 0.1 to 1.0 Å s^{-1}. The typical electrode thickness was 30 nm. When gold was used as a bottom electrode, a 2 nm chromium adhesion layer was evaporated first. Top electrodes were evaporated directly onto the device.

Gold nanoparticles were inkjet printed by Martin Held at the InnovationLab, Heidelberg, Germany, from a commercial ink based on a mixture of water and ethylene glycol. The PEN substrate was rubbed with isopropanol for homogenization immediately before printing and placed on the printer stage heated to 60 °C. The side of the substrate that was not pre-treated by the manufacturer was facing upwards. The ink was printed as received from 1 or 10 pL cartridges with a drop spacing of 10–20 µm. The jetting frequency and the tickle control (used to prevent nozzle clogging while not jetting) were both set to 1 kHz while the distance between substrate and printer nozzle was 750 µm. The printing pattern was optimized to reach an optimal trade-off between deposition time, resolution, ink consumption, and resistivity. Hence, the wider leads (325 µm) and the contact pads were printed as a single layer with a drop spacing of 10 µm. The ends of the leads were triangular in shape to improve the connection to the narrower contacts. The actual top and bottom contacts were printed with only 5 adjacent lines but 10 layers on top of each other to reduce the overall resistance, resulting in a total width of 70–100 µm. The contact pads, leads, and contacts of the bottom electrode were printed before deposition of CNTs in vertical transistors, while the leads and contacts of the top electrode were printed afterwards. Refer to **Figure 7.1** for the printing pattern used with inkjet printed gold. After each inkjet printing process, an annealing step at 155 °C in ambient air for several hours was performed to reduce the resistance of the printed gold nanoparticles.

For aerosol-jet printing of **silver nanoparticles**, a commercial ink was used as purchased. In principle, the same process as described for CNTs (see chapter 3.2.3) was used while some parameters had to be adjusted. The maximum sonication power (~ 550 mA transducer current) was used and the temperatures of ink and stage were set to 20 °C and 100 °C, respectively. A 150 µm inner diameter nozzle was chosen and the sheath and carrier gas flow rates were set to 50 and 40 sccm, respectively. The stage speed was set to 5 mm s^{-1} and single lines were printed with 2 passes to form the electrodes. The contact pad was formed by parallel lines with a pitch of 50 µm and had an approximate size of 1 x 1 mm^2. The gate electrode was printed likewise and had a total size of 15 x 1.5 mm^2. **Figure 3.4** illustrates the printing pattern used for VEGTs with silver ink. The ink was annealed at 130 °C overnight in air after each printing step before further processing.

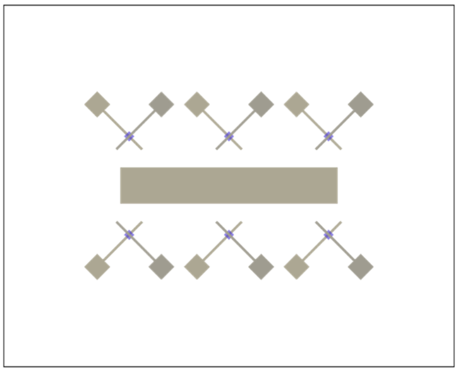

***Figure 3.4**: Electrode structure used for aerosol-jet printing of silver nanoparticles as electrodes in vertical electrolyte-gated transistors including the depiction of printed CNTs (purple).*

3.2.3. Aerosol-Jet Printing of CNTs

Inks of polymer-wrapped CNTs were prepared from pellets or filter cakes redispersed in fresh toluene. The concentration of the dispersion was determined via UV-VIS-NIR absorbance spectroscopy. The final ink usually contained 5 % v/v terpineol and the concentration was adjusted to the desired level of 1.8 to 6.6 mg L^{-1} by addition of toluene.

Details of the commercial aerosol-jet printing system and alterations for a more convenient usage in the lab with different materials are described in section 3.1. The ink vial was filled with 1 mL of ink and the gas inlet and outlet were connected tightly. All O-rings at the printer head were freshly greased directly before the assembly. The printing head was equipped with a 200 µm inner diameter ceramic nozzle. The ink and stage temperatures were set to 20 and 100 °C, respectively.

The ink was aerosolized at maximum sonication power, *i.e.* the displayed transducer current was around 550 mA. Sheath and carrier gas flow rates (both nitrogen) were set to 30 and (15 ± 1) sccm, respectively. The stage speed was set to 0.5 mm s^{-1}. The lateral position and focus of the process camera were adjusted to the output position of the aerosol stream on a silicon substrate. The silicon substrate was chosen due to better visibility and higher contrast of the printed lines and thus easier alignment. After focus adjustment of the alignment camera, its position was aligned to the printing output point with the respective software tool by printing a cross. The AJ printer was then ready to use.

The printing pattern was defined via Autodesk AutoCAD and the VMTOOLS-Plugin provided by Optomec. The desired printing lines were drawn and the resulting toolpath was exported. Note that the printing sequence directly depends on the drawing or insertion sequence in the AutoCAD file. Thus the order of printing could be manually controlled. The positions of alignment markers, so-called fiducials, had to be manually inserted into the output file before loading this file in the printer software and enabled the alignment to previously deposited layers.

Depending on the actual substrate thickness, which varied from the silicon chip thickness used for alignment, the vertical position of the printer head and camera unit was adjusted. This was achieved by bringing the substrate into the focus of the alignment camera with the z-axis micrometer screw of this unit and not with the focus screw of the microscope. With the built-in fiducial manager, the positions of alignment markers or structure edges to the fiducials defined in the toolpath were set and the software performed an angle correction of the printing path.

The printing itself was then performed automatically while droplet formation in the aerosol-tube was observed and avoided. When droplets reach the printer head, a large splash on the substrate occurs, which is especially detrimental for precise structures such as electrodes. For CNT films, those splashes usually did not influence the devices as only little nanotube material was deposited outside the desired printing areas.

After printing, the CNT film was allowed to settle for at least 30 min on the stage to avoid accidental removal during subsequent rinsing with THF and IPA as well as drying with nitrogen. Note that the terpineol did not evaporate and had to be washed off. If further processing was carried out in inert atmosphere, the samples were annealed in nitrogen at 300 °C for at least 30 min to remove residual water and solvents.

3.2.4. Airbrush Spraying of TUBALL Nanotubes

Airbrush spraying was performed for TUBALL nanotube dispersions as electrode material. A commercial airbrush system equipped with a 150 µm inner diameter nozzle was used. The carrier pressure, and needle displacement were set to 1 bar and 300 µm, respectively. At a throwing distance of 100 mm, 2 mL of the dispersion were sprayed through stainless steel shadow masks. The masks were attached to the home-built substrate stage that was heated to 140 °C. A homogeneous material deposition was ensured by shuttling the stage over the whole substrate length of 25 mm. Removal of the sodium cholate surfactant was realized by soaking in deionized water overnight. Finally, the sprayed electrodes were annealed in air at 100 °C for 30 min.

3.2.5. Fabrication of Transistors

Different transistor structures were fabricated in the framework of this thesis. For lateral field-effect transistors as utilized in chapter 5, a staggered top-gate structure was used. Bottom electrodes, *i.e.* interdigitated source and drain, were photolithographically patterned on glass substrates. Subsequently, the semiconductor was deposited via spin-coating or aerosol-jet printing. The hybrid dielectric consisted of a bilayer of spin-coated poly(methyl methacrylate) (PMMA) and hafnium oxide. An 11 nm thick PMMA layer was created by spin-coating from an *n*-butylacetate solution (6 g L^{-1}) at 3000 rpm s^{-1} for 30 s in nitrogen atmosphere. After annealing at 80 °C for 30 min, the samples were directly transferred into the atomic layer deposition (ALD) chamber. After a 60 min annealing step at 100 °C in the chamber under 20 sccm nitrogen flow, alternating pulses of tetrakis(dimethylamino)hafnium (TDMAH) and deionized water formed the oxide layer. A thickness of 61 nm was reached after 500 deposition cycles. The transistors were completed by thermal evaporation of the silver gate (30 nm thickness).

For vertical transistors, the bottom (source) electrode together with the side gate were patterned via photolithography or shadow masks and consisted of 2 nm chromium and 30 nm gold. A thick CNT film was aerosol-jet printed on the electrodes. The pattern was chosen in a way that deposition took place with an additional margin of 100 µm around the electrode overlap area. The top (drain) electrode was then thermally evaporated through a shadow mask (gold, 20 nm thickness). Alternatively, all electrodes were directly aerosol-jet or inkjet printed from silver or gold nanoparticle inks, respectively. As a third electrode fabrication method, airbrush spraying through shadow masks was used. After deposition of the top electrode, the ion-gel was spin-coated at 100 rpm s^{-1} for 60 s. on top of the device. The ion-gel was prepared from [EMIM][FAP] as the electrolyte, P(VDF-HFP) as the polymer binder, and acetone in a mass ratio of 4:1:14.

3.3. Characterization

3.3.1. Absorption Spectroscopy

Absorbance measurements were usually performed on dispersions in cuvettes with an optical path length of 1 cm. The silicon and InGaAs detector of the spectrometer enabled acquisition in the ultraviolet, visible, and near-infrared range and spectra were acquired in the range of 1600–300 nm. All recorded spectra were background corrected by the measurement of a baseline with pure solvent in the same cuvette. Optically dense films were measured with a solid sample holder. The baseline correction was performed with a cleaned substrate.

3.3.2. Profilometry

Profilometer data was recorded to determine the thickness of printed films of carbon nanotubes, silver nanoparticles, and gold nanoparticles. A line scan across the whole feature was acquired and the feature height was averaged in the plateau region. Moreover, the thickness of evaporated metals and atomic layer deposited oxides was determined by scans at the edge of sharp features.

3.3.3. (Conductive) Atomic Force Microscopy

Topography images were recorded with an atomic force microscope (AFM) in tapping or ScanAsyst mode (Bruker) with suitable AFM tips. The resulting images were corrected with Gwyddeon 2.41 to level backgrounds, line errors, offset and z-range. The PeakForce TUNA mode (Bruker) was used for conductive AFM measurements. A sample bias of 1 V was applied to the conductive tip. The resulting contact current images were normalized to the absolute current maxima to account for varying tip conditions, peakforce setpoint, and amplitude.

3.3.4. Scanning Electron Microscopy

When possible, electrodes of the partially completed devices were grounded to the sample holder in the scanning electron microscope (SEM) to reduce sample charging. Images were recorded with the inLens-detector in secondary electron mode at a low acceleration voltage of 1 kV to avoid film damage.

3.3.5. Raman Spectroscopy

Raman spectra and maps of CNT films were collected with resonant laser excitation at 532 nm with a confocal Raman microscope in back scattering configuration with a high-speed encoded sample stage and using different objectives. Additional spectra (RBM region of CNTs) were recorded under 633 nm excitation at various spots to reveal further CNT chiralities. Doping of electrolyte-gated CNT films was investigated by mapping the G^+-band in the whole channel using the Renishaw Streamline mode with a step size of 1.3–2.0 µm while the source and drain electrodes were grounded and a bias was applied to the gate electrode with a semiconductor parameter analyzer.

3.3.6. Electrical Characterization

Device **capacitances** were measured with an impedance spectrometer directly on the respective field-effect transistor. The short-circuited source and drain electrodes as well as the CNTs constituted the bottom electrode of a capacitor, and the gate the top electrode. The measurements were performed in the on-state of the transistor, *i.e.* at sufficiently high bias of ±8 V, and at a frequency of 1 kHz.

Current–voltage characteristics with applied gate voltage (output and transfer characteristics) were measured with a semiconductor parameter analyzer or a source-meter unit in different voltages ranges with different sweep rates as given in the respective representations of acquired data. Measurements without a gate were performed for the determination of the channel resistance with a source-meter unit in a voltage range of ± 1 V.

The response to deformation of **flexible transistors** was determined by manually bending the samples around metal rods of different diameters (see **Figure 3.5**) and contacting the devices in the bent state. For repeated bending, the samples were attached to a home-built and automated machine. The original purpose of this machine was isotropic stretching of samples and the design was adapted from a formerly available commercial setup.[363] The samples were glued to laminated paper to enable attachment to the stretching setup and ensure bending of the transistor area. A software programme written by Peter Jeschka enabled repeated deformation between pre-set positions (see **Figure 3.5**).

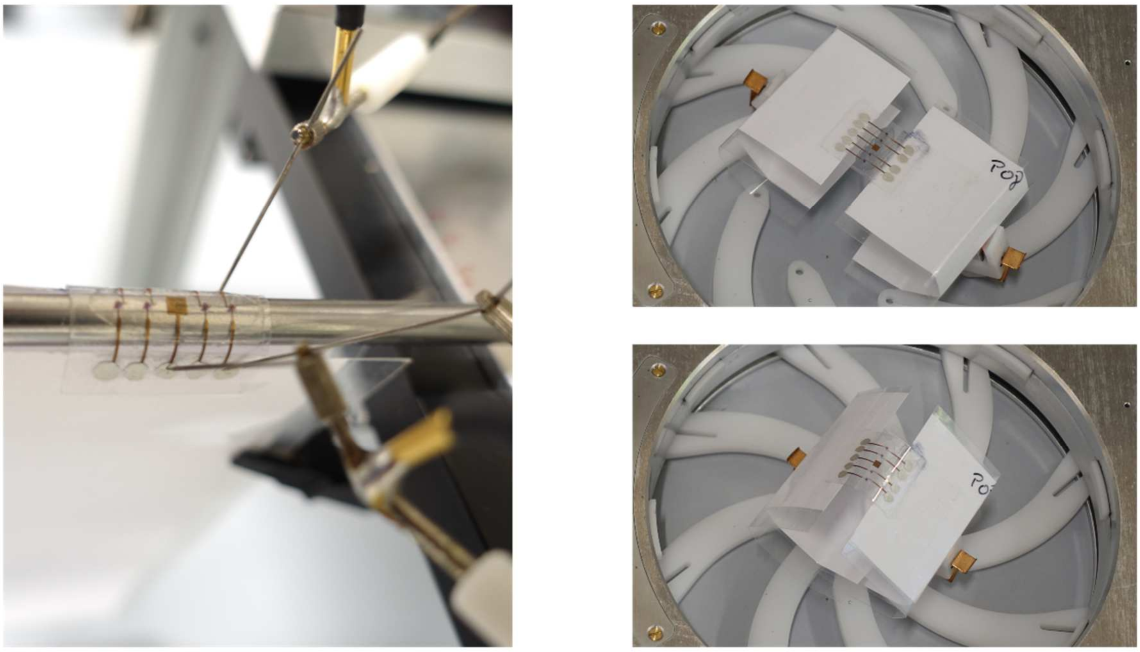

Figure 3.5: *Measurement of flexible transistors: Bending around metal rods with different diameters (left) and automated repeated bending cycles (right).*

CHAPTER 4

MATERIALS AND DEVICES

This chapter describes the materials and devices that were used in this work.

4.1. Materials

The following tables give an overview about the materials used for this work:

- Table 4.1: Carbon nanotube dispersions
- Table 4.2: Photolithography
- Table 4.3: Metals
- Table 4.4: Dielectrics
- Table 4.5: Substrates
- Table 4.6: Other materials

Table 4.1: Carbon nanotube dispersions

Material	Supplier	Item / Specifications
CoMoCAT carbon nanotubes, final devices	CHASM Advanced Materials Inc., Canton, MA, US	SG65i-L58 diameter 0.7–1.0 nm
CoMoCAT carbon nanotubes, initial tests	Sigma-Aldrich GmbH, Steinheim, Germany	Item no. 704148
TUBALL carbon nanotubes	OCSiAL, Leudelange, Luxembourg	black powder supplied free-of-charge
Poly[(9,9-dioctylfluorenyl-2,7-diyl)-alt-co-(6,6′-(2,2′-bipyridine))] (PFO-BPy)	American Dye Source, Baie d'Urfé, QC, Canada	ADS153UV, $M_W = 34$ kg mol^{-1}
Sodium dodecyl sulfate (SDS)	Sigma-Aldrich GmbH, Steinheim, Germany	BioReagent grade, ≥ 98.5 %
Centrifuge tubes	Beckman Coulter GmbH, Krefeld, Germany	Polypropylene tubes 50 ml, Polyallomer tubes 15 ml
PTFE filters	Merck KGaA, Darmstadt, Germany	Omnipore JVWP, pore size 0.1 µm, hydrophilic

Table 4.2: Photolithography

Material	Supplier	Item / Specifications
LOR 5B	micro resist technology GmbH, Berlin, Germany	MicroChem LOR5B used as undercut layer
S1813	micro resist technology GmbH, Berlin, Germany	Microposit S1813 G2 Positive Photoresist
MF-319	micro resist technology GmbH, Berlin, Germany	Microposit MF-319 Developer, active ingredient: Tetramethylammonium hydroxide
Photomasks	Compugraphics Jena GmbH, Jena, Germany	Chrome on soda lime masks, 5“ x 5“ x 0.09“ mask size, feature tolerance 0.1 µm, ≤ 0.2 defects cm^{-1}

Table 4.3: Metals

Material	Supplier	Item / Specifications
Chromium for evaporation	Kurt J. Lesker Company Ltd., Hastings, England	granules, 99.6 % purity
Gold for evaporation	ESG Edelmetall-Handel GmbH & Co. KG, Rheinstetten, Germany	granules, 99.99 % purity
Gold nanoparticle ink	C-Ink Co., Ltd., Akahama, Japan	Dry Cure Au-J 1010B
Silver for evaporation	Umicore AG & Co. KG, Hanau, Germany	pellets, 99.99 % purity
Silver nanoparticle ink	Clariant AG, Muttenz, Switzerland	EXPT Prelect TPS 50

Table 4.4: Dielectrics

Material	**Supplier**	**Item / Specifications**
Poly(methyl methacrylate) (PMMA)	Polymer Source Inc., Dorval, QC, Canada	Syndiotactic $M_W = 350$ kg mol^{-1}
Tetrakis(dimethylamino)hafnium (TDMAH) – HfO_x precursor	Strem Chemicals Inc., Bischheim, France	Item no. 72-8000, >98 %
1-Ethyl-3-methyl-imidazolium-tris(pentafluoroethyl)-trifluorophosphate ([EMIM][FAP])	Merck KGaA, Darmstadt, Germany	high purity grade
Poly(vinylidene fluoride-*co*-hexafluoropropylene) (P(VDF-HFP))	Sigma-Aldrich GmbH, Steinheim, Germany	$M_W \approx 400$ kg mol^{-1}

Table 4.5: Substrates

Material	**Supplier**	**Item / Specifications**
Glass substrates	Advanced Optics SCHOTT AG, Mainz, Germany	AF 32® eco Thin Glass, width 20 mm, length 25 mm, thickness 0.3 mm
Shadow masks	Becktronic GmbH, Weitefeld, Germany **or** CADiLAC Laser GmbH, Hilpoltstein, Germany	Stainless steel, laser-cut patterns, thickness 0.2 mm
Silicon wafers	Siegert Wafer GmbH, Aachen, Germany	thickness 525 ± 25 µm, 100 mm diameter, Si(100), single-side polished, p-doped with Boron
Polyethylene naphthalate (PEN) foil	Pütz GmbH + Co. Folien KG, Taunusstein, Germany *Originally*: Teijin Film Solutions Ltd., Tokyo, Japan	Teonex Q65HA, thickness 125 µm

Table 4.6: Other materials

Material	**Supplier**	**Item / Specifications**
Terpineol, CAS Number 8000-41-7	Sigma-Aldrich GmbH, Steinheim, Germany	Mixture of isomers, anhydrous
Other solvents	Merck KGaA, Darmstadt, Germany, **or** Sigma-Aldrich GmbH, Steinheim, Germany	Analytical grade
Deionized water	In-house, directly from water purification system	Ultra-pure water, $R \geq 18$ MΩ cm

4.2. Devices

The following tables give an overview about the materials used for this work:

- Table 4.7: Carbon Nanotube dispersions
- Table 4.8: Device Fabrication
- Table 4.9: Characterization

Table 4.7: Carbon Nanotube dispersions

Device	**Manufacturer**	**Type**
Centrifuge, > 60000 g	Beckman-Coulter GmbH, Krefeld, Germany	Optima XPN-80 ultracentrifuge with swing-bucket rotor
Centrifuge, ≤ 60000 g	Beckman-Coulter GmbH, Krefeld, Germany	Avanti J-26XP ultracentrifuge
Glovebox for chemicals	MBraun Inertgas-Systeme GmbH, Garching, Germany	LabStar
Shear-Force Mixer	Silverson Machines Ltd., Chesham, UK	L5M-A **or** L2/Air equipped with screw-on general purpose disintegrating head and square hole high shear screen
Tip Sonicator	Sonics & Materials Inc., Newtown, CT, US	Vibra-Cell VCX-500
Ultrasonication Bath	Branson Ultrasonics, Danbury, CT, US	Ultrasonic Cleaner 2510
Ultrasonication Bath	Bandelin electronic GmbH & Co. KG, Berlin, Germany	Sonorex Digitec DT 102 H
Vacuum Filtration	Merck KGaA, Darmstadt, Germany	Merck Millipore glass filter holders (XX1004730 **or** XX1002530), vacuum filtering flask (XX1004705 **or** XX1002505), and chemical duty membrane pump (WP6122050)

Table 4.8: Device Fabrication

Device	**Manufacturer**	**Type**
Aerosol-jet printer	Optomec Inc., Albuquerque, NM, US	AJ 200
Atomic layer deposition (ALD)	Ultratech / Cambridge NanoTech, Waltham, MA, US	Savannah S100
Evaporator, e-beam	Winter Vakuumtechnik GbR, Steinheim, Germany	HVB-130
Evaporator, thermal	MBraun Inertgas-Systeme GmbH, Garching, Germany	MB-ProVap-3
Glovebox for processing	MBraun Inertgas-Systeme GmbH, Garching, Germany	MB200G
Inkjet printer	Fujifilm Holdings K.K., Tokyo, Japan	Dimatix Materials Printer DMP-2889
Mask aligner	SÜSS MicroTec AG, Garching, Germany	MA/BA6 Gen4 **or** MA/BA6 Gen2 *each* with Hg lamp (350 W) and i-line bandpass filter
Spin-coater (for CNTs)	Laurell Technologies, North Wales, PA, US	WS-400BZ-6NPP-Lite
Spin-coater (for dielectrics)	MBraun Inertgas-Systeme GmbH, Garching, Germany	MB-SC-210
Spin-coater (for photoresist)	Obducat Europe GmbH, Lund, Sweden	EL S 200 BM (*Former* solar-semi GmbH)

Table 4.9: Characterization

Device	**Manufacturer**	**Type**
Atomic-force microscope (AFM)	Bruker Corporation, Billerica, MA, US	Dimension Icon
AFM tips for c-AFM	Bruker Corporation, Billerica, MA, US	SCM-PIT
AFM tips for tapping and ScanAsyst mode	Bruker Corporation, Billerica, MA, US	ScanAsyst-Air, TESPA-V2, OTESPA-R3
Impedance Spectrometer	Solartron Analytical, Farnborough, UK	ModuLab XM MTS
Optical microscope	Olympus Corporation, Tokyo, Japan	BX51, polarizers, bright field and dark field available
Glovebox for electrical measurements	Inter Corporation, Amesbury, MA, US	IL-3GB
Profilometer	Bruker Corporation, Billerica, MA, US	DektakXT Stylus Profiler
Raman spectrometer	Renishaw plc, Wotton-under-Edge, UK	inVia Reflex confocal Raman microscope
Scanning-electron microscope (SEM)	Jeol Ltd., Akishima, Japan	JSM-7610F
Semiconductor Parameter Analyzer	Keysight Technologies Inc., Santa Rosa, CA, US	Agilent 4156 C
Semiconductor Parameter Analyzer	Keysight Technologies Inc., Santa Rosa, CA, US	B1500A
Source-Meter Unit	Keysight Technologies Inc., Santa Rosa, CA, US	Agilent B2902A
Source-Meter Unit	Tektronix Inc., Beaverton, OR, US	Keithley 2400
UV-vis-NIR spectrometer	Agilent Technologies Inc., Santa Clara, CA, US	Cary 6000i (Varian Inc.)

CHAPTER 5

AEROSOL-JET PRINTING OF CARBON NANOTUBES

This chapter investigates the stability of (6,5) CNT inks during aerosol-jet printing as well as the reproducibility of field-effect transistors fabricated with aerosol-jet printed (6,5) CNTs.

The results presented in this chapter were published in part in *Advanced Electronic Materials* (WILEY-VCH Verlag GmbH & Co. KGaA, Weinheim, Germany) at DOI 10.1002/aelm.201700080.[150] All figures and data previously published were reprinted with permission. Parts of the measurements resulting in the data presented in chapters 5.2 and 5.3 were performed by Shuyi Yang, the Bachelor student I supervised during this project.

5.1. Introduction

Solution-processing is essential for the success of applications in organic photovoltaics, lighting, and field-effect transistors. The implementation of printing processes at ambient conditions in contrast to vacuum deposition or large area coating can reduce the overall cost of materials and fabrication process. Ongoing research thus further investigates and improves material and deposition methods.[307, 343] This is especially important for devices with structured layers such as transistors or displays. For large area applications like lighting and photovoltaics non-patterning techniques, *e.g.* slot-die or blade-coating, can be used for fast, reproducible and effective material deposition.[364-367] While the application of semiconductors in FETs via spin-coating, blade-coating, or immersion techniques were shown successfully and reproducibly,[1, 146, 173] often post-deposition patterning is necessary for material structuring. Unpatterned semiconductors can cause device cross-talk and increased leakage currents and masking and etching is thus necessary. These additional processing steps increase the fabrication costs and can introduce defects, *e.g.* photoresist residues and damages by plasma etching. Furthermore, the semiconducting materials are still rather expensive and the majority of material deposited is wasted when relying on those top-down approaches. Depending on the final application, only 1 to 10 % of the substrate area is ultimately covered with active materials, as evident in display and sensor backplanes or small integrated circuits such as a 4-bit adder.[368-370] A more effective deposition of active layers and electrodes ideally involves a direct-write approach to avoid those disadvantages.

Different printing techniques were adapted for organic electronics, *e.g.* screen,[371-373] gravure,[223, 303, 304] or offset printing.[217, 224, 374] However, not all materials can be patterned and deposited utilizing these methods. Other techniques for high-resolution printing especially of active layers might thus be necessary. One of the approaches to solve this problem is the well-studied and widely used inkjet printing, but the limited variation of ink parameters such as viscosity may hinder potential applications.[234, 319, 348]

A more recently emerging method and possible challenger is aerosol-jet (AJ) printing commercialized by Optomec Inc. in 2004,[5] facilitating a higher ink variability and printing on uneven, three-dimensionally structured, and even curved substrates.[5, 375] In contrast to the more established printing methods, the amount of studies about suitable ink formulations, printing parameters, and reproducibility of fabricated devices is still limited.[221, 225, 266, 313, 316, 318, 348, 376, 377] On top of the direct-write approach, AJ printing has the capability to work with low material volumes when using an ultrasonic atomizer. It is thus especially interesting for materials that are either expensive or not (yet) available in large amounts and, besides the possibility to be integrated in roll-to-roll fabrication processes, an interesting tool to process and evaluate materials on the lab scale.

Carbon nanotubes were previously printed via AJ printing from aqueous and organic dispersion,[148, 153] however, in all cases a mixture of different CNT chiralities with a limited semiconducting purity was used and thus a channel length of several tens of micrometers to achieve reasonable off-currents was required. For this project, (6,5) nanotubes with a high purity were dispersed utilizing selective polymer-wrapping in toluene by shear-force mixing, which also enables rather large output quantities.[110] First the optimized ink composition and printing parameters had to be determined. As the ink is aerosolized via ultrasonication, which can shorten nanotubes and introduce structural defects,[110, 378] the stability of the ink was examined next before evaluating the reproducibility of devices printed consecutively while also considering batch-to-batch variations. The unwanted hysteresis exhibited by the devices was reduced by increasing the film thickness and other approaches. Finally, a brief overview of further applications and experiments based on the presented optimized AJ printing of carbon nanotubes will be given and the limits of CNT deposition with this method will be discussed.

5.2. Ink Formulation

Within this work, the commercial aerosol-jet printing system AJ 200 by Optomec Inc. was utilized with some changes to the standard configuration as described in chapter 3.1. The system is equipped with an ultrasonic atomizer that creates the aerosol in the ink vial. The most important property of the ink therefore is the ability to form a dense aerosol that can then be transported by nitrogen as a carrier gas into the printer head. The appropriate viscosity of the ink is in the range of 1 to 5 mPa s for the available setup. A larger range (1 to 1000 mPa s) could be covered if the pneumatic atomizer, that is commercially available as an alternative aerosolization source, was used.[379] This atomizer however would need larger ink volumes and would thus be less suitable for materials only available on the lab scale. Before starting this work, aerosol-jet printing of carbon nanotubes was reported based on aqueous dispersions only,[148, 149] whereas here dispersions of polymer-wrapped (6,5) carbon nanotubes in toluene were employed. This system was chosen because the polymer-wrapping method can produce almost purely semiconducting CNT dispersions with very low metallic residues with a suitable wrapping-polymer in a one pot method.[52, 94] Furthermore, the output of purified material can be upscaled by using a shear-force mixing process instead of ultrasonication and thus should also allow the eventual use in processes at a larger scale.[110] The detailed procedure to gain almost purely (6,5) CNTs with poly[(9,9-dioctylfluorenyl-2,7-diyl)-*alt-co*-(6,6′-(2,2′-bipyridine))] (PFO-BPy) in toluene is described in the experimental section (chapter 3).

The chirality-selected dispersion can be easily characterized by absorbance spectroscopy in the ultraviolet, visible and near-infrared range. The absorbance spectra (see Figure 5.1) show the characteristic E_{11} (at $\lambda = 995$ nm) and E_{22} (at $\lambda = 573$ nm) peaks of the (6,5) CNTs as well as the polymer absorption below 400 nm. The less intense but broader peaks at 542 and 855 nm correspond to the respective phonon sidebands of the CNT transitions. While the polymer signal is rather high in the initial dispersion, *i.e.* after removing undispersed material via centrifugation at 60 000 g, the amount of residual polymer can be significantly reduced by either pelletization at 284 600 g or vacuum filtration onto a PTFE filter (pore size 0.1 µm). In either case, the pellet or filter cake is subsequently washed and finally redispersed in pure toluene. The E_{11} peak appeared slightly broader in the redispersed material than in the fresh dispersion before the removal of excess polymer. This could be a hint towards slight bundling due to the increased CNT concentration and/or the reduced polymer content in the redispersed material.[380, 381] However, as PFO-BPy is an insulator, excess polymer in the final devices would hinder efficient charge transport and is therefore unwanted.

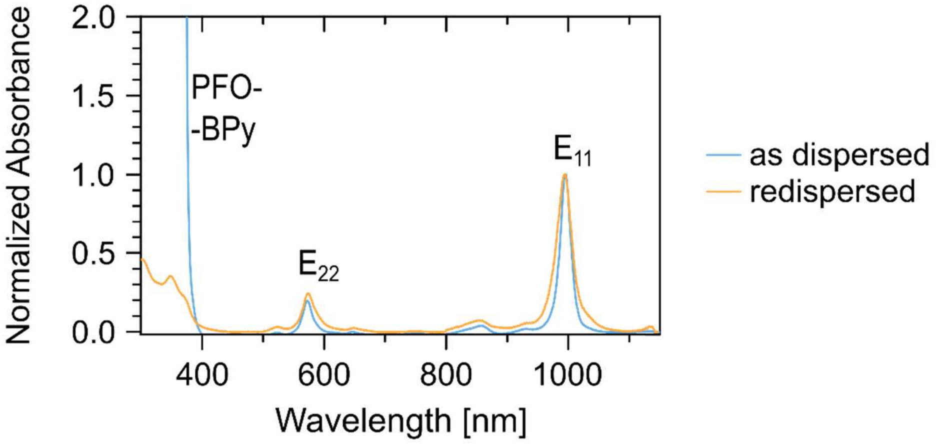

Figure 5.1: Absorbance spectra of polymer-wrapped (6,5) CNTs in toluene as dispersed (blue) and after washing and redispersion (yellow). Both spectra are normalized to the E11 peak at 995 nm and were background corrected to achieve a linear baseline. The polymer absorbance (< 400 nm) for the as dispersed material is about 6 times larger than the E11 transition of the CNTs.

As demonstrated before, aqueous dispersions can be AJ printed as produced,[148, 149] although it might be necessary to reduce the surfactant concentration via dialysis to prevent excessive foaming during sonication.[148] In contrast to that, pure toluene dispersions do not form a dense aerosol due to the low viscosity of the solvent which is around 0.5 mPa·s and thus out of the specified range.[382] The viscosity of the ink can be increased by adding a highly viscous co-solvent. Terpineol was used for this purpose with a concentration of 10 % v/v in an aerosol-jet printing process of poly(3-hexylthiophen) in chloroform before.[239] Chloroform has a similar viscosity as toluene,[383] and thus these parameters were used as a starting point. The high boiling point of terpineol (above 200 °C) prevents its evaporation even on the heated substrate stage of the printer which is limited to a maximum temperature of 100 °C. The amount of liquid on the substrate should however be minimized to avoid excessive flow when printing larger areas with overlapping lines or eventually even multiple layers. Different concentrations from 1 to 10 % v/v terpineol in toluene were tested for a dense aerosol formation and continuous printing output. It should be noted here, that continuous printing does not automatically yield a connected line. At low carrier gas flow rates, the amount of aerosol droplets transported to the substrate surface is not sufficient to cover the surface with a continuous ink film (see **Figure 5.2**). The optical images shown here were taken during initial printing tests at a comparable AJP system installed at the University of Minnesota. The terpineol concentration was set to 10 % v/v while the CNT concentration could not be reliably determined at the time. The total flow, *i.e.* sheath plus carrier gas, was held constant at 90 sccm.

For actual device manufacturing later, the sheath gas flow was reduced to 30 sccm independent of the carrier gas flow. The resulting increase in the linewidth from around 25 µm to around 60 µm is favorable for printing larger areas as it reduces the number of lines necessary to cover a certain area. During printing, the stage was heated to 100 °C and thus the toluene evaporated rather quickly. The alignment camera images shown in **Figure 5.2** are a result of the terpineol remaining on the substrate. As evident from the images, already slight variations significantly alter the appearance of the printing output. While there were still only slightly connected droplets at a carrier flow of 13 sccm, a continuous line with an approximate linewidth of 25 µm was found at 14 sccm (and a corresponding sheath gas flow of 76 sccm). This line became thicker and wider for further increased carrier flow which resulted in more liquid remaining on the substrate. The carrier flow was thus set to the minimum value resulting in continuous film.

Depending on the exact setup, *e.g.* the position of the pickup tube within the vial, the ink vial shape and size, and the material, the carrier flow necessary to print a continuous film had to be determined at the beginning of each printing session, before starting deposition on the actual samples. While this seems difficult at first, it was observed that the adjustment of only the carrier gas flow towards a continuous output was sufficient. This process was best done on the reference silicon chip that was also used for the alignment of nozzle and camera, because of the good contrast of printed material and substrate visible in both – the alignment and the process – cameras. Additionally, the range of necessary variation was relatively small and a good output for toluene/terpineol based CNT inks was usually attained at (14 ± 1) sccm. For some configurations however, the flow had to be increased to up to 20 sccm to achieve the desired dense deposition on the substrate.

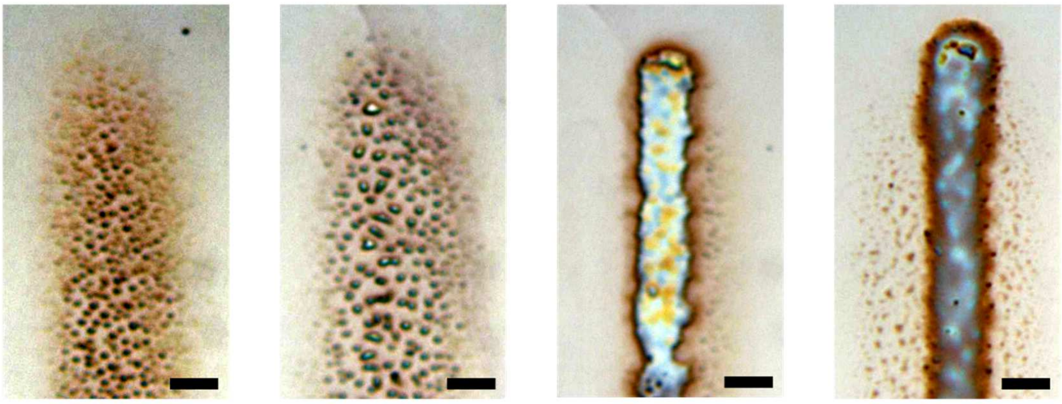

***Figure 5.2**: Optical images of printing output at different carrier gas flows (left to right: 12 – 13 – 14 – 15 sccm) showing the shift from individual droplets to a complete film filling the printed line. All micrographs were adjusted for contrast and brightness for better visibility. Scale bars are 20 µm.*

While continuous lines could be easily observed and might even be quantified with respect to thickness and width, the formation of a dense aerosol could only be evaluated by the naked eye and was thus not completely objective. However, a measurement of the aerosol density, *i.e.* by absorbance measurements, was impossible due to reflections at the ink vial and the surrounding water cooling system whose continuous flow introduced air bubbles and turbulences into the water stream. It was found, that concentrations from 5 to 10 % v/v terpineol resulted in a seemingly dense aerosol. A concentration of 5 % v/v was chosen as a good tradeoff between maximized aerosol density and minimized liquid remaining on the sample surface for all future ink formulations.

Special attention towards the ink vial should be paid during the evaluation of different solvents and solvent mixtures or final inks. The bottom of the used ink vials was blown out into a hemisphere to reduce the glass thickness and remove sharp edges. Differences in the handling by the glassblower performing this task might lead to slightly different shapes or glass thicknesses that are not visible to the naked eye. The suitability of all ink vials was thus first validated with pure deionized water. Almost identical looking vials sometimes gave a very strong aerosol and other times no aerosol at all. Comparing different solvents or material concentrations should thus always be performed using a single ink vial. Additionally, the reproducibility of one printing process with set parameters also relied on an unchanged setup, *i.e.* also the use of the same ink vial. If the utilized vial gave a strong aerosol, only slight carrier flow changes had to be performed, if at all.

The second variable parameter is the concentration of the active material, *i.e.* for this study the carbon nanotubes. Although the volumes of the dispersions significantly improved by shifting from bath sonication in small vials (~ 10 mL of dispersion in one batch) towards shear-force mixing (up to 500 mL), the material availability was still limited. On the other hand, high concentrations increase the probability of re-aggregation especially due to the low polymer-content remaining after washing the CNT pellet or filter cake as discussed before (see Figure 5.1). While excess polymer was used to initially disperse the nanotubes, the insulating polymer should be removed as much as possible while avoiding aggregates and bundles as they have a negative influence on the charge transport properties of the CNT network.[45] Ideally only polymer wrapped around the nanotubes should remain after the redispersion of the washed pellet in fresh toluene. Therefore, a relatively low CNT concentration is preferred during the material deposition process. However, if the active material content in the ink is too low, the stage speed has to be decreased or several layers have to be printed to form percolating networks of carbon nanotubes. Both options resulted in an increased deposition of terpineol on the substrate (as the toluene is evaporating almost immediately on the stage heated to 100 °C) which led to a higher flow of material, thus a larger spread around the desired printing area and a loss in resolution. Additionally, the processing times were longer especially for the thicker CNT films described later. While this is not a serious issue on the lab-scale, it would be problematic in roll-to-roll fabrication processes. One possible solution to tackle the problem of extended printing times without altering the ink composition would be to multiplex the printing process, *i.e.* use several printing heads in series.

For the fabrication of transistors, a homogeneous network density is desired, *i.e.* the network should not exhibit any holes or areas with increased bundling. At very low CNT concentrations, both effects could be observed simultaneously – holes due to the low amount of material deposited as well as bundling most probably due to drying effects. The morphology of the nanotube network was determined by AFM imaging. Representative AFM images showing the range of unwanted printing results, *i.e.* coverage below the percolation threshold, bundling, and sparse networks, together with a CNT film printed with improved printing parameters are presented in **Figure 5.3**.

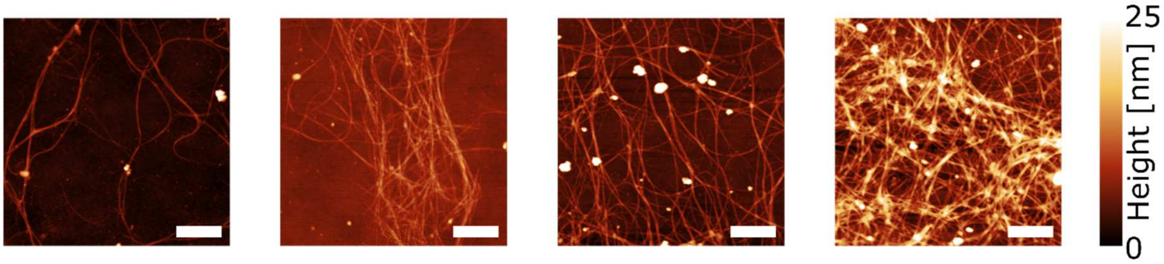

***Figure 5.3**: AFM images of printed (6,5) CNTs showing very low density, bundling, a sparse network and a reasonably homogeneous CNT film (left to right). Scale bars are 500 nm.*

While sparse networks are not completely unwanted and might be even helpful for some studies, they tend to be less reproducible and often exhibit completely uncovered areas (see section 5.7). Continuous and dense networks from a single printing layer could be obtained for an initial CNT concentration of at least 1.8 mg L^{-1} in 1 mL initial ink volume placed in the printer vial. This value corresponds to an optical density of 1.0 at the E_{11} peak (λ = 995 nm) for a 1 cm long cuvette and was used for all further experiments if not noted otherwise. Adjustment of concentrations from the dispersion to the final ink were always based on absorbance measurements to enable a quick and reliable determination of the CNT concentration.

5.3. Stability of Carbon Nanotube Inks

The desired properties of carbon nanotubes, in particular large length and low defect-density, are generally reduced by strong sonication as the energy input introduces more defects and breaks the nanotubes thus reducing the average length.[110, 378, 384] The aerosol-jet process however relies, at least when not utilizing the more gentle pneumatic atomizer, on sonicating of the ink to push small droplets from the liquid into the aerosol phase. This raises questions about the suitability of this process for carbon nanotubes and was hence investigated.

All material used in the following were prepared by applying ultrasonication to debundle the nanotubes and enable efficient polymer-wrapping during the dispersion process. The mean length of the nanotubes in the starting material was thus slightly longer than 1 µm after redispersion in fresh toluene.[110, 385] Both possible effects, shortening and increase of defect density, were simultaneously studied by printing two different patterns from the same ink after different times of sonication at maximum power. A dense network was used for Raman analysis to provide sufficient signal for reliable peak fits and sparse individualized nanotubes were necessary for length determination. Printing individualized CNTs was realized by a pattern of dots instead of continuous lines, *i.e.* only depositing very small amounts of material during the short opening period of the shutter. The CNT lengths were determined from atomic force microscopy images using a JAVA program written by Andreas Malhofer. Several points along the nanotube were manually selected and the length of the connecting spline was calculated and saved by the program. A typical AFM image with only few CNTs is shown in **Figure 5.4**. The blue lines mark the manually traced nanotubes chosen for length determination because they were undoubtedly individual nanotubes and not overlapping or bundled. For each sonication time, more than 50 CNTs were measured and incorporated into the statistical evaluation. The patterns were printed right after setting up the printer and after 15, 30, and 46 hours of continuous sonication at the maximum possible atomizer power. The nanotube length obtained from the first sample was in the expected range of around 1 µm.[110]

For the first 30 h of constant sonication by the atomizer of the AJ printer no significant decrease in the nanotube length was observed. Other sonication methods frequently used during nanotube dispersion such as tip sonicating show a significantly larger impact on the nanotube length, shortening the same material to around 0.6 µm within several hours.[110] Experimental studies showed a strong influence of the nanotube length on photoluminescence yield an device performance, especially for rather short (<1 µm) nanotubes.[386] Simulations support these observations also for longer nanotubes however with a less pronounced impact.[74] In composites of nanotubes and insulating polymers with a CNT concentration close to the percolation limit, small changes of around 15 % of the average length can already have a strong influence on the device performance, *i.e.* effective mobility or on-current, even for CNTs longer than 1 µm.[385] The shortening of printed nanotubes observed here, after almost 2 days of constant sonication was rather small (less than 10 %) and most tubes still exhibited a length of around 1 µm or above. The influence on the device performance of nanotube network transistors should thus be rather small, especially as the tested sonication times exceeded the usual processing times by at least one order of magnitude.

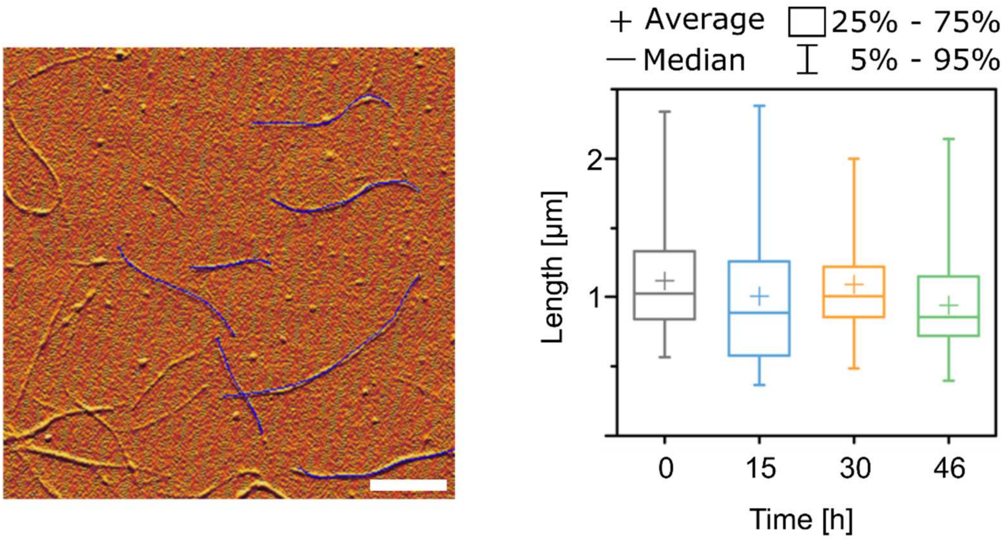

***Figure 5.4**: Left: Typical AFM image for length determination of printed nanotubes showing manually inserted measurement splines (blue). The scale bar is 500 nm. The statistical evaluation of CNT length versus sonication time (right) shows almost no decrease in length.*

The second question regarding negative influences of sonication concerns the defect density along the CNTs. After the same sonication times as for the AFM length analysis, squares of dense networks were printed as well. Theses squares were mapped via Raman spectroscopy to evaluate the amount of defects in the CNTs after printing. The representative Raman spectrum in **Figure 5.5** shows the barely visible radial breathing mode (RBM), the peak of the silicon substrate, small D and G^- bands, as well as large signals for the G^+ and 2D bands. According to literature, the ratio of the G^+ band and the 2D band increases with defect density and is thus a good figure-of-merit.[387] For quantification of the G^+ to 2D ratio, the Raman spectra of the printed dense films were mapped under resonant excitation with a 532 nm laser and both relevant peaks were fitted using the Renishaw Raman software Wire 3.4. The statistical analysis shows almost no change within the first 15 hours of continuous sonication. Only after this already long sonication period, a significant increase of the G^+/2D-ratio and thus a decrease in nanotube quality was observed. It should be noted that the long sonication times of the same ink were realized by overnight sonication without any output, *i.e.* carrier and sheath gas flow rates were set to zero. The gas flows were increased only during deposition for sample preparation. In contrast to that, the usual processing times of 1 mL ink volume were less than 5 hours when printing multiple samples with interruptions – thus no output – for the alignment of the samples and maybe additional processing steps. If an uninterrupted aerosol output is used for continuous device fabrication, the ink is consumed completely even faster. It can thus be concluded from the length and defect analysis that within the timeframe of typical printing processes no negative influence of the continuous sonication necessary to create the aerosol occurs.

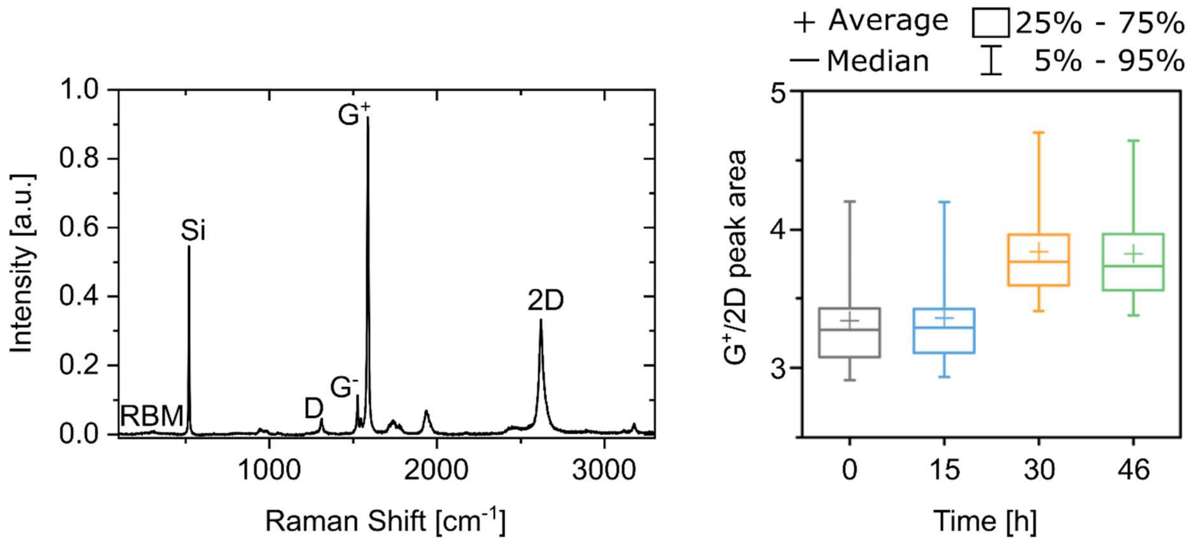

***Figure 5.5**: Raman spectrum of (6,5) CNTs and statistical evaluation of the G^+/2D-ratio versus sonication time.*

Another important factor is the composition of the aerosol for reproducible output results over extended periods. The first hint is the concentration of nanotubes of the ink remaining in the vial. While literature often reports an increase in the concentration of solid components in the remaining liquid, the opposite trend was observed for aerosol-jet printing of carbon nanotubes. The increasing concentration reported in literature is mostly attributed to the evaporation of solvent.[388-390] However, these studies on aerosol processes focused on medical applications where different aerosolizers were used and to the best of my knowledge, there has been no study on aerosol-jet printing processes dealing with the ink composition over time. Here, the absorbance of the ink in the vial was measured after consecutive 150 mm of printed path length and showed a decrease of around 80 % over a total of 600 mm long path (see **Figure 5.6**). During this process around 300 µL of ink were consumed from an initial starting volume of 1 mL at an initial concentration of 1.8 mg L^{-1}. While maintaining all other process parameters constant, reducing the concentration to 0.3 mg L^{-1} resulted in an increase of the ink volume consumed for the same printing path by a factor of 1.5 to 2.

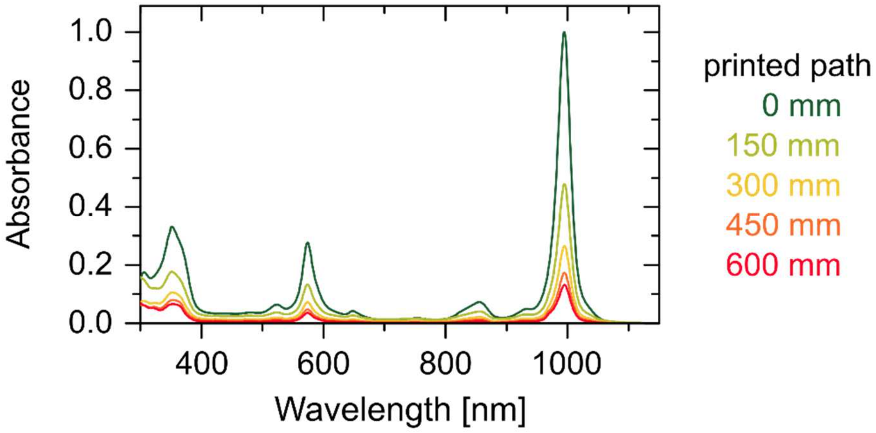

***Figure 5.6**: Absorbance spectra of CNT ink remaining in the ink* vial *measured after printing different CNT path lengths.*

The aerosolization process strongly depends on the density, surface tension, and viscosity of the ink as well as the input of ultrasonic power.[391] This means, that the (local) ink composition and the filling level of the vial can have a strong influence on the aerosol droplet formation. As the viscosity of CNT dispersions increases with CNT concentration and length,[392-394] CNT-rich droplets might be aerosolized preferentially and thereby reduce the CNT concentration in the remaining ink. A simpler reason for the reduction of CNT concentration was the observed deposition of CNTs on the upper parts of the ink vial where the aerosol was still present in the vial but well above the liquid filling level. While the solvent ran down the side of the vial, CNTs remained on the vial wall. This deposition was almost impossible to observe after just a few printing runs even over extended times as the CNTs are not visible for the naked eye unless they form relatively thick films of more than 30 nm. Ink vials re-used for the same CNT material and thus not thoroughly cleaned after each ink were showing the typical blue-purple color of (6,5) nanotubes after a large amount of sample sets produced for different projects as shown in **Figure 5.7**.

***Figure 5.7**: Photograph of ink* vial*s fresh (left) and after printing (6,5) nanotubes for several projects (right) illustrating the material deposition in the upper part of the* vial*. The photographs were adjusted for brightness and contrast to increase visibility.*

Even more important than the composition of the ink remaining in the vial was the actual output printed on the substrate. One indicator for constant or varying output were the device characteristics of the final FET that will be discussed in section 5.4. Additionally, the output could be quantified by Raman mapping at least to some degree using the G^+ band intensity. Squares of 500x500 μm^2 were printed for that purpose from inks with different CNT concentrations of 0.2 to 1.8 mg L^{-1} and two different initial ink volumes (1.0 and 0.4 mL). As shown in **Figure 5.8**, the output indeed varied significantly and decreased with both, CNT concentration and initial ink volume. At half of the usually used concentration, *i.e.* 0.9 mg L^{-1}, the output decreased to 46 % and 40 % of the initial value for $V = 1.0$ mL and $V = 0.4$ mL, respectively. As expected, the output was further reduced for lower CNT concentrations, however, at very low concentrations of 0.2 and 0.4 mg L^{-1}, the obtained values were very similar. It was not thus possible to extract a linear relation between output and ink composition within the measured range.

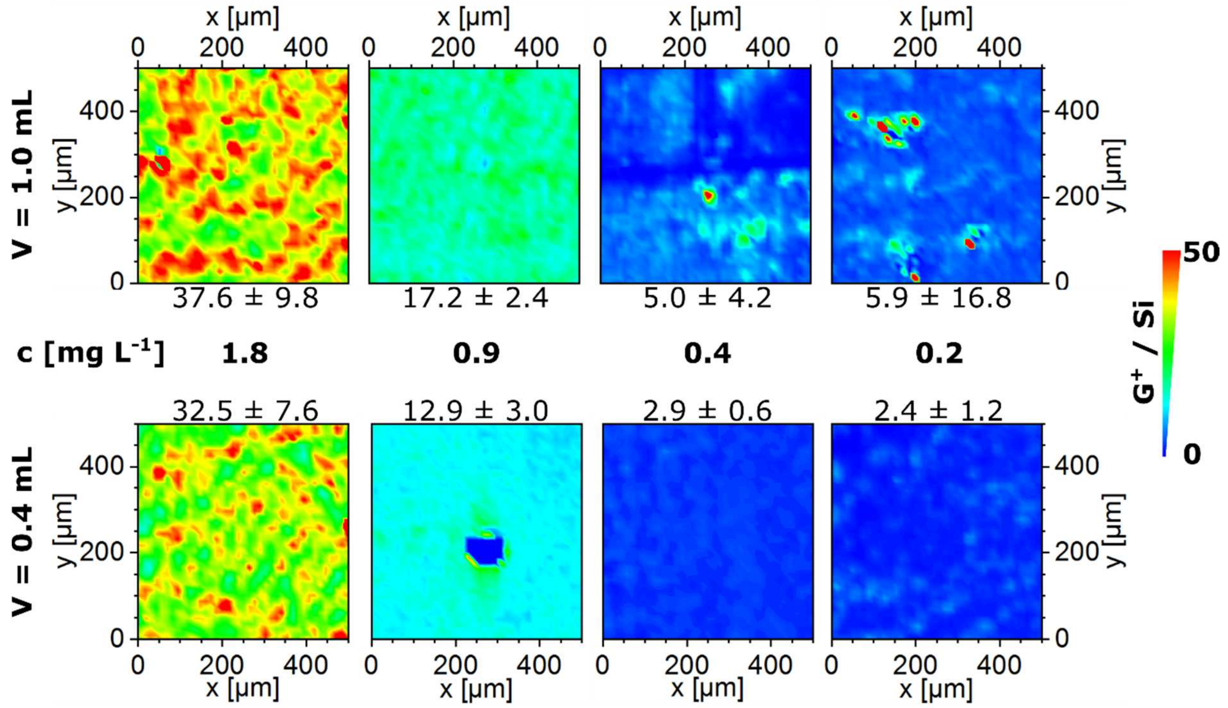

***Figure 5.8**: G^+-band intensity normalized to the silicon peak intensity at 520 cm^{-1} of squares printed on silicon substrates from inks with different initial ink volumes (top: 1.0 mL, bottom: 0.4 mL) and CNT concentration (left to right: 1.8, 0.9, 0.4, and 0.2 mg L^{-1}) acquired by Raman mapping. The average values including the standard deviation are given next to the individual images.*

The hot spots with high signals might be explained by drying effects while at higher concentrations slight bundling might play an additional role. The 5x5 μm^2 AFM images, recorded in the middle of the printed area, however do not show increased bundling but a CNT film with variations in the local density for inks with higher concentrations (see **Figure 5.9**). The images at lower concentrations show large areas completely uncovered and only small spots with nanotubes. It should be noted that squares with a line pitch of 25 µm were printed on silicon chips to enable a better Raman evaluation by facilitating the normalization to the silicon peak at 520 cm^{-1}. Since the transistors were eventually fabricated on glass substrates with pre-patterned gold electrodes, the situation may be different within the actual FET channels due to the substrate profile with steep steps at the electrode edges and different surface properties.

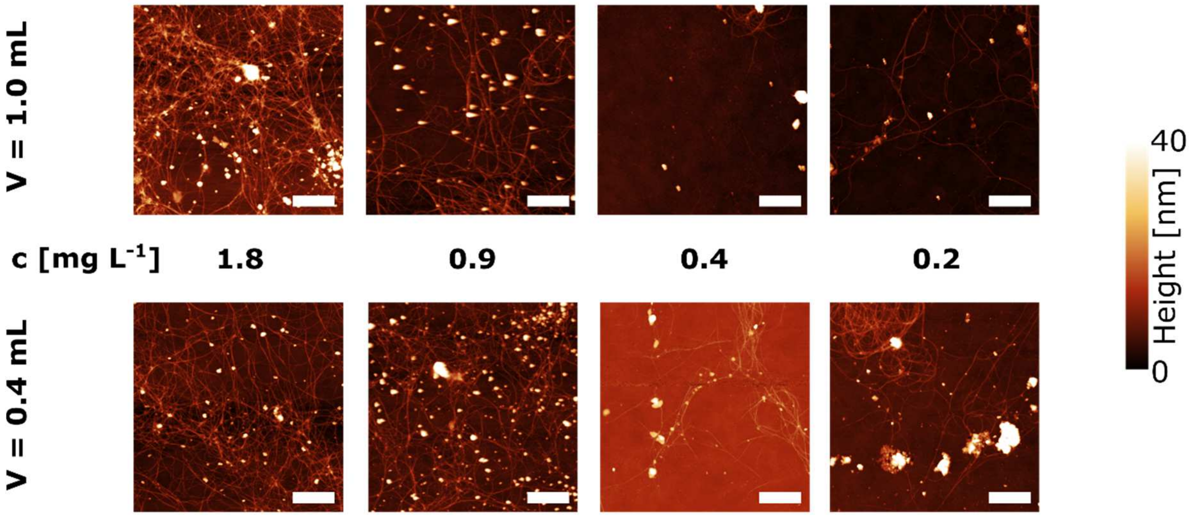

***Figure 5.9**: AFM images taken in the middle of the printed squares printed on silicon from inks with different initial ink volumes (top: 1.0 mL, bottom: 0.4 mL) and CNT concentrations (left to right: 1.8, 0.9, 0.4, and 0.2 mg L^{-1}). Scale bars are 1 µm.*

The Raman intensity was thus mapped directly on the 1st and last, *i.e.* 128th, transistor printed from the same ink (see **Figure 5.10**). Here, a decrease by only around 33 % was observed in the Raman intensity while the CNT concentration in the ink vial decreased by about 80 % while printing these transistors. As visible in the AFM images, a percolating network was still observed at a CNT concentration decreased by 50 % and the reduced output may not have a high impact on the FETs. The influence of the variable output on device parameters such as on-current and on/off-ratio will be discussed in the next chapter.

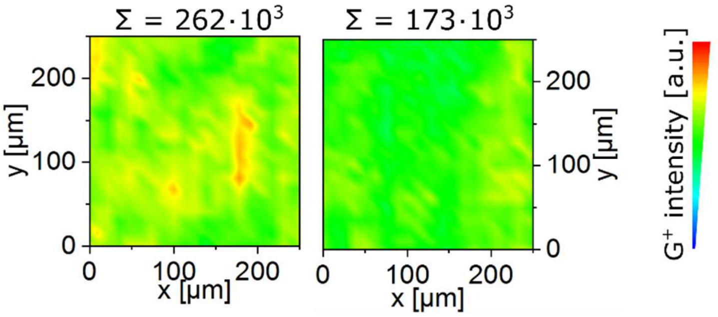

***Figure 5.10**: Decrease of Raman intensity, i.e. amount of CNTs deposited, from the 1st FET (left) and last, i.e. 128th FET, all printed consecutively from one ink. The total Raman intensity count of the displayed area is given above the Raman maps.*

5.4. Reproducibility of Transistor Characteristics

The possibility to move from lab scale device fabrication of a few FETs towards application of these devices in circuits that require more than one working transistor crucially depends on the reproducibility of the device characteristics. This reproducibility not only refers to the similarity of devices produced from one ink but also batch-to-batch variations given that the same process parameters are used. Although the ultimate goal of printed electronics is all-printed devices, the focus here is on the semiconducting layer, *i.e.* the CNTs, and therefore a well-established device architecture was utilized (see **Figure 5.11**). Interdigitated source and drain electrodes were patterned by standard photolithography on glass substrates. A positive double-layer resist was exposed to the *i*-line of a mercury lamp through a chrome-on-glass mask followed by development in a static bath. After electron-beam evaporation of chromium (2 nm) as adhesion layer and gold (30 nm), the subsequent lift-off in NMP finalized the electrode structure. Each substrate compromised the source and drain electrodes of 4 transistors of each channel length L, *i.e.* 5, 10, 20, and 40 µm, with a channel width of 10 mm for all L but 40 µm, where the channel width was 5 mm. Aerosol-jet printing was performed from a CNT ink with a concentration of 1.8 mg L^{-1} by printing a single line in the middle of each 5 and 40 µm channel. The 10 and 20 µm channels were only partially printed for the sake of material conservation. For evaluating the reproducibility of the FETs thus the two extremes, rather short (5 µm) and rather long (40 µm) channels, were used. Printing in the middle of each channel resulted in different network densities for the different channel lengths as the pitch, resulting from electrode width plus channel length, was 25 µm for $L = 5$ µm and 60 µm for $L = 40$ µm. A direct comparison between the different channel lengths was thus not possible for these devices. The linewidth for the employed stage speed (0.5 mm s^{-1}), sheath (30 sccm) and carrier (14 ± 1 sccm) flows, was around 60 µm and resulted in a continuous film across the whole device area for both pitches. The stage temperature of 100 °C promoted fast toluene evaporation and thereby reduced flow on the substrate. The remaining terpineol and potentially present excess polymer were removed by a rinsing step with THF and de-ionized water followed by drying with a nitrogen gun.

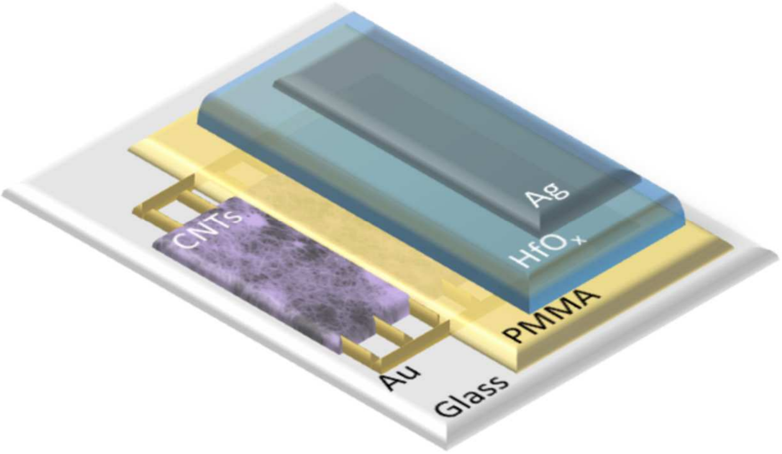

***Figure 5.11**: Schematic device structure: Interdigitated source and drain gold electrodes on glass, printed CNTs, a hybrid dielectric of PMMA and HfO_x, and a silver top gate.*

After printing, the devices were annealed in a dry nitrogen atmosphere at 300 °C for at least 30 min to remove residual solvent and moisture. The chosen device architecture enabled operation at low voltages (< 5 V) due to the hybrid dielectric and its high capacitance.[163] The oxide layer simultaneously served as an encapsulation layer and the devices showed almost balanced hole and electron transport and were air-stable. Averaging over at least 40 transistors of each channel length give the transfer characteristics displayed in **Figure 5.12**. The standard deviation is shown as a shaded area and inks prepared from three different dispersions were included in the statistics which hence also contain batch-to-batch variations. At low source–drain bias (V_{ds} =–0.1 V) the averaged and width-normalized on-currents for holes were 1.8 times higher in devices with $L = 5$ µm ($I_{on}/W = 290$ nA mm^{-1}) than in those with $L = 40$ µm ($I_{on}/W = 170$ nA mm^{-1}). This ratio of on-currents is further increased to 2.3 for $V_{ds} = -5$ V. For the generally lower electron on-currents the differences were even larger and a ratio of 3.2 was calculated for V_{ds} =–0.1 V from $I_{on}/W = 26$ nA mm^{-1} and $I_{on}/W = 8$ nA mm^{-1} for channel lengths of 5 and 40 µm, respectively. The channel-length and width normalized on-conductances $I_{on}/(V \cdot W \cdot L)$ are thus always higher for longer channels which hints towards non-negligible contact resistance at the electrode–nanotube interface.

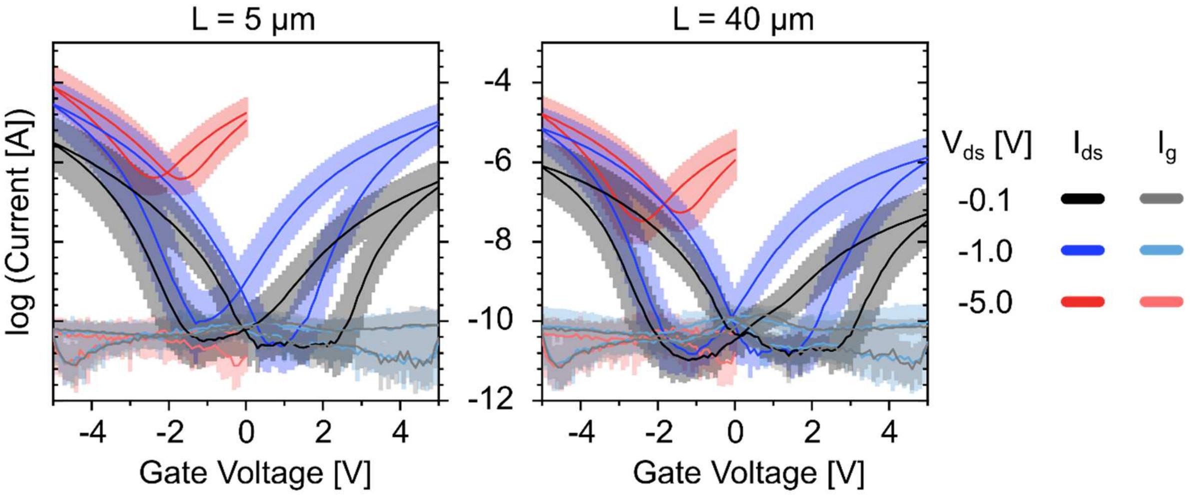

__Figure 5.12__: Averaged transfer characteristics for FETs with printed (6,5) CNTs with channel lengths of 5 µm (left, 44 FETs) and 40 µm (right, 48 FETs) including the standard deviation (shaded areas) for three different source–drain voltages: −0.1 V (black), −1.0 V (blue), and −5 V (red). Note that the standard deviation was determined from the logarithmized current values.

A closer evaluation of the individual device metrics, *i.e.* on-current I_{on}, on-voltage V_{on}, on/off-ratio, and mobility μ, for the individual FETs is useful to compare the device-to-device variations better to literature values published for different deposition methods. Additionally, as discussed above, the CNT concentration within the ink varied over the printing time and the influence of this variation should be investigated. **Figure 5.13** illustrates the width-normalized on- and off-conductances for consecutively printed devices from three different inks. For short channels ($L = 5$ µm), no significant change was observed for more than 80 consecutively printed FETs. Only for longer channels ($L = 40$ µm) a decrease in the electron conductance was visible after more than 60 printed transistors. As the network was less dense from the start for these devices, the reduced CNT concentration of the ink and thus reduced CNT output produced a higher impact here. Although some influence was seen here, this issue could be easily resolved for large scale printing by continuously adding fresh dispersion into the ink vial and thereby maintaining a constant ink concentration. The characteristic device parameters, however, also varied from device to device independent of the printing time.

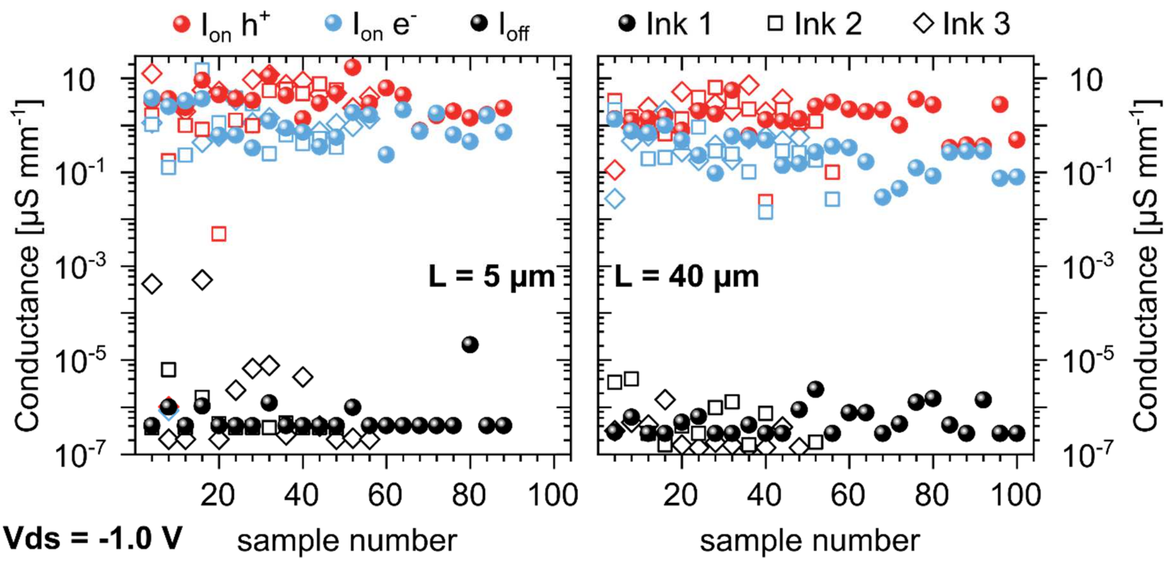

***Figure 5.13**: On- (at $V_g = -5$ V) and off-conductances for $V_{ds} = -1$ V versus total number of transistors with printed (6,5) CNTs. Three separately prepared inks are shown for two channel lengths (left: 5 µm and right: 40 µm). The total printed path length of 100 samples is more than 900 mm.*

The turn-on voltages for a source–drain bias of −0.1 V were between −1.5 V to +1.5 V for more than 90 % of the measured transistors. The distribution of device parameters is shown in the bar graphs in **Figure 5.14**. On average, FETs with a channel length of 40 µm turned on at a gate voltage of (1.0 ± 0.8) V and (−0.5 ± 0.7) V for electrons and holes, respectively. Even smaller average values for V_{on} – although with a similar spread – could be extracted for the devices with a denser network of CNTs at a channel length of 5 µm with (0.7 ± 1.1) V and (−0.4 ± 1.0) V for electrons and holes, respectively. These and the following average values include all outliers. The turn-on voltage was determined from the transfer characteristics at the point where – coming from the off-state – the source–drain current consistently became larger than the gate leakage.

As already seen in the averaged transfer characteristics and as expected for a random carbon nanotube network, the width-normalized on-conductances extracted at $V_{ds} = -1$ V were higher for the shorter channel length with higher CNT density: (4.4 ± 3.6) *vs* (2.0 ± 1.6) µS mm^{-1} for holes and (1.5 ± 2.2) *vs* (0.4 ± 0.4) µS mm^{-1} for electrons. The different channel widths ($W = 5$ mm for $L = 40$ µm and $W = 10$ mm for $L = 5$ µm) lead to even larger differences in the on-currents. In short channels the on-currents reached (44 ± 36) µA for holes and (15 ± 22) µA for electrons while in long channels I_{on} was about 4 to 8 times lower: (10 ± 8) µA for holes and (2 ± 2) µA for electrons.

Table 5.1: Overview of device parameters extracted from FETs with AJ printed (6,5) CNTs.

	$L = 5$ µm		$L = 40$ µm	
Parameter	h^+	e^-	h^+	e^-
Turn-on voltage [V]	–0.4 ± 1.0	0.7 ± 1.1	–0.5 ± 0.7	1.0 ± 0.8
On-conductance [µS mm^{-1}]	4.4 ± 3.6	1.5 ± 2.2	2.0 ± 1.6	0.4 ± 0.4
On-current [µA]	44 ± 36	15 ± 22	10 ± 8	2 ± 2
Log (on/off-ratio)	6.4 ± 1.2	6.0 ± 1.2	6.6 ± 0.6	5.8 ± 0.6
Mobility [cm^2 V^{-1} s^{-1}]	0.34 ± 0.11	0.03 ± 0.03	1.90 ± 1.17	0.11 ± 0.11

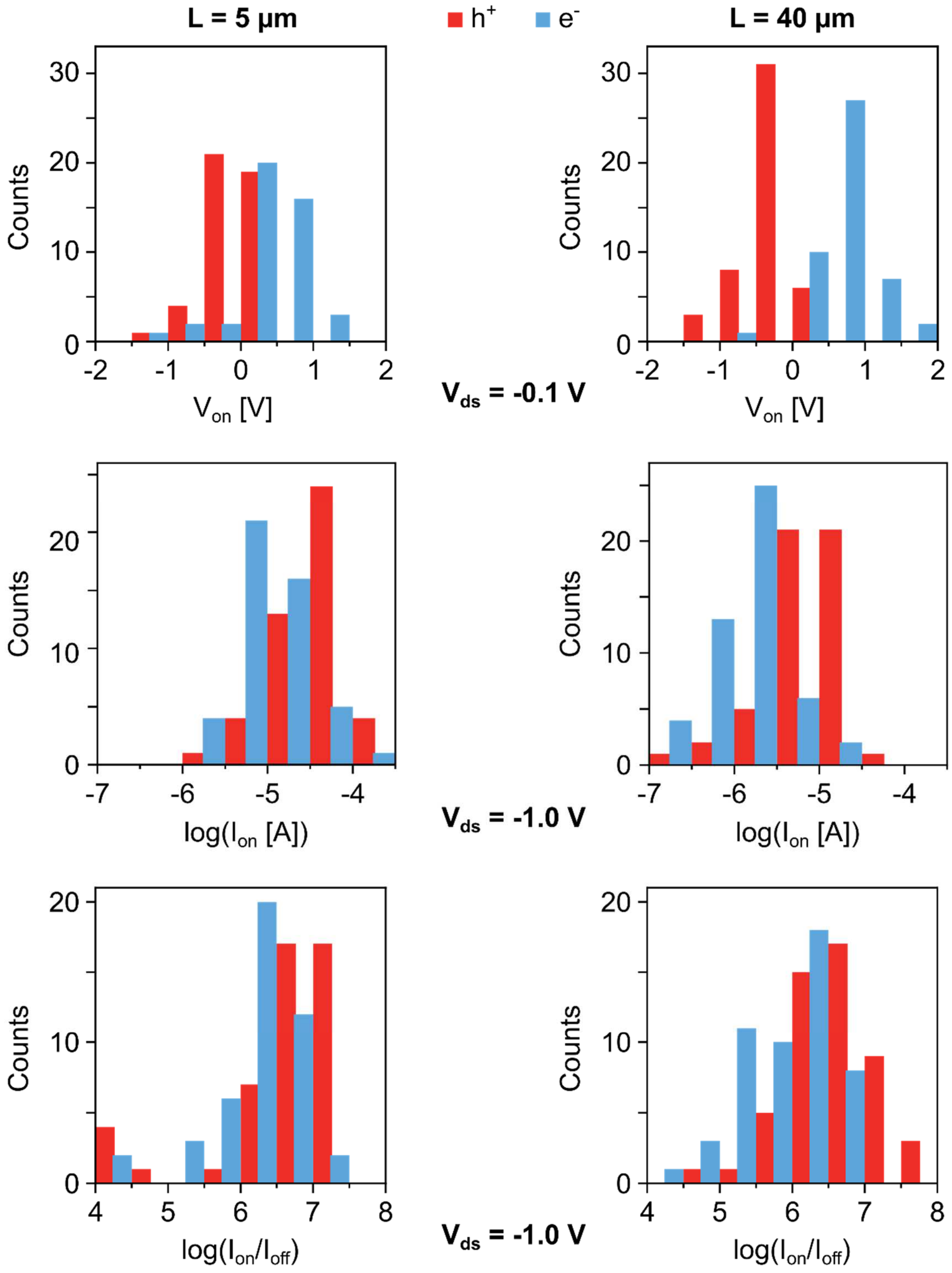

***Figure 5.14**: Statistical evaluation of device characteristics for L = 5 µm (left column) and L = 40 µm (right column): Turn-on-voltage (top) extracted at V_{ds} =−0.1 V, on-current (middle) and on/off-ratio, both extracted at V_{ds} = −1.0 V.*

The variations in currents, turn-on voltage and on-off ratio might raise the question if this variability is sufficient for applications. However, most publications showing more than a few FETs and reporting device-to-device variations for CNT transistors state similar distributions for printed nanotube layers.[221, 265] Alternative deposition methods such as spin-coating,[168] dip-coating,[368] or simple immersion,[147, 369, 395, 396] also do not show a much higher uniformity. With such FETs and their associated spread of device characteristics presented in literature it was still possible to fabricate simple logic gates.[396] Furthermore, even integrated circuits,[368] static random access memories,[397] and active matrix backplanes for tactile sensors,[369] were reported. The here obtained device variations should thus be sufficiently small to enable the use of FETs in circuitry and more complex applications.

The high purity of the polymer-wrapped large bandgap (6,5) nanotubes and especially the absence of metallic species resulted in very low off-currents which were basically only limited by the gate leakage. As the hybrid dielectric also enabled low gate leakages ($\lesssim 1$ nA) as demonstrated before,[33, 163] high on/off-ratios of 10^6–10^7 could be reached for low source–drain voltages ($V_{ds} = -1$ V). Due to the lower on-currents of the 40 μm long channels, these devices exhibit slightly lower on/off-ratios. As the probability of percolating paths by residual metallic CNTs decreases with the channel length, lower on/off-ratios (in the order of 10^4) due to increased off-currents were found less often among those devices as well. For the best FETs with $L = 5$ μm on/off-ratios of up to $1.8 \cdot 10^8$ for holes and $6.1 \cdot 10^7$ for electrons were reached at a source–drain bias of ± 3 V (see **Figure 5.15**), thus exceeding values reported in the existing literature.[1, 146] Further reduction of the gate leakage was achieved by measuring with triaxial instead of the usually used coaxial cables and thus reduced noise levels of the measurement setup. The off-current was thus limited by the drain current minimum point of the transfer curve, which was slightly above the gate leakage. The V-shape of the transfer characteristic results from the ambipolar behavior, *i.e.* the simultaneous transport of holes and electrons (compare chapter 2.2.6), that becomes apparent at elevated V_{ds}. For larger V_{ds}, the off-currents of the devices increase and thus reduce the on/off-ratio again as evident from the averaged transfer characteristics shown in **Figure 5.12**. For smaller bandgap nanotubes the increase of the off-current already starts at much lower source–drain bias due to the lower turn-on voltages.[52] The large bandgap and comparably large turn-on voltages of (6,5) CNTs thus support reaching higher on/off-ratios. Ambipolar transport is often unfavorable in applications not only because of the limitations concerning on/off-ratios but also in integrated, complimentary circuits where it results in increased power dissipation. This problem could be addressed by p- or n-doping of the nanotube network and thus unipolar transport. A successful attempt of completely suppressing hole transport was recently demonstrated by doping (6,5) CNTs with a guanidino-functionalized aromatic compound. With the same device architecture as used here, Schneider *et al.* demonstrated the complete absence of hole transport even at high V_{ds} of up to −5 V and reached on/off-ratios for electrons of up to $2{\cdot}10^8$.[144]

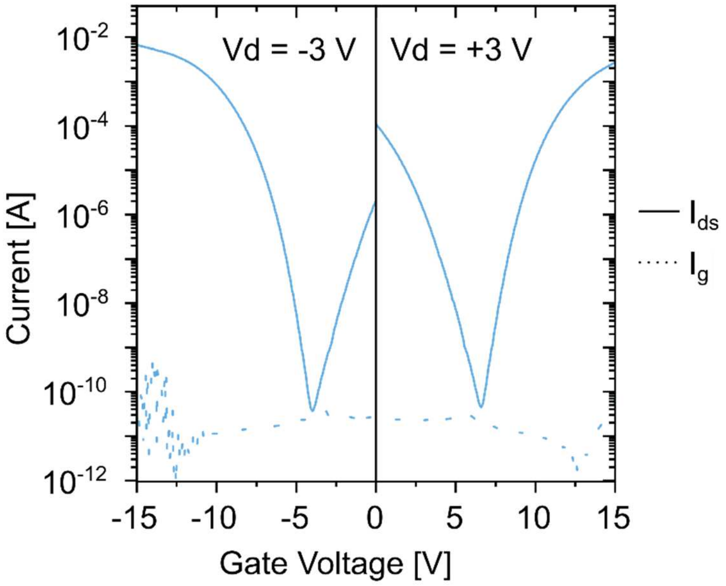

Figure 5.15*: Best on/off-ratios achieved with an FET with of AJ printed (6,5) CNTs with L = 5 μm: $1.8{\cdot}10^8$ for holes at V_{ds} = −3 V and $6.1{\cdot}10^7$ for electrons at V_{ds} = +3 V.*

For the AJ printed FETs, higher channel length normalized currents for longer channels and thus also higher apparent device mobilities were extracted. The linear field-effect mobilities for holes were (0.34 ± 0.21) and (1.90 ± 1.17) $cm^2\ V^{-1}\ s^{-1}$ for 5 and 40 µm long channels, respectively. They were calculated using standard transistor equations within the gradual channel approximation and with the capacitance measured directly at the channel. The electron mobilities were about one order of magnitude lower with (0.03 ± 0.03) and (0.11 ± 0.11) $cm^2\ V^{-1}\ s^{-1}$. **Figure 5.16** shows that there is no systematic decrease of the hole mobility with the number of printed transistors from one ink but rather a device-to-device variation. It further demonstrates a large dependence of the mobilities on the channel length that can be mainly explained by contact resistance. A decrease of the apparent device mobility by a factor of 3 to 4 was even demonstrated for large diameter (and thus small bandgap) nanotubes and different channel lengths.[52] For the here employed large bandgap CNTs, this effect is expected to be even more pronounced.[41, 398]

The already rather low electron mobility showed a further decrease with the number of printed transistors besides the also evident device-to-device variations.

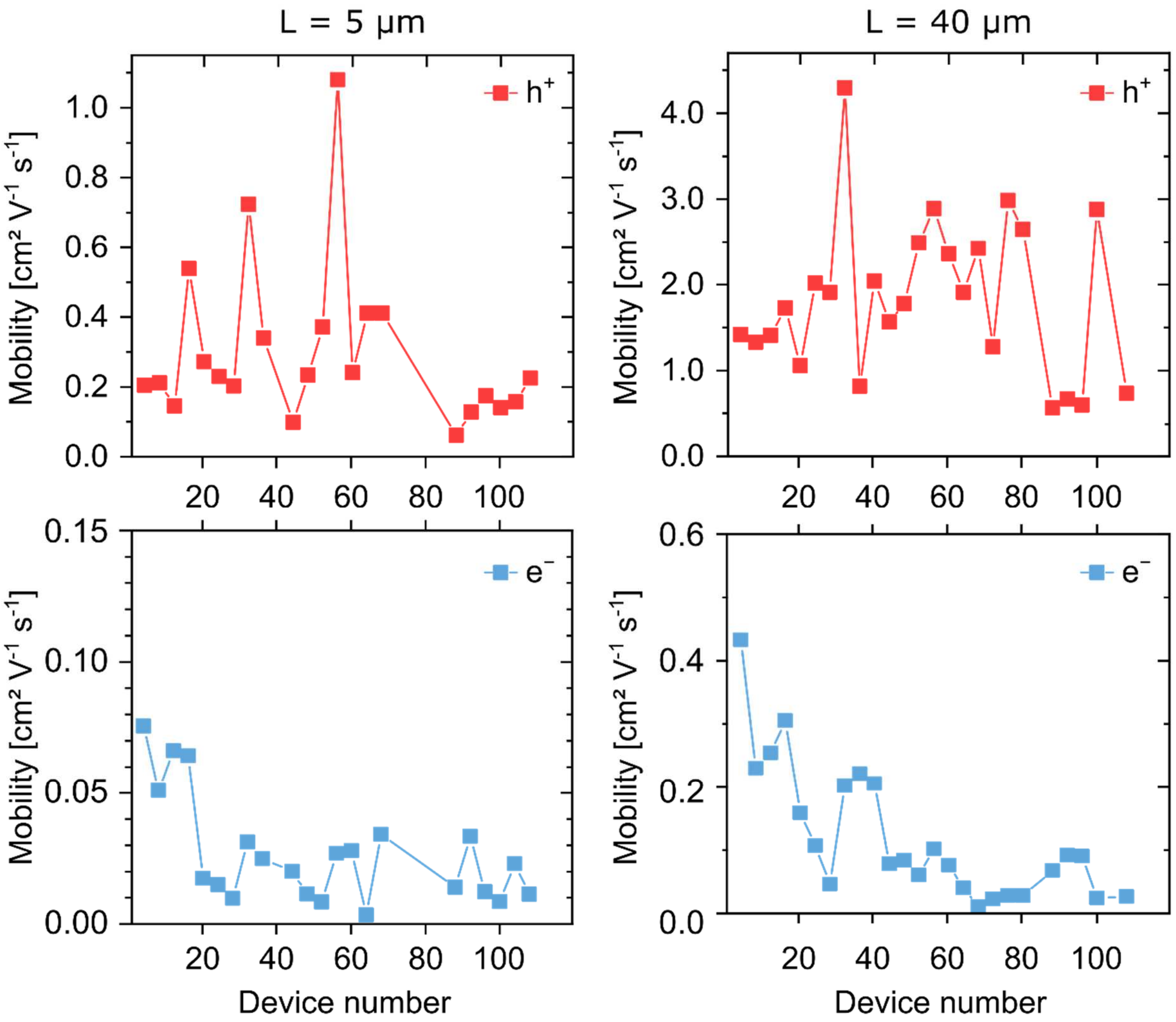

***Figure 5.16**: Calculated device mobilities for one set of consecutively printed transistors from one (6,5) CNT ink for L = 5 µm (left) and L = 40 µm (right). While the hole mobilities (red, top) show device-to-device variations, the electron mobility (blue, bottom) decreases with the number of printed FETs. Note the different mobility scales for the long and short channels.*

As a reference, spin-coated samples were prepared from the same dispersion. They showed slightly lower mobilities ($L = 40$ µm) for thin nanotube networks with (0.14 ± 0.14) and (1.25 ± 0.05) cm^2 V^{-1} s^{-1} for electrons and holes, respectively. In contrast to the inherently patterned printed films, the unpatterned spin-coated films exhibited high gate leakage currents especially at elevated V_g as shown in **Figure 5.17**. Furthermore, the devices showed a large current hysteresis. For an increased film thickness (about 25 nm) however, the hysteresis of the spin-coated film decreased to almost zero but the gate leakage remained rather high. The hysteresis present in the AJ printed devices and possible ways to tackle it are examined in the following section based on these observations for spin-coated CNTs.

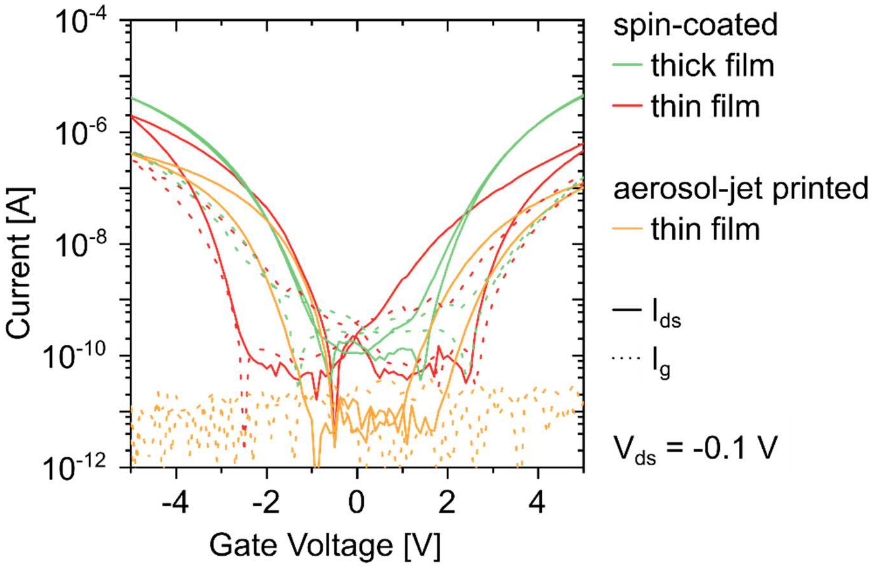

***Figure 5.17**: Comparison of AJ printed (yellow) and spin-coated FETs with a thin (red) and thick (green) CNT film for a channel length of 40 µm.*

5.5. Decreasing the Hysteresis of Aerosol-Jet-Printed CNTs

The printed networks examined so far were well above the percolation threshold and were not sensitive to changes of the ink composition or vial filling level. However, they showed some device-to-device variation and especially a rather large hysteresis. While the variations are comparable to other reports on carbon nanotube FETs, other solution-processable materials outperformed aerosol-jet printed transistors with respect to uniformity. Some of those materials, *e.g.* small molecules with polymer binder or conjugated polymers, are also printable and thus CNT devices require further improvement.[256, 399] As seen for spin-coated samples, hysteresis could be significantly decreased by depositing a thicker film. Additionally, a thicker nanotube layer could lead to a higher network uniformity and thus less variation in the characteristic device metrics.

The aerosol-jet process provides several adjustable parameters to control the material deposition per area and thereby the resulting film thickness: Stage speed, flow rates, ink composition, printing pattern, and printing of multiple layers. The least labor-intensive change would be the decrease of the stage speed or increase of the carrier flow rate. For both cases, only one parameter would have to be altered before the material deposition. However, both lead to more aerosol droplet deposition per area and thus also more solvent deposition. While the main solvent toluene evaporates rather quickly, the high boiling point co-solvent terpineol (T_B = 213–218 °C) that is necessary for proper aerosol formation would accumulate on the substrate. As the stage heating is limited to a temperature of 100 °C, also toluene remains for some time on the substrate before evaporating, especially when changing the deposition location only very slowly. This would lead to a solvent film on the sample surface and thus an increased flow of material on the substrate. This might lead to less uniformity and a larger overall deposition area of the CNTs. The resulting lower spatial resolution would eventually reduce the packing density of the FETs on the substrate and lead to severe device cross-talk. The increased material consumption, limited controllability, and loss in patterning accuracy exclude these simple approaches for increasing the thickness of the deposited film.

When changing the ink composition all other parameters could in principle remain constant, only the carrier gas flow may have to be adjusted. Increasing the CNT content is only possible up to a certain limit, as for too high concentrations two negative effects can occur. The dispersion can become less stable and thus more bundling takes place which is unfavorable for efficient charge transport.[44, 45] Additionally, a high solids content in the aerosol leads to faster clogging of the 200 µm inner diameter nozzle of the printer.

A change of the printing pattern, *e.g.* reducing the pitch between adjacent lines, might induce similar problems as reducing the stage speed or increasing the flow. However, the pattern can be designed so that adjacent lines are not directly printed one after the other. Instead, every second line could be printed in the first cycle and the remaining lines in a second cycle. Thereby, the deposited material has some time to dry before more material is deposited next to it. Printing several layers on top of each other relies on the premise that nanotubes are not washed away by the next printed layer. This has already been shown for spin-coating where consecutive spin steps are used to increase the density of CNT films.[121, 400] Likewise, no removal of previously deposited nanotubes was observed for printing of several layers. A reduction of the amount of solvent remaining on the sample from the previous printing step can be realized by rinsing with THF and IPA or deionized water and subsequent drying with a nitrogen gun. The rinsing step also reduces the amount of excess wrapping-polymer in each layer and not only at the surface of the film which would be the case if performed only at the end of printing.

The effect of the described techniques on the device characteristics and hysteresis in particular was tested by printing on pre-patterned electrodes with a 40 µm channel. The lowest CNT coverage was realized with a CNT concentration of 2.2 mg L^{-1} and a printing pitch of 60 µm between adjacent lines, *i.e.* one line in the center of each channel. As the lines were 60 µm wide this led to a complete coverage of the printing area. For a second set of samples, the pitch between two lines was then decreased by a factor of 2.4 to 25 µm while keeping the ink concentration constant. A third sample set was fabricated by printing with a 60 µm pitch and a 3 times increased ink concentration (6.6 mg L^{-1}). **Figure 5.18** shows representative transfer characteristics for devices with all three printing parameter sets. The hysteresis was quantified by the difference between the turn-on voltage of the forward and reverse sweep ΔV_{on} and depicted in the bar graph. The mean values with standard deviations as error bars clearly indicate the positive effect of a thicker nanotube layer as the hysteresis was decreased by a factor of 2 to 3 for both methods. As expected, the 3-fold increased ink concentration gave slightly better results than the 2.4-fold decreased pitch as more material was deposited per area.[401] Besides the decreased hysteresis, a significant increase in apparent device mobilities could be observed. Mobility values of 0.58 and 6.43 $cm^2 V^{-1} s^{-1}$ were obtained for electrons and holes, respectively.

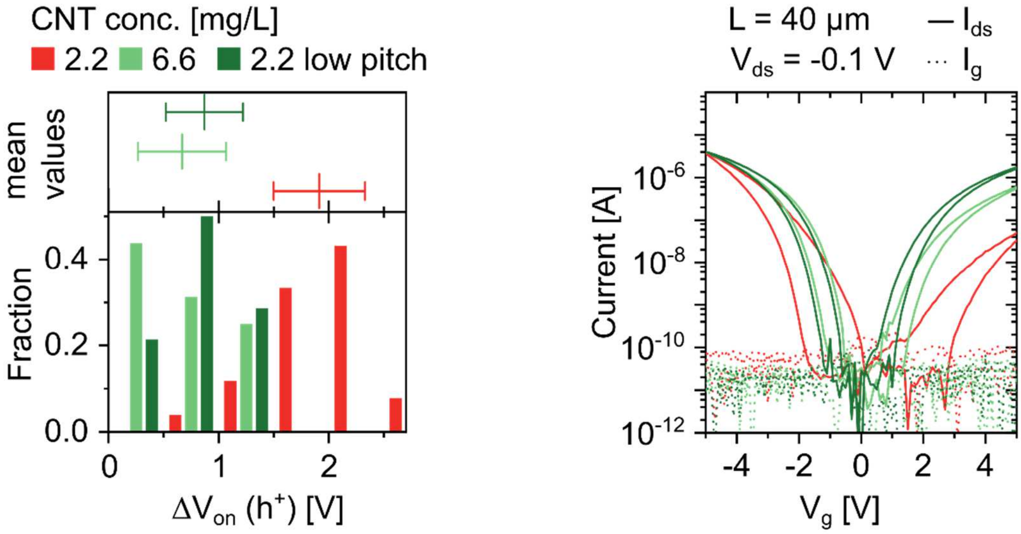

Figure 5.18*: Reduction of hysteresis by increased material deposition (statistical quantification on the left and representative transfer characteristics on the right) by printing from a higher CNT concentration (light green) or reducing the pitch between adjacent lines (dark green) compared to the original material deposition (red).*

As a second method for increasing the film thickness, printing of several layers from an ink with a nanotube concentration of 1.8 mg L^{-1} was performed. Each layer consisted of the printing pattern used before, *i.e.* lines in the channel center with a pitch of 60 µm between adjacent lines. The hysteresis decreased significantly with the number of layers as shown in **Figure 5.19**. This result was further improved by implementing a washing step with THF and deionized water followed by drying with a nitrogen gun after each layer and not only at the end of the complete printing process. The hysteresis present in the fabricated FETs can be mostly attributed to the impact of water adsorbed on the polar glass substrate as well as in the film.[401] While moisture on top of the CNT film could be removed by annealing in ideal, *i.e.* completely dry, conditions, water trapped on the surface of the substrate may still remain. Although the devices were annealed at high temperatures in a nitrogen-filled glovebox, increased humidity values within the glovebox might be additionally accountable for a larger hysteresis in the samples presented in section 5.4. Nevertheless, the increase of the film thickness had a positive effect as it reduced the influence of trapped water as charge transport in a top-gate FET only takes place at the upper part of the nanotube layer.[402] Repeated rinsing steps might further remove more of the wrapping-polymer. Voids present in the polymer can also store water molecules and hence increase charge trapping and thus hysteresis is further reduced by removing as much of the polymer as possible.[403]

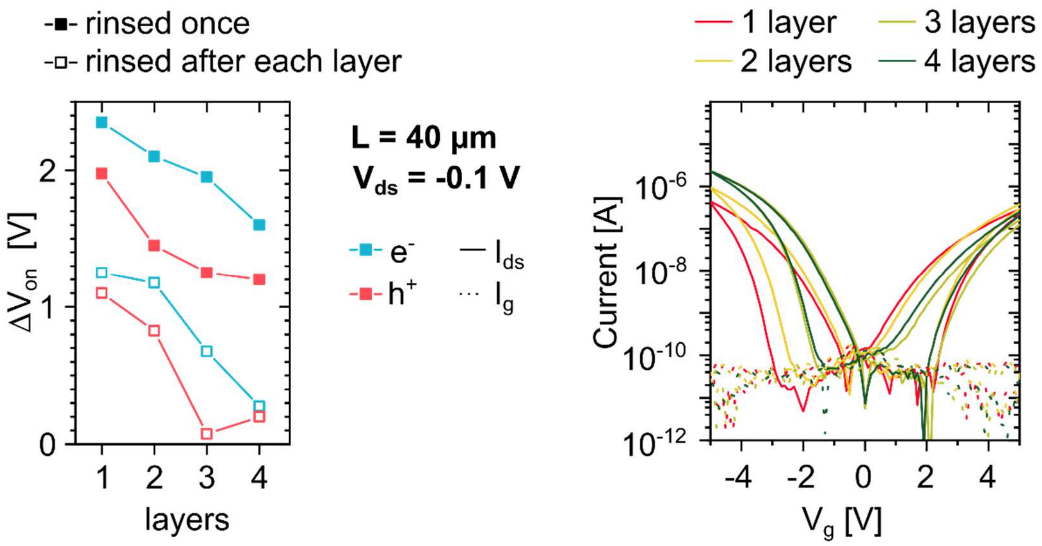

***Figure 5.19**: Reduction of hysteresis by depositing multiple layers of CNTs: Quantification* via *the reduction in the difference between the turn-on voltages in forward and reverse sweep* ΔV_{on} *(left) for both, holes (red) and electrons (blue). Rinsing after each deposited layer (open symbols) instead of rinsing only after printing all layers (solid symbols) further reduces the hysteresis. Representative transfer characteristics for 1 to 4 printed layers are shown on the right.*

Even thicker and eventually optically dense nanotube films could be created by aerosol-jet printing of multiple layers from inks with higher concentration or by increasing the total number of layers. Printing 4 consecutive layers from an ink with a concentration of 6.3 mg L^{-1} resulted in about 30 nm thick films that are easily visible to the naked eye (see photograph in **Figure 5.20**). Absorbance spectra show an optical density of 0.5 of the film at the E_{11} peak of the (6,5) CNTs. According to the ink absorbance, the absorption cross section,[404] and the ink consumption, the transistors presented in section 5.4 required around 40 ng mm^{-2} of nanotubes. Here, the thick films required still less than 600 ng mm^{-2}. Alternative deposition methods for thick films are at a disadvantage here. Spin-coating of films with a thickness of several tens of nanometers is possible by multiple steps only, and a very high material consumption is inevitable.[405] A large fraction of the material consumed during spin-coating flies off the spinning substrate. Vacuum filtration or drop-casting of highly concentrated dispersions on the other hand either need subsequent transfer steps or lead to very inhomogeneous films.[406-409] While direct patterning is possible by printing, the deposited material has to be patterned in further processing steps such as photolithography-assisted plasma etching for other methods to create thick CNT film. This may lead to the introduction of further impurities, *e.g.* by residual photoresist, and defects especially at the edges of the patterned area.

Transistors fabricated from aerosol-jet printed thick films showed a negligible hysteresis and on/off-ratios of more than 10^6 for L = 5 μm at V_{ds} =–0.1 mV. For a channel length of 40 μm, an on-conductance of 17 μS mm^{-1} was observed while the mobilities were 0.7 and 2.8 cm^2 V^{-1} s^{-1} for electrons and holes, respectively. Channels with L = 5 μm and doubled width exhibited an on-current increase by one order of magnitude while the off-current was slightly elevated above the gate leakage. The on/off-ratio was however still larger than 10^6. Compared to the FETs with only slightly increased layer thickness presented before, the hole mobility decreased by a factor of 2.3 while the electron mobility was almost constant. This reduction can be attributed to the necessary vertical charge transport through the semiconducting layer, requiring hopping over many nanotube junctions. For optimized charge transport the thickness has to be chosen in an optimized range where trapping by adsorbed water is reduced but vertical transport through the semiconductor is minimized. In addition, a high density of the network and repeated rinsing steps to maximize the removal of polymer are favorable.

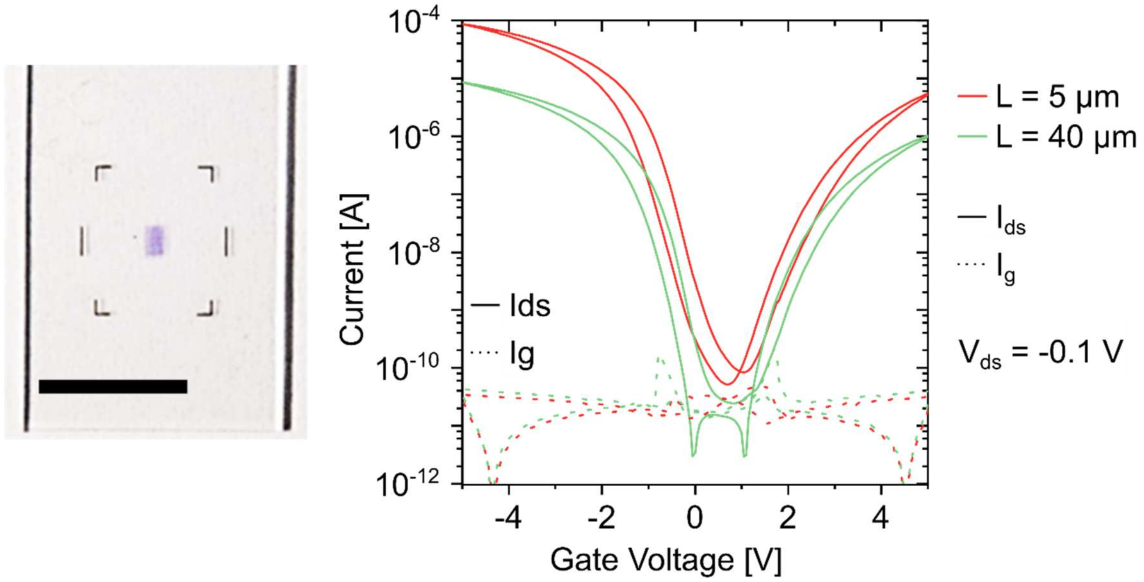

***Figure 5.20**: Photograph of a printed CNT films visible to the naked eye (left) and transfer characteristics of FETs fabricated from such thick films for two channel lengths. Scale bar in the left image is 5 mm, the film is surrounded by alignment markers printed with Ag ink.*

5.6. Applications of Printed CNT Films

In this section, some examples of applications of aerosol-jet printed (6,5) CNTs based on the introduced and optimized procedures described here will be very briefly presented.

Berger *et al.* used very thick, optically dense (6,5) CNTs for electrochromic notch filters.[111] Film thicknesses of 10 to 360 nm were prepared by printing multiple layers of an orthogonal grid (line pitch 25 µm) onto glass with spray-deposited mixed CNT electrodes. In combination with an ion-gel the CNT layer could be tuned from an optical density of 4.5 at the E_{11} peak (997 nm) to 0.2 by electrochemical doping.

Held *et al.* used printed (6,5) nanotubes in combination with dense films of mixed CNTs and an ion-gel for low-voltage all-carbon semi-transparent transistors.[3] These devices might be applicable for flexible or even stretchable electronics. Although the device characteristics of reference samples with gold electrodes were superior due to the high sheet resistance of the nanotube contacts, the device performance was still good.

Zakharko *et al.* used a 40–50 nm thick layer of AJ-printed (6,5) CNTs for the investigation of plexciton propagation in plasmonic crystals.[410] Choosing printing as the deposition method enabled homogeneous layers with a rather controlled thickness. Furthermore, the nanotubes could be directly printed onto the pre-patterned array of plasmonic particles without the need of post-structuring.

Brohmann *et al.* expanded the printing process from solely (6,5) nanotubes to mixtures of different CNT chiralities prepared by polymer-wrapping of different CNT sources with different wrapping-polymers.[44] With the printed networks of nanotubes they then studied temperature-dependent charge transport to further investigate the transport mechanism.

The range of different successful applications of aerosol-jet printed CNT networks shows the potential of this method to fabricate reproducible devices with a low material consumption for electronic and optical applications. Although the patterning accuracy was not optimized, it was already sufficient for most applications where simply continuous areas of CNTs were needed and only some precise measurements such as the temperature-dependence study required more detailed structuring performed on the printed films via photolithography.[44] However, there are also limitations that will be discussed in the next section.

5.7. Limitations of Aerosol-Jet Printing for CNTs

After printing thin but dense networks, the creation of a CNT film with a controlled low density was attempted. For this, the established ink with polymer-wrapped (6,5) nanotubes was used at a concentration of 1.8 mg L^{-1} in toluene with 5 % terpineol. As discussed before, the thickness of printed CNT films can be controlled by the printing speed. While decreasing the speed to achieve thicker layers is problematic because of the increased solvent deposition, this problem does not occur when increasing the stage speed. At constant sheath and carrier flows of 30 and 18 sccm, respectively, the stage speed v was varied from 0.5 to 2.0 mm s^{-1}. The rather low CNT concentration led to a full coverage but thin CNT film as shown above. Accordingly, in combination with a higher speed, this process should lead to a change in network density.

However, as evident from the AFM images presented in **Figure 5.21**, the network density does not systematically decrease with the increased stage speed. While full coverage is maintained for $v = 0.5$ mm s^{-1}, for faster printing speeds the CNT density varied. Additionally, there were some areas with a high nanotube density while neighboring areas were completely free of CNTs, as seen for the lowest tested speed of 0.3 mm s^{-1}. This might be a drying effect that led to a kind of coffee ring formation. It is also possible, that partly CNT-rich droplets and almost CNT-free droplets were deposited and thus resulted in non-uniform deposition. While for dense films this effect evens out, it may play a significant role when trying to produce nanotube films with a controlled – but low – CNT density. Films with several layers of printed nanotubes showed a further increased homogeneity as seen for the thick layers in section 5.5. While further optimization of different ink concentrations might lead to the desired low-density films, this topic was not pursued further. For the parameters presented in this work it must be concluded, that AJ printing is best suitable for the fabrication of dense CNT films of varying thickness. So far, no limit in film thickness was observed. Thus nanotube films with thicknesses exceeding 50 nm were created as a next step and investigated. The results and their implementation in transistors are discussed in the next chapter.

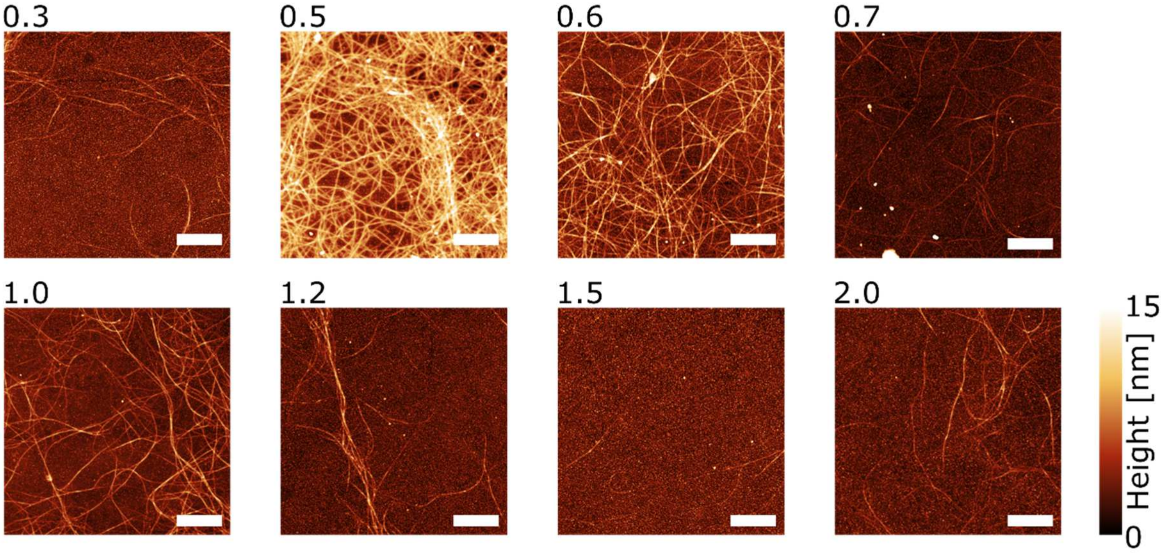

***Figure 5.21**: AFM images of CNT networks printed with varying stage speed (0.3 to 2.0 mm s^{-1} as labelled above the individual images) illustrating the non-linear behavior of CNT density with printing speed.*

CHAPTER 6

VERTICAL ELECTROLYTE-GATED TRANSISTORS

In this chapter, electrolyte-gating of a vertical device architecture for CNT transistors is investigated and different electrode materials are examined for the fabrication of all-printed devices.

The results presented in this chapter were published in part in *ACS Applied Nanomaterials* (ACS Publications, Washington, DC, USA) at DOI 10.1021/acsanm.8b00756.[112] All figures and data previously published were reprinted with permission based on the ACS AuthorChoice Usage Agreement. The gold nanoparticle electrodes (chapter 6.6) were inkjet printed by M. Held (group of Dr. G. Hernández-Sosa at KIT, Karlsruhe, Germany). Parts of the measurements resulting in the data presented in chapter 6.2 were performed by Adelaide Kruse, the DAAD RISE intern I supervised during this project.

6.1. Introduction

The previous chapter showed that aerosol-jet printing is a feasible method to deposit semiconducting carbon nanotubes with low material consumption and direct patterning different applications. However, a printed semiconductor is only one step towards all-printed and ideally roll-to-roll compatible processing of transistors and eventually integrated circuits. Major challenges are alignment accuracy of consecutive layers and restrictions in feature size.[294] These issues are particularly important for transistors with short channel lengths that are desired for high currents, *i.e.* in case of CNTs to reduce the number of nanotube–nanotube junctions. Channel lengths of less than 20 µm and even down to 2 µm were demonstrated for gravure printed lines from a silver nanoparticle paste with a linewidth of less than 10 µm.[223, 294, 411] Although no conductivities were reported, the thin electrodes might be a limiting factor for on-currents especially when used with a high-mobility semiconductor such as CNTs. Additionally, the reported fully-printed transistors required annealing temperatures above 200 °C which are not compatible with all substrate materials, especially when flexibility is desired.[223] Another issue concerning a rather coarse layer-to-layer alignment in the range of 20 µm still remains. The often used organic semiconductors with low charge carrier mobilities require rather large channel widths to reach high on-currents. Long electrodes, however, increase the probability of source–drain shorts for short channel lengths resulting from small broadenings of the printed electrode lines. Alternative approaches for lateral short channel transistors use self-alignment techniques that enable feature sizes of less than 10 µm.[222, 230, 238, 311, 412] However, additional processing steps such as a treatment with self-assembled monolayers (SAMs) are often necessary and the scope of materials is very limited.

A recently introduced novel concept decouples the alignment accuracy, linewidth, and proximity of printed electrodes from the channel length. Instead of the common lateral architecture, *i.e.* source and drain electrodes side by side and current flow parallel to the substrate surface, a vertical electrolyte-gated transistor (VEGT) with a porous SnO_2 nanoparticle semiconductor layer was introduced by Baby *et al*.[197] In this architecture, the semiconductor is sandwiched between the source and drain electrodes and gated via an electrolyte and a side-gate (see **Figure 6.1**). The channel and current direction are thus vertical to the substrate and the channel length is directly determined by the thickness of the semiconductor layer independent from the resolution of the electrode deposition process.

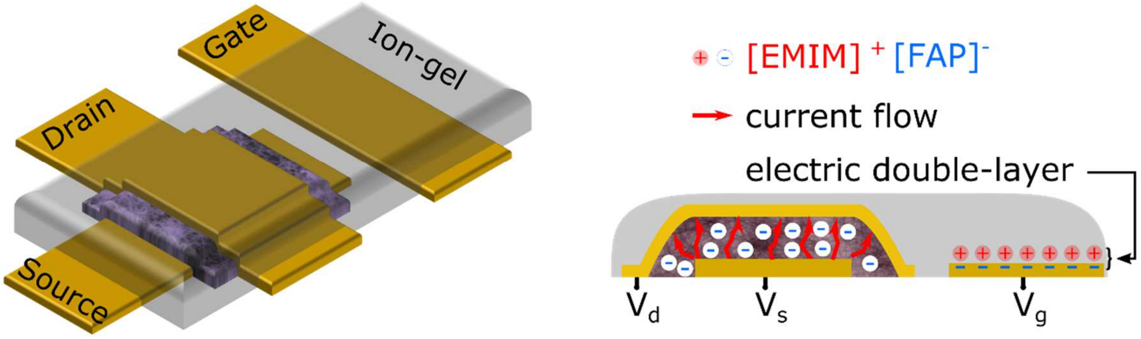

Figure 6.1: *Schematic 3D (left) and cross-sectional (right) view of the VEGT structure. The CNT network is colored in purple and the ion-gel consisting of the polymer P(VDF-HFP) and the [EMIM][FAP] ionic liquid in grey. In the cross-sectional view the state for* $V_g < 0$ *V is depicted with negative charging of the gate electrode and the resulting accumulation of* $[FAP]^-$ *ions in the channel area and thus hole current (red).*

Other vertical transistor structures were previously used but exhibited certain disadvantages. When the source electrode is placed within the semiconductor in a stack of gate–dielectric–source/semiconductor–drain, the electric field of the gate has to be able to penetrate the source electrode.[413] Otherwise, charge injection, accumulation and conductivity cannot be modulated. The penetration of the electric field was usually enabled by very thin,[414] structured,[415] or network electrodes based on nanowires or nanotubes.[229, 416] The alternative stack of source–gate/semiconductor–drain with the gate electrode placed triode-like within the semiconductor results in rather high leakage currents.[417, 418]

Semiconducting materials suitable for the newly proposed vertical electrolyte-gated structure have to fulfill several requirements: first, the electrolyte has to be able to penetrate the semiconductor for efficient three-dimensional gating. On the other hand, the porous semiconductor layer must still be sufficiently stable, dense and thick to allow for the deposition of the top electrode without creating shorts between the source and drain electrodes. Additionally, the porous layer has to be well above the percolation threshold and enable unhindered charge transport perpendicular to the substrate. Semiconducting carbon nanotubes seem to be a good choice as an active material here as they should form an inherently porous layer upon deposition. The fulfillment of the introduced requirements as well as the influence of device dimensions and the occurrence of lateral charge transport paths are investigated in the following. Initially, evaporated gold electrodes were used to facilitate precise control of dimensions and a smooth substrate before finally realizing all-printed devices with different electrode materials.

6.2. Three-Dimensional Charge Transport and Efficient Gating

The crucial property of a semiconductor suitable for vertical transistors is the ability to transport charges perpendicular to the substrate. The main resistance within a CNT network is caused by charge transfer across nanotube–nanotube junctions, especially in networks with mixed nanotube species.[33, 44, 74] Charge transport along an individual nanotube on the other hand is very fast due to high charge carrier mobilities. For a CNT network that is highly conducting in the on-state of the transistor it is thus desirable to have an out-of-plane orientation of the nanotubes. If the CNTs were oriented in completely horizontal layers on top of each other, the whole channel would have to be bridged by inter-tube hopping instead of exploiting the fast transport within the tubes. The mere existence of vertical charge transport can be examined most easily by sandwiching a thick carbon nanotube network between two electrodes, performing a current–voltage measurement, and extracting the device resistance. Lateral structures with a channel length of 20 µm and a width of 10 mm typically exhibited a resistance of several 100 kΩ for thin (<10 nm) CNT layers, as determined by current–voltage measurements without any applied gate voltage. For vertical transport, this value depended on the thickness d of the nanotube layer and generally increased with d. For an electrode overlap area of 0.04 mm^2 the measured resistances were in the range from 10 kΩ (d = 174 nm) to 54 kΩ (d = 609 nm) as shown in **Figure 6.2**. The dependence on d showed the increased length of the charge transport paths for thicker layers. As the resistance was an order of magnitude lower in the vertical device architecture than in lateral structures even for very thick CNT films, at least some nanotubes must be oriented out of plane.

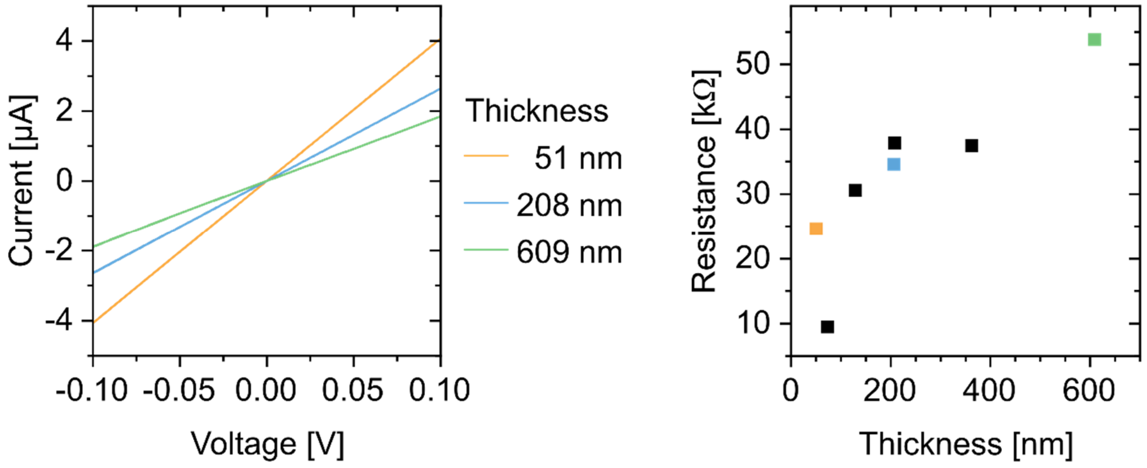

Figure 6.2*: Representative current–voltage measurements (left) and extracted device resistances for vertical transport through CNT networks depending on the CNT film thickness (right).*

More detailed insight into the vertical transport paths through a thick aerosol-jet printed CNT network was possible via conductive atomic force microscopy (c-AFM), *i.e.* a constant voltage was applied between a bottom electrode and a conductive AFM tip during image acquisition. Here, the height and the respective current at each acquisition position were recorded simultaneously to obtain a topography and conductivity image. The bottom electrode was connected via a microprobe to the AFM chuck and a bias of 1 V was applied. Note that the measurements were performed after printing the (6,5) CNT film and without any electrolyte or gate. Hence the observed conductivity originated from p-doping of the CNTs in air. In laterally oriented CNT films, a correlation of the height image (clearly showing the nanotube network) and the current map was previously observed with the same setup.[3] In contrast to that, the observed contact current for thick printed networks (150 to 650 nm) appeared to be distributed randomly and the resulting map had no correlation with the height. The contact current maps shown in **Figure 6.3** were normalized as the absolute currents strongly depend on tip condition, peakforce setpoint and amplitude as well as other environmental conditions such as humidity and were thus not completely reproducible between different measurements. From the random distribution of the current signal and the conductivity perpendicular to the surface was concluded that the printed networks exhibited at least a certain degree of three-dimensionality and thus fulfilled the basic requirement for vertical transistors. After evaporation of the top electrode and spin-coating of the ion-gel, the next question to be answered was, whether it was possible to effectively gate the whole nanotube network when applying a voltage to the side-gate.

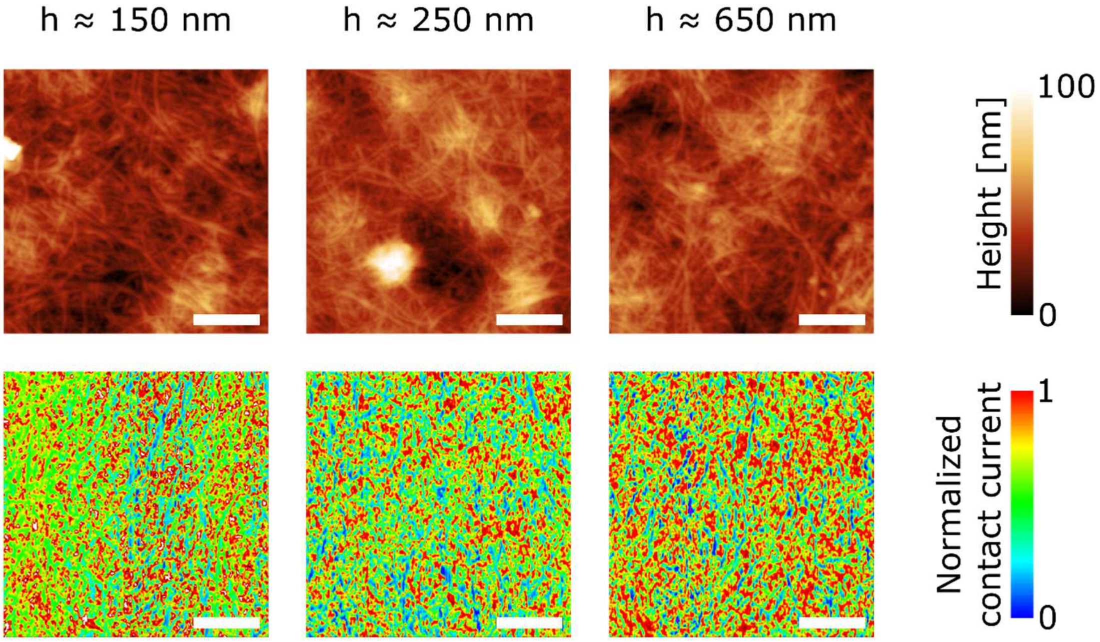

Figure 6.3: *Height images (top row) and normalized contact current maps (bottom row) recorded simultaneously for CNT films with different thicknesses: approx. 150 nm (left), 250 nm (middle), and 650 nm (right). Scale bars are 500 nm.*

One major drawback of the semiconductor used by Baby *et al.* when introducing the VEGT was the extremely small penetration depth of the electrolyte into the porous SnO_2 of only around 300 nm.[197] This problem was "overcome" by using very narrow electrodes (width < 300 nm) fabricated by electron-beam lithography. With this approach, they were able to reach high current densities (with respect to the electrode overlap area), but maximum on-currents were very limited. Furthermore, an annealing step at 550 °C was required to remove the polymer filler that was mixed with the printed ink to create a porous network. While the high temperature process is compatible with certain substrates, there is no possibility for integration in roll-to-roll processes with plastic foils as flexible substrates. An even more severe drawback of the presented structure are the feature sizes that require electron-beam lithography and are thus not achievable with printing processes.

Carbon nanotubes on the other hand inherently form porous networks upon deposition in thick films. The ability to efficiently gate the nanotubes with an electrolyte can be investigated with confocal Raman microscopy. All Raman modes exhibited by CNTs, *e.g.* radial breathing mode (RBM), G^+-mode, and 2D-mode, are reversibly reduced in intensity by doping, which was exploited previously to show charge distribution in electrolyte-gated CNT transistors.[159, 419] The completed CNT VEGTs were resonantly excited with a 532 nm laser and the G^+-mode was chosen for quantitative analysis because it exhibited the highest intensity and thus signal-to-noise ratio of all modes. Time-dependent single spot measurements in the middle of the electrode overlap area showed, that the Raman signal responded within seconds to a gate bias change from 0 V to −2 V (see **Figure 6.4**). The confocal Raman microscope equipped with a 50× objective results in a lateral resolution of 1.3 µm. As the Raman measurements were performed in air, the CNTs were inherently p-doped and no complete turn-off was expected at $V_g = 0$ V. The following Raman signal intensity maps were thus recorded at −2 V in the doped state and at +2 V in the undoped state after a 2 min hold time at the beginning of each measurement to allow a static state after completed ion movement for the measurement.

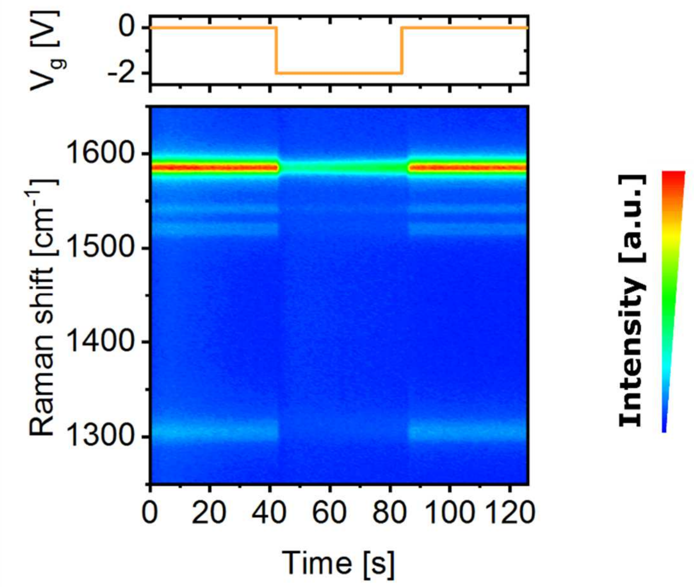

***Figure 6.4**: Temporal response of the Raman signal to an applied gate field change from 0 V to −2 V and vice versa, recorded in the middle of the electrode overlap area in a VEGT excited by a 532 nm laser.*

Figure 6.5 shows the resulting Raman map of the G^+ peak area for the whole device area. The signal intensity in the electrode overlap area was quite homogenous and only reduced at the edges of the printed CNT film. A higher signal was observed for CNTs on top of the bottom electrode acting as a mirror while a decreased intensity for areas below the top electrode was found. However, the very thin top electrode (20 nm gold) that was still semi-transparent was used and enabled spectral acquisition and peak fitting even in the doped state as shown in the representative spectra. Peak fitting only became unreliable for very thin nanotube layers at the edges of the film. The resulting non-reliable intensity ratios were excluded from the final maps.

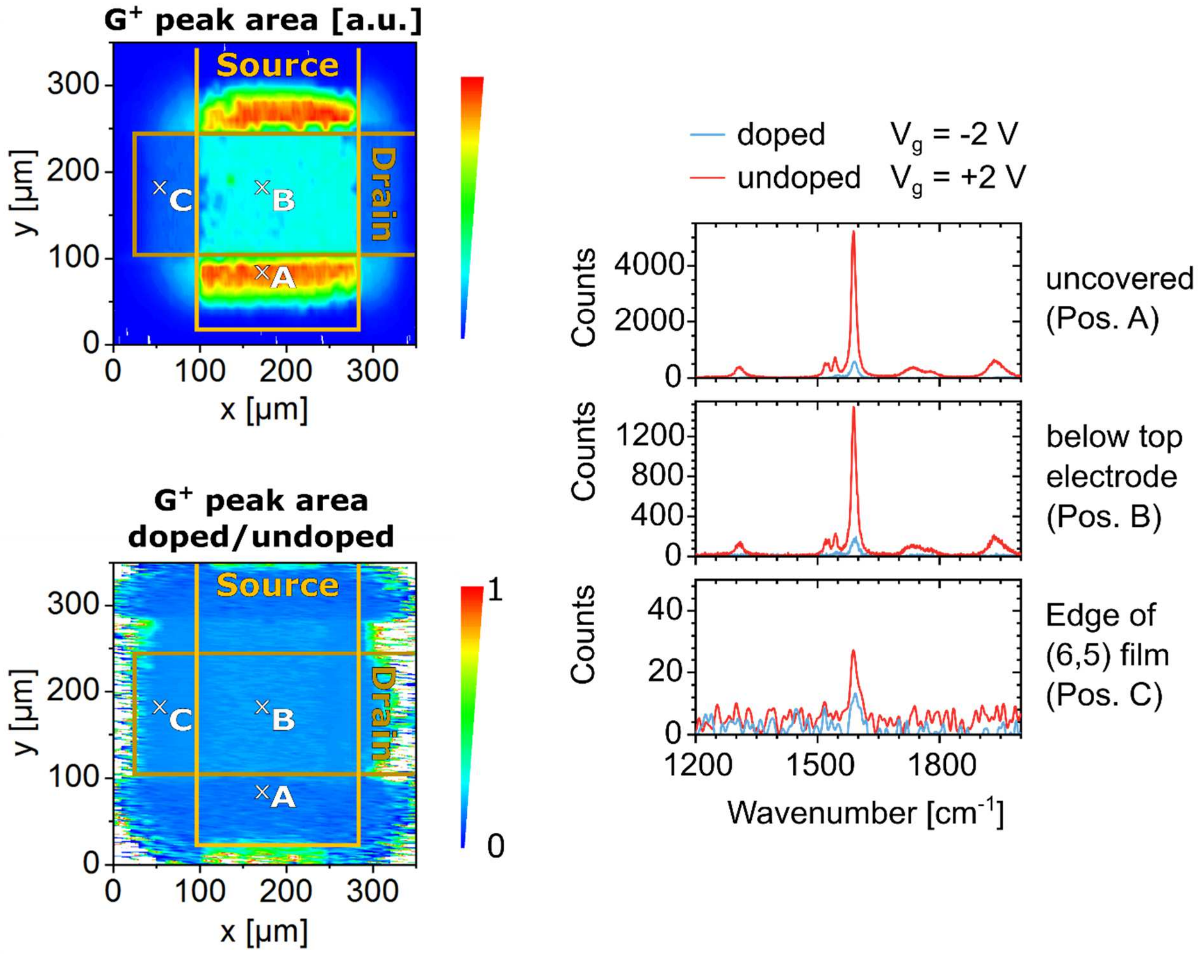

***Figure 6.5**: Raman map of G^+-band peak area (left top), ratio of the G^+-band peak area of doped to undoped state (left bottom) and representative Raman spectra at different positions of the VEGT (right).*

The ratio of the G^+ peak area in the doped *vs* the undoped state was very uniform at less than 0.15 throughout the whole device area. Although the electrodes were still slightly visible due to less efficient doping below the top electrode, *i.e.* an increased signal ratio, even at positions in the middle of the electrode overlap and thus around 100 µm away from the electrode edges the doping effect was clearly visible. The same measurements were repeated for a smaller electrode width of around 100 µm and showed similar results independent from the nanotube film thickness as depicted in **Figure 6.6**. The decreased Raman signal below the top electrode was still clearly visible. For very thick films the mirror effect of the bottom electrode, *i.e.* the increased signal observed at low *d*, was not relevant anymore. The aerosol-jet printed network of CNTs was thus suitable for electrolyte gating with an ion-gel even for feature sizes of several hundred microns and a wide range of film thicknesses. It was not necessary to introduce and later remove any filler as the nanotube network inherently showed a sufficiently high porosity for the electrolyte ions. The final performance of the produced VEGTs will be discussed in detail in the next section.

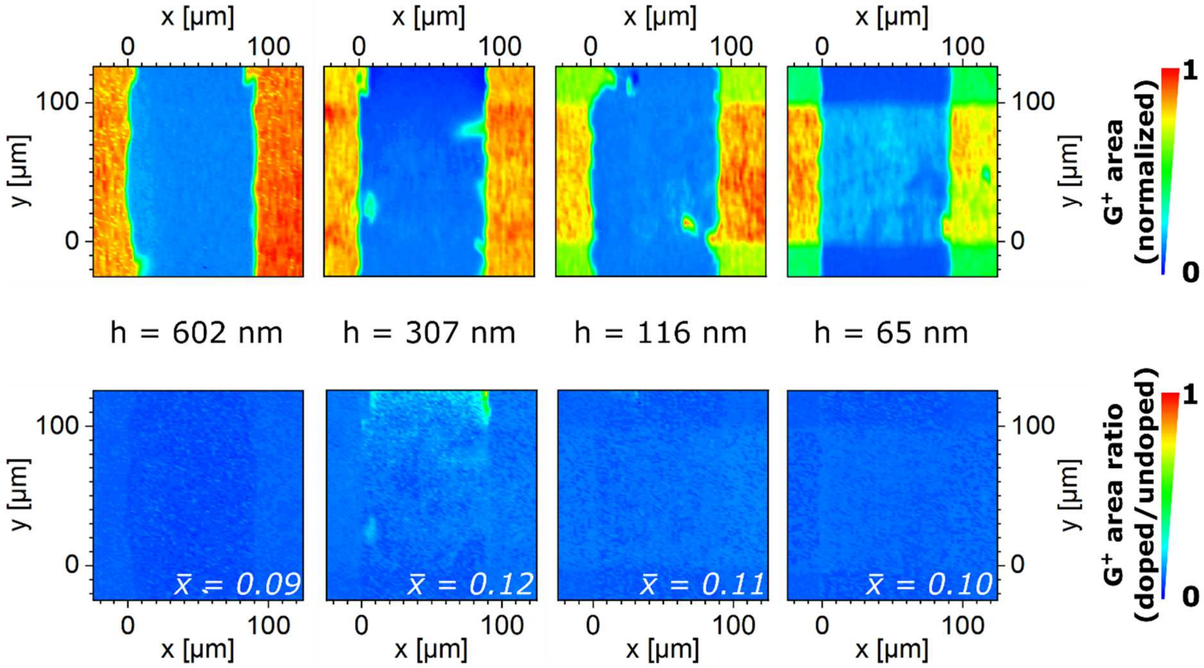

***Figure 6.6**: Raman maps of normalized G^+ peak area (top row). The ratio of the G^+ peak area of doped to undoped state is shown in the bottom row for CNT layers with a thickness of 602, 307, 116, and 65 nm (left to right). The average ratios are given in the images and indicate complete doping of the whole network areas in all samples.*

6.3. Device Characteristics of VEGTs

The main advantage of the presented vertical device architecture is the decoupling of the printing accuracy from the critical device dimension, *i.e.* the channel length *L*. As *L* depends only on the thickness of the semiconductor, a geometrical channel length of less than 100 nm is easily possible. However, the short channels also create a major challenge when using CNTs as semiconducting material. It is still almost impossible to grow solely semiconducting nanotubes or even single nanotube species. Polymer-wrapping can separate metallic (m-CNTs) from semiconducting nanotubes quite efficiently when using the right materials and processing conditions. The residual concentration of m-CNTs can be below the detection limit of optical characterization tools such as Raman and absorbance spectroscopy.[52, 91, 110, 146, 420] However, for very short channel lengths as in the vertical architecture, even a few metallic CNTs can severely reduce the transistor modulation. It was shown for sub-micron channel length transistors, that even 1 metallic out of a total of 7 nanotubes almost completely prohibits the ability to modulate the source–drain current of the device via the gate voltage.[421] Even at a channel length of 4 µm, a content of 5 % metallic CNTs decreased the on/off-ratio to less than 10.[422] Here, CNT film thicknesses and thus channel lengths of 50 to 600 nm were studied, *i.e.* a nanotube with an average length of 1 µm could bridge the top and bottom electrodes at a tilt angle of 3° (for $d = 50$ nm) or 37° (for $d = 600$ nm). Given the demonstrated three-dimensionality of the printed network (see section 6.2), it was thus very likely for a direct connection between the two electrodes to occur even at very low concentrations of m-CNTs. While the dispersions seemed to consist of solely (6,5) nanotubes according to absorbance spectroscopy, subsequent Raman analysis in the RBM region revealed additional semiconducting and also metallic CNT chiralities as depicted in **Figure 6.7**.

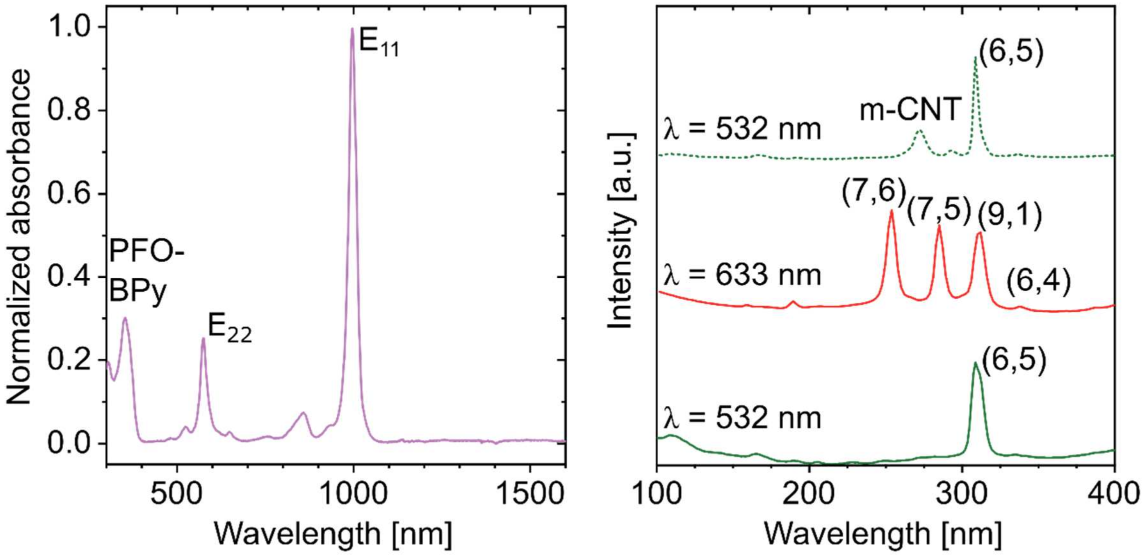

***Figure 6.7**: Absorbance spectrum showing only (6,5) CNTs (left) and Raman spectra of a drop-cast film from the same CNT dispersion revealing more chiralities (right, solid lines) for excitation at 532 (green) and 633 nm (red). For other samples, Raman spectroscopy also resolved slightly increased m-CNT content (right, dashed green line, excitation at 532 nm) that were not visible in the absorbance spectra.*

While absorbance and even Raman spectroscopy could not resolve very low m-CNT contents here, the final transistors sometimes showed a significantly increased off-current. For dispersions with a slightly increased m-CNT content that was visible in the Raman spectra (see **Figure 6.7**) further increased off-currents and thus reduced on/off-ratios of less than 10 were observed. These devices were not used for any further studies as this was an unmistakable evidence for metallic paths across the channel. This illustrates that even an m-CNT content below the detection limit of spectroscopic tools was sufficient to have a severe negative impact on the device performance, mainly the on/off-ratio. **Figure 6.8** shows the transfer characteristics of solely semiconducting CNT devices as well as of devices with different degrees of m-CNT impurities. The sample with the highest off-current (red) was exceptionally bad while slightly increased off-currents (yellow) were observed frequently. Although even the slightly reduced on/off-ratio might prevent possible applications, it was in general not detrimental for the following studies concerned with the on-currents of the devices. Only devices with severely increased off-currents were excluded from further analysis.

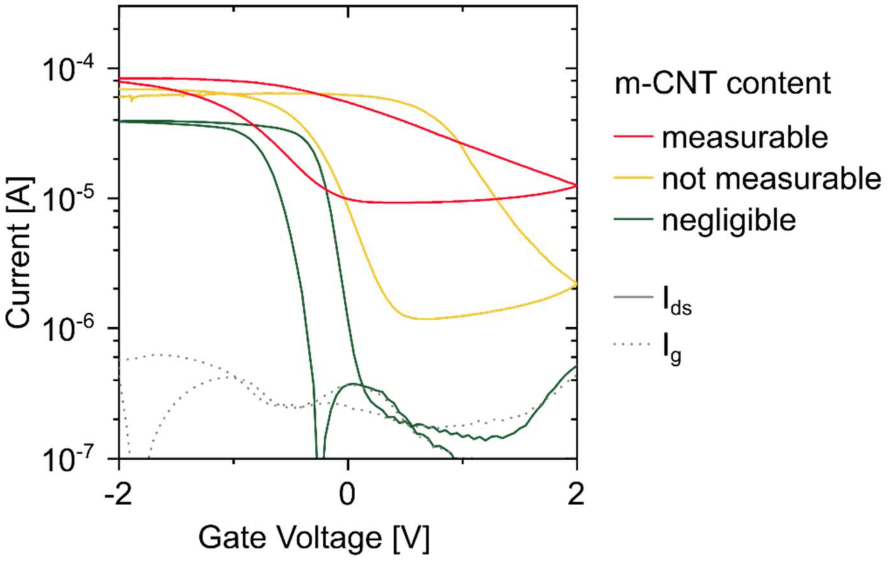

Figure 6.8*: Transfer characteristics at V_{ds} = −100 mV of VEGTs with a negligible m-CNT content (green) in contrast to devices with CNT layers containing different degrees of m-CNT impurities from not measurable by Raman spectroscopy (yellow) to a measurable content (red).*

The transistor behavior of the VEGT was initially tested with pure ionic liquid instead of an ion-gel. This should lead to a faster response to the applied gate field in contrast to ions bound in and thus slowed down by a polymer matrix. The transfer characteristics (see **Figure 6.9**) showed a steep subthreshold swing of less than 150 mV/dec as well as high on-currents at low source–drain bias resulting in an on/off-ratio of more than 10^4 and on-current densities exceeding 25 A cm^{-2}. The off-current was limited by the gate leakage which was in the range of 10^{-8} to 10^{-7} A, a typical value for electrolyte gated transistors.[157, 159] Cyclic switching between the on-state at $V_g = -2$ V and $V_g = 0$ V showed a turn-on of the transistor within seconds while the current decreased only very slowly, *i.e.* in the timeframe of half an hour, for $V_g = 0$ V. As evident from the current–voltage characteristics, the transfer curve was shifted towards positive voltages, thus a faster turn-off might be expected if positive voltages were applied. The on-currents did not decrease over time and were stable even after 12 hours of measurement. Immediately after turning on the device, the gate current indicated capacitive charging and remained at a higher level than without applied gate voltage. Although the ion movement is faster in the pure ionic liquid, practical devices require a solid electrolyte such as an ion-gel, which was used for the following devices.

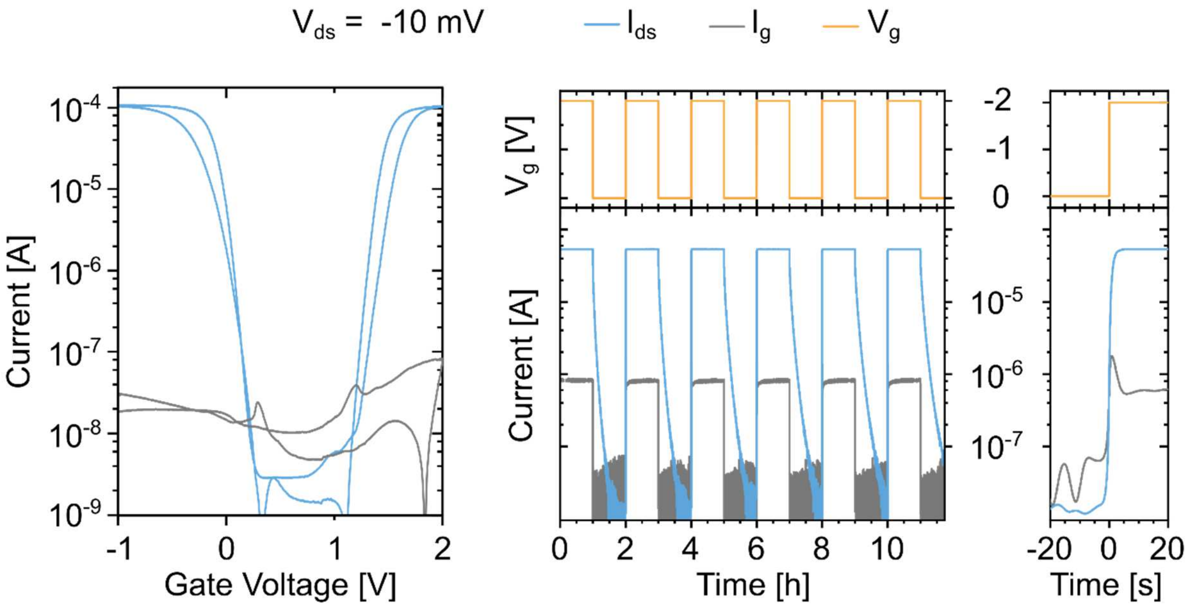

***Figure 6.9**: Transfer characteristics (left) and switching behavior over several cycles (middle) of an ionic liquid gated VEGT for $V_{ds} = -10$ mV. A zoom-in to an on-switching process shows the current response within seconds to the applied negative gate voltage (right).*

The transistor performance with respect to the on-current density should ideally be independent from the lateral device dimensions but was expected to depend on the CNT film thickness. **Figure 6.10** depicts the different electrode structures used to investigate the geometry-dependent device characteristics. The bottom electrodes and the side-gate, both consisting of 2 nm chromium as adhesion layer and 30 nm of gold, were deposited in an electron-beam evaporator and patterned by photolithography and lift-off. The top electrode (20 nm gold) was always defined using stainless steel shadow masks in a thermal evaporator. The top electrode masks consisted of two long electrode stripes with 200 and 100 µm width for the upper and lower set of 7 transistors, respectively, and were used for all devices. The actual dimensions resulting from shadow mask deposition were measured individually with an optical microscope due to possible variations between sample sets. To investigate the influence of the nanotube film thickness, bottom electrodes with the same widths were used and structured either photolithographically or via shadow masks. The influence of the device area was examined by varying the bottom electrode width from 50 to 500 µm, realized by photolithography. The purple regions in the sample layouts visualize the areas where CNTs were aerosol-jet printed usually exceeding the expected electrode overlap area by 100 µm on all sides. The area, where nanotubes were deposited may also influence the device performance. A large excess area might lead to longer ion diffusion paths and thus it might be necessary to optimize the alignment of the different layers and reduce CNT deposition to the actual electrode overlap area.

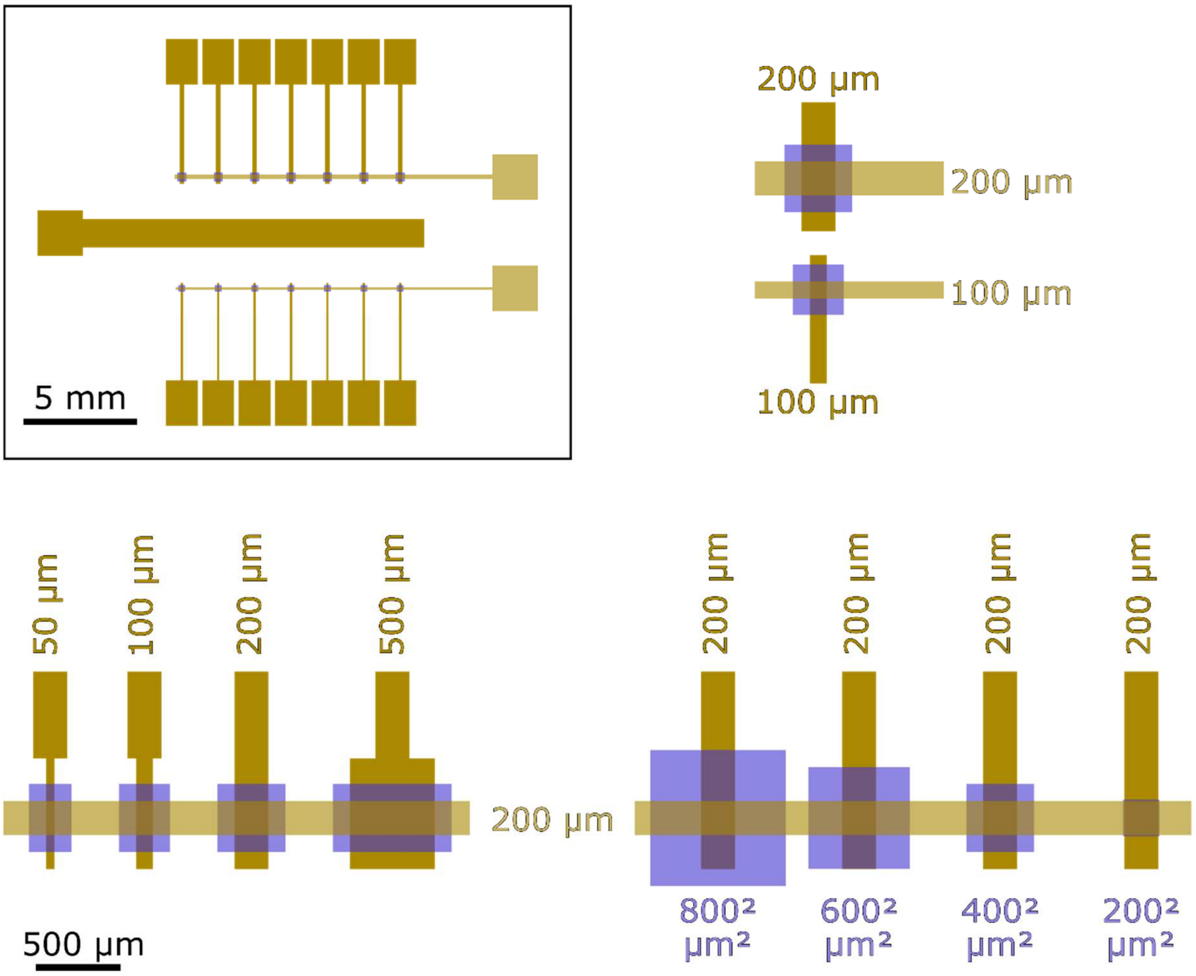

Figure 6.10*: Sample layouts to study their impact on the device characteristics: One complete substrate with 14 VEGTs (top left) and the standard configuration with 100 x 100 and 200 x 200 µm^2 electrode overlap (7 VEGTs each, top right) used for determining reproducibility and CNT film thickness dependence. The variable electrode overlap areas (bottom left) are shown for W_d = 200 µm (a corresponding structure was used for W_d = 100 µm). Different CNT printing area sizes at constant electrode width (bottom right) complete the possible geometric variations. The CNT deposition area is shaded in purple, bottom electrodes are dark gold and top electrodes light gold.*

With an electrode overlap area of 200 x 200 µm^2, *i.e.* 0.04 mm^2, several samples with printed square CNT films of edge lengths from 200, 400, 600, and 800 µm were fabricated to evaluate the possible influence of the size of the printing area. The resulting films exhibited a thickness of 78–97 nm. The transfer characteristics shown in **Figure 6.11** already reveal some device-to-device variations. For a more detailed evaluation, the on-currents were extracted from these curves and plotted *vs* the film thickness and the edge length of the printed CNT film. Overall the on-currents varied from 0.15 to 0.35 mA while 85 % of the samples were within (0.18 ± 0.03) mA. Furthermore, there was no systematic trend, neither within the small thickness range, nor within the large variation of the printing area. As there was no visible influence of the CNT printing area, the final size was a trade-off between alignment tolerance and material consumption. For easy alignment with the naked eye, the printing area was chosen so that around the electrode overlap an additional margin of 100 µm in all directions was covered with CNTs. This alignment tolerance even exceeds the requirements of other printing methods and enables the fabrication of all-printed devices later.

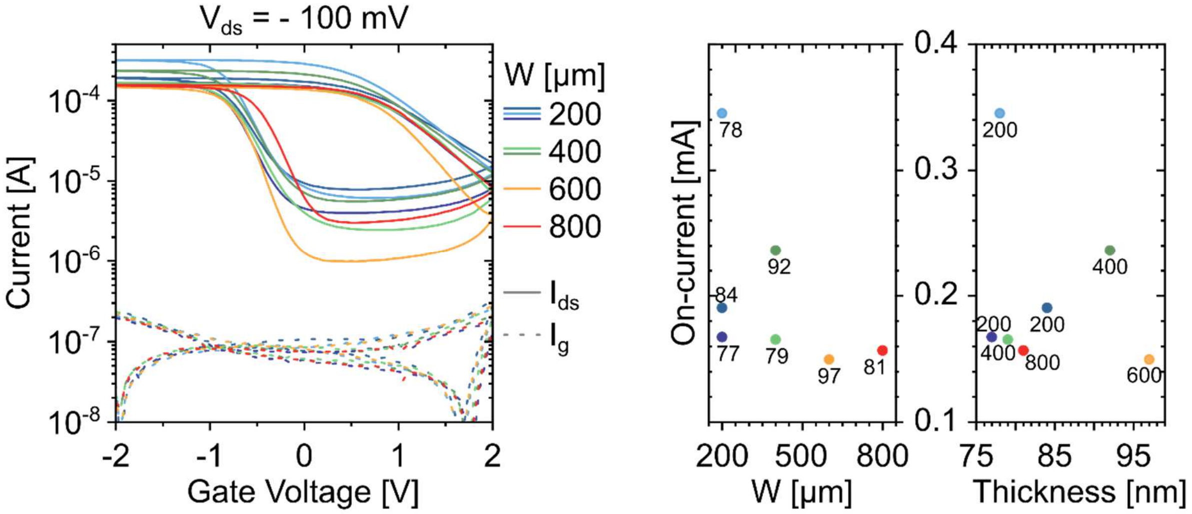

***Figure 6.11**: Transfer characteristics of VEGTs at $V_{ds} = -100$ mV with different areas of CNT deposition defined by the edge length of the printed squares W (left) and evaluation of the respective on-currents with respect to the edge length of the printed film (middle) and the CNT film thickness (right). The data point labels given in the middle and on the right refer to the thickness in nm and W in µm, respectively.*

Next, devices with different film thicknesses were fabricated with an electrode overlap area of 0.04 mm^2 and 0.01 mm^2. As the channel length should directly depend on the film thickness *d*, a decrease of current was expected with increasing *d*. Devices with CNT films of less than 50 nm very often resulted in source–drain shorts, most probably due to penetration of the upper gold electrode through the thin CNT network. This value was thus determined as the minimum film thickness and films of up to 600 nm were prepared by consecutive printing of several layers. Two observations could already be made based on the transfer characteristics depicted in **Figure 6.12**: The on-currents decreased with increasing thickness as expected and for layers of more than 300 nm a significant increase in hysteresis was observed. The hysteresis may be attributed to electron traps created by water molecules that were introduced during the printing process in ambient conditions.[402] Although the devices were annealed at 300 °C in nitrogen atmosphere prior to spin-coating of the ion-gel, residual water may still be present especially in thick CNT films. In contrast to the lateral transistors presented in chapter 5, charge transport takes place through the whole three-dimensional CNT film as the electric double layer forms around each nanotube. In the lateral devices, charge transport only occurred at the interface of the CNTs with the dielectric and thus an increased thickness reduced the influence of water trapped on the substrate surface. Additionally, the material consumption was directly proportional to *d* and it was therefore advisable to reduce the film thickness but keep the film thick enough to prevent source–drain shorts. Extracting the on-current densities for both electrode overlap areas showed the expected decrease but also revealed a saturation for films thicker than 200 nm. It was also observed that the current densities were deviating for the two different electrode widths for thin films while they were almost the same for thicker ones. This was a first hint that transport might not only occur completely vertical through the device as will be discussed in section 6.4.

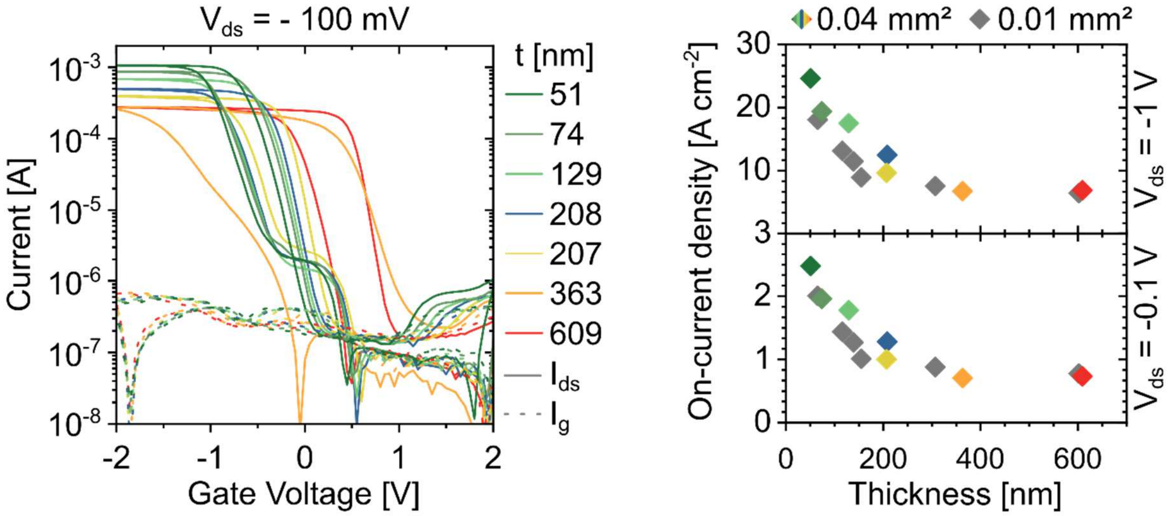

Figure 6.12: *Thickness-dependent transfer characteristics for CNT films of 51 to 609 nm thickness with an electrode overlap of 0.04 mm^2 (left) and evaluation of respective on-current densities also for an electrode overlap of 0.014 mm^2 at source drain biases of −0.1 V and −1 V (right).*

Varying the electrode overlap area from 47 x 50 µm^2 to 140 x 500 µm^2 was used to further investigate the influence of the lateral device dimensions. For a constant top electrode width W_d, the on-currents increased with increasing bottom electrode width as expected. The on-current densities however followed the opposite trend and decreased with an increasing bottom electrode width W_s from more than 70 A cm^{-2} to less than 20 A cm^{-2} at a source–drain bias of −1 V (see **Figure 6.13**). Moreover, the current density for samples with a wider top electrode (140 µm) was always smaller when comparing devices with the same bottom electrode width. The CNT dispersion used for printing these devices contained some metallic CNT species as evident from the off-current plateau which was above the gate leakage. The off-currents at low source–drain bias were further increased with increasing electrode width as the probability of percolating metallic paths or individual tubes bridging the whole channel increased with a larger electrode overlap area. The large influence of the device dimensions on the on-current densities points towards the large role of non-vertical charge transport pathways which will be discussed in the following section.

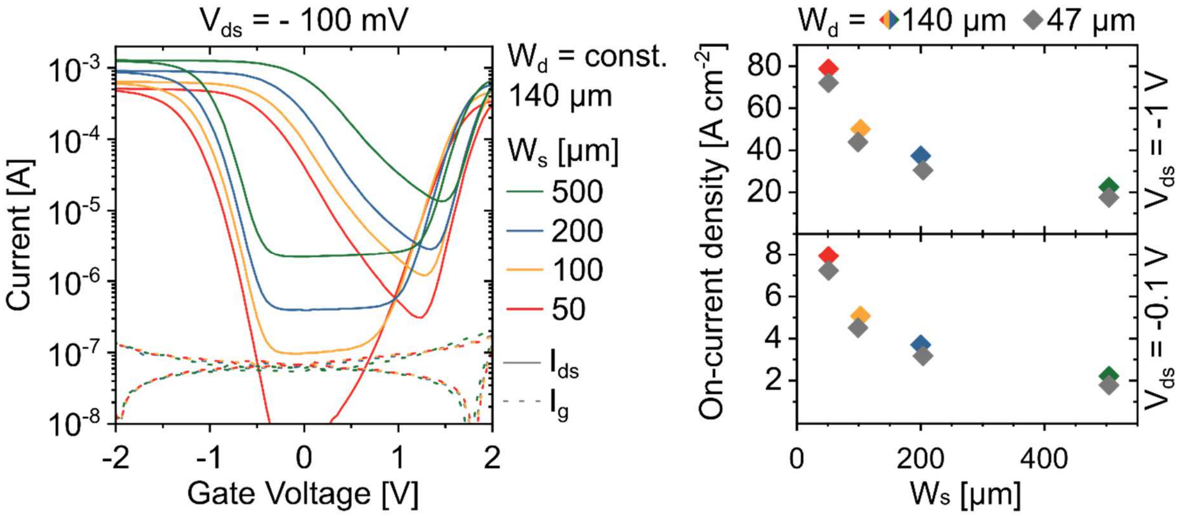

Figure 6.13: Influence of lateral device geometry tested for different electrode overlap areas: Transfer characteristics for different bottom electrode widths W_s from 50 to 500 µm and constant top electrode width W_d of 140 µm (left). Evaluation of on-current densities additionally also for W_d = 47 µm at different source–drain biases of −0.1 V and −1 V (right).

6.4. Lateral Charge Transport Pathways

The thin semiconductor layer in the VEGTs is supposed to strongly favor charge transport in the vertical direction from the source to the drain electrode. However, the transport along CNTs is much faster than inter-nanotube charge transfer. Here, relatively long tubes of about 1 µm were used. These should also enable charge transport pathways at the edges of the electrodes with only a small number of nanotube–nanotube junctions involved. **Figure 6.14** depicts the possible lateral pathways for charge carriers that were present in the vertical transistors as a consequence of the device design. In general, a lateral current I_{ws} that depended on the width of the bottom electrode W_s could be distinguished from I_{wd} that was related to the top electrode width W_d.

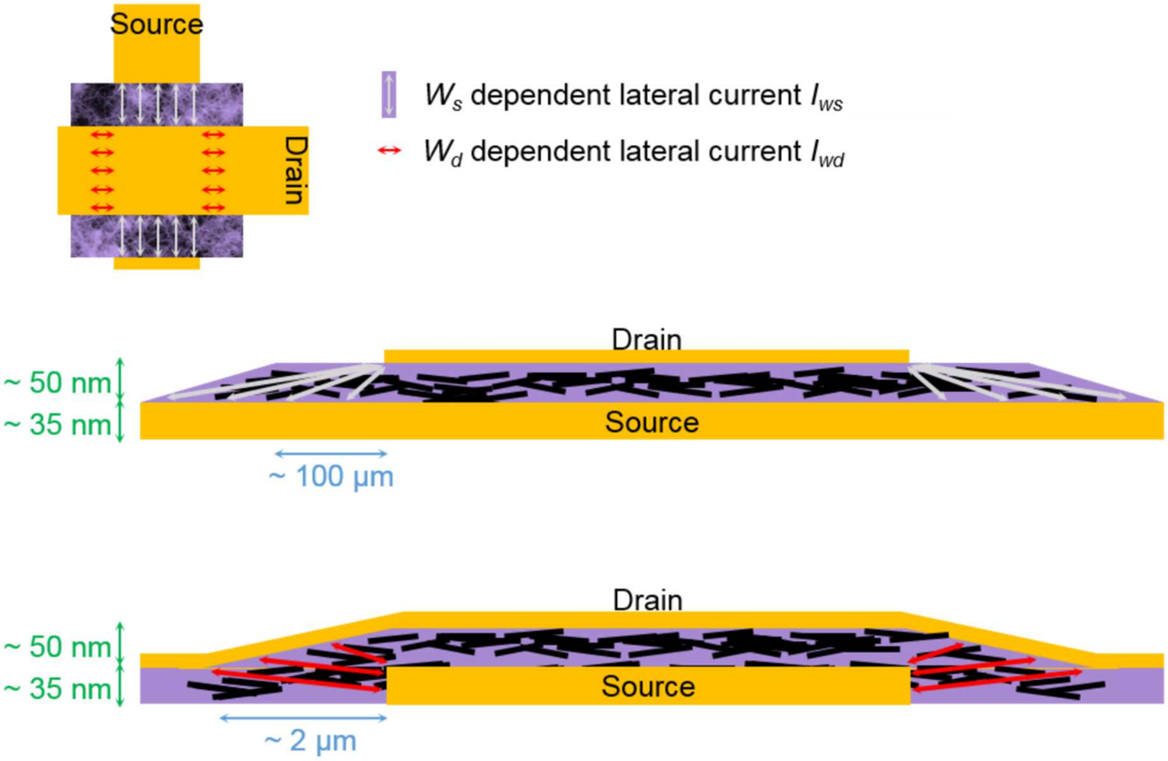

***Figure 6.14**: Depiction of possible lateral current pathways in top view (top) and cross-sectional views for I_{ws} (middle) and I_{wd} (bottom).*

Charge transport occurred at the edge of the top electrode through the CNT film towards the bottom electrode. The current pathway from the edge of the bottom electrode towards the top electrode that was directly evaporated on the CNT film was especially short as profilometer data of the electrodes and the CNT film revealed (see **Figure 6.15**). At the electrode edge, the CNT film followed the gold slope within 2 µm lateral distance and directly created a lateral transistor with a rather short channel length and a width of W_d.

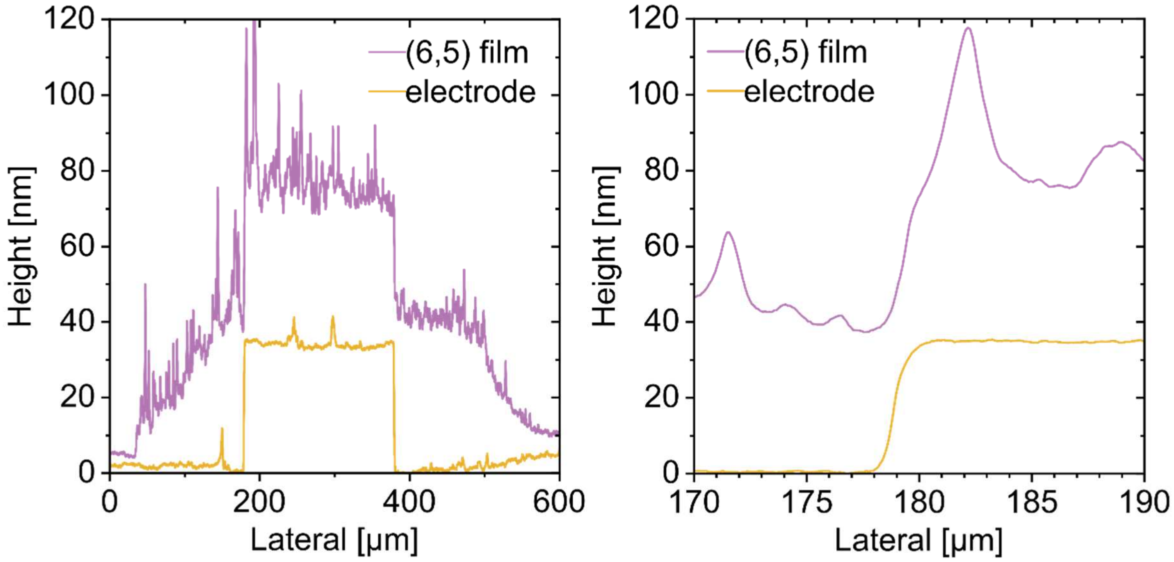

***Figure 6.15**: Height profiles of gold electrode and CNT film (left) with a zoom in at the edge (right) showing the short lateral channel (~2 µm) at the edge of the bottom electrode.*

Assuming the existence of both lateral current pathways, the total current through the device was composed of three parts: The area dependent vertical current I_{area} as well as the 2 lateral components:

$$I_{ds} = I_{area} + I_{ws} + I_{wd}$$

The currents along these 3 channels depended on the device dimensions W_d and W_s where c_i are constants:

$$I_{area} = c_a \cdot W_d \cdot W_s$$

$$I_{wd} = c_d \cdot W_d$$

$$I_{ws} = c_s \cdot W_s$$

For a larger dataset, different source–drain bias were taken into account by evaluating the on-conductance G rather than the on-currents using

$$G = I_{ds} \cdot V_{ds}^{-1}$$

and thus resulting into the following equation for the total current:

$$G = c_a \cdot W_d \cdot W_s \cdot V_{ds}^{-1} + c_d \cdot W_d \cdot V_{ds}^{-1} + c_s \cdot W_s \cdot V_{ds}^{-1}$$

When one of the lateral dimensions (W_d or W_s) is constant, the equation for the on-conductivity becomes linear with respect to W_d (or W_s) with a slope of m_s (m_d) and offset of t_s (t_d):

$$G = (c_a \cdot W_s + c_d) \cdot V_{ds}^{-1} \cdot W_d + c_s \cdot V_{ds}^{-1} \cdot W_s = m_s \cdot W_d + t_s \qquad \text{for} \qquad W_s = \text{const.}$$

$$G = (c_a \cdot W_d + c_s) \cdot V_{ds}^{-1} \cdot W_s + c_d \cdot V_{ds}^{-1} \cdot W_d = m_d \cdot W_s + t_d \qquad \text{for} \qquad W_d = \text{const.}$$

Linear extrapolation of this data towards $W_d = 0$ µm ($W_s = 0$ µm) resulted in values of the on-conductance for the respective W_s (W_d) as shown in **Figure 6.16**.

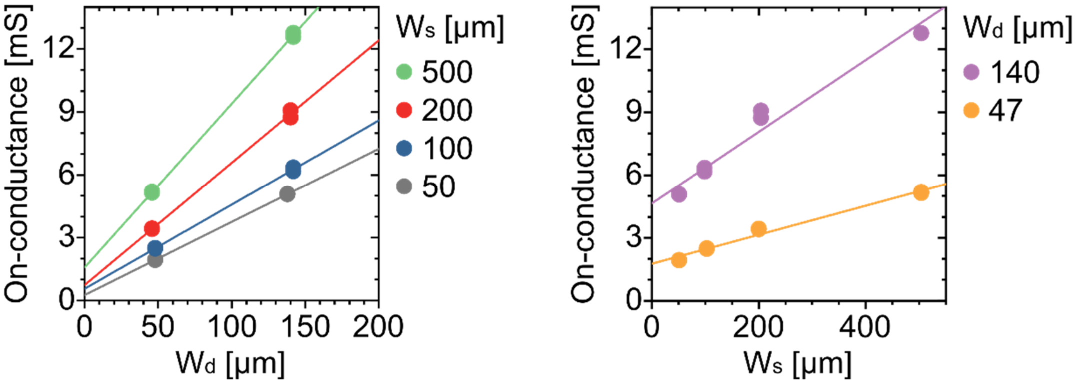

Figure 6.16: *Linear extrapolation of on-conductance towards zero electrode width:* W_d*-dependent (left) and* W_s*-dependent (right)*

The y-intercepts were then plotted *vs* the width of the other electrode, *i.e.* W_s or W_d (see **Figure 6.17**). Here the origin of the plot was fixed to (0|0) for the linear fit, as at zero electrode width for both, top and bottom electrode, no current should flow. From the slope of the linear fits, the on-conductance solely depending on W_s (W_d) and thus the lateral conductance per micrometer electrode width was determined as $G_s = 3.8$ µS µm^{-1} and $G_d = 36$ µS µm^{-1}. The significantly higher value determined for the W_d–dependent conductance supports the existence of a very short lateral channel presumed from the profilometer data as explained above. Comparing these to the overall currents through the VEGTs, the share of lateral currents varied between 10 % for small electrodes, *i.e.* 47 x 50 µm^2, to up to 49 % for the largest measured electrodes of 142 x 500 µm^2. Despite these possibly large contributions by the lateral currents, they did not adversely influence the device performance. The lateral currents could even be exploited by minimizing the width of the bottom electrode while utilizing broad top electrodes and thereby taking advantage of I_{wd}. As the circumference of this configuration is larger compared to a square electrode overlap with the same area, the current density is maximized. Additionally, the off-currents increased with increasing electrode overlap area due to the increased probability of metallic paths. An increased on/off-ratio could hence be achieved with smaller active areas as the currents through metallic CNTs did not significantly contribute to the on-currents. Although a certain degree of three-dimensionality in the nanotube network was assumed from earlier experiments, the high impact of lateral currents showed that there still was a high number of CNTs with more or less planar orientation. Charge transport then favors lateral current pathways with a minimum of necessary hops to bridge the distance in between source and drain electrode.

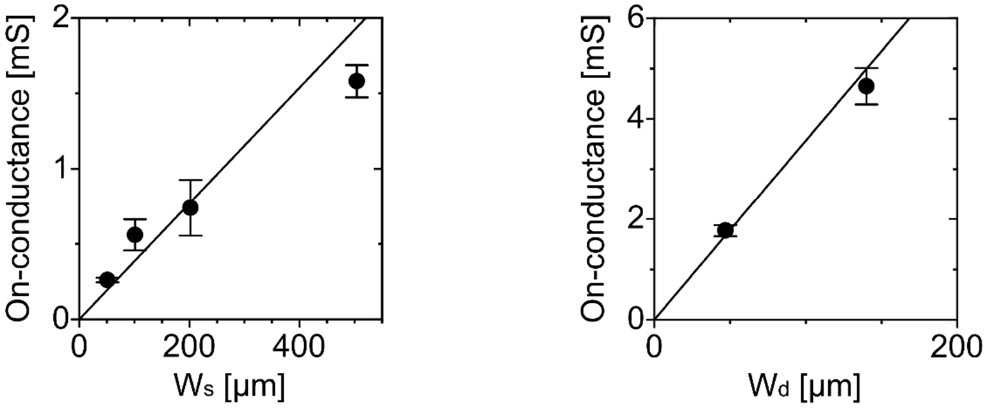

***Figure 6.17**: On-conductances at W_d = 0 µm vs W_s (left) and W_s = 0 µm vs W_d (right) including linear fits. The error bars were derived from the error of the y-intercept in Figure 6.16.*

6.5. Comparison to Lateral Transistors

The vertical electrolyte-gated transistors showed on/off-ratios exceeding 10^4 and high on-currents. Additionally, they exhibited a significantly smaller footprint than lateral electrolyte-gated (6,5) CNT transistors that showed comparable on-currents (compare **Figure 6.18**). A typical lateral transistor with interdigitated electrodes, channel lengths of 2 to 5 µm, required an active area of around 0.9 mm^2 to reach an on-conductance in the range of 10 mS. The same values were reached in the vertical architecture with a much smaller area of 0.16 mm^2 already including a 100 µm alignment margin on all sides of the channel area. The actual active area was only 0.04 mm^2. For printed electrodes, the lateral structure would need even more space, as the channel length and electrode width would increase due to limited printing resolution (compare chapter 7). Furthermore, the channel width would need to be increased to compensate the larger channel length and thus lower on-currents. The vertical structure was estimated to be smaller by at least a factor of 10 considering these necessary alterations. The consumed material – estimated from the film volume – was similar for the devices compared here: Using a CNT film thickness of 5 to 10 nm for lateral FETs, the CNT film volume was 4500 to 9000 µm^3, compared to around 8000 µm^3 for a 51 nm thick nanotube film in the VEGT. The necessary CNT volume for the VEGTs could be further decreased by reducing the alignment margin.

With respect to device performance, subthreshold swings of less than 200 mV dec^{-1} and onset-voltages of less than 1 V were observed for both device structures. One drawback of the vertical architecture were the increased gate currents that were mostly attributed to ionic conductance between the source/drain and gate electrodes and capacitive charging. The gate currents could probably be further reduced by optimizing the exact device geometry especially with respect to the gate electrode. While the lateral FETs were driven with a 2.4 mm^2 large side-gate, the VEGTs were controlled by a common side-gate pad for all 14 transistors on one substrate that had a total area of around 19 mm^2. Adjustment of the gate size, reduction of the distance between gate and channel (which was around 1.7 mm) and addressing each transistor with an individual gate are proposed measures to tackle this effect. Considering the integration density of printed devices, the vertical architecture is promising even before taking into account the possibility of all-printed devices that will be discussed in the following section.

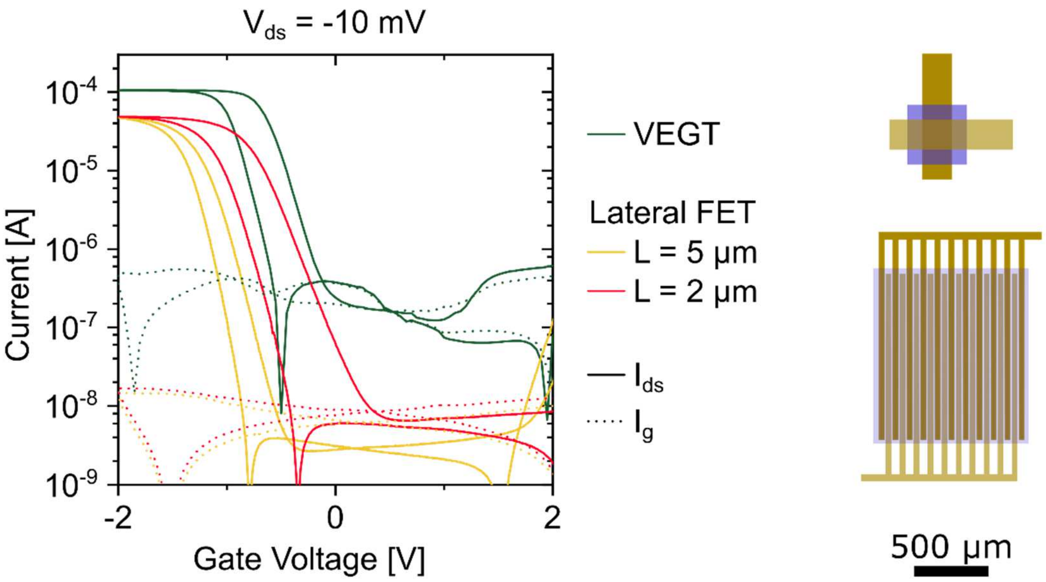

***Figure 6.18**: Comparison of device characteristics (left) and layouts (to scale) of a VEGT and an interdigitated lateral FET (right).*

6.6. All-Printed VEGTs

So far, only the semiconducting layer, *i.e.* (6,5) CNTs, was deposited by aerosol-jet printing while the electrodes were evaporated and the ion-gel was spin-coated. While printed ion-gels with similar ionic liquids were reported before,[255] spin-coating was maintained to avoid the additional optimization process. Other methods such as blade-coating, dip-coating, or spray-coating are possible alternative deposition methods for the integration of ion-gels in a roll-to-roll process. Three different materials were evaluated for printed electrodes: mixed metallic/semiconducting carbon nanotubes (TUBALL) deposited with an airbrush system through shadow masks, aerosol-jet printed silver nanoparticles and inkjet printed gold nanoparticles (see optical micrographs in **Figure 6.19**). For all architectures, the (6,5) CNTs were AJ printed as described before, while a film thickness of 150 to 250 nm was used to compensate the potential roughness of the bottom electrode and avoid shorts with the upper electrode. The electrodes were deposited with the same parameters before or after deposition of the semiconductor followed by the necessary annealing steps.

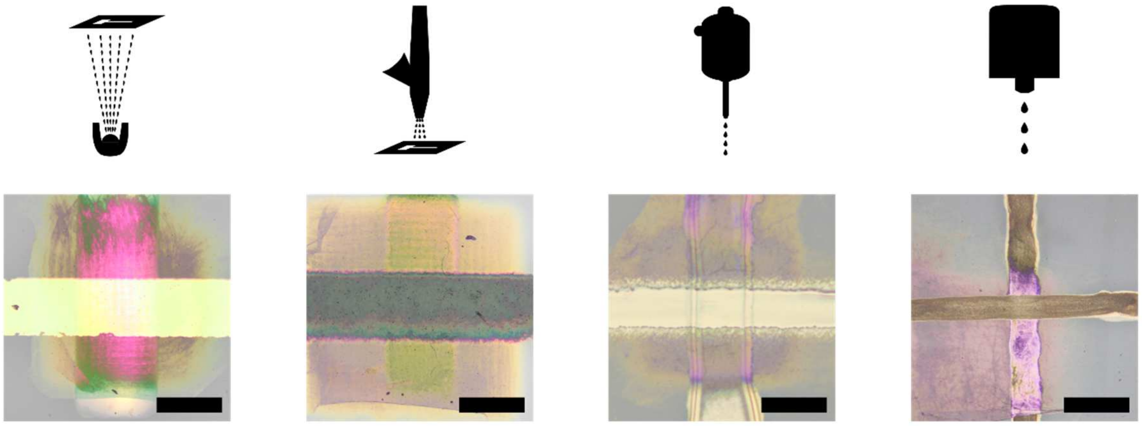

***Figure 6.19**: Optical micrographs of VEGTs with different electrode deposition methods and materials: Evaporated gold, airbrushed TUBALL nanotubes, AJ printed silver nanoparticles, and inkjet printed gold nanoparticles (left to right). All images were recorded prior to spin-coating the ion-gel on top of the devices. Scale bars are 200 μm.*

6.6.1. Airbrush-sprayed Mixed Carbon Nanotube Electrodes

The commercially available TUBALL material is a mixture of rather long (> 5 μm) metallic and semiconducting single-walled carbon nanotubes. It is produced on a large scale at low cost and thus excess material is not a problem. Hence, large area deposition via airbrush spraying and structure definition with stainless steel shadow masks was sufficient. The raw material was dispersed by multiple sonication steps in an aqueous sodium cholate solution (see chapter 3 for details). Centrifugation and filtration removed undispersed material such as large bundles and amorphous carbon. The dispersion was diluted and directly used for spraying with a commercial airbrush system onto the substrates through shadow masks that were fixed to a home-built stage. The stage was heated to 140 °C for quick drying and moved with respect to the airbrush nozzle to homogenize material deposition. The final active area was near the center of the substrate and thus uniformly covered with TUBALL nanotubes. For each sprayed substrate and layer, 2 mL of the diluted dispersion were used and resulted in an approximately 250 nm thick nanotube film (see **Figure 6.20** for profilometer data). An overnight soaking step in deionized water was used to remove the sodium cholate after deposition. Although only shadow masks were used to define the electrode structure, SEM images (see **Figure 6.20**) revealed a sharp but not straight edge of the electrode. (6,5) CNTs were aerosol-jet printed onto the bottom electrode resulting in films with a similar thickness to ensure complete and hole-free coverage of the rough film before the top electrode was deposited in similar fashion as the bottom electrode. Shadow masks with openings of 100 and 200 µm were used and the resulting electrodes were about 10–20 % wider than that. SEM images of the stack of mixed / (6,5) / mixed nanotubes showed a higher charging of the semiconducting nanotubes during image acquisition. This enabled the discrimination of the (6,5) CNTs that appeared brighter in the images than the darker mixed nanotubes that contained metallic species (see **Figure 6.20**).

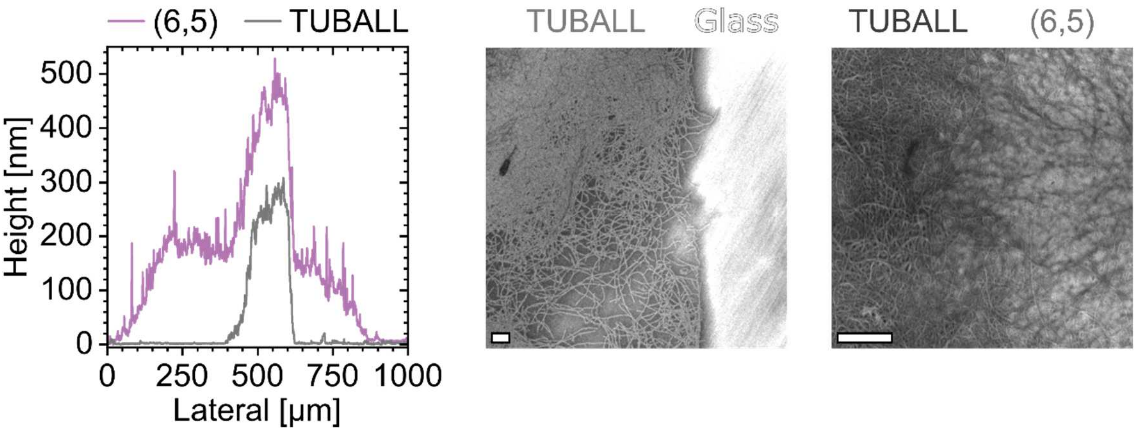

***Figure 6.20**: Height profiles of the TUBALL electrode (grey) and the (6,5) CNT film (purple) illustrating a complete coverage (left). SEM images of TUBALL bottom electrode on glass exhibiting a sharp edge (middle) and TUBALL top electrode on (6,5) CNTs distinguishable by increased charging of the semiconducting nanotubes (right). Scale bars are 1 µm.*

Although the TUBALL nanotubes exhibited sheet resistances of less than 100 Ω □$^{-1}$, voltage drops along the leads still influenced the device performance, as shown by the much lower drain currents. Additionally, as shown in **Figure 6.21**, the conductivity was also modulated by the gate voltage which was tested by directly spraying the top and bottom electrode on top of each other without any semiconducting layer between. This was expected due to the relatively large number of semiconducting nanotubes in the TUBALL electrodes. Although the TUBALL-VEGTs clearly showed gate modulation of the drain currents, their performance was far from usable and not at all comparable to those with evaporated gold electrodes.

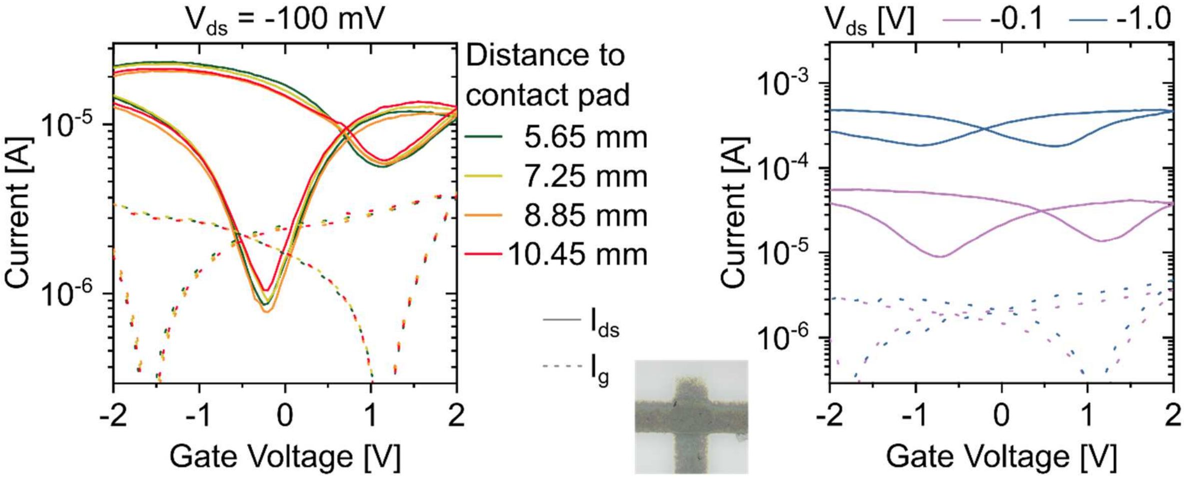

***Figure 6.21**: Transfer characteristics of TUBALL / (6,5) CNTs / TUBALL VEGTs showing a slight dependence on the lead length at $V_{ds} = -0.1$ V (left). Modulation of a TUBALL-TUBALL junction by V_g without any semiconductor (right). The small inset shows a micrograph of this junction with 200 µm wide TUBALL lines.*

6.6.2. Aerosol-jet Printed Silver Nanoparticle Electrodes

To overcome especially the low currents in all-nanotube devices, a silver nanoparticle ink was investigated as an electrode material. The commercial ink (details in section 3.2.2) was aerosol-jet printed as received and electrodes were formed by several passes over a single line. The resulting structures were 100 to 200 µm wide and had a mean thickness of around 70 to 80 nm. As the printing process was not completely optimized, large drying edges occurred with a height of up to 1.5 µm (see **Figure 6.22**). The ink consisted of silver nanoparticles and required an annealing step to form a completely connected conductive film. In order to stay at low temperatures to maintain the possibility to fabricate the devices also on flexible substrates, a long overnight annealing step at only 130 °C was used here. A negative influence of the drying edges on the device performance was avoided by printing a 150 to 200 nm thick (6,5) CNT layer which even covered the high edges with a hole-free and dense nanotube network as evident from the transfer characteristics. Note that the profilometer scans were performed on the completed devices before spin-coating the ion-gel and at different positions along the electrode. As the electrode width varied significantly, the depicted scans of bottom electrode and (6,5) CNT film do not match each other. The electrode edges were still visible in the profilometer data acquired on top of the

CNT film. Nevertheless, the optical micrographs suggested a complete coverage of the bottom electrodes.

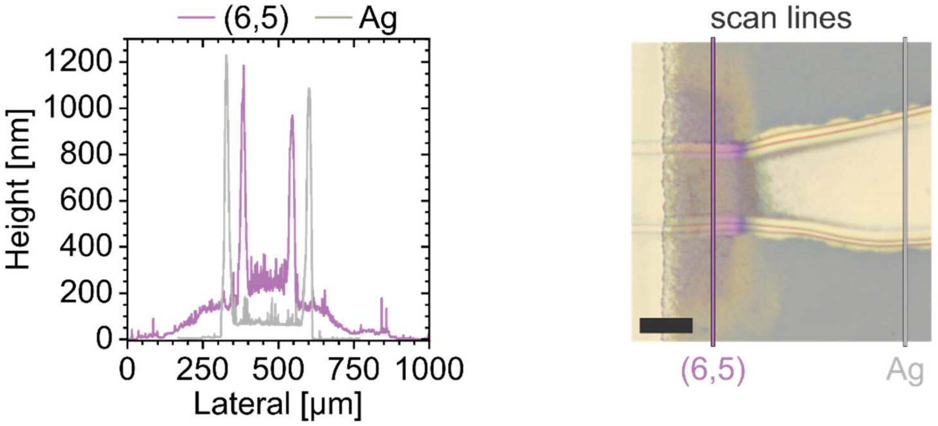

Figure 6.22: *Height profiles showing the large drying edges of the silver ink (grey) that were nevertheless covered with (6,5) CNTs (purple). Note, that the electrode drying edges varied in width and height as seen in the optical micrograph with indicated profilometer scan lines (right). The scale bar in the optical micrograph is 100 µm.*

The current–voltage characteristics of these devices again showed an off-current plateau caused by residual metallic nanotubes even at a very low source–drain bias of −1 mV (see **Figure 6.23**). The on/off-ratio was limited by the off-current and values above 10^3 could only be reached at low V_{ds}. At increased source–drain bias, the transistor showed on-currents of more than 100 mA, *i.e.* on-current densities of up to 570 A cm^{-2}, were realized at $V_g = -2$ V and $V_d = -1$ V. The high currents were attributed to an increased active area due to the drying edges, better wetting behavior of the aerosol-jet printed ink compared to the thermally evaporated gold, and a thicker electrode that was less prone to cracks and discontinuities. The turn-on time of the transistors was relatively short, but complete de-doping – even at slightly positive gate voltages – again required more than 10 minutes. A possible reason for a slow response are the rather small applied electric fields at a relatively large distance between gate and active area. Additionally, the sponge-like nanotube film that is only accessible from the sides can hinder fast ion movement.

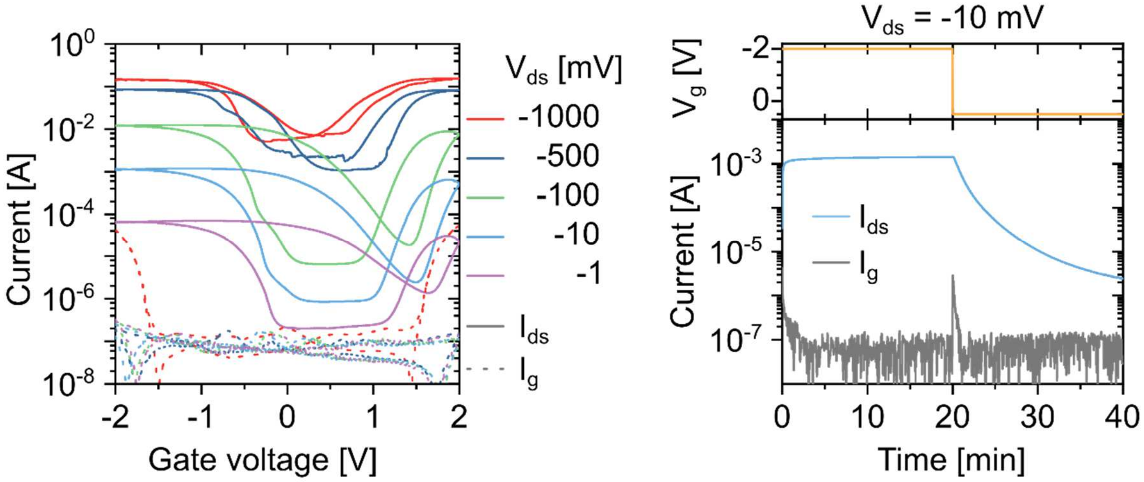

***Figure 6.23**: Transfer characteristics of printed Ag / (6,5) CNTs / printed Ag VEGTs for source–drain biases of −1 mV to −1 V (left). On/off switching cycle of a VEGT at V_{ds} = −10 mV showing the fast response to V_g = −2 V (on) and slow response over 30 min to V_g = 0.5 V (off).*

6.6.3. Inkjet-printed Gold Nanoparticle Electrodes

Besides good wettability for closed CNT films and good contact between semiconductor and electrode, the contact resistance significantly affects the device performance. The contact resistance at the metal–nanotube interface was found to be lower for gold than silver.[153] Gold was thus examined as a third printed electrode material that exhibits a suitable work function. The number of printable gold nanoparticle inks is limited and not all inks are suitable for all printing methods. Inkjet printing of a commercial ink was thus chosen as a direct-write approach to define both, top and bottom, electrodes of the VEGTs. The gold nanoparticle ink was based on a mixture of water and ethylene glycol and a stage temperature of 60 °C was chosen to dry the ink on the substrate before the deposition of the subsequent layer. The complete contact structure was inkjet printed, *i.e.* the source and drain electrode with a width of around 100 µm, the leads with a width of 375 µm, the gate electrode, and the contact pads. After printing the bottom electrodes, a sintering step at 155 °C for several hours was necessary to reduce the overall resistance. The (6,5) CNT film was printed as described previously before the top electrodes together with the side gate electrode were printed. The increased width of contact pads and leads as well as the relaxed resolution needed for these structures enabled a single layer printing process using 5 nozzles in parallel to deposit a 200–300 nm thick gold film with a low sheet resistance of about 3 $\Omega\ \square^{-1}$. For the electrodes at the active area, *i.e.* where top and bottom electrode overlapped, a defined width of around 100–200 µm was required to fabricate VEGTs comparable to the devices presented before. Thus only a single nozzle was used and 5 parallel lines were printed resulting in an electrode width of 80–100 µm. Printing of 10 layers reduced the resistance of this fine part of the electrode but led to a thickness of up to 1.2 µm with a rather rough surface (see profilometer data in **Figure 6.24**). The subsequently printed (6,5) nanotube film nevertheless completely covered the sintered gold and prevented any shorts between top and bottom electrode. Although the surface of the nanotube film reproduced the roughness of the bottom electrode, the equally thick gold printed on top formed a conductive electrode as evident from current–voltage characteristics. The CNT film thickness was estimated from the height differences between a scan on the bottom electrode next to the active area and a scan over the (6,5) CNT film next to the top electrode. The resulting data gave a rough estimation of the local thickness but nevertheless depicted the variation of the film thickness and large roughness of the CNT layer (see **Figure 6.24**). The average film thickness calculated from this data was approx. 130 nm and mostly exceeded 100 nm on top of the bottom electrode.

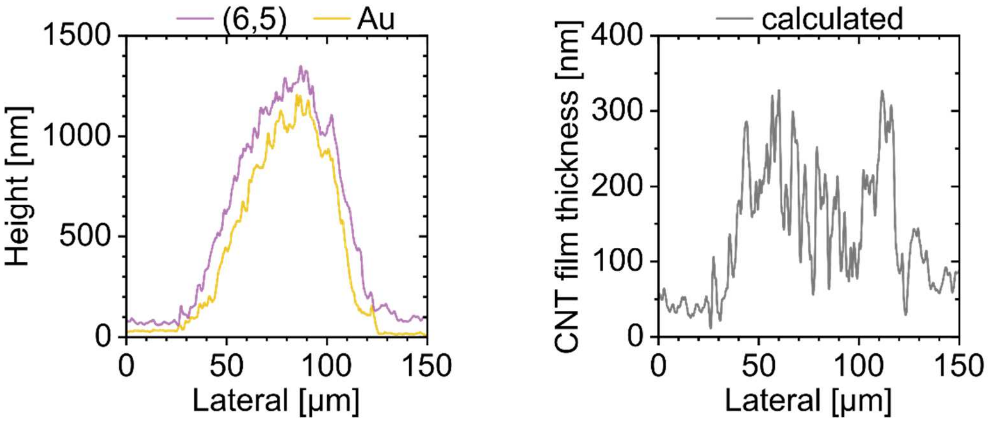

***Figure 6.24**: Height profiles of the bottom Au electrode and the (6,5) CNT film on top of it (left) and the CNT film thickness calculated from the height difference between those two scans (right). Note that the scans could not be performed at the exact same spot.*

The VEGTs completed by ion-gel spin-coating showed no traces of metallic nanotubes as their off-currents decreased below the gate leakage for source–drain biases of −10 and −100 mV. Transfer characteristics at higher V_{ds} revealed electron transport resulting in the typical ambipolar behavior (see **Figure 6.25**). Although the data shown here were acquired under dry nitrogen atmosphere, the ambipolar transport persisted upon exposure to air as shown in section 7.2. The hysteresis of the devices was remarkably low, especially when compared to the other printed electrode materials shown above. The difference between the turn-on voltage of the forward and reverse sweep was around 200 mV at $V_{ds} = -100$ mV for all devices measured with an integration time of 0.1 s and a gate voltage step size of 50 mV. Repeated switching from the on-state ($V_g = -1.5$ V) to the off-state ($V_g = +1.5$ V) and *vice versa* illustrated the fast response time within less than 1 s while maintaining an on/off-ratio of more than 300, mainly limited by the gate-leakage. The maximum on/off-ratio at $V_{ds} = -100$ mV even exceeded 10^4. In contrast to the previously used structures, the distance to the side-gate was slightly increased while its area was significantly decreased thus it cannot be the cause of the faster response. One of the most likely reasons for the slow response observed before was the ion movement within the sponge-like nanotube film. The thick and thus relatively heavy top gold contact might have compressed the CNT network and thus limited the length of connected pores into the film. It is however almost impossible to gain any insight into the actual network without high-resolution three-dimensional imaging such as electron tomography. Due to the non-transparent gold film on top of the device it was also not possible to perform the Raman measurements as in chapter 6.2. Although truly three-dimensional gating and thus charge transport might be limited in these all-printed structures, the device performance was still remarkable especially with respect to the footprint of the active area.

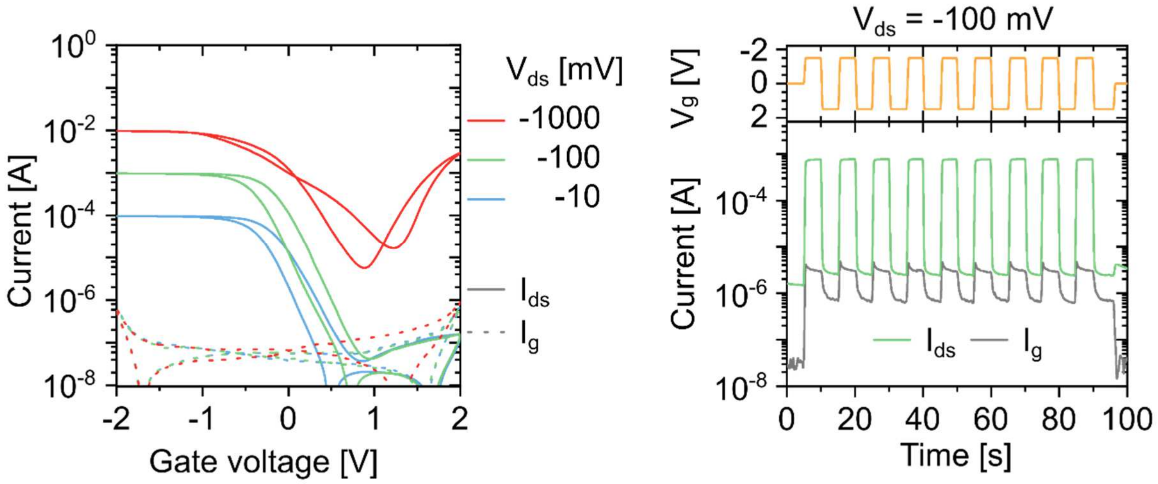

***Figure 6.25**: Transfer characteristics of printed Au / (6,5) CNTs / printed Au VEGTs for source–drain bias of −10 mV, −100 mV, and −1 V (left). On/off switching cycles of the VEGT at $V_{ds} = -100$ mV show the fast response to on- and off-switching at $V_g = \pm 1.5$ V.*

6.6.4. Comparison of the Different Electrode Materials

A comparison between printed and evaporated gold electrodes illustrates the superior performance of the inkjet printed gold nanoparticle films. The different fabrication methods resulted in varying sizes of the geometric electrode overlap, the lead length and the distance between side-gate and channel area. The measured device characteristics are hence only comparable to a limited extent. The current density referring to the electrode overlap could at least exclude the influence of the size of the active area (see **Figure 6.26**). However, the lateral current pathways and thus the electrode edges also influenced the total current as discussed in section 6.4. The measured on-currents nevertheless reflected the same qualitative trends. The on-current densities of printed gold electrodes exceeded those of evaporated material by about one order of magnitude. The evaporated electrodes could be limited by the thin (20–30 nm) top contact. Additionally, the increased roughness of the printed electrodes results in an underestimation of the actual device area. Using the bulk resistivity of gold (22 nΩ m),[423] the calculated total electrode resistance for these samples was around 50–100 Ω. The thin gold layer on the rough CNT surface possibly exhibited discontinuities leading to an actual electrode resistance higher than the calculated values.

The more than 1 µm thick printed gold film was however unlikely to suffer from discontinuities and the thereby increased resistance. Conductivity measurements across the whole length of the inkjet printed gold electrodes revealed a total resistance on the order of 10–100 Ω. In the off-state of the transistor, this accounted for a comparably low fraction of the overall device resistance. However, in the on-state, the lead resistance might eventually be limiting the on-currents as the total resistance of the device in the on-state was around 100 Ω.

Devices fabricated with aerosol-jet printed silver electrodes exhibited the highest current-densities among the tested materials. While the total electrode length for all gold electrodes was around 15 mm, the printing pattern for aerosol-jet printed silver was optimized to minimize the lead length to about 1.5 mm in total. Although the resistance could not be measured on those samples, it was expected to be significantly lower based on reported values of aerosol-jet printed silver lines exhibiting a resistivity of less than 100 nΩ m.[345, 424] Assuming a cross-section of 50–100 μm^2 based on the profile of the silver electrode the resulting resistance of the silver leads was in the order of 1–10 Ω and thus about one order of magnitude lower than that of the inkjet printed gold leads. Here, only the complete devices – including the differences in geometric dimensions – could be compared. It would be necessary to optimize the printing processes of all electrode materials to fabricate geometrically identical devices for a comparison of the different CNT–metal interfaces and their influence on the device performance.

The poorest performance was observed for the nanotube electrodes airbrushed from TUBALL dispersions. One major drawback of mixed nanotube electrodes might be the limited contact area between electrode-nanotubes and semiconducting CNTs which was observed before.[425] Additionally, the sheet resistances were significantly higher than those of the other materials used here which led to an overall lead resistance of up to several kΩ and a significant voltage drop across the leads of the device. The resulting current densities were almost two orders of magnitude lower than for evaporated gold electrodes. The maximum current density achieved in the on-state was 0.05 A cm^{-2}, compared to 1.7 A cm^{-2} for evaporated gold, each measured at $V_{ds} = -100$ mV.

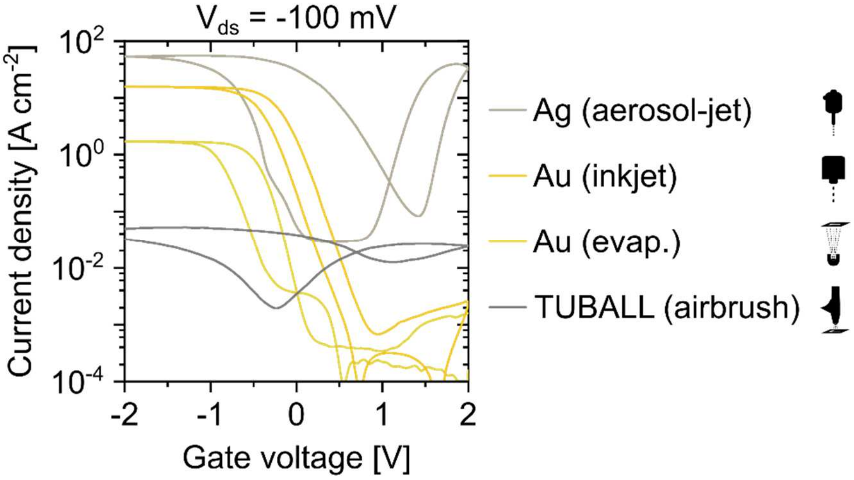

***Figure 6.26**: Current density (I_{ds} divided by electrode overlap area) at $V_{ds} = -100$ mV of VEGTs with different electrode materials: Aerosol-jet printed silver, inkjet printed gold, evaporated gold, and airbrushed TUBALL nanotubes (highest to lowest on-current density).*

As the printed films outperformed the vacuum-deposited gold reaching 15.8 A cm^{-2} and 55.6 A cm^{-2} for gold and silver, respectively, they were compared further. The two printed metal nanoparticle inks showed an almost constant conductivity in the on-state at negative V_g for a source–drain bias of −10 mV to −1 V. The devices with silver electrodes surpassed the VEGTs with printed gold by a factor of 4–5 (see **Figure 6.27**). However, they also exhibited an increased conductivity in the off-state, especially at $V_{ds} = -1$ V. The highest on-conductivities were reached at $V_g = -2$ V with 6.9 S mm^{-2} and 1.6 S mm^{-2} for silver and gold electrodes, respectively. As discussed before, the conductivity in the on-state was most probably limited by the lead resistance which was significantly smaller for the silver electrodes due to the device design with very short contacts. The output characteristics (see **Figure 6.27**) showed a linear behavior for low source–drain voltages for both devices. Besides identical lead dimensions, a thorough analysis of contact resistances would require either different channel lengths with identical three-dimensional networks, or voltage probes within the channel. As both options are hard to realize with the vertical device structure, no reliable information about the contact resistance can be given here. Furthermore, the printed metal films could form a film partly wrapping around nanotubes at the top electrode. This increased contact area was shown to be beneficial to reduce the contact resistance.[153] Considering the bottom electrode, the increased roughness – compared to the evaporated metals – might additionally improve charge injection by electric field enhancement.

While short lead lengths (< 2 mm) were used for printed silver electrodes, applications in all-printed devices beyond individual transistors require longer interconnects. The printed gold electrodes however exhibited lead lengths of more than 15 mm. The so far limiting resistances along the gold leads could be overcome by increasing the lead width or thickness. The inkjet printed gold electrodes were hence chosen for flexible, all-printed carbon nanotube transistors that will be investigated in the next chapter.

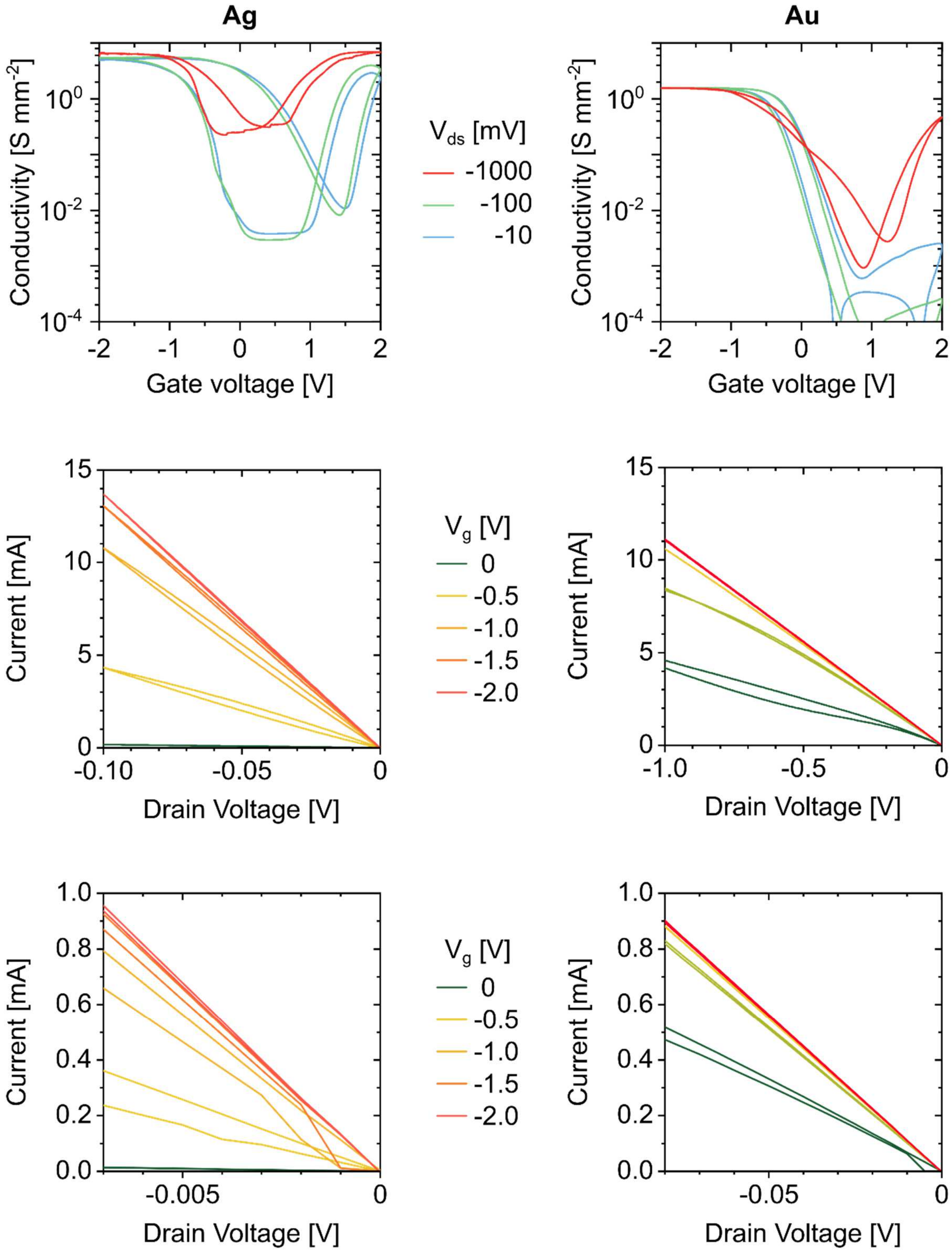

***Figure 6.27**: Comparison of printed silver (left) and gold (right) electrodes: Area-normalized conductivity at different source–drain bias (top) and output characteristics (middle, bottom: zoom-in). Note the different drain voltage scales for silver and gold electrodes.*

CHAPTER 7

FLEXIBLE TRANSISTORS

In this chapter vertical and lateral all-printed CNT transistors are fabricated on flexible substrates and their performance is evaluated with respect to bending.

This chapter contains yet unpublished results. The gold nanoparticle electrodes used here were inkjet printed by M. Held (group of Dr. G. Hernández-Sosa at KIT, Karlsruhe, Germany).

7.1. Introduction

Over the past few years it has been shown that carbon nanotubes can be integrated in flexible and even stretchable devices while still largely maintaining their good charge transport properties (see section 2.3.2). CNTs were printed with various methods, *e.g.* inkjet and gravure printing, and incorporated into devices. In this work, the reproducibility of aerosol-jet printed CNTs in field-effect transistors was studied (see chapter 5). The vertical device architecture presented in chapter 6 utilized electrolyte-gating, a method that was also previously used in various flexible devices.[148, 149, 151, 152, 233, 234, 239, 255, 277] Furthermore, printed electrodes were introduced with this structure. It should thus be possible to create all-printed, flexible devices by combining these methods and transferring the manufacturing processes to a flexible substrate.

Flexible vertical device architectures demonstrated previously relied on advanced manufacturing techniques and are not compatible with printing processes.[426-429] Additionally, either high voltages were required or low currents were achieved while no gate leakages were reported. In this chapter, vertical and lateral electrolyte-gated transistors with inkjet printed gold electrodes, an aerosol-jet printed CNT semiconductor, and drop-cast ion-gels on flexible plastic substrates are presented. The two device architectures with identical materials are compared with respect to their footprint at similar on-conductances, switching behavior in inert and ambient atmosphere as well as their response to repeated bending.

7.2. Vertical and Lateral CNT Transistors Directly Printed on Plastic Substrates

The all-printed VEGTs presented in section 6.6 were prepared on polyethylene naphthalate (PEN) foils (thickness 125 µm) cut into 20x25 mm^2 pieces, *i.e.* the same substrate size as the glass used before. The PEN foil is stable at temperatures below 160 °C and resists at least temporary exposure to solvents such as isopropanol, toluene, and THF. It is thus compatible with the temperatures required during printing (up to 100 °C) and annealing (155 °C) and can withstand the chemicals used for cleaning, printing, and subsequent rinsing. In addition to the vertical devices, lateral electrolyte-gated transistors (LEGTs) were fabricated and analyzed. The sample layout for both structures is depicted in **Figure 7.1**. The gold electrodes were inkjet printed with a subsequent annealing step while the (6,5) nanotubes were aerosol-jet printed followed by careful rinsing with THF and IPA in each case. 10 layers of CNTs were printed from an initial ink concentration of 3.0 mg L^{-1} to reach a thickness of around 150 nm for the VEGTs. The LEGT electrodes were covered with 2 layers printed from the same CNT dispersion at a concentration of 1.5 mg L^{-1}. The printing pattern in both cases was a rectangular grid with a line-spacing of 25 µm thus ensuring a dense network over the whole channel area. The channel length of the lateral devices was around 50 µm as defined by the distance between the gold electrodes. The relatively large channel length was chosen to prevent source–drain shorts due to ink spills or uneven edges. For the vertical transistors, the channel length was defined by the CNT film thickness and thus around 130 nm as discussed in section 6.6. The ion-gel was drop-cast instead of spin-coated on top of the devices after annealing for at least 1 hour at 150 °C under nitrogen atmosphere.

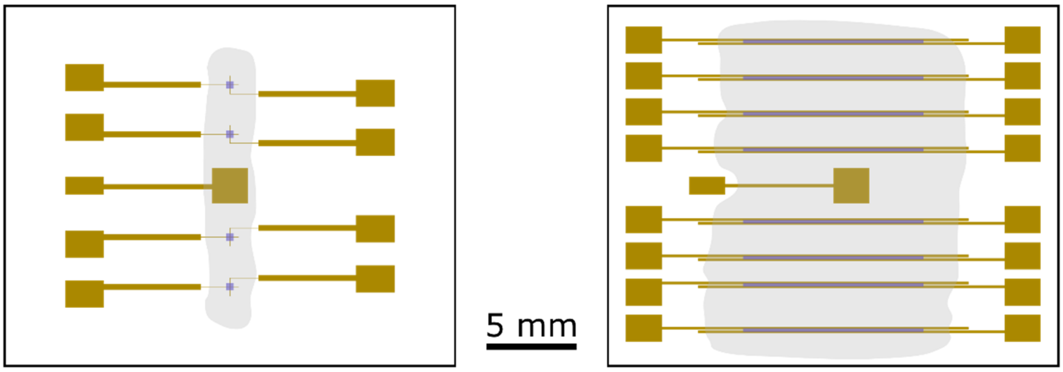

***Figure 7.1**: Sample layout for vertical (left) and lateral (right) electrolyte-gated transistors on flexible PEN substrates. The printed CNTs are colored purple and the drop-casted ion-gel is grey.*

For the electrical characterization of the initial transistor properties, the devices were kept within nitrogen atmosphere, but had to be exposed to air for bending experiments later (see section 7.3). Both device architectures showed comparable device performances as evident from the transfer characteristics (see **Figure 7.2**). The on-currents for holes were within the same order of magnitude, *i.e.* (9.6 ± 0.3) mA and (6.2 ± 0.4) mA were obtained at $V_{ds} = -1$ V for VEGTs and LEGTs, respectively. The off-currents were on average around 100 nA for VEGTs and twice as high for the lateral architecture which might be explained by the larger ion-gel and electrode areas leading to increased ionic and capacitive currents in the device. Although the LEGTs showed a lower turn-on voltage (50 to 450 mV) for the sweep from the off- towards the on-state, the variations between individual transistors and the hysteresis were larger. The VEGTs showed almost identical transfer characteristics with a turn-on voltage of 550 mV measured at $V_{ds} = -100$ mV. It should be noted that the hysteresis decreased after repeated measurement of the transfer characteristics in inert atmosphere for all devices. **Figure 7.2** illustrates this for representative transistors with the 1st set of measurements shown together with the 5th or 3rd set of measurements for the same VEGT or LEGT, respectively. The depicted transfer characteristics were measured with the same settings, *i.e.* an integration time of 0.1 s and gate voltage steps of 0.05 V, while different gate voltage steps and integration times were used between these measurements. The hysteresis was further decreased during subsequent measurements that were performed in air after storing the devices under nitrogen atmosphere overnight (compare **Figure 7.4**).

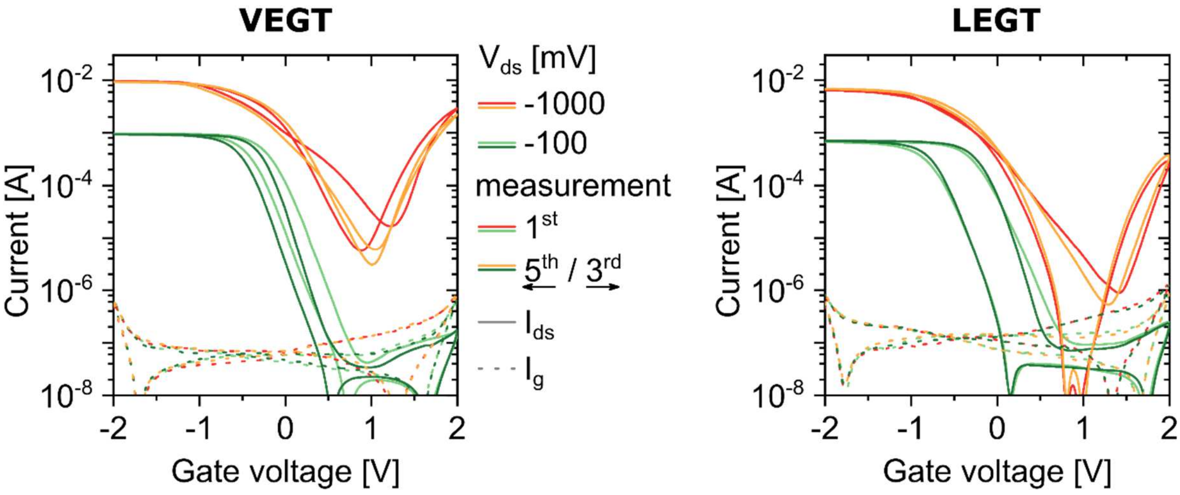

Figure 7.2*: Representative transfer characteristics of a VEGT (left) and an LEGT (right) at a source–drain bias of −100 mV and −1000 mV. For both devices, the 1st measurement is shown (red and light green) together with the 5th (VEGT) or 3rd (LEGT) measurement of a transfer characteristics (yellow and dark green) performed with the same settings, illustrating the decrease of hysteresis after repeated measurements.*

The response of the device to the applied gate voltage in electrolyte-gated devices generally depends on the sweep rate as the velocity of the ion drift within the ion-gel is limited. The transistors closest to the gate pad were measured at $V_{ds} = -100$ mV with different gate voltage steps ΔV_g of 0.01 V to 0.1 V to evaluate the influence of the sweep rate (see **Figure 7.3**). Both devices exhibited basically unchanged turn-on voltages for all sweep rates. With larger gate voltage steps the turn-off of the transistor shifted towards more positive gate voltages and the hysteresis increased significantly. Remarkably, the hysteresis was generally lower for the vertical architecture. Even a measurement with a gate voltage step of 0.5 V resulted in clearly visible switching of the device, although with further increased hysteresis. The on-currents were reproducible for all gate voltage step widths while the off-currents increased slightly due to higher gate leakages caused by capacitive charging. Although the smallest used ΔV_g resulted in the least hysteresis, the duration of a single measurement was around 10 min for these settings. For further experiments a step size of 0.05 V was chosen as compromise between hysteresis and duration of the measurement.

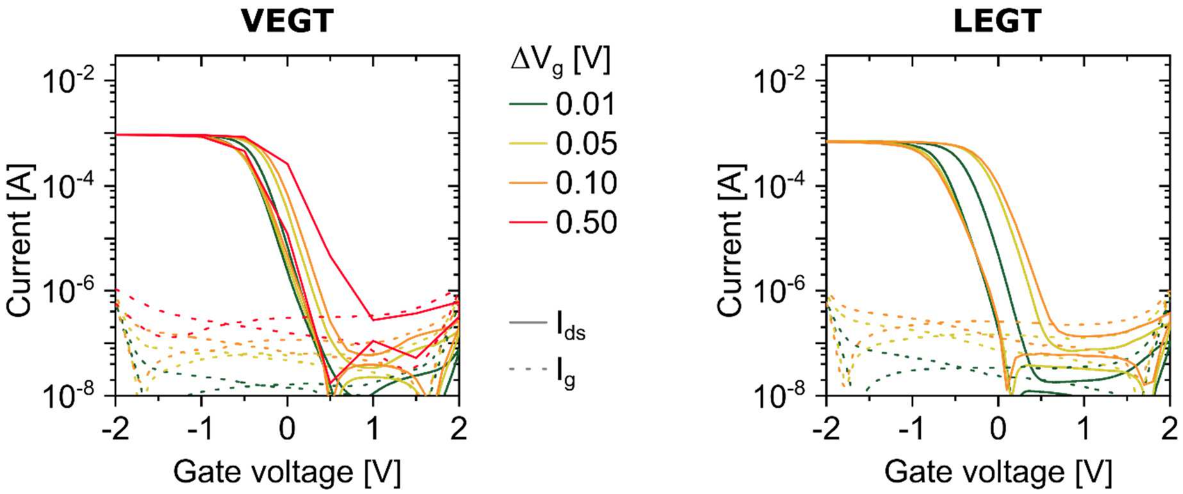

***Figure 7.3**: Transfer characteristics depending on the gate voltage step width (0.01 V to 0.5 V, green to red) acquired for the VEGT (left) and LEGT (right) closest to the gate pad at $V_{ds} = -100$ mV.*

Both types of electrolyte-gated transistors were able to reach on-currents of several mA while maintaining an off-current level in the μA regime. It should thus be possible to drive light-emitting diodes (LEDs) with these transistors, as the required currents are in the same range even for large area display backplanes.[430] For visualization of the switching process the source and drain contacts were connected in series with a red LED. Due to the voltage drop across the diode, a total external potential of −2.5 V was applied. **Figure 7.4** shows the resulting transfer characteristics with on-currents around 5 mA. During a gate voltage sweep, the intensity of the LED could be tuned from completely on to completely off. The LED was slightly brighter at $V_g = -2$ V when driven by the VEGT due to the higher on-currents. As the LEGT exhibited higher electron currents for positive gate voltages, the diode also turned on partly at $V_g = +2$ V. This example demonstrates that both architectures of printed electrolyte-gated transistors can supply sufficiently high currents to drive light-emitting diodes.

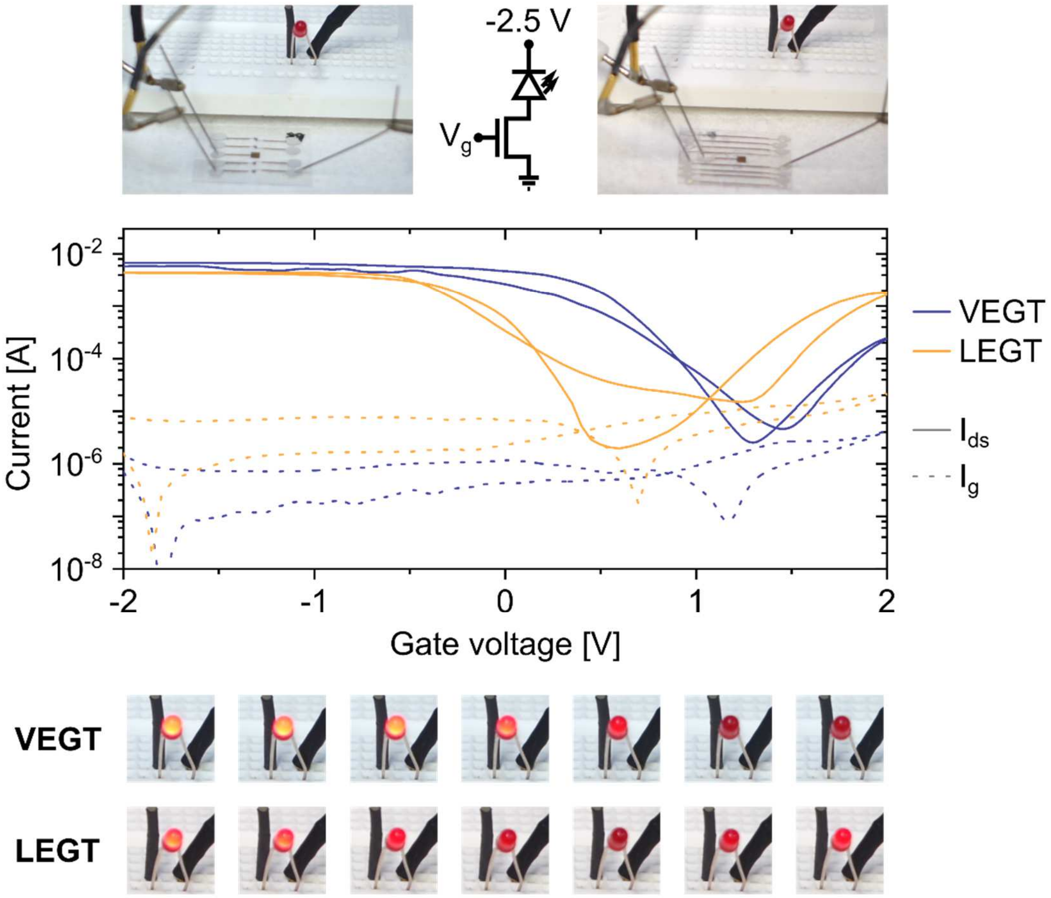

Figure 7.4: *Printed electrolyte-gated transistors used to drive a red LED: Photographs of the setup (top) for VEGT (left) and LEGT (right). The transfer characteristics (middle) were recorded during the measurement with a drive bias of -2.5 V according to the circuit diagram (top middle). The photographs at the bottom show the status of the LED during a single gate voltage sweep from* $V_g = -2$ *V to* $V_g = +2$ *V.*

7.3. Bending Vertical and Lateral EGTs

The response towards deformation of devices printed on PEN substrates was investigated by bending the samples around metal rods with different diameters. The substrates were fixed with tape and/or clamps and the electrodes were contacted via needles on micro-positioners. This ensured a good contact and reliable bending radii which were extracted from the rod diameter. The given bending radius R of the active transistor does not take into account the negligible thickness of the PEN substrate (125 µm). The transistors were exposed to air for at least 4 days before starting the measurements. While the transfer characteristics did not show any significant differences to those measured in dry nitrogen, the gate currents of the LEGTs were increased by one order of magnitude (compare **Figure 7.2** and **Figure 7.5**). Although the PEN substrate is mechanically flexible, plastic deformation at bending radii of less than 2 mm was observed and thus limited the minimal bending radius. While the bending direction does not play a role for VEGTs, it was chosen to be perpendicular to the channel for the lateral transistors. The electrode geometry thus prevented complete and uniform bending of the LEGTs around rods with a radius of less than 5 mm.

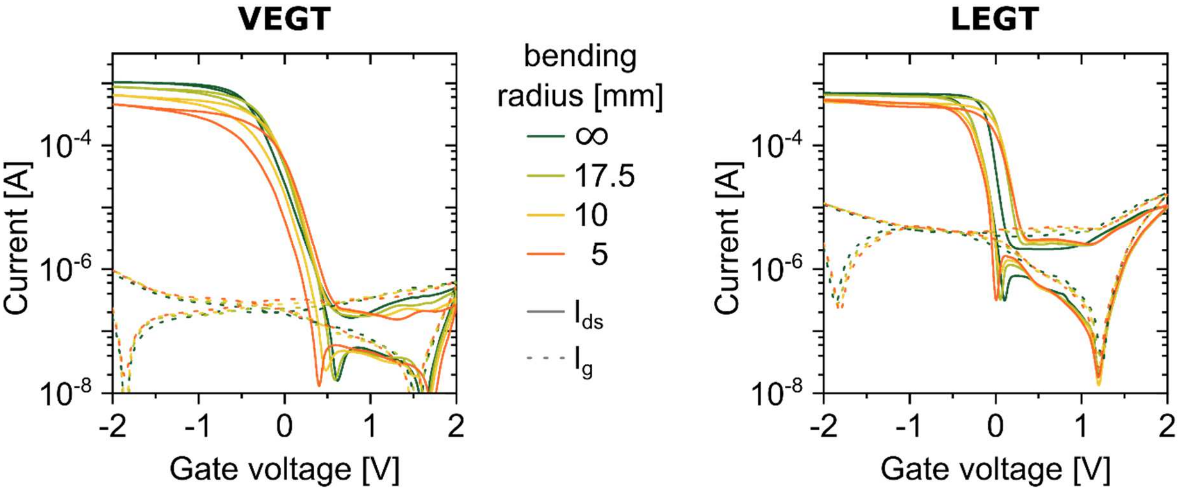

Figure 7.5: Transfer characteristics at $V_{ds} = -100$ mV of a VEGT (left) and LEGT (right) at different bending radii compared to the unbent sample (green, ∞).

For both architectures, an increase of hysteresis and a decrease of the on-currents were observed with decreasing bending radius, but the LEGTs seemed to be slightly less affected by the deformation. Regarding the LEGTs, a shift towards more positive gate voltages of the forward sweep (−2 V → +2 V) during bending at $R = 17.5$ mm occurred and remained thereafter. In contrast to that, the reverse sweep (+2 V → −2 V) shifted continuously with decreasing R towards more negative V_g and thereby increased the hysteresis in VEGTs. However, the on-currents also decreased (compared to the measurement performed at $R = 5$ mm) with a subsequent measurement in the unbent position while the hysteresis remained unchanged (see **Figure 7.6**). It should be noted that the sequence of measurements was from the unbent status towards smaller bending radii. The measurement of 10 consecutive transfer characteristics at $R = \infty$ also resulted in continuously decreasing on-currents yet constant hysteresis. Hence, the previously observed changes in on-currents cannot be reliably attributed to the bending of the devices but might also be a degradation effect of the devices during repeated measurements in air.

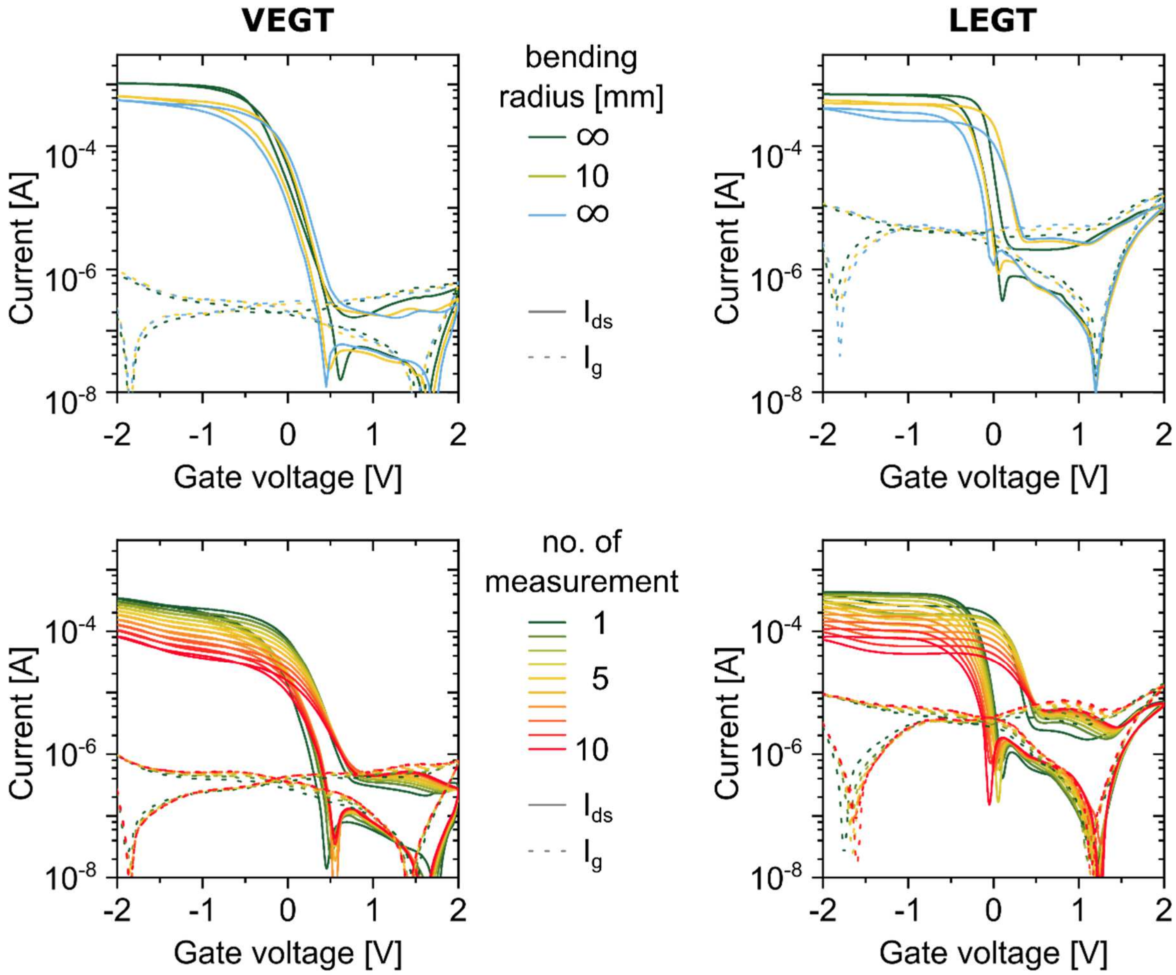

Figure 7.6: *The influence of repeated measurements of transfer characteristics at* $V_{ds} = -100$ *mV for a VEGT (left) and an LEGT (right) can be seen when returning to a flat substrate after bending (top) as well as in consecutive measurements of the same device without bending (bottom).*

In addition to stable device performance at different bending radii, it is also important that the devices can withstand repeated bending. The VEGTs were thus bent automatically from $R = \infty$ to $R \approx 5$ mm and measured in the flat position at the beginning and after 100 and 1000 cycles. The same experiment was repeated for the LEGTs with measurements after 100 and 680 cycles. The lower cycle number here originates from a detachment of the sample from the machine used for bending during the experiment. The transfer characteristics exhibited a constant hysteresis for all devices (see **Figure 7.7**) and successively decreasing on-currents for the LEGTs. Measurements at $V_{ds} = -1$ V overall showed a current decrease by a factor of 2 for hole as well as electron transport. The VEGTs however exhibited increasing on-currents and a slight shift of the entire transfer curve towards more positive gate voltages. Measurements at higher source-drain bias reproduced the same trend with additionally increasing electron current at positive gate voltages. The overall increased currents might originate from a deformation of the CNT film, *e.g.* decreased thickness, thus shortening of the effective length of charge-transport paths through the vertical channel. Additionally, doping by oxygen and water from ambient air might increase during bending and thus cause these effects.[431, 432] Overall, the observed changes were relatively small with an average increase of the on-currents by a factor of 1.3 and a shift of the turn-on voltages of 150 mV. Especially the vertical architecture seems to be almost unaffected by repeated bending, however, the issue of decreasing currents with repeated measurements remains to be solved. As this phenomenon only occurred during measurements in air, encapsulation of the device might already be sufficient.

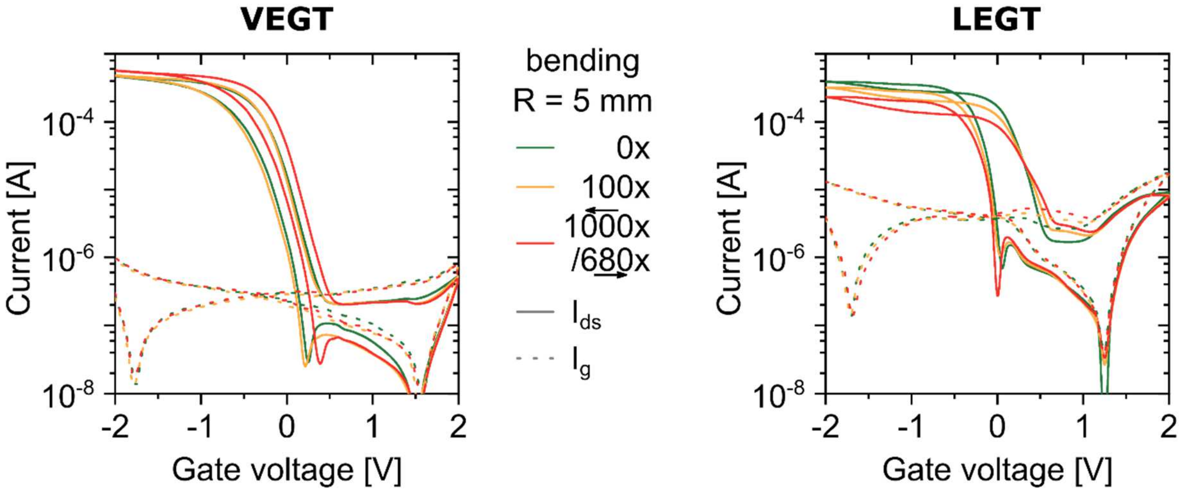

***Figure 7.7**: Change of transfer characteristics at $V_{ds} = -100$ mV for repeated bending to a radius of 5 mm for a VEGT (left) and an LEGT (right). The measurements were performed in the unbent position before (green) and after 100 (yellow) and 1000 (VEGT, red) or 680 (LEGT, red) bending cycles.*

Both device architectures exhibited similar properties with respect to the achievable on-currents, operation voltages, and persistence to deformation as shown in this chapter. Depending on the individual measurement, the performance of the lateral or the vertical transistors seemed to be superior with slight advantages for the VEGTs. For fabrication on the flexible PEN substrates, the same materials were used, *i.e.* inkjet printed gold electrodes, aerosol-jet printed (6,5) CNTs, and the drop-cast ion-gel containing [EMIM][FAP] and P(VDF-HFP). While the channel length of the lateral transistors was limited by the inkjet printing process, the relatively thin CNT film enabled high on-currents and a small footprint for the vertical structure. The active area necessary for comparable on-currents in the lateral transistors was around 0.5 mm^2, in contrast to less than 0.01 mm² for the VEGTs. Including the area of electrodes and – in the case of the vertical architecture – the increased area of CNTs to ensure a sufficient alignment margin, the total footprint of the devices was around 0.1 mm^2 and 3.4 mm^2 for VEGTs and LEGTs, respectively. This difference in footprint demonstrates again the potential of the vertical architecture with semiconducting CNTs for all-printed transistors in applications where electrolyte-gating is feasible.

The combination of flexibility, printability, and high on-currents for a small device footprint highlights the advantages of VEGTs compared to earlier reports. Previous lateral transistors with similar on-conductances as the vertical transistors either required photolithographic structuring,[284, 433] or additional processing steps such as CNT transfer and subsequent etching,[220, 433] each in combination with higher operation voltages of 5 to 100 V. Another report on a lateral architecture with a footprint comparable to the printed LEGT relied on transfer of the evaporated gold electrodes from a PDMS stamp onto the flexible substrate to form the short channel lengths of 5 µm necessary to reach the corresponding on-conductances.[434] All-printed devices used either a composite of barium titanate and PMMA or ion-gels to ensure the printability and flexibility of the dielectric layer.[147, 152, 221, 267] While the devices with composite dielectrics showed stable device performances over extended storing periods and up to 1000 measurement cycles, the area-normalized on-conductances were several orders of magnitude lower.[147, 221] Moreover, although the devices were fabricated on flexible substrates, there was either no information about bending experiments at all,[221] or data concerning the device performance with respect to repeated bending was missing.[147] Electrolyte-gated devices were suffering from extremely low on/off-ratios of only 138, [267] or additional nanoimprinting was required to define the electrode printing area more exactly,[152] yet only low on-conductances could be reached. Unfortunately, many reports do not provide information about the change of device performance with respect to bending, especially with respect to repeated bending. However, using photolithographically structured electrodes, inverters that showed an extremely good stability even after bending more than 1000 times to a bending radius as low as 1.27 mm, were demonstrated.[284] Concerning all-printed devices, bending to radii as small as 1 mm was presented without significant change of the transistor characteristics.[147] In conclusion, the here fabricated all-printed VEGTs with gold nanoparticle electrodes, but also the LEGTs, performed extremely well with high on-conductances while being resistant to bending.

CHAPTER 8

CONCLUSIONS AND OUTLOOK

In this chapter the insights gained in this thesis are summarized and an outlook for further experiments and applications based on aerosol-jet printed transistors with CNTs is given.

The goal of this thesis was to establish printed CNT networks as semiconductors in fully printed and flexible transistors. To achieve this goal, aerosol-jet printing was demonstrated to be a versatile tool to create directly patterned films of semiconducting (6,5) carbon nanotubes with variable thickness. These films were successfully incorporated in different field-effect and electrolyte-gated transistors with lateral or vertical charge transport through the semiconductor. Eventually, all-printed transistors were fabricated on plastic substrates and stable performance even after bending stress was observed.

As a first step, the composition of the ink based on polymer-wrapped carbon nanotubes in toluene for aerosol-jet printing was investigated. The addition of terpineol resulted in good printability. However, the influence of varying CNT concentration – and hence slightly altered viscosity – on the aerosolization and deposition process requires further studies. An examination of the stability of the nanotubes during the printing process over time showed that the sonication strength of the ultrasonic atomizer was low enough to avoid damage to the dispersed (6,5) CNTs, but still powerful enough to create a dense aerosol. The observed long-time stability corroborated the suitability of aerosol-jet printing for large-area and reproducible deposition of CNT for electronic devices. The ultrasonic atomizer requires relatively small ink volumes and offers the possibility to test materials that are only available in small quantities and for small sample numbers, it is thus well-suited for lab-scale experiments. The alternative pneumatic atomizer is even gentler and can process larger ink volumes, hence aerosol-jet printing of CNTs is also promising with respect to future upscaling and large area printing.

The aerosol-jet printed films of (6,5) carbon nanotubes were used in an established top-gate field-effect transistor geometry. The achieved reproducibility of dense but thin networks was comparable to previously published results for CNT films prepared from dispersion, *i.e.* by spin-coating, dip-coating, or immersion. An increased thickness of the CNT films resulted in a significantly decreased hysteresis as well as increased mobilities and on-conductance while maintaining low off-currents. Thickness control was achieved by altering the printing pattern and number of layers without changing the ink composition, hence the improved device performance was achieved at the expense of increased processing times and material consumption. Nevertheless, the established printing parameters could be kept basically constant. For sparse CNT networks, aerosol-jet printing resulted in a large variation in local density. With the process developed in this work, a precise control of low CNT coverage was not possible. However, dense films could be produced with variable thickness and also for different carbon nanotube types dispersed in toluene with respective wrapping polymers. Such printed films have already been used in various studies, *e.g.* for electrochromic devices, and are interesting for further applications in printed circuitry and sensing.

For all-printed transistors the resolution and alignment accuracy was considered as the limiting factor. In lateral architectures, *i.e.* with current flow across the channel parallel to the substrate, the achievable conductances are limited by the channel dimensions. While a large channel width increases the total current along with device footprint, short channel lengths are restricted by the printing processes. Based on a recently reported vertical architecture, thick CNT films were printed between a bottom source and an overlapping top drain electrode, resulting in current flow perpendicular to the substrate using electrolyte-gating. The CNT network exhibited a sufficient porosity to enable electrolyte-gating even for overlapping electrode areas with edge lengths of several hundred micrometers. The sponge-like nanotube film and low electric fields resulted in a response time of the transistors in the range of seconds to minutes. Three-dimensional charge transport could be assumed for CNT films with a thickness of up to several hundred nanometers. Aerosol-jet printed (6,5) CNT films with a thickness of 100–200 nm were free of source–drain shorts even for printed electrodes with a large roughness. Although most of the current was transported vertically between source and drain electrode, the electrode edges played an important role as well. Depending on the electrode dimensions, up to almost 50 % of current were conducted across quasi-lateral channels at the electrode edges. However, this observation does not invalidate the usability of the vertical device architecture as the decoupling of critical device dimensions from the printing accuracy was still achieved. Moreover, the vertical transistors outperformed comparable electrolyte-gated lateral short-channel transistors with photographically structured electrodes and printed nanotubes while exhibiting a more than 10-fold smaller footprint.

While the transport within the printed semiconducting layer was fairly reproducible, the measured on-conductance depended strongly on the electrode material (evaporated or printed, metal or mixed CNTs). In addition to the lead resistance and contact at the semiconductor–conductor interface, the actual geometric device dimensions probably had an impact on the overall performance. Especially variations of the dimensions of the channel area, electrode cross-section, and lead length caused by different deposition methods made a one-to-one comparison of the devices difficult or impossible. Moreover, the printing parameters were not entirely optimized for the electrode materials (mixed CNTs or colloidal silver nanoparticles) and drying edges as well as ohmic losses due to the total resistance of the conductors occurred. Nevertheless, aerosol-jet printing of a porous CNT film for vertical electrolyte-gated transistors was found to be compatible with different printed electrode materials. With adapted electrode geometries and printing parameters, fully printed devices should become reproducible and competitive. Optimizing the device design especially with respect to the side-gate dimensions and individual addressing of each transistor will further improve transistor performance. The use of printed electrodes here simplifies the refinement process as pattern changes can be easily implemented and tested.

All-printed vertical and lateral transistors were also manufactured on flexible PEN substrates with inkjet printed gold electrodes. While both device types showed good transfer characteristics, the lateral transistors required a 30 times larger footprint to achieve on-currents comparable to those of vertical transistors. Both architectures were largely resistant to repeated outward bending (tensile strain) but unfortunately showed degradation during measurement in air. The total on-currents were sufficiently high to drive a red LED and outperformed previously reported values for transistors with printed CNTs. However, the devices presented here only showed the proof-of-concept and further experiments are necessary to reveal their full potential. Future work on flexible aerosol-jet printed nanotube transistors should also include inward and outward bending. Furthermore, the device performance should be evaluated after bending along different directions. While it is expected that a potential performance change does not depend on the bending direction for the vertical devices, the lateral transistors might show differences upon bending parallel or perpendicular to the channel. Encapsulation might be helpful to avoid degradation in air and additionally prevent possible detachment of structures from the substrate. The minimum bending radius could be further improved with alternative substrate materials such as silicone elastomers that enable three-dimensional deformation with sub-millimeter bending radii and possibly stretchability.[282] With these substrates, the true limitations especially of VEGTs could also be evaluated. So far, it remains unclear, how tolerant the transistors are to wrinkling, folding, and stretching. The limiting factor for these investigations was the necessity of mechanically stable and conductive electrodes on ultra-flexible and stretchable substrates while nanotube networks are expected to be ideal for all kinds of deformations. Although stretchable conductors have been presented before, the adoption of the respective processes was beyond the scope of this thesis. Preliminary experiments on aerosol-jet printing of CNTs on stretchable substrates already resulted in closed and stable films that were visible to the naked eye. With suitable electrodes, stretchable devices based on aerosol-jet printed nanotubes should thus be feasible.

Within this thesis, the suitability of carbon nanotubes for vertical electrolyte-gated transistors was demonstrated. The response time of the electrolyte-gated, three-dimensional CNT networks presented in this work was too long for high-frequency applications. Optimization of the entire device geometry could however further improve the device performance and enable integrated circuits. Additionally, the compatibility of this architecture to printing processes in combination with electrolyte-gating offers the opportunity for high throughput – and thus low-cost – fabrication of single-use sensors. The high drain-currents that were achieved would simplify the readout. CNTs have already been successfully used for electrostatic biosensing,[158] and similar functionality should be possible for the vertical transistors. Especially for sensing applications, the reproducibility of devices is not as critical as calibration experiments are usually performed prior to the actual measurement.

The already good reproducibility of the performance of aerosol-jet printed CNT transistors could be further improved by ensuring an optimized and steady ink composition. To achieve that, the influence of different ink parameters, *e.g.* material loading, filling level, and viscosity, on the aerosol formation and composition should be further investigated. Continuous monitoring of the ink composition may enable tailored addition of nanotube dispersion or solvents to obtain a constant filling level and ink formulation over extended printing times.

In this work, aerosol-jet printing of semiconducting CNTs for different transistor architectures was demonstrated with promising results even on flexible substrates. Optimized processing and device geometries could further improve the transistor performance. In conclusion, this work represents another step towards the successful utilization of fully printed transistors based on carbon nanotubes for a variety of applications.

BIBLIOGRAPHY

[1] J. Zaumseil, "Single-walled carbon nanotube networks for flexible and printed electronics". *Semicond. Sci. Technol.*, **2015,** *30*, 074001. *https://doi.org/10.1088/0268-1242/30/7/074001*

[2] Q. Cao, S.-J. Han, G. S. Tulevski, A. D. Franklin, W. Haensch, "Evaluation of Field-Effect Mobility and Contact Resistance of Transistors That Use Solution-Processed Single-Walled Carbon Nanotubes". *ACS Nano*, **2012,** *6*, 6471. *https://doi.org/10.1021/nn302185d*

[3] M. Held, P. Laiho, A. Kaskela, F. Gannott, M. Rother, E. Kauppinen, J. Zaumseil, "Dense Carbon Nanotube Films as Transparent Electrodes in Low-Voltage Polymer and All-Carbon Transistors". *Adv. Electron. Mater.*, **2017**, 1700331. *https://doi.org/10.1002/aelm.201700331*

[4] A. G. Nasibulin, A. Kaskela, K. Mustonen, A. S. Anisimov, V. Ruiz, S. Kivistö, ..., E. I. Kauppinen, "Multifunctional Free-Standing Single-Walled Carbon Nanotube Films". *ACS Nano*, **2011,** *5*, 3214. *https://doi.org/10.1021/nn200338r*

[5] B. King, M. Renn, "Aerosol Jet® Direct Write Printing for Mil-Aero Electronic Applications", presented at *Palo Alto Colloquia, Lockheed Martin*, **2009**.

[6] A. Hirsch, "The era of carbon allotropes". *Nat. Mater.*, **2010,** *9*, 868. *https://doi.org/10.1038/nmat2885*

[7] H. W. Kroto, J. R. Heath, S. C. O'Brien, R. F. Curl, R. E. Smalley, "C60: Buckminsterfullerene". *Nature*, **1985,** *318*, 162. *https://doi.org/10.1038/318162a0*

[8] S. Iijima, "Helical microtubules of graphitic carbon". *Nature*, **1991,** *354*, 56. *https://doi.org/10.1038/354056a0*

[9] K. S. Novoselov, A. K. Geim, S. V. Morozov, D. Jiang, Y. Zhang, S. V. Dubonos, ..., A. A. Firsov, "Electric Field Effect in Atomically Thin Carbon Films". *Science*, **2004,** *306*, 666. *https://doi.org/10.1126/science.1102896*

[10] M. Ezawa, "Peculiar width dependence of the electronic properties of carbon nanoribbons". *Phys. Rev. B*, **2006,** *73*, 045432. *https://doi.org/10.1103/PhysRevB.73.045432*

[11] K. Tanaka, K. Ohzeki, S. Nankai, T. Yamabe, H. Shirakawa, "The electronic structures of polyacene and polyphenanthrene". *J. Phys. Chem. Solids*, **1983,** *44*, 1069. *https://doi.org/10.1016/0022-3697(83)90089-6*

[12] E. D. Obraztsova, M. Fujii, S. Hayashi, V. L. Kuznetsov, Y. V. Butenko, A. L. Chuvilin, "Raman identification of onion-like carbon". *Carbon*, **1998,** *36*, 821. *https://doi.org/10.1016/S0008-6223(98)00014-1*

[13] D. Ugarte, "Curling and closure of graphitic networks under electron-beam irradiation". *Nature*, **1992,** *359*, 707. *https://doi.org/10.1038/359707a0*

[14] S. Iijima, M. Yudasaka, R. Yamada, S. Bandow, K. Suenaga, F. Kokai, K. Takahashi, "Nano-aggregates of single-walled graphitic carbon nano-horns". *Chem. Phys. Lett.*, **1999,** *309*, 165. *https://doi.org/10.1016/S0009-2614(99)00642-9*

[15] X. Peng, N. Komatsu, S. Bhattacharya, T. Shimawaki, S. Aonuma, T. Kimura, A. Osuka, "Optically active single-walled carbon nanotubes". *Nat. Nanotechnol.*, **2007,** *2*, 361. *https://doi.org/10.1038/nnano.2007.142*

[16] A. A. Green, M. C. Duch, M. C. Hersam, "Isolation of single-walled carbon nanotube enantiomers by density differentiation". *Nano Res.*, **2009,** *2*, 69. *https://doi.org/10.1007/s12274-009-9006-y*

[17] G. Ao, J. K. Streit, J. A. Fagan, M. Zheng, "Differentiating Left- and Right-Handed Carbon Nanotubes by DNA". *J. Am. Chem. Soc.*, **2016,** *138*, 16677. *https://doi.org/10.1021/jacs.6b09135*

[18] S. Reich, J. Maultzsch, C. Thomsen, P. Ordejón, "Tight-binding description of graphene". *Phys. Rev. B*, **2002,** *66*, 035412. *https://doi.org/10.1103/PhysRevB.66.035412*

[19] R. Saito, G. Dresselhaus, M. S. Dresselhaus, *Physical properties of carbon nanotubes*, Imperial College Press, London **1998**.

[20] S. Reich, C. Thomsen, J. Maultzsch, *Carbon nanotubes: basic concepts and physical properties*, John Wiley & Sons, Weinheim **2008**.

[21] S. Ilani, P. L. McEuen, "Electron Transport in Carbon Nanotubes". *Annu. Rev. Condens. Matter Phys.*, **2010,** *1*, 1. *https://doi.org/10.1146/annurev-conmatphys-070909-103928*

[22] M. Huang, Y. Wu, B. Chandra, H. Yan, Y. Shan, T. F. Heinz, J. Hone, "Direct Measurement of Strain-Induced Changes in the Band Structure of Carbon Nanotubes". *Phys. Rev. Lett.*, **2008,** *100*, 136803. *https://doi.org/10.1103/PhysRevLett.100.136803*

[23] E. D. Minot, Y. Yaish, V. Sazonova, J.-Y. Park, M. Brink, P. L. McEuen, "Tuning Carbon Nanotube Band Gaps with Strain". *Phys. Rev. Lett.*, **2003,** *90*, 156401. *https://doi.org/10.1103/PhysRevLett.90.156401*

[24] G. G. Samsonidze, A. R. Saito, D. A. Jorio, E. Pimenta, F. Souza, F. A. Grüneis, ..., M. Dresselhaus, "The concept of cutting lines in carbon nanotube science". *Journal of Nanoscience and Nanotechnology*, **2003,** *3*, 431. *https://doi.org/10.1166/jnn.2003.231*

[25] J.-C. Charlier, X. Blase, S. Roche, "Electronic and transport properties of nanotubes". *Rev. Mod. Phys.*, **2007,** *79*, 677. *https://doi.org/10.1103/RevModPhys.79.677*

[26] R. Saito, G. Dresselhaus, M. S. Dresselhaus, "Trigonal warping effect of carbon nanotubes". *Phys. Rev. B*, **2000,** *61*, 2981. *https://doi.org/10.1103/PhysRevB.61.2981*

[27] S. Maruyama, 2018, accessed: 11/10/2018, *http://www.photon.t.u-tokyo.ac.jp/~maruyama/kataura/1D_DOS.html*

[28] H. Kataura, Y. Kumazawa, Y. Maniwa, I. Umezu, S. Suzuki, Y. Ohtsuka, Y. Achiba, "Optical properties of single-wall carbon nanotubes". *Synth. Met.*, **1999,** *103*, 2555. *https://doi.org/10.1016/S0379-6779(98)00278-1*

[29] S. M. Bachilo, M. S. Strano, C. Kittrell, R. H. Hauge, R. E. Smalley, R. B. Weisman, "Structure-Assigned Optical Spectra of Single-Walled Carbon Nanotubes". *Science*, **2002,** *298*, 2361. *https://doi.org/10.1126/science.1078727*

[30] S. Lebedkin, F. Hennrich, T. Skipa, M. M. Kappes, "Near-Infrared Photoluminescence of Single-Walled Carbon Nanotubes Prepared by the Laser Vaporization Method". *J. Phys. Chem. B*, **2003,** *107*, 1949. *https://doi.org/10.1021/jp027096z*

[31] R. B. Weisman, S. M. Bachilo, "Dependence of Optical Transition Energies on Structure for Single-Walled Carbon Nanotubes in Aqueous Suspension: An Empirical Kataura Plot". *Nano Lett.*, **2003,** *3*, 1235. *https://doi.org/10.1021/nl034428i*

[32] S. Maruyama, 2018, accessed: 11/10/2018, *http://www.photon.t.u-tokyo.ac.jp/~maruyama/kataura/kataura.html*

[33] M. Rother, S. P. Schießl, Y. Zakharko, F. Gannott, J. Zaumseil, "Understanding Charge Transport in Mixed Networks of Semiconducting Carbon Nanotubes". *ACS Appl. Mater. Interfaces*, **2016,** *8*, 5571. *https://doi.org/10.1021/acsami.6b00074*

[34] J. Maultzsch, H. Telg, S. Reich, C. Thomsen, "Radial breathing mode of single-walled carbon nanotubes: Optical transition energies and chiral-index assignment". *Phys. Rev. B*, **2005,** *72*, 205438. *https://doi.org/10.1103/PhysRevB.72.205438*

[35] A. Jorio, R. Saito, J. H. Hafner, C. M. Lieber, M. Hunter, T. McClure, ..., M. S. Dresselhaus, "Structural (n,m) Determination of Isolated Single-Wall Carbon Nanotubes by Resonant Raman Scattering". *Phys. Rev. Lett.*, **2001,** *86*, 1118. *https://doi.org/10.1103/PhysRevLett.86.1118*

[36] P. C. Eklund, J. M. Holden, R. A. Jishi, "Vibrational modes of carbon nanotubes; Spectroscopy and theory". *Carbon*, **1995,** *33*, 959. *https://doi.org/10.1016/0008-6223(95)00035-C*

[37] F. Dragin, A. Pénicaud, M. Iurlo, M. Marcaccio, F. Paolucci, E. Anglaret, R. Martel, "Raman Doping Profiles of Polyelectrolyte SWNTs in Solution". *ACS Nano*, **2011,** *5*, 9892. *https://doi.org/10.1021/nn203591j*

[38] L. Kavan, L. Dunsch, "Spectroelectrochemistry of Carbon Nanotubes". *ChemPhysChem*, **2011,** *12*, 47. *https://doi.org/10.1002/cphc.201000882*

[39] C. Fantini, A. Jorio, M. Souza, M. S. Strano, M. S. Dresselhaus, M. A. Pimenta, "Optical Transition Energies for Carbon Nanotubes from Resonant Raman Spectroscopy: Environment and Temperature Effects". *Phys. Rev. Lett.*, **2004,** *93*, 147406. *https://doi.org/10.1103/PhysRevLett.93.147406*

[40] C. A. Cooper, R. J. Young, M. Halsall, "Investigation into the deformation of carbon nanotubes and their composites through the use of Raman spectroscopy". *Composites Part A: Applied Science and Manufacturing*, **2001,** *32*, 401. *https://doi.org/10.1016/S1359-835X(00)00107-X*

[41] X. Zhou, J.-Y. Park, S. Huang, J. Liu, P. L. McEuen, "Band Structure, Phonon Scattering, and the Performance Limit of Single-Walled Carbon Nanotube Transistors". *Phys. Rev. Lett.*, **2005,** *95*, 146805. *https://doi.org/10.1103/PhysRevLett.95.146805*

[42] P. R. Bandaru, "Electrical Properties and Applications of Carbon Nanotube Structures". *Journal of Nanoscience and Nanotechnology*, **2007,** *7*, 1239. *https://doi.org/10.1166/jnn.2007.307*

[43] S. Li, Z. Yu, C. Rutherglen, P. J. Burke, "Electrical Properties of 0.4 cm Long Single-Walled Carbon Nanotubes". *Nano Lett.*, **2004,** *4*, 2003. *https://doi.org/10.1021/nl048687z*

[44] M. Brohmann, M. Rother, S. P. Schiessl, E. Preis, S. Allard, U. Scherf, J. Zaumseil, "Temperature-Dependent Charge Transport in Polymer-Sorted Semiconducting Carbon Nanotube Networks with Different Diameter Distributions". *J. Phys. Chem. C*, **2018**. *https://doi.org/10.1021/acs.jpcc.8b04302*

[45] P. N. Nirmalraj, P. E. Lyons, S. De, J. N. Coleman, J. J. Boland, "Electrical connectivity in single-walled carbon nanotube networks". *Nano Lett.*, **2009,** *9*, 3890. *https://doi.org/10.1021/nl9020914*

[46] M. S. Fuhrer, J. Nygård, L. Shih, M. Forero, Y.-G. Yoon, M. S. C. Mazzoni, ..., P. L. McEuen, "Crossed Nanotube Junctions". *Science*, **2000,** *288*, 494. *https://doi.org/10.1126/science.288.5465.494*

[47] M. Stadermann, S. J. Papadakis, M. R. Falvo, J. Novak, E. Snow, Q. Fu, ..., S. Washburn, "Nanoscale study of conduction through carbon nanotube networks". *Phys. Rev. B*, **2004,** *69*, 201402. *https://doi.org/10.1103/PhysRevB.69.201402*

[48] J. Gao, Y.-L. L. Loo, "Temperature-Dependent Electrical Transport in Polymer-Sorted Semiconducting Carbon Nanotube Networks". *Adv. Funct. Mater.*, **2015,** *25*, 105. *https://doi.org/10.1002/adfm.201402407*

[49] M. E. Itkis, A. Pekker, X. Tian, E. Bekyarova, R. C. Haddon, "Networks of Semiconducting SWNTs: Contribution of Midgap Electronic States to the Electrical Transport". *Acc. Chem. Res.*, **2015,** *48*, 2270. *https://doi.org/10.1021/acs.accounts.5b00107*

[50] N. Rouhi, D. Jain, K. Zand, P. J. Burke, "Fundamental Limits on the Mobility of Nanotube-Based Semiconducting Inks". *Adv. Mater.*, **2011,** *23*, 94. *https://doi.org/10.1002/adma.201003281*

[51] G. J. Brady, Y. Joo, M. Y. Wu, M. J. Shea, P. Gopalan, M. S. Arnold, "Polyfluorene-sorted, carbon nanotube array field-effect transistors with increased current density and high on/off ratio". *ACS Nano*, **2014,** *8*, 11614. *https://doi.org/10.1021/nn5048734*

[52] S. P. Schießl, N. Fröhlich, M. Held, F. Gannott, M. Schweiger, M. Forster, ..., J. Zaumseil, "Polymer-Sorted Semiconducting Carbon Nanotube Networks for High-Performance Ambipolar Field-Effect Transistors". *ACS Appl. Mater. Interfaces*, **2015,** *7*, 682. *https://doi.org/10.1021/am506971b*

[53] V. K. Sangwan, R. P. Ortiz, J. M. P. Alaboson, J. D. Emery, M. J. Bedzyk, L. J. Lauhon, ..., M. C. Hersam, "Fundamental Performance Limits of Carbon Nanotube Thin-Film Transistors Achieved Using Hybrid Molecular Dielectrics". *ACS Nano*, **2012,** *6*, 7480. *https://doi.org/10.1021/nn302768h*

[54] Y. Zhao, D. Candebat, C. Delker, Y. Zi, D. Janes, J. Appenzeller, C. Yang, "Understanding the Impact of Schottky Barriers on the Performance of Narrow Bandgap Nanowire Field Effect Transistors". *Nano Lett.*, **2012,** *12*, 5331. *https://doi.org/10.1021/nl302684s*

[55] T. Guo, P. Nikolaev, A. Thess, D. T. Colbert, R. E. Smalley, "Catalytic growth of single-walled manotubes by laser vaporization". *Chem. Phys. Lett.*, **1995,** *243*, 49. *https://doi.org/10.1016/0009-2614(95)00825-O*

[56] A. Thess, R. Lee, P. Nikolaev, H. Dai, P. Petit, J. Robert, ..., R. E. Smalley, "Crystalline Ropes of Metallic Carbon Nanotubes". *Science*, **1996,** *273*, 483. *https://doi.org/10.1126/science.273.5274.483*

[57] O. Smiljanic, B. L. Stansfield, J. P. Dodelet, A. Serventi, S. Désilets, "Gas-phase synthesis of SWNT by an atmospheric pressure plasma jet". *Chem. Phys. Lett.*, **2002,** *356*, 189. *https://doi.org/10.1016/S0009-2614(02)00132-X*

[58] M. R. Predtechensky, O. M. Tukhto, I. Y. Koval, *United States Patent 8137653*, **2012**.

[59] M. R. Predtechensky, O. M. Tukhto, I. Y. Koval, *United States Patent 8551413*, **2013**.

[60] G. D. Nessim, "Properties, synthesis, and growth mechanisms of carbon nanotubes with special focus on thermal chemical vapor deposition". *Nanoscale*, **2010,** *2*, 1306. *https://doi.org/10.1039/B9NR00427K*

[61] Y. Zhang, A. Chang, J. Cao, Q. Wang, W. Kim, Y. Li, ..., H. Dai, "Electric-field-directed growth of aligned single-walled carbon nanotubes". *Appl. Phys. Lett.*, **2001,** *79*, 3155. *https://doi.org/10.1063/1.1415412*

[62] E. Joselevich, C. M. Lieber, "Vectorial Growth of Metallic and Semiconducting Single-Wall Carbon Nanotubes". *Nano Lett.*, **2002,** *2*, 1137. *https://doi.org/10.1021/nl025642u*

[63] A. Ural, Y. Li, H. Dai, "Electric-field-aligned growth of single-walled carbon nanotubes on surfaces". *Appl. Phys. Lett.*, **2002,** *81*, 3464. *https://doi.org/10.1063/1.1518773*

[64] A. Ismach, D. Kantorovich, E. Joselevich, "Carbon Nanotube Graphoepitaxy: Highly Oriented Growth by Faceted Nanosteps". *J. Am. Chem. Soc.*, **2005,** *127*, 11554. *https://doi.org/10.1021/ja052759m*

[65] C. M. Orofeo, H. Ago, T. Ikuta, K. Takahasi, M. Tsuji, "Growth of horizontally aligned single-walled carbon nanotubes on anisotropically etched silicon substrate". *Nanoscale*, **2010,** *2*, 1708. *https://doi.org/10.1039/C0NR00170H*

[66] M. Schweiger, M. Schaudig, F. Gannott, M. S. Killian, E. Bitzek, P. Schmuki, J. Zaumseil, "Controlling the diameter of aligned single-walled carbon nanotubes on quartz via catalyst reduction time". *Carbon*, **2015,** *95*, 452. *https://doi.org/10.1016/j.carbon.2015.08.058*

[67] P. Nikolaev, M. J. Bronikowski, R. K. Bradley, F. Rohmund, D. T. Colbert, K. A. Smith, R. E. Smalley, "Gas-phase catalytic growth of single-walled carbon nanotubes from carbon monoxide". *Chem. Phys. Lett.*, **1999,** *313*, 91. *https://doi.org/10.1016/S0009-2614(99)01029-5*

[68] M. J. Bronikowski, P. A. Willis, D. T. Colbert, K. A. Smith, R. E. Smalley, "Gas-phase production of carbon single-walled nanotubes from carbon monoxide via the HiPco process: A parametric study". *J. Vac. Sci. Technol., A*, **2001,** *19*, 1800. *https://doi.org/10.1116/1.1380721*

[69] S. M. Bachilo, L. Balzano, J. E. Herrera, F. Pompeo, D. E. Resasco, R. B. Weisman, "Narrow (n,m)-Distribution of Single-Walled Carbon Nanotubes Grown Using a Solid Supported Catalyst". *J. Am. Chem. Soc.*, **2003,** *125*, 11186. *https://doi.org/10.1021/ja036622c*

[70] F. Yang, X. Wang, M. Li, X. Liu, X. Zhao, D. Zhang, ..., Y. Li, "Templated Synthesis of Single-Walled Carbon Nanotubes with Specific Structure". *Acc. Chem. Res.*, **2016,** *49*, 606. *https://doi.org/10.1021/acs.accounts.5b00485*

[71] F. Yang, X. Wang, D. Zhang, K. Qi, J. Yang, Z. Xu, ..., Y. Li, "Growing Zigzag (16,0) Carbon Nanotubes with Structure-Defined Catalysts". *J. Am. Chem. Soc.*, **2015,** *137*, 8688. *https://doi.org/10.1021/jacs.5b04403*

[72] F. Yang, X. Wang, D. Zhang, J. Yang, LuoDa, Z. Xu, ..., Y. Li, "Chirality-specific growth of single-walled carbon nanotubes on solid alloy catalysts". *Nature*, **2014,** *510*, 522. *https://doi.org/10.1038/nature13434*

[73] J. Liu, C. Wang, X. Tu, B. Liu, L. Chen, M. Zheng, C. Zhou, "Chirality-controlled synthesis of single-wall carbon nanotubes using vapour-phase epitaxy". *Nat. Commun.*, **2012,** *3*, 1199. *https://doi.org/10.1038/ncomms2205*

[74] S. P. Schießl, X. de Vries, M. Rother, A. Massé, M. Brohmann, P. A. Bobbert, J. Zaumseil, "Modeling carrier density dependent charge transport in semiconducting

carbon nanotube networks". *Phys. Rev. Mater.*, **2017,** *1*, 046003. *https://doi.org/10.1103/PhysRevMaterials.1.046003*

[75] M. Zheng, A. Jagota, E. D. Semke, B. A. Diner, R. S. McLean, S. R. Lustig, ..., N. G. Tassi, "DNA-assisted dispersion and separation of carbon nanotubes". *Nat. Mater.*, **2003,** *2*, 338. *https://doi.org/10.1038/nmat877*

[76] M. Zheng, A. Jagota, M. S. Strano, A. P. Santos, P. Barone, S. G. Chou, ..., D. J. Walls, "Structure-Based Carbon Nanotube Sorting by Sequence-Dependent DNA Assembly". *Science*, **2003,** *302*, 1545. *https://doi.org/10.1126/science.1091911*

[77] X. Tu, S. Manohar, A. Jagota, M. Zheng, "DNA sequence motifs for structure-specific recognition and separation of carbon nanotubes". *Nature*, **2009,** *460*, 250. *https://doi.org/10.1038/nature08116*

[78] M. S. Arnold, A. A. Green, J. F. Hulvat, S. I. Stupp, M. C. Hersam, "Sorting carbon nanotubes by electronic structure using density differentiation". *Nat. Nanotechnol.*, **2006,** *1*, 60. *https://doi.org/10.1038/nnano.2006.52*

[79] M. S. Arnold, S. I. Stupp, M. C. Hersam, "Enrichment of Single-Walled Carbon Nanotubes by Diameter in Density Gradients". *Nano Lett.*, **2005,** *5*, 713. *https://doi.org/10.1021/nl050133o*

[80] C. Y. Khripin, J. A. Fagan, M. Zheng, "Spontaneous Partition of Carbon Nanotubes in Polymer-Modified Aqueous Phases". *J. Am. Chem. Soc.*, **2013,** *135*, 6822. *https://doi.org/10.1021/ja402762e*

[81] J. A. Fagan, C. Y. Khripin, C. A. Silvera Batista, J. R. Simpson, E. H. Hároz, A. R. Hight Walker, M. Zheng, "Isolation of Specific Small-Diameter Single-Wall Carbon Nanotube Species via Aqueous Two-Phase Extraction". *Adv. Mater.*, **2014,** *26*, 2800. *https://doi.org/10.1002/adma.201304873*

[82] J. A. Fagan, E. H. Hároz, R. Ihly, H. Gui, J. L. Blackburn, J. R. Simpson, ..., M. Zheng, "Isolation of >1 nm Diameter Single-Wall Carbon Nanotube Species Using Aqueous Two-Phase Extraction". *ACS Nano*, **2015,** *9*, 5377. *https://doi.org/10.1021/acsnano.5b01123*

[83] H. Liu, D. Nishide, T. Tanaka, H. Kataura, "Large-scale single-chirality separation of single-wall carbon nanotubes by simple gel chromatography". *Nat. Commun.*, **2011,** *2*, 309. *https://doi.org/10.1038/ncomms1313*

[84] X. Wei, T. Tanaka, N. Akizuki, Y. Miyauchi, K. Matsuda, M. Ohfuchi, H. Kataura, "Single-Chirality Separation and Optical Properties of (5,4) Single-Wall Carbon

Nanotubes". *J. Phys. Chem. C*, **2016,** *120*, 10705. *https://doi.org/10.1021/acs.jpcc.6b03257*

[85] T. Tanaka, H. Liu, S. Fujii, H. Kataura, "From metal/semiconductor separation to single-chirality separation of single-wall carbon nanotubes using gel". *Phys. Status Solidi RRL*, **2011,** *5*, 301. *https://doi.org/10.1002/pssr.201105289*

[86] A. Hirano, T. Tanaka, H. Kataura, "Thermodynamic Determination of the Metal/Semiconductor Separation of Carbon Nanotubes Using Hydrogels". *ACS Nano*, **2012,** *6*, 10195. *https://doi.org/10.1021/nn303985x*

[87] T. Tanaka, H. Jin, Y. Miyata, S. Fujii, H. Suga, Y. Naitoh, ..., H. Kataura, "Simple and Scalable Gel-Based Separation of Metallic and Semiconducting Carbon Nanotubes". *Nano Lett.*, **2009,** *9*, 1497. *https://doi.org/10.1021/nl8034866*

[88] G. S. Tulevski, A. D. Franklin, A. Afzali, "High Purity Isolation and Quantification of Semiconducting Carbon Nanotubes via Column Chromatography". *ACS Nano*, **2013,** *7*, 2971. *https://doi.org/10.1021/nn400053k*

[89] H. Liu, T. Tanaka, H. Kataura, "Optical Isomer Separation of Single-Chirality Carbon Nanotubes Using Gel Column Chromatography". *Nano Lett.*, **2014,** *14*, 6237. *https://doi.org/10.1021/nl5025613*

[90] T. Tanaka, Y. Urabe, T. Hirakawa, H. Kataura, "Simultaneous Chirality and Enantiomer Separation of Metallic Single-Wall Carbon Nanotubes by Gel Column Chromatography". *Anal. Chem.*, **2015,** *87*, 9467. *https://doi.org/10.1021/acs.analchem.5b02563*

[91] A. Nish, J. Y. Hwang, J. Doig, R. J. Nicholas, "Highly selective dispersion of single-walled carbon nanotubes using aromatic polymers". *Nat. Nanotechnol.*, **2007,** *2*, 640. *https://doi.org/10.1038/nnano.2007.290*

[92] W. Gomulya, G. D. Costanzo, E. J. F. de Carvalho, S. Z. Bisri, V. Derenskyi, M. Fritsch, ..., A. Herrmann, "Semiconducting Single-Walled Carbon Nanotubes on Demand by Polymer Wrapping". *Adv. Mater.*, **2013,** *25*, 2948. *https://doi.org/10.1002/adma.201300267*

[93] M. Tange, T. Okazaki, S. Iijima, "Selective Extraction of Semiconducting Single-Wall Carbon Nanotubes by Poly(9,9-dioctylfluorene-alt-pyridine) for 1.5 μm Emission". *ACS Appl. Mater. Interfaces*, **2012,** *4*, 6458. *https://doi.org/10.1021/am302327j*

[94] O. Hiroaki, I. Natsuko, F. Tsuyohiko, N. Yasuro, N. Naotoshi, "One-pot Separation of Highly Enriched (6,5)-Single-walled Carbon Nanotubes Using a Fluorene-based Copolymer". *Chem. Lett.*, **2011,** *40*, 239. *https://doi.org/10.1246/cl.2011.239*

[95] K. S. Mistry, B. A. Larsen, J. L. Blackburn, "High-Yield Dispersions of Large-Diameter Semiconducting Single-Walled Carbon Nanotubes with Tunable Narrow Chirality Distributions". *ACS Nano*, **2013,** *7*, 2231. *https://doi.org/10.1021/nn305336x*

[96] N. Berton, F. Lemasson, J. Tittmann, N. Stürzl, F. Hennrich, M. M. Kappes, M. Mayor, "Copolymer-Controlled Diameter-Selective Dispersion of Semiconducting Single-Walled Carbon Nanotubes". *Chem. Mater.*, **2011,** *23*, 2237. *https://doi.org/10.1021/cm200275v*

[97] F. Chen, B. Wang, Y. Chen, L.-J. Li, "Toward the extraction of single species of single-walled carbon nanotubes using fluorene-based polymers". *Nano Lett.*, **2007,** *7*, 3013. *https://doi.org/10.1021/nl071349o*

[98] J.-Y. Hwang, A. Nish, J. Doig, S. Douven, C.-W. Chen, L.-C. Chen, R. J. Nicholas, "Polymer structure and solvent effects on the selective dispersion of single-walled carbon nanotubes". *J. Am. Chem. Soc.*, **2008,** *130*, 3543. *https://doi.org/10.1021/ja0777640*

[99] J. Ouyang, J. Ding, J. Lefebvre, Z. Li, C. Guo, A. J. Kell, P. R. L. Malenfant, "Sorting of Semiconducting Single-Walled Carbon Nanotubes in Polar Solvents with an Amphiphilic Conjugated Polymer Provides General Guidelines for Enrichment". *ACS Nano*, **2018,** *12*, 1910. *https://doi.org/10.1021/acsnano.7b08818*

[100] H. W. Lee, Y. Yoon, S. Park, J. H. Oh, S. Hong, L. S. Liyanage, ..., Z. Bao, "Selective dispersion of high purity semiconducting single-walled carbon nanotubes with regioregular poly(3-alkylthiophene)s". *Nat. Commun.*, **2011,** *2*, 541. *https://doi.org/10.1038/ncomms1545*

[101] H. Wang, G. I. Koleilat, P. Liu, G. Jiménez-Osés, Y.-C. Lai, M. Vosgueritchian, ..., Z. Bao, "High-Yield Sorting of Small-Diameter Carbon Nanotubes for Solar Cells and Transistors". *ACS Nano*, **2014,** *8*, 2609. *https://doi.org/10.1021/nn406256y*

[102] F. A. Lemasson, T. Strunk, P. Gerstel, F. Hennrich, S. Lebedkin, C. Barner-Kowollik, ..., M. Mayor, "Selective Dispersion of Single-Walled Carbon Nanotubes with Specific Chiral Indices by Poly(N-decyl-2,7-carbazole)". *J. Am. Chem. Soc.*, **2011,** *133*, 652. *https://doi.org/10.1021/ja105722u*

[103] W. Gomulya, V. Derenskyi, E. Kozma, M. Pasini, M. A. Loi, "Polyazines and Polyazomethines with Didodecylthiophene Units for Selective Dispersion of Semiconducting Single-Walled Carbon Nanotubes". *Adv. Funct. Mater.*, **2015,** *25*, 5858. *https://doi.org/10.1002/adfm.201502912*

[104] J. M. Salazar-Rios, W. Gomulya, V. Derenskyi, J. Yang, S. Z. Bisri, Z. Chen, ..., M. A. Loi, "Selecting Semiconducting Single-Walled Carbon Nanotubes with Narrow Bandgap Naphthalene Diimide-Based Polymers". *Adv. Electron. Mater.*, **2015,** *1*, 1500074. *https://doi.org/10.1002/aelm.201500074*

[105] T. Lei, G. Pitner, X. Chen, G. Hong, S. Park, P. Hayoz, ..., Z. Bao, "Dispersion of High-Purity Semiconducting Arc-Discharged Carbon Nanotubes Using Backbone Engineered Diketopyrrolopyrrole (DPP)-Based Polymers". *Adv. Electron. Mater.*, **2016,** *2*, 1500299. *https://doi.org/10.1002/aelm.201500299*

[106] F. Jakubka, S. P. Schießl, S. Martin, J. M. Englert, F. Hauke, A. Hirsch, J. Zaumseil, "Effect of polymer molecular weight and solution parameters on selective dispersion of single-walled carbon nanotubes". *ACS Macro Lett.*, **2012,** *1*, 815. *https://doi.org/10.1021/mz300147g*

[107] J. Han, Q. Ji, S. Qiu, H. Li, S. Zhang, H. Jin, Q. Li, "A versatile approach to obtain a high-purity semiconducting single-walled carbon nanotube dispersion with conjugated polymers". *Chem. Commun.*, **2015,** *51*, 4712. *https://doi.org/10.1039/C5CC00167F*

[108] N. A. Rice, A. V. Subrahmanyam, S. E. Laengert, A. Adronov, "The effect of molecular weight on the separation of semiconducting single-walled carbon nanotubes using poly(2,7-carbazole)s". *J. Polym. Sci., Part A: Polym. Chem.*, **2015,** *53*, 2510. *https://doi.org/10.1002/pola.27715*

[109] H. Ozawa, N. Ide, T. Fujigaya, Y. Niidome, N. Nakashima, "One-pot Separation of Highly Enriched (6,5)-Single-walled Carbon Nanotubes Using a Fluorene-based Copolymer". *Chem. Lett.*, **2011,** *40*, 239. *https://doi.org/10.1246/cl.2011.239*

[110] A. Graf, Y. Zakharko, S. P. Schießl, C. Backes, M. Pfohl, B. S. Flavel, J. Zaumseil, "Large scale, selective dispersion of long single-walled carbon nanotubes with high photoluminescence quantum yield by shear force mixing". *Carbon*, **2016,** *105*, 593. *https://doi.org/10.1016/j.carbon.2016.05.002*

[111] F. J. Berger, T. M. Higgins, M. Rother, A. Graf, Y. Zakharko, S. Allard, ..., J. Zaumseil, "From Broadband to Electrochromic Notch Filters with Printed Monochiral Carbon

Nanotubes". *ACS Appl. Mater. Interfaces*, **2018,** *10*, 11135. *https://doi.org/10.1021/acsami.8b00643*

[112] M. Rother, A. Kruse, M. Brohmann, M. Matthiesen, S. Grieger, T. M. Higgins, J. Zaumseil, "Vertical Electrolyte-Gated Transistors Based on Printed Single-Walled Carbon Nanotubes". *ACS Appl. Nano Mater.*, **2018**. *https://doi.org/10.1021/acsanm.8b00756*

[113] T. Lei, X. Chen, G. Pitner, H. S. P. Wong, Z. Bao, "Removable and Recyclable Conjugated Polymers for Highly Selective and High-Yield Dispersion and Release of Low-Cost Carbon Nanotubes". *J. Am. Chem. Soc.*, **2016,** *138*, 802. *https://doi.org/10.1021/jacs.5b12797*

[114] Y. Joo, G. J. Brady, M. J. Shea, M. B. Oviedo, C. Kanimozhi, S. K. Schmitt, ..., P. Gopalan, "Isolation of Pristine Electronics Grade Semiconducting Carbon Nanotubes by Switching the Rigidity of the Wrapping Polymer Backbone on Demand". *ACS Nano*, **2015,** *9*, 10203. *https://doi.org/10.1021/acsnano.5b03835*

[115] Y. Joo, G. J. Brady, C. Kanimozhi, J. Ko, M. J. Shea, M. T. Strand, ..., P. Gopalan, "Polymer-Free Electronic-Grade Aligned Semiconducting Carbon Nanotube Array". *ACS Appl. Mater. Interfaces*, **2017,** *9*, 28859. *https://doi.org/10.1021/acsami.7b06850*

[116] J. Zaumseil, H. Sirringhaus, "Electron and ambipolar transport in organic field-effect transistors". *Chem. Rev.*, **2007,** *107*, 1296. *https://doi.org/10.1021/cr0501543*

[117] H. Klauk, "Organic thin-film transistors". *Chem. Soc. Rev.*, **2010,** *39*, 2643. *https://doi.org/10.1039/B909902F*

[118] Y. Xu, H. Sun, A. Liu, H. Zhu, B. Li, T. Minari, ..., Y.-Y. Noh, "Essential Effects on the Mobility Extraction Reliability for Organic Transistors". *Adv. Funct. Mater.*, **2018,** *28*, 1803907. *https://doi.org/10.1002/adfm.201803907*

[119] Z. A. Lamport, H. F. Haneef, S. Anand, M. Waldrip, O. D. Jurchescu, "Tutorial: Organic field-effect transistors: Materials, structure and operation". *J. Appl. Phys.*, **2018,** *124*, 071101. *https://doi.org/10.1063/1.5042255*

[120] E. G. Bittle, J. I. Basham, T. N. Jackson, O. D. Jurchescu, D. J. Gundlach, "Mobility overestimation due to gated contacts in organic field-effect transistors". *Nat. Commun.*, **2016,** *7*. *https://doi.org/10.1038/ncomms10908*

[121] S. P. Schießl, M. Rother, J. Lüttgens, J. Zaumseil, "Extracting the field-effect mobilities of random semiconducting single-walled carbon nanotube networks: A critical

comparison of methods". *Appl. Phys. Lett.*, **2017,** *111*, 193301. *https://doi.org/10.1063/1.5006877*

[122] D. Natali, M. Caironi, "Charge Injection in Solution-Processed Organic Field-Effect Transistors: Physics, Models and Characterization Methods". *Adv. Mater.*, **2012,** *24*, 1357. *https://doi.org/10.1002/adma.201104206*

[123] J. Swensen, D. Moses, A. J. Heeger, "Light emission in the channel region of a polymer thin-film transistor fabricated with gold and aluminum for the source and drain electrodes". *Synth. Met.*, **2005,** *153*, 53. *https://doi.org/10.1016/j.synthmet.2005.07.258*

[124] J. Zaumseil, C. L. Donley, J. S. Kim, R. H. Friend, H. Sirringhaus, "Efficient Top-Gate, Ambipolar, Light-Emitting Field-Effect Transistors Based on a Green-Light-Emitting Polyfluorene". *Adv. Mater.*, **2006,** *18*, 2708. *https://doi.org/10.1002/adma.200601080*

[125] E. Menard, V. Podzorov, S. H. Hur, A. Gaur, M. E. Gershenson, J. A. Rogers, "High-Performance n- and p-Type Single-Crystal Organic Transistors with Free-Space Gate Dielectrics". *Adv. Mater.*, **2004,** *16*, 2097. *https://doi.org/10.1002/adma.200401017*

[126] T. Takahashi, T. Takenobu, J. Takeya, Y. Iwasa, "Ambipolar organic field-effect transistors based on rubrene single crystals". *Appl. Phys. Lett.*, **2006,** *88*, 033505. *https://doi.org/10.1063/1.2166698*

[127] S. Amriou, A. Mehta, M. R. Bryce, "Functionalised 9-(1,3-dithiol-2-ylidene)thioxanthene derivatives: a C60 conjugate as an ambipolar organic field effect transistor (OFET)". *J. Mater. Chem.*, **2005,** *15*, 1232. *https://doi.org/10.1039/B500500K*

[128] T. D. Anthopoulos, F. B. Kooistra, H. J. Wondergem, D. Kronholm, J. C. Hummelen, D. M. de Leeuw, "Air-Stable n-Channel Organic Transistors Based on a Soluble C84 Fullerene Derivative". *Adv. Mater.*, **2006,** *18*, 1679. *https://doi.org/10.1002/adma.200600068*

[129] T. D. Anthopoulos, C. Tanase, S. Setayesh, E. J. Meijer, J. C. Hummelen, P. W. M. Blom, D. M. de Leeuw, "Ambipolar Organic Field-Effect Transistors Based on a Solution-Processed Methanofullerene". *Adv. Mater.*, **2004,** *16*, 2174. *https://doi.org/10.1002/adma.200400309*

[130] E. J. Meijer, D. M. de Leeuw, S. Setayesh, E. van Veenendaal, B. H. Huisman, P. W. M. Blom, ..., T. M. Klapwijk, "Solution-processed ambipolar organic field-effect transistors and inverters". *Nat. Mater.*, **2003,** *2*, 678. *https://doi.org/10.1038/nmat978*

[131] R. J. Chesterfield, C. R. Newman, T. M. Pappenfus, P. C. Ewbank, M. H. Haukaas, K. R. Mann, ..., C. D. Frisbie, "High Electron Mobility and Ambipolar Transport in Organic

Thin-Film Transistors Based on a π-Stacking Quinoidal Terthiophene". *Adv. Mater.*, **2003,** *15*, 1278. *https://doi.org/10.1002/adma.200305200*

[132] C. Rost, S. Karg, W. Riess, M. A. Loi, M. Murgia, M. Muccini, "Ambipolar light-emitting organic field-effect transistor". *Appl. Phys. Lett.*, **2004,** *85*, 1613. *https://doi.org/10.1063/1.1785290*

[133] A. Dodabalapur, H. E. Katz, L. Torsi, R. C. Haddon, "Organic Heterostructure Field-Èffect Transistors". *Science*, **1995,** *269*, 1560. *https://doi.org/10.1126/science.269.5230.1560*

[134] M. S. Kang, C. D. Frisbie, "A Pedagogical Perspective on Ambipolar FETs". *ChemPhysChem*, **2013,** *14*, 1547. *https://doi.org/10.1002/cphc.201300014*

[135] A. D. Franklin, M. Luisier, S.-J. Han, G. Tulevski, C. M. Breslin, L. Gignac, ..., W. Haensch, "Sub-10 nm Carbon Nanotube Transistor". *Nano Lett.*, **2012,** *12*, 758. *https://doi.org/10.1021/nl203701g*

[136] R. Martel, T. Schmidt, H. R. Shea, T. Hertel, P. Avouris, "Single- and multi-wall carbon nanotube field-effect transistors". *Appl. Phys. Lett.*, **1998,** *73*, 2447. *https://doi.org/10.1063/1.122477*

[137] S. J. Tans, A. R. M. Verschueren, C. Dekker, "Room-temperature transistor based on a single carbon nanotube". *Nature*, **1998,** *393*, 49. *https://doi.org/10.1038/29954*

[138] S. J. Kang, C. Kocabas, T. Ozel, M. Shim, N. Pimparkar, M. A. Alam, ..., J. A. Rogers, "High-performance electronics using dense, perfectly aligned arrays of single-walled carbon nanotubes". *Nat. Nanotechnol.*, **2007,** *2*, 230. *https://doi.org/10.1038/nnano.2007.77*

[139] Y. Asada, Y. Miyata, Y. Ohno, R. Kitaura, T. Sugai, T. Mizutani, H. Shinohara, "High-Performance Thin-Film Transistors with DNA-Assisted Solution Processing of Isolated Single-Walled Carbon Nanotubes". *Adv. Mater.*, **2010,** *22*, 2698. *https://doi.org/10.1002/adma.200904006*

[140] J. Ding, Z. Li, J. Lefebvre, F. Cheng, G. Dubey, S. Zou, ..., G. P. Lopinski, "Enrichment of large-diameter semiconducting SWCNTs by polyfluorene extraction for high network density thin film transistors". *Nanoscale*, **2014,** *6*, 2328. *https://doi.org/10.1039/C3NR05511F*

[141] B. Chen, P. Zhang, L. Ding, J. Han, S. Qiu, Q. Li, ..., L.-M. Peng, "Highly Uniform Carbon Nanotube Field-Effect Transistors and Medium Scale Integrated Circuits". *Nano Lett.*, **2016,** *16*, 5120. *https://doi.org/10.1021/acs.nanolett.6b02046*

[142] J. Gu, J. Han, D. Liu, X. Yu, L. Kang, S. Qiu, ..., J. Zhang, "Solution-Processable High-Purity Semiconducting SWCNTs for Large-Area Fabrication of High-Performance Thin-Film Transistors". *Small*, **2016,** *12*, 4993. *https://doi.org/10.1002/smll.201600398*

[143] M. C. LeMieux, M. Roberts, S. Barman, Y. W. Jin, J. M. Kim, Z. Bao, "Self-Sorted, Aligned Nanotube Networks for Thin-Film Transistors". *Science*, **2008,** *321*, 101. *https://doi.org/10.1126/science.1156588*

[144] S. Schneider, M. Brohmann, R. Lorenz, Y. J. Hofstetter, M. Rother, E. Sauter, ..., J. Zaumseil, "Efficient n-Doping and Hole-Blocking in Single-Walled Carbon Nanotube Transistors with 1, 2, 4, 5-Tetrakis (tetramethyl-guanidino) benzene". *ACS Nano*, **2018**. *https://doi.org/10.1021/acsnano.8b02061*

[145] S. Z. Bisri, J. Gao, V. Derenskyi, W. Gomulya, I. Iezhokin, P. Gordiichuk, ..., M. A. Loi, "High Performance Ambipolar Field-Effect Transistor of Random Network Carbon Nanotubes". *Adv. Mater.*, **2012,** *24*, 6147. *https://doi.org/10.1002/adma.201202699*

[146] V. Derenskyi, W. Gomulya, J. M. S. Rios, M. Fritsch, N. Fröhlich, S. Jung, ..., M. A. Loi, "Carbon Nanotube Network Ambipolar Field-Effect Transistors with 108 On/Off Ratio". *Adv. Mater.*, **2014,** *26*, 5969. *https://doi.org/10.1002/adma.201401395*

[147] P. H. Lau, K. Takei, C. Wang, Y. Ju, J. Kim, Z. Yu, ..., A. Javey, "Fully Printed, High Performance Carbon Nanotube Thin-Film Transistors on Flexible Substrates". *Nano Lett.*, **2013,** *13*, 3864. *https://doi.org/10.1021/nl401934a*

[148] M. Ha, Y. Xia, A. A. Green, W. Zhang, M. J. Renn, C. H. Kim, ..., C. D. Frisbie, "Printed, Sub-3V Digital Circuits on Plastic from Aqueous Carbon Nanotube Inks". *ACS Nano*, **2010,** *4*, 4388. *https://doi.org/10.1021/nn100966s*

[149] M. Ha, J.-W. T. Seo, P. L. Prabhumirashi, W. Zhang, M. L. Geier, M. J. Renn, ..., C. D. Frisbie, "Aerosol Jet Printed, Low Voltage, Electrolyte Gated Carbon Nanotube Ring Oscillators with Sub-5 µs Stage Delays". *Nano Lett.*, **2013,** *13*, 954. *https://doi.org/10.1021/nl3038773*

[150] M. Rother, M. Brohmann, S. Yang, S. B. Grimm, S. P. Schießl, A. Graf, J. Zaumseil, "Aerosol-Jet Printing of Polymer-Sorted (6,5) Carbon Nanotubes for Field-Effect Transistors with High Reproducibility". *Adv. Electron. Mater.*, **2017,** *3*, 1700080. *https://doi.org/10.1002/aelm.201700080*

[151] C. S. Jones, X. Lu, M. Renn, M. Stroder, W.-S. Shih, "Aerosol-jet-printed, high-speed, flexible thin-film transistor made using single-walled carbon nanotube solution". *Microelectron. Eng.*, **2010,** *87*, 434. *https://doi.org/10.1016/j.mee.2009.05.034*

[152] J. Zhao, Y. Gao, W. Gu, C. Wang, J. Lin, Z. Chen, Z. Cui, "Fabrication and electrical properties of all-printed carbon nanotube thin film transistors on flexible substrates". *J. Mater. Chem.*, **2012,** *22*, 20747. *https://doi.org/10.1039/C2JM34598F*

[153] C. Cao, J. B. Andrews, A. Kumar, A. D. Franklin, "Improving Contact Interfaces in Fully Printed Carbon Nanotube Thin-Film Transistors". *ACS Nano*, **2016,** *10*, 5221. *https://doi.org/10.1021/acsnano.6b00877*

[154] X. Q. Chen, T. Saito, H. Yamada, K. Matsushige, "Aligning single-wall carbon nanotubes with an alternating-current electric field". *Appl. Phys. Lett.*, **2001,** *78*, 3714. *https://doi.org/10.1063/1.1377627*

[155] M. Senthil Kumar, S. H. Lee, T. Y. Kim, T. H. Kim, S. M. Song, J. W. Yang, ..., E. K. Suh, "DC electric field assisted alignment of carbon nanotubes on metal electrodes". *Solid·State Electron.*, **2003,** *47*, 2075. *https://doi.org/10.1016/s0038-1101(03)00258-2*

[156] F. Hennrich, W. Li, R. Fischer, S. Lebedkin, R. Krupke, M. M. Kappes, "Length-Sorted, Large-Diameter, Polyfluorene-Wrapped Semiconducting Single-Walled Carbon Nanotubes for High-Density, Short-Channel Transistors". *ACS Nano*, **2016,** *10*, 1888. *https://doi.org/10.1021/acsnano.5b05572*

[157] F. Jakubka, S. B. Grimm, Y. Zakharko, F. Gannott, J. Zaumseil, "Trion Electroluminescence from Semiconducting Carbon Nanotubes". *ACS Nano*, **2014,** *8*, 8477. *https://doi.org/10.1021/nn503046y*

[158] M. S. Filipiak, M. Rother, N. M. Andoy, A. C. Knudsen, S. Grimm, C. Bachran, ..., A. Tarasov, "Highly sensitive, selective and label-free protein detection in physiological solutions using carbon nanotube transistors with nanobody receptors". *Sens. Actuators, B*, **2018,** *255*, 1507. *https://doi.org/10.1016/j.snb.2017.08.164*

[159] S. Grimm, S. P. Schießl, Y. Zakharko, M. Rother, M. Brohmann, J. Zaumseil, "Doping-dependent G-mode shifts of small diameter semiconducting single-walled carbon nanotubes". *Carbon*, **2017,** *118*, 261. *https://doi.org/10.1016/j.carbon.2017.03.040*

[160] Y. Joo, G. J. Brady, M. S. Arnold, P. Gopalan, "Dose-Controlled, Floating Evaporative Self-assembly and Alignment of Semiconducting Carbon Nanotubes from Organic Solvents". *Langmuir*, **2014,** *30*, 3460. *https://doi.org/10.1021/la500162x*

[161] G. J. Brady, A. J. Way, N. S. Safron, H. T. Evensen, P. Gopalan, M. S. Arnold, "Quasi-ballistic carbon nanotube array transistors with current density exceeding Si and GaAs". *Sci. Adv.*, **2016,** *2*, e1601240. *https://doi.org/10.1126/sciadv.1601240*

[162] M. Engel, J. P. Small, M. Steiner, M. Freitag, A. A. Green, M. C. Hersam, P. Avouris, "Thin Film Nanotube Transistors Based on Self-Assembled, Aligned, Semiconducting Carbon Nanotube Arrays". *ACS Nano*, **2008,** *2*, 2445. *https://doi.org/10.1021/nn800708w*

[163] M. Held, S. P. Schießl, D. Miehler, F. Gannott, J. Zaumseil, "Polymer/metal oxide hybrid dielectrics for low voltage field-effect transistors with solution-processed, high-mobility semiconductors". *Appl. Phys. Lett.*, **2015,** *107*, 083301. *https://doi.org/10.1063/1.4929461*

[164] Q. Qian, G. Li, Y. Jin, J. Liu, Y. Zou, K. Jiang, ..., Q. Li, "Trap-State-Dominated Suppression of Electron Conduction in Carbon Nanotube Thin-Film Transistors". *ACS Nano*, **2014,** *8*, 9597. *https://doi.org/10.1021/nn503903y*

[165] C. M. Aguirre, P. L. Levesque, M. Paillet, F. Lapointe, B. C. St-Antoine, P. Desjardins, R. Martel, "The Role of the Oxygen/Water Redox Couple in Suppressing Electron Conduction in Field-Effect Transistors". *Adv. Mater.*, **2009,** *21*, 3087. *https://doi.org/10.1002/adma.200900550*

[166] E. S. Snow, J. P. Novak, P. M. Campbell, D. Park, "Random networks of carbon nanotubes as an electronic material". *Appl. Phys. Lett.*, **2003,** *82*, 2145. *https://doi.org/10.1063/1.1564291*

[167] E. S. Snow, P. M. Campbell, M. G. Ancona, J. P. Novak, "High-mobility carbon-nanotube thin-film transistors on a polymeric substrate". *Appl. Phys. Lett.*, **2005,** *86*. *https://doi.org/10.1063/1.1854721*

[168] N. Izard, S. Kazaoui, K. Hata, T. Okazaki, T. Saito, S. Iijima, N. Minami, "Semiconductor-enriched single wall carbon nanotube networks applied to field effect transistors". *Appl. Phys. Lett.*, **2008,** *92*, 243112. *https://doi.org/10.1063/1.2939560*

[169] C. Wang, K. Ryu, L. De Arco, A. Badmaev, J. Zhang, X. Lin, ..., C. Zhou, "Synthesis and device applications of high-density aligned carbon nanotubes using low-pressure chemical vapor deposition and stacked multiple transfer". *Nano Res.*, **2010,** *3*, 831. *https://doi.org/10.1007/s12274-010-0054-0*

[170] X. Ho, L. Ye, S. V. Rotkin, Q. Cao, S. Unarunotai, S. Salamat, ..., J. A. Rogers, "Scaling Properties in Transistors That Use Aligned Arrays of Single-Walled Carbon Nanotubes". *Nano Lett.*, **2010,** *10*, 499. *https://doi.org/10.1021/nl903281v*

[171] Y. Miyata, K. Shiozawa, Y. Asada, Y. Ohno, R. Kitaura, T. Mizutani, H. Shinohara, "Length-sorted semiconducting carbon nanotubes for high-mobility thin film transistors". *Nano Res.*, **2011,** *4*, 963. *https://doi.org/10.1007/s12274-011-0152-7*

[172] Y. Asada, Y. Miyata, K. Shiozawa, Y. Ohno, R. Kitaura, T. Mizutani, H. Shinohara, "Thin-Film Transistors with Length-Sorted DNA-Wrapped Single-Wall Carbon Nanotubes". *J. Phys. Chem. C*, **2010,** *115*, 270. *https://doi.org/10.1021/jp107361n*

[173] D.-M. Sun, M. Y. Timmermans, Y. Tian, A. G. Nasibulin, E. I. Kauppinen, S. Kishimoto, ..., Y. Ohno, "Flexible high-performance carbon nanotube integrated circuits". *Nat. Nanotechnol.*, **2011,** *6*, 156. *https://doi.org/10.1038/nnano.2011.1*

[174] Q. Cao, S.-j. Han, G. S. Tulevski, Y. Zhu, D. D. Lu, W. Haensch, "Arrays of single-walled carbon nanotubes with full surface coverage for high-performance electronics". *Nat. Nanotechnol.*, **2013,** *8*, 180. *https://doi.org/10.1038/nnano.2012.257*

[175] W. Gomulya, G. D. Costanzo, E. J. F. de Carvalho, S. Z. Bisri, V. Derenskyi, M. Fritsch, ..., M. A. Loi, "Semiconducting Single-Walled Carbon Nanotubes on Demand by Polymer Wrapping". *Adv. Mater.*, **2013,** *25*, 2948. *https://doi.org/10.1002/adma.201300267*

[176] H. Wang, P. Wei, Y. Li, J. Han, H. R. Lee, B. D. Naab, ..., Z. Bao, "Tuning the threshold voltage of carbon nanotube transistors by n-type molecular doping for robust and flexible complementary circuits". *Proc. Natl. Acad. Sci. U. S. A.*, **2014,** *111*, 4776. *https://doi.org/10.1073/pnas.1320045111*

[177] C. Tanase, E. J. Meijer, P. W. M. Blom, D. M. de Leeuw, "Local charge carrier mobility in disordered organic field-effect transistors". *Org. Electron.*, **2003,** *4*, 33. *https://doi.org/10.1016/S1566-1199(03)00006-5*

[178] M. J. Panzer, C. D. Frisbie, "Polymer Electrolyte Gate Dielectric Reveals Finite Windows of High Conductivity in Organic Thin Film Transistors at High Charge Carrier Densities". *J. Am. Chem. Soc.*, **2005,** *127*, 6960. *https://doi.org/10.1021/ja051579+*

[179] S. Thiemann, S. Sachnov, S. Porscha, P. Wasserscheid, J. Zaumseil, "Ionic Liquids for Electrolyte-Gating of ZnO Field-Effect Transistors". *J. Phys. Chem. C*, **2012,** *116*, 13536. *https://doi.org/10.1021/jp3024233*

[180] D. A. Bernards, G. G. Malliaras, "Steady-State and Transient Behavior of Organic Electrochemical Transistors". *Adv. Funct. Mater.*, **2007,** *17*, 3538. *https://doi.org/10.1002/adfm.200601239*

[181] J. Rivnay, S. Inal, A. Salleo, R. M. Owens, M. Berggren, G. G. Malliaras, "Organic electrochemical transistors". *Nat. Rev. Mater.*, **2018,** *3*, 17086. *https://doi.org/10.1038/natrevmats.2017.86*

[182] S. H. Kim, K. Hong, W. Xie, K. H. Lee, S. Zhang, T. P. Lodge, C. D. Frisbie, "Electrolyte-Gated Transistors for Organic and Printed Electronics". *Adv. Mater.*, **2013,** *25*, 1822. *https://doi.org/10.1002/adma.201202790*

[183] J. Zaumseil, X. Ho, J. R. Guest, G. P. Wiederrecht, J. A. Rogers, "Electroluminescence from Electrolyte-Gated Carbon Nanotube Field-Effect Transistors". *ACS Nano*, **2009,** *3*, 2225. *https://doi.org/10.1021/nn9005736*

[184] M. S. Kang, J. Lee, D. J. Norris, C. D. Frisbie, "High Carrier Densities Achieved at Low Voltages in Ambipolar PbSe Nanocrystal Thin-Film Transistors". *Nano Lett.*, **2009,** *9*, 3848. *https://doi.org/10.1021/nl902062x*

[185] H. Bong, W. H. Lee, D. Y. Lee, B. J. Kim, J. H. Cho, K. Cho, "High-mobility low-temperature ZnO transistors with low-voltage operation". *Appl. Phys. Lett.*, **2010,** *96*, 192115. *https://doi.org/10.1063/1.3428357*

[186] H. Yuan, H. Shimotani, A. Tsukazaki, A. Ohtomo, M. Kawasaki, Y. Iwasa, "High-Density Carrier Accumulation in ZnO Field-Effect Transistors Gated by Electric Double Layers of Ionic Liquids". *Adv. Funct. Mater.*, **2009,** *19*, 1046. *https://doi.org/10.1002/adfm.200801633*

[187] D. Braga, N. C. Erickson, M. J. Renn, R. J. Holmes, C. D. Frisbie, "High-Transconductance Organic Thin-Film Electrochemical Transistors for Driving Low-Voltage Red-Green-Blue Active Matrix Organic Light-Emitting Devices". *Adv. Funct. Mater.*, **2012,** *22*, 1623. *https://doi.org/10.1002/adfm.201102075*

[188] X. Shao, B. Bao, J. Zhao, W. Tang, S. Wang, X. Guo, "Low-Voltage Large-Current Ion Gel Gated Polymer Transistors Fabricated by a “Cut and Bond” Process". *ACS Appl. Mater. Interfaces*, **2015,** *7*, 4759. *https://doi.org/10.1021/am508487z*

[189] L. Torsi, M. Magliulo, K. Manoli, G. Palazzo, "Organic field-effect transistor sensors: a tutorial review". *Chem. Soc. Rev.*, **2013,** *42*, 8612. *https://doi.org/10.1039/c3cs60127g*

[190] E. Macchia, K. Manoli, B. Holzer, C. Di Franco, M. Ghittorelli, F. Torricelli, ..., L. Torsi, "Single-molecule detection with a millimetre-sized transistor". *Nat. Commun.*, **2018,** *9*, 3223. *https://doi.org/10.1038/s41467-018-05235-z*

[191] L. Kergoat, B. Piro, M. Berggren, G. Horowitz, M.-C. Pham, "Advances in organic transistor-based biosensors: from organic electrochemical transistors to electrolyte-gated

organic field-effect transistors". *Anal. Bioanal. Chem.*, **2012,** *402*, 1813. *https://doi.org/10.1007/s00216-011-5363-y*

[192] S. P. White, K. D. Dorfman, C. D. Frisbie, "Label-Free DNA Sensing Platform with Low-Voltage Electrolyte-Gated Transistors". *Anal. Chem.*, **2015,** *87*, 1861. *https://doi.org/10.1021/ac503914x*

[193] W. H. Brattain, R. B. Gibney, *Unted States Patent 2524034*, **1948**.

[194] J. H. Cho, J. Lee, Y. He, B. S. Kim, T. P. Lodge, C. D. Frisbie, "High-Capacitance Ion Gel Gate Dielectrics with Faster Polarization Response Times for Organic Thin Film Transistors". *Adv. Mater.*, **2008,** *20*, 686. *https://doi.org/10.1002/adma.200701069*

[195] S. Zhang, K. H. Lee, C. D. Frisbie, T. P. Lodge, "Ionic Conductivity, Capacitance, and Viscoelastic Properties of Block Copolymer-Based Ion Gels". *Macromolecules*, **2011,** *44*, 940. *https://doi.org/10.1021/ma102435a*

[196] J. Lee, L. G. Kaake, J. H. Cho, X. Y. Zhu, T. P. Lodge, C. D. Frisbie, "Ion Gel-Gated Polymer Thin-Film Transistors: Operating Mechanism and Characterization of Gate Dielectric Capacitance, Switching Speed, and Stability". *J. Phys. Chem. C*, **2009,** *113*, 8972. *https://doi.org/10.1021/jp901426e*

[197] T. T. Baby, M. Rommel, F. von Seggern, P. Friederich, C. Reitz, S. Dehm, ..., S. Dasgupta, "Sub-50 nm Channel Vertical Field-Effect Transistors using Conventional Ink-Jet Printing". *Adv. Mater.*, **2017,** *29*, 1603858. *https://doi.org/10.1002/adma.201603858*

[198] D. Tobjörk, R. Österbacka, "Paper Electronics". *Adv. Mater.*, **2011,** *23*, 1935. *https://doi.org/10.1002/adma.201004692*

[199] J. Minhun, K. Jaeyoung, N. Jinsoo, L. Namsoo, L. Chaemin, L. Gwangyong, ..., C. Gyoujin, "All-Printed and Roll-to-Roll-Printable 13.56-MHz-Operated 1-bit RF Tag on Plastic Foils". *IEEE Trans. Electron Devices*, **2010,** *57*, 571. *https://doi.org/10.1109/TED.2009.2039541*

[200] S.-I. Park, Y. Xiong, R.-H. Kim, P. Elvikis, M. Meitl, D.-H. Kim, ..., J. A. Rogers, "Printed Assemblies of Inorganic Light-Emitting Diodes for Deformable and Semitransparent Displays". *Science*, **2009,** *325*, 977. *https://doi.org/10.1126/science.1175690*

[201] H. Zheng, Y. Zheng, N. Liu, N. Ai, Q. Wang, S. Wu, ..., S. Han, "All-solution processed polymer light-emitting diode displays". *Nat. Commun.*, **2013,** *4*, 1971. *https://doi.org/10.1038/ncomms2971*

[202] P. Andersson, D. Nilsson, P.-O. Svensson, M. Chen, A. Malmström, T. Remonen, ..., M. Berggren, "Active Matrix Displays Based on All-Organic Electrochemical Smart Pixels Printed on Paper". *Adv. Mater.*, **2002,** *14*, 1460. *https://doi.org/10.1002/1521-4095(20021016)14:20<1460::aid-adma1460>3.0.co;2-s*

[203] C. Jiang, L. Mu, J. Zou, Z. He, Z. Zhong, L. Wang, ..., Y. Cao, "Full-color quantum dots active matrix display fabricated by ink-jet printing". *Sci. China Chem.*, **2017,** *60*, 1349. *https://doi.org/10.1007/s11426-017-9087-y*

[204] L. Lan, J. Zou, C. Jiang, B. Liu, L. Wang, J. Peng, "Inkjet printing for electroluminescent devices: emissive materials, film formation, and display prototypes". *Front. Optoelectron.*, **2017,** *10*, 329. *https://doi.org/10.1007/s12200-017-0765-x*

[205] A. C. Arias, J. Daniel, B. Krusor, S. Ready, V. Sholin, R. Street, "All-additive ink-jet-printed display backplanes: Materials development and integration". *J. Soc. Inf. Disp.*, **2007,** *15*, 485. *https://doi.org/10.1889/1.2759554*

[206] Y. van de Burgt, A. Melianas, S. T. Keene, G. Malliaras, A. Salleo, "Organic electronics for neuromorphic computing". *Nat. Electron.*, **2018**, 1. *https://doi.org/10.1038/s41928-018-0103-3*

[207] W. Clemens, W. Fix, J. Ficker, A. Knobloch, A. Ullmann, "From polymer transistors toward printed electronics". *J. Mater. Res.*, **2011,** *19*, 1963. *https://doi.org/10.1557/JMR.2004.0263*

[208] H. K. Seung, P. Heng, P. G. Costas, K. L. Christine, M. J. F. Jean, P. Dimos, "All-inkjet-printed flexible electronics fabrication on a polymer substrate by low-temperature high-resolution selective laser sintering of metal nanoparticles". *Nanotechnology*, **2007,** *18*, 345202. *https://doi.org/10.1088/0957-4484/18/34/345202*

[209] J. Chung, S. Ko, N. R. Bieri, C. P. Grigoropoulos, D. Poulikakos, "Conductor microstructures by laser curing of printed gold nanoparticle ink". *Appl. Phys. Lett.*, **2004,** *84*, 801. *https://doi.org/10.1063/1.1644907*

[210] P. Mishra, A. Upadhyaya, G. Sethi, "Modeling of microwave heating of particulate metals". *Metall. Mater. Trans. B*, **2006,** *37*, 839. *https://doi.org/10.1007/s11663-006-0066-z*

[211] J. Perelaer, B.-J. de Gans, U. S. Schubert, "Ink-jet Printing and Microwave Sintering of Conductive Silver Tracks". *Adv. Mater.*, **2006,** *18*, 2101. *https://doi.org/10.1002/adma.200502422*

[212] J. J. P. Valeton, K. Hermans, C. W. M. Bastiaansen, D. J. Broer, J. Perelaer, U. S. Schubert, ..., P. J. Smith, "Room temperature preparation of conductive silver features using spin-coating and inkjet printing". *J. Mater. Chem.*, **2010,** *20*, 543. *https://doi.org/10.1039/B917266A*

[213] L. A. Mark, A. Mikko, M. Tomi, A. Ari, O. Kimmo, S. Mika, S. Heikki, "Electrical sintering of nanoparticle structures". *Nanotechnology*, **2008,** *19*, 175201. *https://doi.org/10.1088/0957-4484/19/17/175201*

[214] Y. Wu, Y. Li, B. S. Ong, "A Simple and Efficient Approach to a Printable Silver Conductor for Printed Electronics". *J. Am. Chem. Soc.*, **2007,** *129*, 1862. *https://doi.org/10.1021/ja067596w*

[215] K. Fukuda, T. Sekine, Y. Kobayashi, D. Kumaki, M. Itoh, M. Nagaoka, ..., S. Tokito, "Stable organic thin-film transistors using full solution-processing and low-temperature sintering silver nanoparticle inks". *Org. Electron.*, **2012,** *13*, 1660. *https://doi.org/10.1016/j.orgel.2012.05.016*

[216] D. Kim, S. Jeong, S. Lee, B. K. Park, J. Moon, "Organic thin film transistor using silver electrodes by the ink-jet printing technology". *Thin Solid Films*, **2007,** *515*, 7692. *https://doi.org/10.1016/j.tsf.2006.11.141*

[217] H. Kang, R. Kitsomboonloha, J. Jang, V. Subramanian, "High-Performance Printed Transistors Realized Using Femtoliter Gravure-Printed Sub-10 μm Metallic Nanoparticle Patterns and Highly Uniform Polymer Dielectric and Semiconductor Layers". *Adv. Mater.*, **2012,** *24*, 3065. *https://doi.org/10.1002/adma.201200924*

[218] Y. Noguchi, T. Sekitani, T. Yokota, T. Someya, "Direct inkjet printing of silver electrodes on organic semiconductors for thin-film transistors with top contact geometry". *Appl. Phys. Lett.*, **2008,** *93*, 043303. *https://doi.org/10.1063/1.2959728*

[219] A. C. Huebler, F. Doetz, H. Kempa, H. E. Katz, M. Bartzsch, N. Brandt, ..., U. Hahn, "Ring oscillator fabricated completely by means of mass-printing technologies". *Org. Electron.*, **2007,** *8*, 480. *https://doi.org/10.1016/j.orgel.2007.02.009*

[220] M. Michihiko, H. Jun, M. Ryotaro, H. Kentaro, K. Shigeru, T. Takuya, ..., O. Yutaka, "Printed, short-channel, top-gate carbon nanotube thin-film transistors on flexible plastic film". *Appl. Phys. Express*, **2015,** *8*, 045102. *https://doi.org/10.7567/APEX.8.045102*

[221] C. M. Homenick, R. James, G. P. Lopinski, J. Dunford, J. Sun, H. Park, ..., P. R. L. Malenfant, "Fully Printed and Encapsulated SWCNT-Based Thin Film Transistors via a

Combination of R2R Gravure and Inkjet Printing". *ACS Appl. Mater. Interfaces*, **2016,** *8*, 27900. *https://doi.org/10.1021/acsami.6b06838*

[222] H.-Y. Tseng, V. Subramanian, "All inkjet-printed, fully self-aligned transistors for low-cost circuit applications". *Org. Electron.*, **2011,** *12*, 249. *https://doi.org/10.1016/j.orgel.2010.11.013*

[223] A. de la Fuente Vornbrock, D. Sung, H. Kang, R. Kitsomboonloha, V. Subramanian, "Fully gravure and ink-jet printed high speed pBTTT organic thin film transistors". *Org. Electron.*, **2010,** *11*, 2037. *https://doi.org/10.1016/j.orgel.2010.09.003*

[224] G. Grau, V. Subramanian, "Fully High-Speed Gravure Printed, Low-Variability, High-Performance Organic Polymer Transistors with Sub-5 V Operation". *Adv. Electron. Mater.*, **2016,** *2*, 1500328. *https://doi.org/10.1002/aelm.201500328*

[225] E. Sowade, E. Ramon, K. Y. Mitra, C. Martínez-Domingo, M. Pedró, J. Pallarès, ..., R. R. Baumann, "All-inkjet-printed thin-film transistors: manufacturing process reliability by root cause analysis". *Sci. Rep.*, **2016,** *6*, 33490. *https://doi.org/10.1038/srep33490*

[226] H. Kentaro, K. Shigeru, N. Yuta, T. Takuya, T. Masafumi, H. Katsuhiko, ..., O. Yutaka, "High-Mobility, Flexible Carbon Nanotube Thin-Film Transistors Fabricated by Transfer and High-Speed Flexographic Printing Techniques". *Appl. Phys. Express*, **2013,** *6*, 085101. *https://doi.org/10.7567/APEX.6.085101*

[227] X. Cao, H. Chen, X. Gu, B. Liu, W. Wang, Y. Cao, ..., C. Zhou, "Screen Printing as a Scalable and Low-Cost Approach for Rigid and Flexible Thin-Film Transistors Using Separated Carbon Nanotubes". *ACS Nano*, **2014,** *8*, 12769. *https://doi.org/10.1021/nn505979j*

[228] J. Vaillancourt, H. Zhang, P. Vasinajindakaw, H. Xia, X. Lu, X. Han, ..., M. Renn, "All ink-jet-printed carbon nanotube thin-film transistor on a polyimide substrate with an ultrahigh operating frequency of over 5 GHz". *Appl. Phys. Lett.*, **2008,** *93*, 243301. *https://doi.org/10.1063/1.3043682*

[229] L. G. S. Albano, M. H. Boratto, O. Nunes-Neto, C. F. O. Graeff, "Low voltage and high frequency vertical organic field effect transistor based on rod-coating silver nanowires grid electrode". *Org. Electron.*, **2017,** *50*, 311. *https://doi.org/10.1016/j.orgel.2017.08.011*

[230] Y.-Y. Noh, N. Zhao, M. Caironi, H. Sirringhaus, "Downscaling of self-aligned, all-printed polymer thin-film transistors". *Nat. Nanotechnol.*, **2007,** *2*, 784. *https://doi.org/10.1038/nnano.2007.365*

[231] S. H. Ko, H. Pan, C. P. Grigoropoulos, C. K. Luscombe, J. M. J. Fréchet, D. Poulikakos, "Air stable high resolution organic transistors by selective laser sintering of ink-jet printed metal nanoparticles". *Appl. Phys. Lett.*, **2007,** *90*, 141103. *https://doi.org/10.1063/1.2719162*

[232] Y. Wu, Y. Li, B. S. Ong, P. Liu, S. Gardner, B. Chiang, "High-Performance Organic Thin-Film Transistors with Solution-Printed Gold Contacts". *Adv. Mater.*, **2005,** *17*, 184. *https://doi.org/10.1002/adma.200400690*

[233] W. J. Hyun, E. B. Secor, G. A. Rojas, M. C. Hersam, L. F. Francis, C. D. Frisbie, "All-Printed, Foldable Organic Thin-Film Transistors on Glassine Paper". *Adv. Mater.*, **2015,** *27*, 7058. *https://doi.org/10.1002/adma.201503478*

[234] H. Okimoto, T. Takenobu, K. Yanagi, Y. Miyata, H. Shimotani, H. Kataura, Y. Iwasa, "Tunable Carbon Nanotube Thin-Film Transistors Produced Exclusively via Inkjet Printing". *Adv. Mater.*, **2010,** *22*, 3981. *https://doi.org/10.1002/adma.201000889*

[235] Q. Cao, Z.-T. Zhu, M. G. Lemaitre, M.-G. Xia, M. Shim, J. A. Rogers, "Transparent flexible organic thin-film transistors that use printed single-walled carbon nanotube electrodes". *Appl. Phys. Lett.*, **2006,** *88*. *https://doi.org/10.1063/1.2181190*

[236] L. Cai, S. Zhang, J. Miao, Z. Yu, C. Wang, "Fully Printed Stretchable Thin-Film Transistors and Integrated Logic Circuits". *ACS Nano*, **2016,** *10*, 11459. *https://doi.org/10.1021/acsnano.6b07190*

[237] D. Zielke, A. C. Hübler, U. Hahn, N. Brandt, M. Bartzsch, U. Fügmann, ..., S. Ogier, "Polymer-based organic field-effect transistor using offset printed source/drain structures". *Appl. Phys. Lett.*, **2005,** *87*, 123508. *https://doi.org/10.1063/1.2056579*

[238] H. Sirringhaus, T. Kawase, R. Friend, T. Shimoda, M. Inbasekaran, W. Wu, E. Woo, "High-resolution inkjet printing of all-polymer transistor circuits". *Science*, **2000,** *290*, 2123. *https://doi.org/10.1126/science.290.5499.2123*

[239] S. H. Kim, K. Hong, K. H. Lee, C. D. Frisbie, "Performance and Stability of Aerosol-Jet-Printed Electrolyte-Gated Transistors Based on Poly(3-hexylthiophene)". *ACS Appl. Mater. Interfaces*, **2013,** *5*, 6580. *https://doi.org/10.1021/am401200y*

[240] K. Reuter, H. Kempa, K. D. Deshmukh, H. E. Katz, A. C. Hübler, "Full-swing organic inverters using a charged perfluorinated electret fabricated by means of mass-printing technologies". *Org. Electron.*, **2010,** *11*, 95. *https://doi.org/10.1016/j.orgel.2009.10.004*

[241] T. Mäkelä, S. Jussila, H. Kosonen, T. G. Bäcklund, H. G. O. Sandberg, H. Stubb, "Utilizing roll-to-roll techniques for manufacturing source-drain electrodes for all-

polymer transistors". *Synth. Met.*, **2005,** *153*, 285. *https://doi.org/10.1016/j.synthmet.2005.07.140*

[242] J. Li, S. Qi, J. Liang, L. Li, Y. Xiong, W. Hu, Q. Pei, "Synthesizing a Healable Stretchable Transparent Conductor". *ACS Appl. Mater. Interfaces*, **2015,** *7*, 14140. *https://doi.org/10.1021/acsami.5b03482*

[243] Y. G. Seol, T. Q. Trung, O.-J. Yoon, I.-Y. Sohn, N.-E. Lee, "Nanocomposites of reduced graphene oxide nanosheets and conducting polymer for stretchable transparent conducting electrodes". *J. Mater. Chem.*, **2012,** *22*, 23759. *https://doi.org/10.1039/C2JM33949H*

[244] M.-S. Lee, K. Lee, S.-Y. Kim, H. Lee, J. Park, K.-H. Choi, ..., J.-U. Park, "High-Performance, Transparent, and Stretchable Electrodes Using Graphene–Metal Nanowire Hybrid Structures". *Nano Lett.*, **2013,** *13*, 2814. *https://doi.org/10.1021/nl401070p*

[245] S. Rosset, H. R. Shea, "Flexible and stretchable electrodes for dielectric elastomer actuators". *Appl. Phys. A*, **2013,** *110*, 281. *https://doi.org/10.1007/s00339-012-7402-8*

[246] B. Y. Ahn, E. B. Duoss, M. J. Motala, X. Guo, S.-I. Park, Y. Xiong, ..., J. A. Lewis, "Omnidirectional Printing of Flexible, Stretchable, and Spanning Silver Microelectrodes". *Science*, **2009,** *323*, 1590. *https://doi.org/10.1126/science.1168375*

[247] T. Adrega, S. P. Lacour, "Stretchable gold conductors embedded in PDMS and patterned by photolithography: fabrication and electromechanical characterization". *J. Micromech. Microeng.*, **2010,** *20*, 055025. *https://doi.org/10.1088/0960-1317/20/5/055025*

[248] L. Cai, S. Zhang, Y. Zhang, J. Li, J. Miao, Q. Wang, ..., C. Wang, "Direct Printing for Additive Patterning of Silver Nanowires for Stretchable Sensor and Display Applications". *Adv. Mater. Technol.*, **2018,** *3*, 1700232. *https://doi.org/10.1002/admt.201700232*

[249] S. P. Lacour, S. Wagner, Z. Huang, Z. Suo, "Stretchable gold conductors on elastomeric substrates". *Appl. Phys. Lett.*, **2003,** *82*, 2404. *https://doi.org/10.1063/1.1565683*

[250] A. Chortos, J. Lim, J. W. F. To, M. Vosgueritchian, T. J. Dusseault, T.-H. Kim, ..., Z. Bao, "Highly Stretchable Transistors Using a Microcracked Organic Semiconductor". *Adv. Mater.*, **2014,** *26*, 4253. *https://doi.org/10.1002/adma.201305462*

[251] H.-C. Wu, S. J. Benight, A. Chortos, W.-Y. Lee, J. Mei, J. W. F. To, ..., Z. Bao, "A Rapid and Facile Soft Contact Lamination Method: Evaluation of Polymer Semiconductors for Stretchable Transistors". *Chem. Mater.*, **2014,** *26*, 4544. *https://doi.org/10.1021/cm502271j*

[252] T. Cheng, Y. Zhang, W.-Y. Lai, W. Huang, "Stretchable Thin-Film Electrodes for Flexible Electronics with High Deformability and Stretchability". *Adv. Mater.*, **2015,** *27*, 3349. *https://doi.org/10.1002/adma.201405864*

[253] J. Leppäniemi, O.-H. Huttunen, H. Majumdar, A. Alastalo, "Flexography-Printed In2O3 Semiconductor Layers for High-Mobility Thin-Film Transistors on Flexible Plastic Substrate". *Adv. Mater.*, **2015,** *27*, 7168. *https://doi.org/10.1002/adma.201502569*

[254] S. Dilfer, R. C. Hoffmann, E. Dörsam, "Characteristics of flexographic printed indium–zinc-oxide thin films as an active semiconductor layer in thin film field-effect transistors". *Appl. Surf. Sci.*, **2014,** *320*, 634. *https://doi.org/10.1016/j.apsusc.2014.09.106*

[255] J. H. Cho, J. Lee, Y. Xia, B. Kim, Y. He, M. J. Renn, ..., C. Daniel Frisbie, "Printable ion-gel gate dielectrics for low-voltage polymer thin-film transistors on plastic". *Nat. Mater.*, **2008,** *7*, 900. *https://doi.org/10.1038/nmat2291*

[256] S. G. Higgins, B. V. O. Muir, G. Dell'Erba, A. Perinot, M. Caironi, A. J. Campbell, "Complementary Organic Logic Gates on Plastic Formed by Self-Aligned Transistors with Gravure and Inkjet Printed Dielectric and Semiconductors". *Adv. Electron. Mater.*, **2016,** *2*, 1500272. *https://doi.org/10.1002/aelm.201500272*

[257] H. Yan, Z. Chen, Y. Zheng, C. Newman, J. R. Quinn, F. Dötz, ..., A. Facchetti, "A high-mobility electron-transporting polymer for printed transistors". *Nature*, **2009,** *457*, 679. *https://doi.org/10.1038/nature07727*

[258] K. Fukuda, Y. Yoshimura, T. Okamoto, Y. Takeda, D. Kumaki, Y. Katayama, S. Tokito, "Reverse-Offset Printing Optimized for Scalable Organic Thin-Film Transistors with Submicrometer Channel Lengths". *Adv. Electron. Mater.*, **2015,** *1*, 1500145. *https://doi.org/10.1002/aelm.201500145*

[259] J.-M. Verilhac, M. Benwadih, A.-L. Seiler, S. Jacob, C. Bory, J. Bablet, ..., C. Serbutoviez, "Step toward robust and reliable amorphous polymer field-effect transistors and logic functions made by the use of roll to roll compatible printing processes". *Org. Electron.*, **2010,** *11*, 456. *https://doi.org/10.1016/j.orgel.2009.11.027*

[260] J. Y. Oh, S. Rondeau-Gagné, Y.-C. Chiu, A. Chortos, F. Lissel, G.-J. N. Wang, ..., Z. Bao, "Intrinsically stretchable and healable semiconducting polymer for organic transistors". *Nature*, **2016,** *539*, 411. *https://doi.org/10.1038/nature20102*

[261] M. Shin, J. Y. Oh, K.-E. Byun, Y.-J. Lee, B. Kim, H.-K. Baik, ..., U. Jeong, "Polythiophene Nanofibril Bundles Surface-Embedded in Elastomer: A Route to a

Highly Stretchable Active Channel Layer". *Adv. Mater.*, **2015,** *27*, 1255. *https://doi.org/10.1002/adma.201404602*

[262] M. Shin, J. H. Song, G.-H. Lim, B. Lim, J.-J. Park, U. Jeong, "Highly Stretchable Polymer Transistors Consisting Entirely of Stretchable Device Components". *Adv. Mater.*, **2014,** *26*, 3706. *https://doi.org/10.1002/adma.201400009*

[263] N. Jinsoo, J. Minhun, J. Kyunghwan, L. Gwangyong, K. Joonseok, L. Soyeon, ..., C. Gyoujin, "Fully Gravure-Printed D Flip-Flop on Plastic Foils Using Single-Walled Carbon-Nanotube-Based TFTs". *IEEE Electron Device Lett.*, **2011,** *32*, 638. *https://doi.org/10.1109/LED.2011.2118732*

[264] N. Jinsoo, K. Sungho, J. Kyunghwan, K. Joonseok, C. Sungho, C. Gyoujin, "Fully Gravure Printed Half Adder on Plastic Foils". *IEEE Electron Device Lett.*, **2011,** *32*, 1555. *https://doi.org/10.1109/LED.2011.2165695*

[265] W. Xu, Z. Liu, J. Zhao, W. Xu, W. Gu, X. Zhang, ..., Z. Cui, "Flexible logic circuits based on top-gate thin film transistors with printed semiconductor carbon nanotubes and top electrodes". *Nanoscale*, **2014,** *6*, 14891. *https://doi.org/10.1039/C4NR05471G*

[266] S. G. Bucella, J. M. Salazar-Rios, V. Derenskyi, M. Fritsch, U. Scherf, M. A. Loi, M. Caironi, "Inkjet Printed Single-Walled Carbon Nanotube Based Ambipolar and Unipolar Transistors for High-Performance Complementary Logic Circuits". *Adv. Electron. Mater.*, **2016,** *2*, 1600094. *https://doi.org/10.1002/aelm.201600094*

[267] J. Vaillancourt, H. Zhang, P. Vasinajindakaw, H. Xia, X. Lu, X. Han, ..., M. Renn, "All ink-jet-printed carbon nanotube thin-film transistor on a polyimide substrate with an ultrahigh operating frequency of over 5 GHz". *Appl. Phys. Lett.*, **2008,** *93*. *https://doi.org/10.1063/1.3043682*

[268] A. Sekiguchi, F. Tanaka, T. Saito, Y. Kuwahara, S. Sakurai, D. N. Futaba, ..., K. Hata, "Robust and Soft Elastomeric Electronics Tolerant to Our Daily Lives". *Nano Lett.*, **2015,** *15*, 5716. *https://doi.org/10.1021/acs.nanolett.5b01458*

[269] J. Zhao, Z. Chi, Z. Yang, X. Chen, M. Arnold, Y. Zhang, ..., M. P. Aldred, "Recent developments of truly stretchable thin film electronic and optoelectronic devices". *Nanoscale*, **2018**. *https://doi.org/10.1039/C7NR09472H*

[270] F. Xu, M.-Y. Wu, N. S. Safron, S. S. Roy, R. M. Jacobberger, D. J. Bindl, ..., M. S. Arnold, "Highly Stretchable Carbon Nanotube Transistors with Ion Gel Gate Dielectrics". *Nano Lett.*, **2014,** *14*, 682. *https://doi.org/10.1021/nl403941a*

[271] Q. Cao, H.-s. Kim, N. Pimparkar, J. P. Kulkarni, C. Wang, M. Shim, ..., J. A. Rogers, "Medium-scale carbon nanotube thin-film integrated circuits on flexible plastic substrates". *Nature*, **2008,** *454*, 495. *https://doi.org/10.1038/nature07110*

[272] M. Xia, Z. Cheng, J. Han, S. Zhang, "Extremely stretchable all-carbon-nanotube transistor on flexible and transparent substrates". *Appl. Phys. Lett.*, **2014,** *105*, 143504. *https://doi.org/10.1063/1.4897528*

[273] A. Chortos, G. I. Koleilat, R. Pfattner, D. Kong, P. Lin, R. Nur, ..., Z. Bao, "Mechanically Durable and Highly Stretchable Transistors Employing Carbon Nanotube Semiconductor and Electrodes". *Adv. Mater.*, **2016,** *28*, 4441. *https://doi.org/10.1002/adma.201501828*

[274] M.-Y. Wu, J. Zhao, F. Xu, T.-H. Chang, R. M. Jacobberger, Z. Ma, M. S. Arnold, "Highly stretchable carbon nanotube transistors enabled by buckled ion gel gate dielectrics". *Appl. Phys. Lett.*, **2015,** *107*, 053301. *https://doi.org/10.1063/1.4928041*

[275] J. Liang, L. Li, D. Chen, T. Hajagos, Z. Ren, S.-Y. Chou, ..., Q. Pei, "Intrinsically stretchable and transparent thin-film transistors based on printable silver nanowires, carbon nanotubes and an elastomeric dielectric". *Nat. Commun.*, **2015,** *6*, 7647. *https://doi.org/10.1038/ncomms8647*

[276] J. Liang, K. Tong, Q. Pei, "A Water-Based Silver-Nanowire Screen-Print Ink for the Fabrication of Stretchable Conductors and Wearable Thin-Film Transistors". *Adv. Mater.*, **2016,** *28*, 5986. *https://doi.org/10.1002/adma.201600772*

[277] S.-K. Lee, B. J. Kim, H. Jang, S. C. Yoon, C. Lee, B. H. Hong, ..., J.-H. Ahn, "Stretchable graphene transistors with printed dielectrics and gate electrodes". *Nano Lett.*, **2011,** *11*, 4642. *https://doi.org/10.1021/nl202134z*

[278] J. Li, W. Tang, Q. Wang, W. Sun, Q. Zhang, X. Guo, ..., F. Yan, "Solution-processable organic and hybrid gate dielectrics for printed electronics". *Mater. Sci. Eng. R*, **2018,** *127*, 1. *https://doi.org/10.1016/j.mser.2018.02.004*

[279] S. H. Chae, W. J. Yu, J. J. Bae, D. L. Duong, D. Perello, H. Y. Jeong, ..., Y. H. Lee, "Transferred wrinkled Al2O3 for highly stretchable and transparent graphene–carbon nanotube transistors". *Nat. Mater.*, **2013,** *12*, 403. *https://doi.org/10.1038/nmat3572*

[280] G. Cantarella, C. Vogt, R. Hopf, N. Munzenrieder, P. Andrianakis, L. Petti, ..., G. Tröster, "Buckled Thin-Film Transistors and circuits on soft elastomers for stretchable electronics". *ACS Appl. Mater. Interfaces*, **2017,** *9*, 28750. *https://doi.org/10.1021/acsami.7b08153*

[281] M.-Y. Wu, J. Zhao, N. J. Curley, T.-H. Chang, Z. Ma, M. S. Arnold, "Biaxially stretchable carbon nanotube transistors". *J. Appl. Phys.*, **2017,** *122*, 124901. *https://doi.org/10.1063/1.4991710*

[282] K. Fukuda, Y. Takeda, Y. Yoshimura, R. Shiwaku, L. T. Tran, T. Sekine, ..., S. Tokito, "Fully-printed high-performance organic thin-film transistors and circuitry on one-micron-thick polymer films". *Nat. Commun.*, **2014,** *5*, 4147. *https://doi.org/10.1038/ncomms5147*

[283] M. Kaltenbrunner, T. Sekitani, J. Reeder, T. Yokota, K. Kuribara, T. Tokuhara, ..., T. Someya, "An ultra-lightweight design for imperceptible plastic electronics". *Nature*, **2013,** *499*, 458. *https://doi.org/10.1038/nature12314*

[284] C. Wang, J.-C. Chien, K. Takei, T. Takahashi, J. Nah, A. M. Niknejad, A. Javey, "Extremely Bendable, High-Performance Integrated Circuits Using Semiconducting Carbon Nanotube Networks for Digital, Analog, and Radio-Frequency Applications". *Nano Lett.*, **2012,** *12*, 1527. *https://doi.org/10.1021/nl2043375*

[285] F. N. Ishikawa, H.-k. Chang, K. Ryu, P.-c. Chen, A. Badmaev, L. Gomez De Arco, ..., C. Zhou, "Transparent Electronics Based on Transfer Printed Aligned Carbon Nanotubes on Rigid and Flexible Substrates". *ACS Nano*, **2009,** *3*, 73. *https://doi.org/10.1021/nn800434d*

[286] D. Kim, S. H. Lee, S. Jeong, J. Moon, "All-Ink-Jet Printed Flexible Organic Thin-Film Transistors on Plastic Substrates". *Electrochem. Solid-State Lett.*, **2009,** *12*, H195. *https://doi.org/10.1149/1.3098962*

[287] K. Y. Mitra, M. Polomoshnov, C. Martínez-Domingo, D. Mitra, E. Ramon, R. R. Baumann, "Fully Inkjet-Printed Thin-Film Transistor Array Manufactured on Paper Substrate for Cheap Electronic Applications". *Adv. Electron. Mater.*, **2017,** *3*, 1700275. *https://doi.org/10.1002/aelm.201700275*

[288] S. M. F. Cruz, L. A. Rocha, J. C. Viana, "Printing Technologies on Flexible Substrates for Printed Electronics". in *Flexible Electronics* (Ed: S. Rackauskas), **2018**

[289] S. K. Garlapati, M. Divya, B. Breitung, R. Kruk, H. Hahn, S. Dasgupta, "Printed Electronics Based on Inorganic Semiconductors: From Processes and Materials to Devices". *Adv. Mater.*, **2018,** *30*, 1707600. *https://doi.org/10.1002/adma.201707600*

[290] B. E. Kahn, "Patterning Processes for Flexible Electronics". *Proc. IEEE*, **2015,** *103*, 497. *https://doi.org/10.1109/JPROC.2015.2401553*

[291] R. Parashkov, E. Becker, T. Riedl, H. H. Johannes, W. Kowalsky, "Large Area Electronics Using Printing Methods". *Proc. IEEE*, **2005,** *93*, 1321. *https://doi.org/10.1109/JPROC.2005.850304*

[292] F. C. Krebs, N. Espinosa, M. Hösel, R. R. Søndergaard, M. Jørgensen, "25th Anniversary Article: Rise to Power – OPV-Based Solar Parks". *Adv. Mater.*, **2014,** *26*, 29. *https://doi.org/10.1002/adma.201302031*

[293] D. Deganello, J. A. Cherry, D. T. Gethin, T. C. Claypole, "Patterning of micro-scale conductive networks using reel-to-reel flexographic printing". *Thin Solid Films*, **2010,** *518*, 6113. *https://doi.org/10.1016/j.tsf.2010.05.125*

[294] V. Subramanian, J. Cen, A. d. l. F. Vornbrock, G. Grau, H. Kang, R. Kitsomboonloha, ..., H. Y. Tseng, "High-Speed Printing of Transistors: From Inks to Devices". *Proc. IEEE*, **2015,** *103*, 567. *https://doi.org/10.1109/JPROC.2015.2408321*

[295] N. Hugot, H. Casademont, M. Jouni, N. Hanifi, L. Darchy, J. Azevedo, ..., P. Chenevier, "Gram-scale carbon nanotubes as semiconducting material for highly versatile route of integration in plastic electronics". *Phys. Status Solidi A*, **2016,** *213*, 183. *https://doi.org/10.1002/pssa.201532699*

[296] A. Abdellah, A. Yaqub, C. Ferrari, B. Fabel, P. Lugli, G. Scarpa, "Spray deposition of highly uniform CNT films and their application in gas sensing", presented at *11th IEEE Conference on Nanotechnology (IEEE-NANO)*, **2011**.

[297] C. Girotto, B. P. Rand, S. Steudel, J. Genoe, P. Heremans, "Nanoparticle-based, spray-coated silver top contacts for efficient polymer solar cells". *Org. Electron.*, **2009,** *10*, 735. *https://doi.org/10.1016/j.orgel.2009.03.006*

[298] N. A. Azarova, J. W. Owen, C. A. McLellan, M. A. Grimminger, E. K. Chapman, J. E. Anthony, O. D. Jurchescu, "Fabrication of organic thin-film transistors by spray-deposition for low-cost, large-area electronics". *Org. Electron.*, **2010,** *11*, 1960. *https://doi.org/10.1016/j.orgel.2010.09.008*

[299] A. Abdellah, B. Fabel, P. Lugli, G. Scarpa, "Spray deposition of organic semiconducting thin-films: Towards the fabrication of arbitrary shaped organic electronic devices". *Org. Electron.*, **2010,** *11*, 1031. *https://doi.org/10.1016/j.orgel.2010.02.018*

[300] G. Adamopoulos, A. Bashir, S. Thomas, W. P. Gillin, S. Georgakopoulos, M. Shkunov, ..., T. D. Anthopoulos, "Spray-Deposited Li-Doped ZnO Transistors with Electron Mobility Exceeding 50 cm2/Vs". *Adv. Mater.*, **2010,** *22*, 4764. *https://doi.org/10.1002/adma.201001444*

[301] H. Faber, M. Klaumünzer, M. Voigt, D. Galli, B. F. Vieweg, W. Peukert, ..., M. Halik, "Morphological impact of zinc oxide layers on the device performance in thin-film transistors". *Nanoscale*, **2011,** *3*, 897. *https://doi.org/10.1039/C0NR00800A*

[302] R. Kitsomboonloha, S. J. S. Morris, X. Rong, V. Subramanian, "Femtoliter-Scale Patterning by High-Speed, Highly Scaled Inverse Gravure Printing". *Langmuir*, **2012,** *28*, 16711. *https://doi.org/10.1021/la3037132*

[303] M. Hambsch, K. Reuter, M. Stanel, G. Schmidt, H. Kempa, U. Fügmann, ..., A. Hübler, "Uniformity of fully gravure printed organic field-effect transistors". *Mater. Sci. Eng., B*, **2010,** *170*, 93. *https://doi.org/10.1016/j.mseb.2010.02.035*

[304] M. M. Voigt, A. Guite, D. Y. Chung, R. U. Khan, A. J. Campbell, D. D. Bradley, ..., I. McCulloch, "Polymer field-effect transistors fabricated by the sequential gravure printing of polythiophene, two insulator layers, and a metal ink gate". *Adv. Funct. Mater.*, **2010,** *20*, 239. *https://doi.org/10.1002/adfm.200901597*

[305] Y. Cho, Y. Jeong, Y. Kim, S. Kwon, S.-H. Lee, K. Kim, ..., T.-M. Lee, "Printing Speed and Quality Enhancement by Controlling the Surface Energy of Cliché in Reverse Offset Printing". *Appl. Sci.*, **2017,** *7*, 1302.

[306] M. Kim, I.-K. You, H. Han, S.-W. Jung, T.-Y. Kim, B.-K. Ju, J. B. Koo, "Organic Thin-Film Transistors with Short Channel Length Fabricated by Reverse Offset Printing". *Electrochem. Solid-State Lett.*, **2011,** *14*, H333. *https://doi.org/10.1149/1.3591435*

[307] R. R. Søndergaard, M. Hösel, F. C. Krebs, "Roll-to-Roll fabrication of large area functional organic materials". *J. Polym. Sci., Part B: Polym. Phys.*, **2013,** *51*, 16. *https://doi.org/10.1002/polb.23192*

[308] M. Härting, J. Zhang, D. R. Gamota, D. T. Britton, "Fully printed silicon field effect transistors". *Appl. Phys. Lett.*, **2009,** *94*, 193509. *https://doi.org/10.1063/1.3126958*

[309] M. Pudas, N. Halonen, P. Granat, J. Vähäkangas, "Gravure printing of conductive particulate polymer inks on flexible substrates". *Prog. Org. Coat.*, **2005,** *54*, 310. *https://doi.org/10.1016/j.porgcoat.2005.07.008*

[310] T. M. Higgins, S. Finn, M. Matthiesen, S. Grieger, K. Synnatschke, M. Brohmann, ..., J. Zaumseil, "Electrolyte-Gated n-Type Transistors Produced from Aqueous Inks of WS2 Nanosheets". *Adv. Funct. Mater.*, *0*, 1804387. *https://doi.org/10.1002/adfm.201804387*

[311] N. Zhao, M. Chiesa, H. Sirringhaus, Y. Li, Y. Wu, B. Ong, "Self-aligned inkjet printing of highly conducting gold electrodes with submicron resolution". *J. Appl. Phys.*, **2007,** *101*, 064513. *https://doi.org/10.1063/1.2496249*

[312] B. Kim, M. L. Geier, M. C. Hersam, A. Dodabalapur, "Inkjet printed circuits based on ambipolar and p-type carbon nanotube thin-film transistors". *Sci. Rep.*, **2017,** *7*, 39627. *https://doi.org/10.1038/srep39627*

[313] P. Maisch, K. C. Tam, L. Lucera, H.-J. Egelhaaf, H. Scheiber, E. Maier, C. J. Brabec, "Inkjet printed silver nanowire percolation networks as electrodes for highly efficient semitransparent organic solar cells". *Org. Electron.*, **2016,** *38*, 139. *https://doi.org/10.1016/j.orgel.2016.08.006*

[314] N. Liu, Y. Zhou, N. Ai, C. Luo, J. Peng, J. Wang, ..., Y. Cao, "High-Performance, All-Solution-Processed Organic Nanowire Transistor Arrays with Inkjet-Printing Patterned Electrodes". *Langmuir*, **2011,** *27*, 14710. *https://doi.org/10.1021/la2033324*

[315] J. Z. Wang, Z. H. Zheng, H. W. Li, W. T. S. Huck, H. Sirringhaus, "Dewetting of conducting polymer inkjet droplets on patterned surfaces". *Nat. Mater.*, **2004,** *3*, 171. *https://doi.org/10.1038/nmat1073*

[316] R. P. Tortorich, J.-W. Choi, "Inkjet printing of carbon nanotubes". *Nanomaterials*, **2013,** *3*, 453. *https://doi.org/10.3390/nano3030453*

[317] J.-W. Song, J. Kim, Y.-H. Yoon, B.-S. Choi, J.-H. Kim, C.-S. Han, "Inkjet printing of single-walled carbon nanotubes and electrical characterization of the line pattern". *Nanotechnology*, **2008,** *19*, 095702. *https://doi.org/10.1088/0957-4484/19/9/095702*

[318] Y. Takagi, Y. Nobusa, S. Gocho, H. Kudou, K. Yanagi, H. Kataura, T. Takenobu, "Inkjet printing of aligned single-walled carbon-nanotube thin films". *Appl. Phys. Lett.*, **2013,** *102*. *https://doi.org/10.1063/1.4801496*

[319] K. Kordás, T. Mustonen, G. Tóth, H. Jantunen, M. Lajunen, C. Soldano, ..., P. M. Ajayan, "Inkjet printing of electrically conductive patterns of carbon nanotubes". *Small*, **2006,** *2*, 1021. *https://doi.org/10.1002/smll.200600061*

[320] Y. Nobusa, Y. Yomogida, S. Matsuzaki, K. Yanagi, H. Kataura, T. Takenobu, "Inkjet printing of single-walled carbon nanotube thin-film transistors patterned by surface modification". *Appl. Phys. Lett.*, **2011,** *99*. *https://doi.org/10.1063/1.3657502*

[321] B. Kim, S. Jang, M. L. Geier, P. L. Prabhumirashi, M. C. Hersam, A. Dodabalapur, "High-Speed, Inkjet-Printed Carbon Nanotube/Zinc Tin Oxide Hybrid Complementary Ring Oscillators". *Nano Lett.*, **2014,** *14*, 3683. *https://doi.org/10.1021/nl5016014*

[322] B. Kim, S. Jang, P. L. Prabhumirashi, M. L. Geier, M. C. Hersam, A. Dodabalapur, "Low voltage, high performance inkjet printed carbon nanotube transistors with solution

processed ZrO2 gate insulator". *Appl. Phys. Lett.*, **2013,** *103*, 082119. *https://doi.org/10.1063/1.4819465*

[323] B. Kim, S. Jang, M. L. Geier, P. L. Prabhumirashi, M. C. Hersam, A. Dodabalapur, "Inkjet printed ambipolar transistors and inverters based on carbon nanotube/zinc tin oxide heterostructures". *Appl. Phys. Lett.*, **2014,** *104*, 062101. *https://doi.org/10.1063/1.4864629*

[324] C. W. Lee, S. K. Raman Pillai, X. Luan, Y. Wang, C. M. Li, M. B. Chan-Park, "High-Performance Inkjet Printed Carbon Nanotube Thin Film Transistors with High-k HfO2 Dielectric on Plastic Substrate". *Small*, **2012,** *8*, 2941. *https://doi.org/10.1002/smll.201200041*

[325] C. Gray, J. Wang, G. Duthaler, A. Ritenour, P. S. Drzaic, "Screen printed organic thin film transistors (OTFTs) on a flexible substrate", presented at *International Symposium on Optical Science and Technology*, **2001**.

[326] Y. Zhang, C. Liu, D. Whalley, "Direct-write techniques for maskless production of microelectronics: A review of current state-of-the-art technologies", presented at *International Conference on Electronic Packaging Technology & High Density Packaging (ICEPT-HDP)*, **2009**.

[327] K. Hong, S. H. Kim, A. Mahajan, C. D. Frisbie, "Aerosol Jet Printed p-and n-type Electrolyte-Gated Transistors with a Variety of Electrode Materials: Exploring Practical Routes to Printed Electronics". *ACS Appl. Mater. Interfaces*, **2014,** *6*, 18704. *https://doi.org/10.1021/am504171u*

[328] J. A. Cardenas, M. J. Catenacci, J. B. Andrews, N. X. Williams, B. J. Wiley, A. D. Franklin, "In-Place Printing of Carbon Nanotube Transistors at Low Temperature". *ACS Appl. Nano Mater.*, **2018,** *1*, 1863. *https://doi.org/10.1021/acsanm.8b00269*

[329] K. Hong, S. H. Kim, K. H. Lee, C. D. Frisbie, "Printed, sub-2V ZnO Electrolyte Gated Transistors and Inverters on Plastic". *Adv. Mater.*, **2013,** *25*, 3413. *https://doi.org/10.1002/adma.201300211*

[330] K. Hong, Y. H. Kim, S. H. Kim, W. Xie, W. D. Xu, C. H. Kim, C. D. Frisbie, "Transistors: Aerosol Jet Printed, Sub-2 V Complementary Circuits Constructed from P- and N-Type Electrolyte Gated Transistors". *Adv. Mater.*, **2014,** *26*, 7131. *https://doi.org/10.1002/adma.201401330*

[331] L. Qian, W. Xu, X. Fan, C. Wang, J. Zhang, J. Zhao, Z. Cui, "Electrical and Photoresponse Properties of Printed Thin-Film Transistors Based on Poly(9,9-

dioctylfluorene-co-bithiophene) Sorted Large-Diameter Semiconducting Carbon Nanotubes". *J. Phys. Chem. C*, **2013,** *117*, 18243. *https://doi.org/10.1021/jp4055022*

[332] W. Xu, J. Dou, J. Zhao, H. Tan, J. Ye, M. Tange, ..., Z. Cui, "Printed thin film transistors and CMOS inverters based on semiconducting carbon nanotube ink purified by a nonlinear conjugated copolymer". *Nanoscale*, **2016,** *8*, 4588. *https://doi.org/10.1039/C6NR00015K*

[333] C. Zhou, J. Zhao, J. Ye, M. Tange, X. Zhang, W. Xu, ..., Z. Cui, "Printed thin-film transistors and NO2 gas sensors based on sorted semiconducting carbon nanotubes by isoindigo-based copolymer". *Carbon*, **2016,** *108*, 372. *https://doi.org/10.1016/j.carbon.2016.07.035*

[334] J. Zhao, Y. Gao, J. Lin, Z. Chen, Z. Cui, "Printed thin-film transistors with functionalized single-walled carbon nanotube inks". *J. Mater. Chem.*, **2012,** *22*, 2051. *https://doi.org/10.1039/C1JM14773K*

[335] G. Mattana, A. Loi, M. Woytasik, M. Barbaro, V. Noël, B. Piro, "Inkjet-Printing: A New Fabrication Technology for Organic Transistors". *Adv. Mater. Technol.*, **2017,** *2*, 1700063. *https://doi.org/10.1002/admt.201700063*

[336] E. Gracia-Espino, G. Sala, F. Pino, N. Halonen, J. Luomahaara, J. Mäklin, ..., R. Vajtai, "Electrical Transport and Field-Effect Transistors Using Inkjet-Printed SWCNT Films Having Different Functional Side Groups". *ACS Nano*, **2010,** *4*, 3318. *https://doi.org/10.1021/nn1000723*

[337] H. Okimoto, T. Takenobu, K. Yanagi, Y. Miyata, H. Shimotani, H. Kataura, Y. Iwasa, "Tunable Carbon Nanotube Thin-Film Transistors Produced Exclusively via Inkjet Printing". *Adv. Mater.*, **2010,** *22*, 3981. *https://doi.org/10.1002/adma.201000889*

[338] K.-J. Baeg, M. Caironi, Y.-Y. Noh, "Toward Printed Integrated Circuits based on Unipolar or Ambipolar Polymer Semiconductors". *Adv. Mater.*, **2013,** *25*, 4210. *https://doi.org/10.1002/adma.201205361*

[339] R. Søndergaard, M. Hösel, D. Angmo, T. T. Larsen-Olsen, F. C. Krebs, "Roll-to-roll fabrication of polymer solar cells". *Mater. Today*, **2012,** *15*, 36. *https://doi.org/10.1016/S1369-7021(12)70019-6*

[340] S. Park, M. Vosguerichian, Z. Bao, "A review of fabrication and applications of carbon nanotube film-based flexible electronics". *Nanoscale*, **2013,** *5*, 1727. *https://doi.org/10.1039/C3NR33560G*

[341] L. J. Guo, "Nanoimprint Lithography: Methods and Material Requirements". *Adv. Mater.*, **2007,** *19*, 495. *https://doi.org/10.1002/adma.200600882*

[342] M. Berggren, D. Nilsson, N. D. Robinson, "Organic materials for printed electronics". *Nat. Mater.*, **2007,** *6*, 3. *https://doi.org/10.1038/nmat1817*

[343] H. W. Choi, T. Zhou, M. Singh, G. E. Jabbour, "Recent developments and directions in printed nanomaterials". *Nanoscale*, **2015,** *7*, 3338. *https://doi.org/10.1039/c4nr03915g*

[344] M. Hedges, A. B. Marin, "3D Aerosol Jet Printing - Adding Electronics Functionality to RP/RM ", presented at *Direct Digital Manufacturing Conference (DDMC)*, **2012**.

[345] A. Mahajan, C. D. Frisbie, L. F. Francis, "Optimization of Aerosol Jet Printing for High-Resolution, High-Aspect Ratio Silver Lines". *ACS Appl. Mater. Interfaces*, **2013,** *5*, 4856. *https://doi.org/10.1021/am400606y*

[346] E. Jabari, E. Toyserkani, "Aerosol-Jet printing of highly flexible and conductive graphene/silver patterns". *Mater. Lett.*, **2016,** *174*, 40. *https://doi.org/10.1016/j.matlet.2016.03.082*

[347] R. Taibur, R. Luke, H. Deuk, R. Michael, P. Rahul, "Aerosol based direct-write micro-additive fabrication method for sub-mm 3D metal-dielectric structures". *J. Micromech. Microeng.*, **2015,** *25*, 107002. *https://doi.org/10.1088/0960-1317/25/10/107002*

[348] T. Seifert, E. Sowade, F. Roscher, M. Wiemer, T. Gessner, R. R. Baumann, "Additive Manufacturing Technologies Compared: Morphology of Deposits of Silver Ink Using Inkjet and Aerosol Jet Printing". *Ind. Eng. Chem. Res.*, **2015,** *54*, 769. *https://doi.org/10.1021/ie503636c*

[349] M. Abt, A. Roch, J. A. Qayyum, S. Pestotnik, L. Stepien, A. Abu-Ageel, ..., T. Schuelke, "Aerosol-Printed Highly Conductive Ag Transmission Lines for Flexible Electronic Devices". *IEEE Trans. Compon., Packag., Manuf. Technol.*, **2018,** *8*, 1838. *https://doi.org/10.1109/TCPMT.2018.2869977*

[350] R. Eckstein, G. Hernandez-Sosa, U. Lemmer, N. Mechau, "Aerosol jet printed top grids for organic optoelectronic devices". *Org. Electron.*, **2014,** *15*, 2135. *https://doi.org/10.1016/j.orgel.2014.05.031*

[351] M. Hörteis, S. W. Glunz, "Fine line printed silicon solar cells exceeding 20% efficiency". *Prog. Photovoltaics*, **2008,** *16*, 555. *https://doi.org/10.1002/pip.850*

[352] P. Kopola, B. Zimmermann, A. Filipovic, H.-F. Schleiermacher, J. Greulich, S. Rousu, ..., U. Würfel, "Aerosol jet printed grid for ITO-free inverted organic solar cells". *Sol. Energy Mater. Sol. Cells*, **2012,** *107*, 252. *https://doi.org/10.1016/j.solmat.2012.06.042*

[353] B. Thompson, Y. Hwan-Sik, "Aerosol-Printed Strain Sensor Using PEDOT:PSS". *IEEE Sens. J.*, **2013,** *13*, 4256. *https://doi.org/10.1109/JSEN.2013.2264482*

[354] G. Gu, Y. Ling, R. Liu, P. Vasinajindakaw, X. Lu, C. S. Jones, ..., M. Renn, "All-Printed Thin-Film Transistor Based on Purified Single-Walled Carbon Nanotubes with Linear Response". *J. Nanotechnol.*, **2011,** *2011*, 4. *https://doi.org/10.1155/2011/823680*

[355] R. Eckstein, T. Rödlmeier, T. Glaser, S. Valouch, R. Mauer, U. Lemmer, G. Hernandez-Sosa, "Aerosol-Jet Printed Flexible Organic Photodiodes: Semi-Transparent, Color Neutral, and Highly Efficient". *Adv. Electron. Mater.*, **2015,** *1*, 1500101. *https://doi.org/10.1002/aelm.201500101*

[356] A. A. Gupta, S. Arunachalam, S. G. Cloutier, R. Izquierdo, "Fully Aerosol-Jet Printed, High-Performance Nanoporous ZnO Ultraviolet Photodetectors". *ACS Photonics*, **2018,** *5*, 3923. *https://doi.org/10.1021/acsphotonics.8b00829*

[357] G. L. Goh, S. Agarwala, Y. J. Tan, W. Y. Yeong, "A low cost and flexible carbon nanotube pH sensor fabricated using aerosol jet technology for live cell applications". *Sens. Actuators, B*, **2018,** *260*, 227. *https://doi.org/10.1016/j.snb.2017.12.127*

[358] C. Oakley, P. Chahal, "Aerosol-Jet Printed Quasi-Optical Terahertz Components". *IEEE Trans. Terahertz Sci. Technol.*, **2018**, 1. *https://doi.org/10.1109/TTHZ.2018.2873915*

[359] C. Yang, E. Zhou, S. Miyanishi, K. Hashimoto, K. Tajima, "Preparation of Active Layers in Polymer Solar Cells by Aerosol Jet Printing". *ACS Appl. Mater. Interfaces*, **2011,** *3*, 4053. *https://doi.org/10.1021/am200907k*

[360] R. Eckstein, M. Alt, T. Rödlmeier, P. Scharfer, U. Lemmer, G. Hernandez-Sosa, "Digitally Printed Dewetting Patterns for Self-Organized Microelectronics". *Adv. Mater.*, **2016,** *28*, 7708. *https://doi.org/10.1002/adma.201602082*

[361] I. Grunwald, E. Groth, I. Wirth, J. Schumacher, M. Maiwald, V. Zoellmer, M. Busse, "Surface biofunctionalization and production of miniaturized sensor structures using aerosol printing technologies". *Biofabrication*, **2010,** *2*, 014106. *https://doi.org/10.1088/1758-5082/2/1/014106*

[362] C. Muratore, A. T. Juhl, A. J. Stroud, D. W. Lai, A. M. Jawaid, K. M. Burzynski, ..., R. R. Naik, "Printed biomolecular templates for 2D material patterning". *Appl. Phys. Lett.*, **2018,** *112*, 233704. *https://doi.org/10.1063/1.5032090*

[363] H. Majd, P. J. Wipff, L. Buscemi, M. Bueno, D. Vonwil, T. M. Quinn, B. Hinz, "A novel method of dynamic culture surface expansion improves mesenchymal stem cell

proliferation and phenotype". *Stem Cells*, **2009,** *27*, 200. *https://doi.org/10.1634/stemcells.2008-0674*

[364] L. Wengeler, B. Schmidt-Hansberg, K. Peters, P. Scharfer, W. Schabel, "Investigations on knife and slot die coating and processing of polymer nanoparticle films for hybrid polymer solar cells". *Chem. Eng. Process.*, **2011,** *50*, 478. *https://doi.org/10.1016/j.cep.2010.11.002*

[365] A. Sandström, H. F. Dam, F. C. Krebs, L. Edman, "Ambient fabrication of flexible and large-area organic light-emitting devices using slot-die coating". *Nat. Commun.*, **2012,** *3*, 1002. *https://doi.org/10.1038/ncomms2002*

[366] H. Youn, K. Jeon, S. Shin, M. Yang, "All-solution blade–slit coated polymer light-emitting diodes". *Org. Electron.*, **2012,** *13*, 1470. *https://doi.org/10.1016/j.orgel.2012.04.008*

[367] C.-Y. Chen, H.-W. Chang, Y.-F. Chang, B.-J. Chang, Y.-S. Lin, P.-S. Jian, ..., Y.-C. Chao, "Continuous blade coating for multi-layer large-area organic light-emitting diode and solar cell". *J. Appl. Phys.*, **2011,** *110*, 094501. *https://doi.org/10.1063/1.3636398*

[368] B. Chen, P. Zhang, L. Ding, J. Han, S. Qiu, Q. Li, ..., L. M. Peng, "Highly Uniform Carbon Nanotube Field-Effect Transistors and Medium Scale Integrated Circuits". *Nano Lett.*, **2016,** *16*, 5120. *https://doi.org/10.1021/acs.nanolett.6b02046*

[369] C. Yeom, K. Chen, D. Kiriya, Z. Yu, G. Cho, A. Javey, "Large-Area Compliant Tactile Sensors Using Printed Carbon Nanotube Active-Matrix Backplanes". *Adv. Mater.*, **2015,** *27*, 1561. *https://doi.org/10.1002/adma.201404850*

[370] J. Zhang, Y. Fu, C. Wang, P.-C. Chen, Z. Liu, W. Wei, ..., C. Zhou, "Separated Carbon Nanotube Macroelectronics for Active Matrix Organic Light-Emitting Diode Displays". *Nano Lett.*, **2011,** *11*, 4852. *https://doi.org/10.1021/nl202695v*

[371] D. H. Lee, J. S. Choi, H. Chae, C. H. Chung, S. M. Cho, "Highly efficient phosphorescent polymer OLEDs fabricated by screen printing". *Displays*, **2008,** *29*, 436. *https://doi.org/10.1016/j.displa.2008.02.006*

[372] M. Manceau, D. Angmo, M. Jørgensen, F. C. Krebs, "ITO-free flexible polymer solar cells: from small model devices to roll-to-roll processed large modules". *Org. Electron.*, **2011,** *12*, 566. *https://doi.org/10.1016/j.orgel.2011.01.009*

[373] F. C. Krebs, M. Jørgensen, K. Norrman, O. Hagemann, J. Alstrup, T. D. Nielsen, ..., J. Kristensen, "A complete process for production of flexible large area polymer solar cells

entirely using screen printing – first public demonstration". *Sol. Energy Mater. Sol. Cells*, **2009,** *93*, 422. *https://doi.org/10.1016/j.solmat.2008.12.001*

[374] A. C. Hübler, F. Doetz, H. Kempa, H. E. Katz, M. Bartzsch, N. Brandt, ..., J. Granstrom, "Ring oscillator fabricated completely by means of mass-printing technologies". *Org. Electron.*, **2007,** *8*, 480. *https://doi.org/10.1016/j.orgel.2007.02.009*

[375] J. A. Paulsen, M. Renn, K. Christenson, R. Plourde, "Printing conformal electronics on 3D structures with Aerosol Jet technology", presented at *Future of Instrumentation International Workshop (FIIW)*, **2012**.

[376] J. Seonpil, K. Seohee, L. G. Michael, C. H. Mark, D. Ananth, "Inkjet printed carbon nanotubes in short channel field effect transistors: influence of nanotube distortion and gate insulator interface modification". *Flex. Print. Electron.*, **2016,** *1*, 035001. *https://doi.org/10.1088/2058-8585/1/3/035001*

[377] Y. Wang, H. Guo, J.-j. Chen, E. Sowade, Y. Wang, K. Liang, ..., Z.-s. Feng, "Paper-Based Inkjet-Printed Flexible Electronic Circuits". *ACS Appl. Mater. Interfaces*, **2016,** *8*, 26112. *https://doi.org/10.1021/acsami.6b06704*

[378] F. Hennrich, R. Krupke, K. Arnold, J. A. Rojas Stütz, S. Lebedkin, T. Koch, ..., M. M. Kappes, "The mechanism of cavitation-induced scission of single-walled carbon nanotubes". *J. Phys. Chem. B*, **2007,** *111*, 1932. *https://doi.org/10.1021/jp065262n*

[379] J. Navratil, A. Hamacek, J. Reboun, R. Soukup, "Perspective methods of creating conductive paths by Aerosol Jet Printing technology", presented at *38th International Spring Seminar onElectronics Technology (ISSE)*, **2015**.

[380] M. J. O'Connell, S. M. Bachilo, C. B. Huffman, V. C. Moore, M. S. Strano, E. H. Haroz, ..., R. E. Smalley, "Band Gap Fluorescence from Individual Single-Walled Carbon Nanotubes". *Science*, **2002,** *297*, 593. *https://doi.org/10.1126/science.1072631*

[381] A. V. Naumov, S. Ghosh, D. A. Tsyboulski, S. M. Bachilo, R. B. Weisman, "Analyzing Absorption Backgrounds in Single-Walled Carbon Nanotube Spectra". *ACS Nano*, **2011,** *5*, 1639. *https://doi.org/10.1021/nn1035922*

[382] A. H. Krall, J. V. Sengers, J. Kestin, "Viscosity of liquid toluene at temperatures from 25 to 150 °C and at pressures up to 30 MPa". *J. Chem. Eng. Data*, **1992,** *37*, 349. *https://doi.org/10.1021/je00007a021*

[383] S. Oswal, M. V. Rathnam, "Viscosity data of binary mixtures: ethyl acetate+ cyclohexane,+ benzene,+ toluene,+ ethylbenzene+ carbon tetrachloride, and+

chloroform at 303.15 K". *Can. J. Chem.*, **1984,** *62*, 2851. *https://doi.org/doi.org/10.1139/v84-482*

[384] S. Mouri, Y. Miyauchi, K. Matsuda, "Dispersion-Process Effects on the Photoluminescence Quantum Yields of Single-Walled Carbon Nanotubes Dispersed Using Aromatic Polymers". *J. Phys. Chem. C*, **2012,** *116*, 10282. *https://doi.org/10.1021/jp212040y*

[385] A. Malhofer, M. Rother, Y. Zakharko, A. Graf, S. P. Schießl, J. Zaumseil, "Direct visualization of percolation paths in carbon nanotube/polymer composites". *Org. Electron.*, **2017,** *45*, 151. *https://doi.org/10.1016/j.orgel.2017.03.010*

[386] Y. Kuwahara, F. Nihey, S. Ohmori, T. Saito, "Length dependent performance of single-wall carbon nanotube thin film transistors". *Carbon*, **2015,** *91*, 370. *https://doi.org/10.1016/j.carbon.2015.05.008*

[387] M. Kastner, S. Stahl, I. Vollert, C. Loi, N. Rühl, T. Hertel, F. Schöppler, "A comparison of Raman and photoluminescence spectra for the assessment of single-wall carbon nanotube sample quality". *Chem. Phys. Lett.*, **2015,** *635*, 245. *https://doi.org/10.1016/j.cplett.2015.06.076*

[388] H. Steckel, F. Eskandar, "Factors affecting aerosol performance during nebulization with jet and ultrasonic nebulizers". *Eur. J. Pharm. Sci.*, **2003,** *19*, 443. *https://doi.org/10.1016/S0928-0987(03)00148-9*

[389] J. H. Dennis, S. C. Stenton, J. R. Beach, A. J. Avery, E. H. Walters, D. J. Hendrick, "Jet and ultrasonic nebuliser output: use of a new method for direct measurement of aerosol output". *Thorax*, **1990,** *45*, 728. *https://doi.org/10.1136/thx.45.10.728*

[390] R. W. Niven, A. Y. Ip, S. Mittelman, S. J. Prestrelski, T. Arakawa, "Some Factors Associated with the Ultrasonic Nebulization of Proteins". *Pharm. Res.*, **1995,** *12*, 53. *https://doi.org/10.1023/a:1016282502954*

[391] O. N. M. McCallion, K. M. G. Taylor, M. Thomas, A. J. Taylor, "Nebulization of Fluids of Different Physicochemical Properties with Air-Jet and Ultrasonic Nebulizers". *Pharm. Res.*, **1995,** *12*, 1682. *https://doi.org/10.1023/a:1016205520044*

[392] I. A. Kinloch, S. A. Roberts, A. H. Windle, "A rheological study of concentrated aqueous nanotube dispersions". *Polymer*, **2002,** *43*, 7483. *https://doi.org/10.1016/S0032-3861(02)00664-X*

[393] A. N. G. Parra-Vasquez, I. Stepanek, V. A. Davis, V. C. Moore, E. H. Haroz, J. Shaver, ..., M. Pasquali, "Simple length determination of single-walled carbon nanotubes by

viscosity measurements in dilute suspensions". *Macromolecules*, **2007,** *40*, 4043. *https://doi.org/10.1021/ma062003n*

[394] L. Maillaud, P. Poulin, M. Pasquali, C. Zakri, "Effect of the Rheological Properties of Carbon Nanotube Dispersions on the Processing and Properties of Transparent Conductive Electrodes". *Langmuir*, **2015,** *31*, 5928. *https://doi.org/10.1021/acs.langmuir.5b00887*

[395] T. Takahashi, K. Takei, A. G. Gillies, R. S. Fearing, A. Javey, "Carbon Nanotube Active-Matrix Backplanes for Conformal Electronics and Sensors". *Nano Lett.*, **2011,** *11*, 5408. *https://doi.org/10.1021/nl203117h*

[396] L. Cai, S. M. Zhang, J. S. Miao, Z. B. Yu, C. Wang, "Fully Printed Foldable Integrated Logic Gates with Tunable Performance Using Semiconducting Carbon Nanotubes". *Adv. Funct. Mater.*, **2015,** *25*, 5698. *https://doi.org/10.1002/adfm.201502367*

[397] M. L. Geier, J. J. McMorrow, W. Xu, J. Zhu, C. H. Kim, T. J. Marks, M. C. Hersam, "Solution-processed carbon nanotube thin-film complementary static random access memory". *Nat. Nanotechnol.*, **2015,** *10*, 944. *https://doi.org/10.1038/nnano.2015.197*

[398] A. D. Franklin, D. B. Farmer, W. Haensch, "Defining and Overcoming the Contact Resistance Challenge in Scaled Carbon Nanotube Transistors". *ACS Nano*, **2014,** *8*, 7333. *https://doi.org/10.1021/nn5024363*

[399] J. Smith, W. Zhang, R. Sougrat, K. Zhao, R. Li, D. Cha, ..., T. D. Anthopoulos, "Solution-Processed Small Molecule-Polymer Blend Organic Thin-Film Transistors with Hole Mobility Greater than 5 cm2/Vs". *Adv. Mater.*, **2012,** *24*, 2441. *https://doi.org/10.1002/adma.201200088*

[400] S. P. Schießl, F. Gannott, S. H. Etschel, M. Schweiger, S. Grünler, M. Halik, J. Zaumseil, "Self-Assembled Monolayer Dielectrics for Low-Voltage Carbon Nanotube Transistors with Controlled Network Density". *Adv. Mater. Interfaces*, **2016,** *3*, 1600215. *https://doi.org/10.1002/admi.201600215*

[401] W. Kim, A. Javey, O. Vermesh, Q. Wang, Y. Li, H. Dai, "Hysteresis Caused by Water Molecules in Carbon Nanotube Field-Effect Transistors". *Nano Lett.*, **2003,** *3*, 193. *https://doi.org/10.1021/nl0259232*

[402] C. M. Aguirre, P. L. Levesque, M. Paillet, F. Lapointe, B. C. St-Antoine, P. Desjardins, R. Martel, "The Role of the Oxygen/Water Redox Couple in Suppressing Electron Conduction in Field-Effect Transistors". *Adv. Mater.*, **2009,** *21*, 3087. *https://doi.org/10.1002/adma.200900550*

[403] M. Nikolka, I. Nasrallah, B. Rose, M. K. Ravva, K. Broch, A. Sadhanala, ..., A. Brown, "High operational and environmental stability of high-mobility conjugated polymer field-effect transistors through the use of molecular additives". *Nat. Mater.*, **2016**. *https://doi.org/10.1038/nmat4785*

[404] J. K. Streit, S. M. Bachilo, S. Ghosh, C.-W. Lin, R. B. Weisman, "Directly Measured Optical Absorption Cross Sections for Structure-Selected Single-Walled Carbon Nanotubes". *Nano Lett.*, **2014,** *14*, 1530. *https://doi.org/10.1021/nl404791y*

[405] A. Graf, M. Held, Y. Zakharko, L. Tropf, M. C. Gather, J. Zaumseil, "Electrical pumping and tuning of exciton-polaritons in carbon nanotube microcavities". *Nat. Mater.*, **2017,** *16*, 911. *https://doi.org/10.1038/nmat4940*

[406] M. L. Moser, G. Li, M. Chen, E. Bekyarova, M. E. Itkis, R. C. Haddon, "Fast Electrochromic Device Based on Single-Walled Carbon Nanotube Thin Films". *Nano Lett.*, **2016,** *16*, 5386. *https://doi.org/10.1021/acs.nanolett.6b01564*

[407] X. He, W. Gao, L. Xie, B. Li, Q. Zhang, S. Lei, ..., W. Wang, "Wafer-scale monodomain films of spontaneously aligned single-walled carbon nanotubes". *Nat. Nanotechnol.*, **2016,** *11*, 633. *https://doi.org/10.1038/nnano.2016.44*

[408] Y. Zakharko, A. Graf, J. Zaumseil, "Plasmonic Crystals for Strong Light–Matter Coupling in Carbon Nanotubes". *Nano Lett.*, **2016,** *16*, 6504. *https://doi.org/10.1021/acs.nanolett.6b03086*

[409] Y. Zakharko, A. Graf, S. P. Schießl, B. Hähnlein, J. Pezoldt, M. C. Gather, J. Zaumseil, "Broadband Tunable, Polarization-Selective and Directional Emission of (6,5) Carbon Nanotubes Coupled to Plasmonic Crystals". *Nano Lett.*, **2016,** *16*, 3278. *https://doi.org/10.1021/acs.nanolett.6b00827*

[410] Y. Zakharko, M. Rother, A. Graf, B. Hähnlein, M. Brohmann, J. Pezoldt, J. Zaumseil, "Radiative Pumping and Propagation of Plexcitons in Diffractive Plasmonic Crystals". *Nano Lett.*, **2018,** *18*, 4927. *https://doi.org/10.1021/acs.nanolett.8b01733*

[411] D. Sung, A. d. l. F. Vornbrock, V. Subramanian, "Scaling and Optimization of Gravure-Printed Silver Nanoparticle Lines for Printed Electronics". *IEEE Trans. Compon. Packag. Technol.*, **2010,** *33*, 105. *https://doi.org/10.1109/TCAPT.2009.2021464*

[412] C. W. Sele, T. von Werne, R. H. Friend, H. Sirringhaus, "Lithography-free, self-aligned inkjet printing with sub-hundred-nanometer resolution". *Adv. Mater.*, **2005,** *17*, 997. *https://doi.org/10.1002/adma.200401285*

[413] H. Kwon, M. Kim, H. Cho, H. Moon, J. Lee, S. Yoo, "Toward High-Output Organic Vertical Field Effect Transistors: Key Design Parameters". *Adv. Funct. Mater.*, **2016,** *26*, 6888. *https://doi.org/10.1002/adfm.201601956*

[414] L. Ma, Y. Yang, "Unique architecture and concept for high-performance organic transistors". *Appl. Phys. Lett.*, **2004,** *85*, 5084. *https://doi.org/10.1063/1.1821629*

[415] A. J. Ben-Sasson, E. Avnon, E. Ploshnik, O. Globerman, R. Shenhar, G. L. Frey, N. Tessler, "Patterned electrode vertical field effect transistor fabricated using block copolymer nanotemplates". *Appl. Phys. Lett.*, **2009,** *95*, 213301. *https://doi.org/10.1063/1.3266855*

[416] B. Liu, M. A. McCarthy, Y. Yoon, D. Y. Kim, Z. Wu, F. So, ..., A. G. Rinzler, "Carbon-Nanotube-Enabled Vertical Field Effect and Light-Emitting Transistors". *Adv. Mater.*, **2008,** *20*, 3605. *https://doi.org/10.1002/adma.200800601*

[417] K. Swathi, K. S. Narayan, "Self-Assembled Porous Alumina Based Organic Nanotriode Arrays". *Nano Lett.*, **2017,** *17*, 7945. *https://doi.org/10.1021/acs.nanolett.7b04359*

[418] M. P. Klinger, A. Fischer, F. Kaschura, R. Scholz, B. Lüssem, B. Kheradmand-Boroujeni, ..., K. Leo, "Advanced Organic Permeable-Base Transistor with Superior Performance". *Adv. Mater.*, **2015,** *27*, 7734. *https://doi.org/10.1002/adma.201502788*

[419] J. Zaumseil, F. Jakubka, M. Wang, F. Gannott, "In Situ Raman Mapping of Charge Carrier Distribution in Electrolyte-Gated Carbon Nanotube Network Field-Effect Transistors". *J. Phys. Chem. C*, **2013,** *117*, 26361. *https://doi.org/10.1021/jp409849w*

[420] S. K. Samanta, M. Fritsch, U. Scherf, W. Gomulya, S. Z. Bisri, M. A. Loi, "Conjugated Polymer-Assisted Dispersion of Single-Wall Carbon Nanotubes: The Power of Polymer Wrapping". *Acc. Chem. Res.*, **2014**. *https://doi.org/10.1021/ar500141j*

[421] Y. Li, D. Mann, M. Rolandi, W. Kim, A. Ural, S. Hung, ..., H. Dai, "Preferential Growth of Semiconducting Single-Walled Carbon Nanotubes by a Plasma Enhanced CVD Method". *Nano Lett.*, **2004,** *4*, 317. *https://doi.org/10.1021/nl035097c*

[422] C. Wang, J. Zhang, K. Ryu, A. Badmaev, L. G. De Arco, C. Zhou, "Wafer-Scale Fabrication of Separated Carbon Nanotube Thin-Film Transistors for Display Applications". *Nano Lett.*, **2009,** *9*, 4285. *https://doi.org/10.1021/nl902522f*

[423] R. A. Matula, "Electrical resistivity of copper, gold, palladium, and silver". *J. Phys. Chem. Ref. Data*, **1979,** *8*, 1147. *https://doi.org/10.1063/1.555614*

[424] M. Smith, Y. S. Choi, C. Boughey, S. Kar-Narayan, "Controlling and assessing the quality of aerosol jet printed features for large area and flexible electronics". *Flex. Print. Electron.*, **2017,** *2*, 015004. *https://doi.org/10.1088/2058-8585/aa5af9*

[425] M. Held, P. Laiho, A. Kaskela, F. Gannott, M. Rother, E. Kauppinen, J. Zaumseil, "Dense Carbon Nanotube Films as Transparent Electrodes in Low-Voltage Polymer and All-Carbon Transistors". *Adv. Electron. Mater.*, **2017**, 1700331. *https://doi.org/10.1002/aelm.201700331*

[426] N. Stutzmann, R. H. Friend, H. Sirringhaus, "Self-Aligned, Vertical-Channel, Polymer Field-Effect Transistors". *Science*, **2003,** *299*, 1881. *https://doi.org/10.1126/science.1081279*

[427] T. Georgiou, R. Jalil, B. D. Belle, L. Britnell, R. V. Gorbachev, S. V. Morozov, ..., A. Mishchenko, "Vertical field-effect transistor based on graphene–WS2 heterostructures for flexible and transparent electronics". *Nat. Nanotechnol.*, **2012,** *8*, 100. *https://doi.org/10.1038/nnano.2012.224*

[428] Y. Liu, H. Zhou, R. Cheng, W. Yu, Y. Huang, X. Duan, "Highly Flexible Electronics from Scalable Vertical Thin Film Transistors". *Nano Lett.*, **2014,** *14*, 1413. *https://doi.org/10.1021/nl404484s*

[429] J. Chen, R. Könenkamp, "Vertical nanowire transistor in flexible polymer foil". *Appl. Phys. Lett.*, **2003,** *82*, 4782. *https://doi.org/10.1063/1.1587258*

[430] D. R. Dykaar, R. S. Tarighat, F. Chen, T. Davidson-Hall, G. Hill, J. Vieth, ..., S. Sivoththaman, "Active Backplane Design for Digital Video Walls", presented at *Society for Information Display - International Symposium*, **2017**.

[431] P. G. Collins, K. Bradley, M. Ishigami, A. Zettl, "Extreme Oxygen Sensitivity of Electronic Properties of Carbon Nanotubes". *Science*, **2000,** *287*, 1801. *https://doi.org/10.1126/science.287.5459.1801*

[432] V. Chakrapani, G. U. Sumanasekera, B. Abeyweera, A. Sherehiy, J. C. Angus, "Electrochemically Induced p-Type Conductivity in Carbon Nanotubes". *ECS Solid State Lett.*, **2013,** *2*, M57. *https://doi.org/10.1149/2.004311ssl*

[433] Q. Cao, S. H. Hur, Z. T. Zhu, Y. G. Sun, C. J. Wang, M. A. Meitl, ..., J. A. Rogers, "Highly Bendable, Transparent Thin-Film Transistors That Use Carbon-Nanotube-Based Conductors and Semiconductors with Elastomeric Dielectrics". *Adv. Mater.*, **2006,** *18*, 304. *https://doi.org/10.1002/adma.200501740*

[434] S.-H. Hur, C. Kocabas, A. Gaur, O. O. Park, M. Shim, J. A. Rogers, "Printed thin-film transistors and complementary logic gates that use polymer-coated single-walled carbon nanotube networks". *J. Appl. Phys.*, **2005,** *98*, 114302.
https://doi.org/10.1063/1.2135415

APPENDIX

A. LIST OF FREQUENTLY USED ABBREVIATIONS

(c-)AFM	(Conductive) atomic force microscope
AJ	Aerosol-jet
ALD	Atomic layer deposition
CNT	Semiconducting carbon nanotube, if not mentioned otherwise
CVD	Chemical vapor deposition
DNA	Deoxyribonucleic acid
DOS	Density of states
EDLT	Electric double-layer transistor
EGT	Electrolyte-gated transistor
EMIM	1-ethyl-3-methylimidazolium
FAP	tris(pentaflouroethyl)trifluorophosphate
FET	Field-effect transistor
HfO_x	Hafnium oxide
IPA	Isopropyl alcohole (propan-2-ol)
ISFET	Ion-sensitive field-effect transistor
LED	Light-emitting diode
LEGT	Lateral electrolyte-gated transistor
m-CNT	Metallic carbon nanotube
NIR	Near-infrared
NMP	*N*-methylpyrrolidone
OECT	Organic electrochemical transistor

OEGT	Organic electrolyte-gated transistor
P(VDF-HFP)	Poly(vinylidene fluoride-*co*-hexafluoropropylene)
P3HT	Poly(3-hexylthiophene)
PDMS	Poly(dimethylsiloxane)
PEDOT	Poly(3,4-ethylenedioxythiophene)
PEG	Poly(ethylene glycol)
PEN	Poly(ethylene naphthalate)
PFO-BPy	Poly[(9,9-dioctylfluorenyl-2,7-diyl)-*alt-co*-(6,6′-(2,2′-bipyridine))]
PMMA	Poly(methyl methacrylate)
PSS	Poly(styrene sulfonic acid)
PTFE	Poly(tetrafluoroethylene)
PVP	Poly(vynilphenol)
RBM	Radial breathing mode
RFID	Radiofrequency identification
SC	Sodium cholate
SDS	Sodium dodecyl sulfate
SEM	Scanning electron microscope
TDMAH	Tetrakis(dimethylamino)hafnium
TFT	Thin film transistor
UV	Ultraviolet
VEGT	Vertical electrolyte-gated transistor
vis	Visible

B. LIST OF FREQUENTLY USED SYMBOLS

(n,m)	Notation of the CNT chirality
μ	Charge carrier mobility
A	Area
C	Capacitance
c	Concentration
E	Energy
e^-	Electron
F	Electric field
G	Conductance
h^+	Hole
I	Current
I_{ds}	Source–drain current
I_g	Gate current / gate leakage
L	Channel length
Q	Charge
R	Bending radius
SS	Subthreshold slope
t	Thickness
v	Velocity (of the AJ printer stage)
V	Volume
V_{ds}	Source–drain voltage
V_g	Gate voltage
V_{on}	Turn-on voltage
V_{th}	Threshold voltage
W	Channel width
$W_{d/s}$	Width of drain/source electrode
Δ	Difference
$\epsilon_{0/r}$	Vacuum/Relative permittivity
Θ	Chiral angle
λ	Wavelength
ω	Raman shift

C. LIST OF FIGURES

D. LIST OF TABLES

E. PUBLICATIONS

Publications in Peer-Reviewed Journals

[1] **M. Rother**, A. Kruse, M. Brohmann, M. Matthiesen, S. Grieger, T. M. Higgins, J. Zaumseil, "Vertical Electrolyte-Gated Transistors Based on Printed Single-Walled Carbon Nanotubes". ACS Appl. Nano Mater. 2018.
https://doi.org/10.1021/acsanm.8b00756

[2] **M. Rother**, M. Brohmann, S. Yang, S. B. Grimm, S. P. Schießl, A. Graf, J. Zaumseil, "Aerosol-Jet Printing of Polymer-Sorted (6,5) Carbon Nanotubes for Field-Effect Transistors with High Reproducibility". Adv. Electron. Mater. 2017, 3, 1700080.
https://doi.org/10.1002/aelm.201700080

[3] **M. Rother**, S. P. Schießl, Y. Zakharko, F. Gannott, J. Zaumseil, "Understanding Charge Transport in Mixed Networks of Semiconducting Carbon Nanotubes". ACS Appl. Mater. Interfaces 2016, 8, 5571.
https://doi.org/10.1021/acsami.6b00074

[4] T. M. Higgins, S. Finn, M. Matthiesen, S. Grieger, K. Synnatschke, M. Brohmann, **M. Rother**, C. Backes, J. Zaumseil, "Electrolyte-Gated n-Type Transistors Produced from Aqueous Inks of WS_2 Nanosheets". Adv. Funct. Mater. 2018, 1804387.
https://doi.org/10.1002/adfm.201804387

[5] M. Brohmann, **M. Rother**, S. P. Schießl, E. Preis, S. Allard, U. Scherf, J. Zaumseil, "Temperature-Dependent Charge Transport in Polymer-Sorted Semiconducting Carbon Nanotube Networks with Different Diameter Distributions". J. Phys. Chem. C 2018.
https://doi.org/10.1021/acs.jpcc.8b04302

[6] Y. Zakharko, **M. Rother**, A. Graf, B. Hähnlein, M. Brohmann, J. Pezoldt, J. Zaumseil, "Radiative Pumping and Propagation of Plexcitons in Diffractive Plasmonic Crystals". Nano Lett. 2018, 18, 4927.
https://doi.org/10.1021/acs.nanolett.8b01733

[7] S. Schneider, M. Brohmann, R. Lorenz, Y. J. Hofstetter, **M. Rother**, E. Sauter, M. Zharnikov, Y. Vaynzof, H.-J. Himmel, J. Zaumseil, "Efficient n-Doping and Hole-Blocking in Single-Walled Carbon Nanotube Transistors with 1, 2, 4, 5-Tetrakis (tetramethyl-guanidino) benzene". ACS Nano 2018.
https://doi.org/10.1021/acsnano.8b02061

[8] J. Berger, T. M. Higgins, M. Rother, A. Graf, Y. Zakharko, S. Allard, ..., J. Zaumseil, "From Broadband to Electrochromic Notch Filters with Printed Monochiral Carbon Nanotubes". ACS Appl. Mater. Interfaces 2018, 10, 11135. *https://doi.org/10.1021/acsami.8b00643*

[9] M. S. Filipiak, **M. Rother**, N. M. Andoy, A. C. Knudsen, S. Grimm, C. Bachran, ..., A. Tarasov, "Highly sensitive, selective and label-free protein detection in physiological solutions using carbon nanotube transistors with nanobody receptors". Sensors Actuators B: Chem. 2018, 255, 1507. *https://doi.org/10.1016/j.snb.2017.08.164*

[10] M. Held, P. Laiho, A. Kaskela, F. Gannott, **M. Rother**, E. Kauppinen, J. Zaumseil, "Dense Carbon Nanotube Films as Transparent Electrodes in Low-Voltage Polymer and All-Carbon Transistors". Adv. Electron. Mater. 2017, 1700331. *https://doi.org/10.1002/aelm.201700331*

[11] S. P. Schießl, X. de Vries, **M. Rother**, A. Massé, M. Brohmann, P. A. Bobbert, J. Zaumseil, "Modeling carrier density dependent charge transport in semiconducting carbon nanotube networks". Phys. Rev. Mater. 2017, 1, 046003. *https://doi.org/10.1103/PhysRevMaterials.1.046003*

[12] S. P. Schießl, **M. Rother**, J. Lüttgens, J. Zaumseil, "Extracting the field-effect mobilities of random semiconducting single-walled carbon nanotube networks: A critical comparison of methods". Appl. Phys. Lett. 2017, 111, 193301. *https://doi.org/10.1063/1.5006877*

[13] A. Malhofer, **M. Rother**, Y. Zakharko, A. Graf, S. P. Schießl, J. Zaumseil, "Direct visualization of percolation paths in carbon nanotube/polymer composites". Org. Electron. 2017, 45, 151. *https://doi.org/10.1016/j.orgel.2017.03.010*

[14] S. Grimm, S. P. Schießl, Y. Zakharko, **M. Rother**, M. Brohmann, J. Zaumseil, "Doping-dependent G-mode shifts of small diameter semiconducting single-walled carbon nanotubes". Carbon 2017, 118, 261. *https://doi.org/10.1016/j.carbon.2017.03.040*

Conference Contributions – Oral

[1] "Aerosol-Jet Printing of Polymer-wrapped (6,5) Carbon Nanotubes for Field-effect Transistors", *5th Carbon Nanotube Thin Film Electronics and Applications Satellite,* Belo Horizonte, Brazil, June 2017

[2] "Highly Reproducible Aerosol-Jet Printing of polymer-wrapped (6,5) Carbon Nanotubes as Semiconductor in High on/off-ratio Field-effect Transistors", *12th International Thin-Film Transistor Conference,* Austin, TX, United States of America, February 2017

[3] "Carbon Nanotube Electroluminescence as a Quantitative Measure for Charge Transport in mixed Networks", *European Materials Research Society Meeting*, Lille, France, May 2016

Conference Contributions – Poster

[1] "Vertical Electrolyte-Gated Transistors Based on Printed Single-Walled Carbon Nanotubes", *14th International Conference on Organic Electronics*, Bordeaux, France, June 2018, awarded **IdEx Bordeaux Poster Prize**

[2] "Vertical Charge Transport in Printed Networks of Semiconducting Single-walled Carbon Nanotubes", *18th International Conference on the Science and Application of Nanotubes and Low-dimensional Materials*, Belo Horizonte, Brazil, June 2017

[3] "Aerosol-Jet Printing of Polymer-Wrapped (6,5) Carbon Nanotubes for Field-Effect Transistors", *Printed Electronics Europe*, May 2017

[4] "Highly reproducible Aerosol-Jet Printing of chirality-selected Carbon Nanotubes as semiconductor for high on/off-ratio field-effect transistors", *Workshop Carbon nanotubes meet 2D materials*, Heidelberg, Germany, November 2016

[5] "Impact of Aerosol-Jet Printing on Quality of Semiconducting Carbon Nanotubes", *17th International Conference on the Science and Application of Nanotubes and Low-dimensional Material*s, Vienna, Austria, August 2016

[6] "Charge and Energy Transfer in Aligned Carbon Nanotube Networks", *6th Workshop on Nanotube Optics and Nanospectroscopy*, Bad Staffelstein, Germany, June 2015

Eidesstattliche Versicherung gemäß §8 der Promotionsordnung der Naturwissenschaftlich-Mathematischen Gesamtfakultät der Universität Heidelberg

1. Bei der eingereichten Dissertation zu dem Thema
   Engineering of Aerosol-Jet Printed Carbon Nanotube Network Transistors
   handelt es sich um meine eigenständig erbrachte Leistung.
2. Ich habe nur die angegebenen Quellen und Hilfsmittel benutzt und mich keiner unzulässigen Hilfe Dritter bedient. Insbesondere habe ich wörtlich oder sinngemäß aus anderen Werken übernommene Inhalte als solche kenntlich gemacht.
3. Die Arbeit oder Teile davon habe ich bislang nicht an einer Hochschule des In- oder Auslands als Bestandteil einer Prüfungs- oder Qualifikationsleistung vorgelegt.
4. Die Richtigkeit der vorstehenden Erklärung bestätige ich.
5. Die Bedeutung der eidesstattlichen Versicherung und die strafrechtlichen Folgen einer unrichtigen oder unvollständigen eidesstattlichen Versicherung sind mir bekannt.

Ich versichere an Eides statt, dass ich nach bestem Wissen die reine Wahrheit erklärt und nichts verschwiegen habe.

Heidelberg, 11.Januar 2019

Marcel Rother